Doctoral Dissertation
博士論文

Detailed X-ray Spectral Modeling of Circinus X-1 Based on Radiative Transfer

(輻射輸送計算に基づくCircinus X-1の
X線スペクトルの詳細解析)

A Dissertation Submitted for the Degree of Doctor of Philosophy
December 2023

令和5年12月　博士（理学）申請

Department of Astronomy, Graduate School of Science,
The University of Tokyo
東京大学大学院理学系研究科天文学専攻

Mayu Tominaga
富永 愛侑

Abstract

At various levels of the cosmic hierarchy, the mass, energy, and angular momentum are redistributed through multiple astrophysical processes. One of the agents for such redistribution is the accreting compact objects, such as black holes and neutron stars in binaries. They accumulate matter through accretion from the surrounding environment and emit some fraction of it via jets and outflows. They are called "X-ray binaries" and ∼150 of them are known in our Galaxy. X-ray spectroscopy is a unique observational tool to unveil their redistribution processes. The goal of this thesis is to demonstrate that 3D radiative transfer modeling is a requisite to interpret the observed X-ray spectra. We apply the models based on the radiative transfer to the observed data of an actual object, show the effectiveness and limitations of the modeling, and demonstrate that this is the way to go in the X-ray microcalorimeter spectroscopy, which has just begun by the launch of *XRISM*.

We chose Circinus X-1 (Cir X-1 hereafter) as the target of this study. Amongst all the X-ray binaries, Cir X-1 stands out as an exception. None of the known X-ray binaries exhibit all the features observed in Cir X-1; (i) X-ray flux and spectral variability at various time scales, (ii) association to a radio jet and a supernova remnant (SNR) that gave birth to the neutron star, (iii) X-ray P Cygni line profile, which is a direct evidence of the presence of the outflowing material. The association with an SNR and a rapid decay of the 16.7 day orbital period suggest an extremely young age of ∼5000 years, making it the youngest known X-ray binary, hence an active agent of the mass, energy, and angular momentum redistribution. Cir X-1 is also a mysterious source. Despite observations over half a century, it is not even classified as a low-mass or high-mass X-ray binary. The binary inclination is unknown either. The origin of the X-ray continuum emission and significant variability associated with the orbital phase are also unknown.

We conducted the X-ray observations of Cir X-1 using *NICER* to cover an entire 16.7 day orbit. For the first time, the X-ray spectra of a uniform quality capable of resolving major emission lines were obtained at the highest cadence; at least once every four hours, corresponding to four degrees in azimuthal resolution in the viewing direction. Such a data set was not available before the advent of *NICER* in 2017, which features in a large collecting area with optics, moderate energy resolution, and operational flexibility. The observed spectra exhibit a variety of appearances based on which the three (dip, flaring, and stable) phases were defined. Although the spectral appearances are very different, we successfully constructed a common spectral model that explains all the three phases consistently with varying parameters. The model consists of partially covered disk blackbody emission plus H-/He-like Mg, Si, and S emission lines stemming from the photoionized plasma. The emission lines, in particular those of Fe, sometimes switch to the absorption lines.

Based on the phenomenological spectral model, we constructed a 3D geometry model of the binary system. The geometry includes the neutron star and the accretion disk at the center, which provides the incident X-ray emission for the photoionized plasma responsible for the line emission. The accretion stream from the companion star generates a geometrically-flared structure at a certain azimuth at the outer edge of the accretion disk, which makes the dip in the X-ray flux. The tail of the accretion stream is fragmentary, which causes rapid changes in the X-ray flux in the flaring phase after the dip phase. The emission lines suffer from little absorption due to the circumstellar matter even when the incident continuum emission is significantly absorbed, and the ionization

degree derived from the H/He-like line pairs is relatively stable over the entire orbit. This strongly suggests that the photoionized plasma responsible for the emission/absorption lines is located outside of the accretion disk.

Based on the 3D geometry model, we further proceeded to 3D radiative transfer modeling using the three different numerical solvers, `XSTAR`, `SKIRT`, and `MONACO`. We picked up three remarkable observational features to be explained by the radiative transfer model: (1) Change between the emission and absorption lines, (2) P Cygni profile of the Fe XXV and XXVI lines, and (3) Continuum X-ray flux changes in an orbit. We synthesized the X-ray spectra separately for the transmitted, scattered, and diffuse components. By considering a velocity structure and 3D distribution of the partial covering material, all the three observed features are qualitatively reproduced, demonstrating the effectiveness of the 3D radiative transfer modeling.

Our finding above strongly favors the interpretation that Cir X-1 is a LMXB viewed close to edge-on. The absence of an eclipse and the presence of dips constrain the inclination angle to be 60–75 degrees. The interaction of the accretion stream and the accretion disk in LMXBs creates a bulge-like structure at the position where the stream hits the accretion disk, which is observed as the dip phase. We also argue that the photoionized plasma is located outward of the accretion disk, not on the surface of the accretion disk.

In this study, we used a 1D two-stream solver code `XSTAR` and 3D Monte Carlo solver codes `MONACO` and `SKIRT` for numerical radiative transfer calculations. We summarized the differences among them and identified their advantages and disadvantages. None of the code satisfies the needs demanded by the data quality. Developing such codes require substantial investments. As an initial stride, we made an extension to `SKIRT` to calculate non-local thermal equilibrium lines in the X-ray region for the first time.

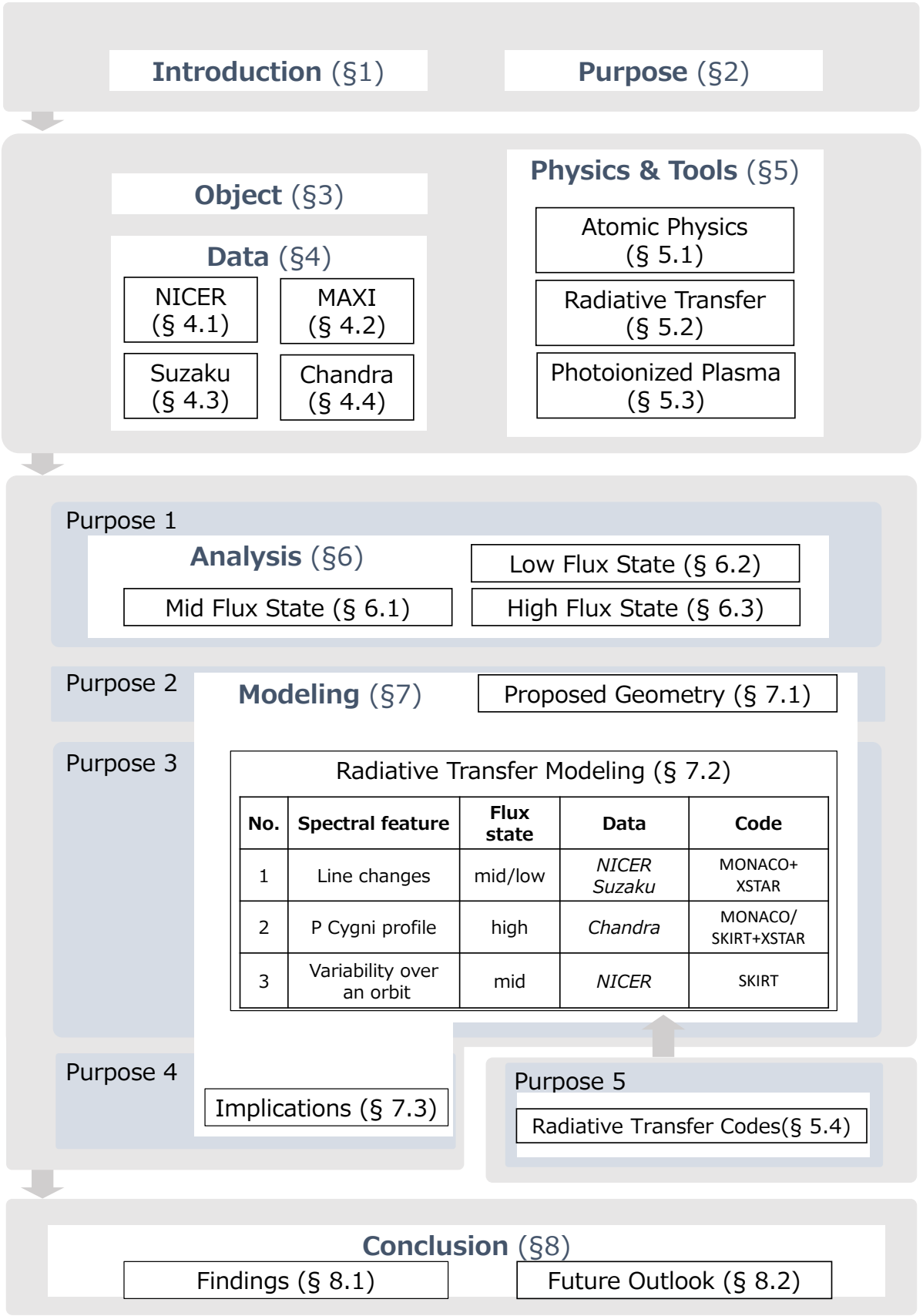

Figure 1: Struture of this thesis.

Contents

List of Figures **8**

List of Tables **11**

1 Introduction **12**

2 Purpose and Structure **16**
2.1 Purposes . . . 17
2.2 Structure . . . 20

3 Object — Circinus X-1 **22**
3.1 Binary Constituents . . . 24
3.1.1 Compact object . . . 24
3.1.2 Companion star . . . 24
3.2 System . . . 27
3.2.1 Binary period and ephemeris . . . 27
3.2.2 Eccentricity of orbit . . . 28
3.2.3 Extinction and distance . . . 29
3.2.4 Inclination . . . 29
3.2.5 Age . . . 32
3.3 X-ray Flux Variability . . . 35
3.3.1 Long term variability . . . 35
3.3.2 Orbital variability . . . 36
3.3.2.1 Periastron . . . 36
3.3.2.2 Apastron . . . 38
3.3.2.3 Long dip . . . 38
3.3.2.4 Short dips . . . 39
3.3.2.5 Variation over an entire orbit . . . 39
3.4 X-ray Energy Spectra . . . 44
3.4.1 Continuum emission . . . 44
3.4.2 Line emission in high flux state . . . 45
3.4.3 Line emission in low flux state . . . 47

4 Instruments & Observations **50**
4.1 *NICER* . . . 51
4.1.1 Mission & Operation . . . 51
4.1.2 Instruments . . . 51
4.1.2.1 Overview . . . 51
4.1.2.2 XRC . . . 51
4.1.2.3 SDD . . . 54

4.1.3 Observations . . . 54
4.1.4 Data reduction . . . 55
4.2 *MAXI* . . . 59
4.2.1 Mission & Operation . . . 59
4.2.2 Instruments . . . 59
4.2.3 Observations . . . 60
4.2.4 Data reduction . . . 60
4.3 *Suzaku* . . . 61
4.3.1 Mission & Operation . . . 61
4.3.2 Instruments . . . 61
4.3.2.1 XRT . . . 61
4.3.2.2 XIS . . . 61
4.3.3 Observations . . . 64
4.3.4 Data reduction . . . 64
4.4 *Chandra* . . . 66
4.4.1 Mission & Operation . . . 66
4.4.2 Instruments . . . 66
4.4.2.1 HRMA . . . 66
4.4.2.2 HETG . . . 68
4.4.2.3 ACIS . . . 69
4.4.3 Observations . . . 70
4.4.4 Data reduction . . . 70

5 Physics & Tools **74**
5.1 Atomic Physics . . . 75
5.1.1 Atomic structure . . . 75
5.1.1.1 Wave equations . . . 75
5.1.1.2 Quantum numbers . . . 77
5.1.1.3 Energy levels and labeling . . . 78
5.1.2 Photon-atom interactions . . . 79
5.1.2.1 Bound-free interactions . . . 79
5.1.2.2 Bound-bound interactions . . . 82
5.1.2.3 Free-free interactions and scattering . . . 83
5.2 Radiative Transfer . . . 87
5.2.1 Concept . . . 87
5.2.1.1 Basic equation . . . 87
5.2.1.2 Related quantities . . . 88
5.2.1.3 Formal solution . . . 89
5.2.2 Detailed balance and equilibrium states . . . 90
5.2.2.1 Thermodynamic equilibrium (TE) . . . 91
5.2.2.2 Local thermodynamic equilibrium (LTE) . . . 92
5.2.2.3 Non-local thermodynamic equilibrium (NLTE) . . . 93
5.2.3 Line formation, profile, and strength . . . 94
5.2.3.1 Line formation . . . 94
5.2.3.2 Line profile . . . 94
5.2.3.3 Line strength . . . 99
5.3 Photoionized Plasma . . . 101

5.3.1 Nebular approximation . . . 101
5.3.1.1 Photoionization and recombination . . . 101
5.3.1.2 Photoexcitation and stimulated/spontaneous emission . . . 102
5.3.2 Ionization parameter . . . 103
5.3.3 Balances . . . 104
5.3.3.1 Thermal balance . . . 104
5.3.3.2 Ionization balance . . . 105
5.3.3.3 Excitation balance . . . 109
5.4 Radiative Transfer Codes . . . 110
5.4.1 Two-stream solver . . . 110
5.4.1.1 XSTAR . . . 110
5.4.2 Monte Carlo Solvers . . . 114
5.4.2.1 MONACO . . . 114
5.4.2.2 SKIRT . . . 115
5.4.3 Further Development . . . 117
5.4.3.1 NLTE calculation in the X-rays . . . 117
5.4.3.2 Benchmarking . . . 117

6 Analysis **125**
6.1 Mid Flux State with *NICER* . . . 126
6.1.1 Definition of phases . . . 126
6.1.2 Spectral modeling . . . 127
6.1.2.1 Stable phase . . . 128
6.1.2.2 Dip phase . . . 128
6.1.2.3 Flaring phase . . . 131
6.1.2.4 All the phases . . . 131
6.1.3 Continuum emission . . . 132
6.1.4 Line emission . . . 133
6.2 Low Flux State with *Suzaku* . . . 138
6.3 High Flux State with *Chandra* . . . 140

7 Discussion **142**
7.1 Proposed Geometry . . . 143
7.1.1 Schematic view . . . 143
7.1.2 Rationale . . . 143
7.1.3 System scales . . . 144
7.2 Radiative Transfer Modeling . . . 147
7.2.1 Changes between line emission and absorption . . . 147
7.2.1.1 Purpose . . . 147
7.2.1.2 Setup . . . 148
7.2.1.3 Results . . . 149
7.2.2 P Cygni line profile . . . 154
7.2.2.1 Purpose . . . 154
7.2.2.2 Setup . . . 154
7.2.2.3 Results (1) — `MONACO` . . . 156
7.2.2.4 Results (2) — `SKIRT` . . . 159
7.2.3 X-ray light curve changes over an orbit . . . 161
7.2.3.1 Purpose . . . 161

7.2.3.2 Setup . . . 161
7.2.3.3 Results . . . 163
7.3 Implications . . . 167
7.3.1 Mass of the companion star . . . 167
7.3.2 Inclination angle . . . 169
7.3.3 Location of the photoionized plasma . . . 173

8 Conclusion **175**
8.1 Summary of Findings . . . 176
8.2 Future Outlook . . . 182

References **184**

Revisions **199**

Acknowledgements **200**

List of Figures

1 Struture of this thesis. . . . 3

1.1 Long-term light curve. . . . 13

3.1 Radial velocity curve obtained with infrared observations. . . . 26
3.2 Evolution of the orbital period of Cir X-1. . . . 27
3.3 Proposed model of Cir X-1. . . . 28
3.4 Spectra in the 8300 and 8900 Å. . . . 30
3.5 Radio image of Cir X-1. . . . 31
3.6 Radio and X-ray image of SNR. . . . 32
3.7 X-ray spectrum of the SNR. . . . 33
3.8 Long-term light curve. . . . 35
3.9 Long-term light curve observed with *MAXI*. . . . 37
3.10 An entire orbit light curve and hardness ratio observed with *ASCA*. . . . 40
3.11 Daily averaged light curve observed with *Chandra*. . . . 41
3.12 Spectra observed with *RXTE*. . . . 42
3.13 An entire orbit observations by *RXTE*. . . . 43
3.14 P Cygni profiles observed by *Chandra*. . . . 46
3.15 P Cygni profiles observed with *Chandra*. . . . 47
3.16 X-ray spectra in low flux state observed with *Chandra*. . . . 49

4.1 Configurations of *NICER*. . . . 52
4.2 Photo of XRC. . . . 53
4.3 An X-ray image bi XRC. . . . 53
4.4 Effective area of XRCs. . . . 54
4.5 Phase folded light curve obtained with *NICER*. . . . 55
4.6 Schematic view of *MAXI*. . . . 59
4.7 Schematic view of GSC. . . . 60
4.8 Schematic view of *Suzaku*. . . . 62
4.9 Schematic view of XRT. . . . 63
4.10 Effective area of XISs. . . . 63
4.11 Energy resolution of XISs. . . . 64
4.12 Schematic view of the *Chandra* satellite and sub-systems (Weisskopf et al., 2002). . . . 67
4.13 Schematic view of HRMA (Chandra-IPI-Teams, 2022). . . . 67
4.14 Effective area of HRMA, HRMA+HRC, and HRMA+ACIS (Chandra-IPI-Teams, 2022). . . . 68
4.15 Photo of the HETG (Canizares et al., 2005). . . . 69
4.16 Schematic view of HETGS. . . . 70
4.17 Effective area of HETGS. . . . 71
4.18 Schematic view of the ACIS focal plane (Chandra-IPI-Teams, 2022). . . . 72

4.19 Epochs of *Chandra* observations. . . . 72
4.20 Spectra observed with *Chandra*/HETGS. . . . 73

5.1 Sub-shell photoionization cross sections. . . . 81
5.2 Grotrian diagram of Fe XVII energy level and transitions (Pradhan and Nahar, 2011; Chen, Pradhan, and Eissner, 2003). . . . 83
5.3 Compton scattering. . . . 85
5.4 Line formation for different optical depth and source function. . . . 95
5.5 Normalized Voigt profile. . . . 97
5.6 Dijkstra profiles. . . . 98
5.7 Normalized Voigt function. . . . 100
5.8 Overview of the atomic processes. . . . 101
5.9 Charge population for representative atoms for $-3 < \log \xi < 5$ . . . 103
5.10 S curve. . . . 106
5.11 Various radiative transitions. . . . 107
5.12 Concept of the Monte-Carlo simulation (Odaka et al., 2011). . . . 115
5.13 Charge state distribution of Mg calculated by `XSTAR`. . . . 119
5.14 Emissivity of Mg XII by electron collisions. . . . 119
5.15 Geometry for the benchmarking. . . . 120
5.16 Radial distributions of parameter calculated by `XSTAR`. . . . 120
5.17 Level populations calculated with `XSTAR` and `SKIRT`. . . . 121
5.18 Simulated spectra with `XSTAR` and `SKIRT`. . . . 123
5.19 Simulated spectra around Mg XII Lyα^2. . . . 124

6.1 Light curve over an orbit observed with *NICER*. . . . 126
6.2 Light curve observed by *MAXI*. . . . 126
6.3 Bayesian blocking. . . . 127
6.4 Representative spectra in the stable phase. . . . 129
6.5 Representative spectra in the dip phase. . . . 130
6.6 Representative spectra in the flaring phase. . . . 131
6.7 changes in best-fit parameters. . . . 134
6.8 Changes in normalizations of line components. . . . 135
6.9 Changes in ionization parameters. . . . 137
6.10 Spectra observed with *Suzaku*. . . . 138
6.11 P Cygni profiles observed with *Chandra*. . . . 140

7.1 Schematic view of physical parameters related to Cir X-1. . . . 143
7.2 Proposed geometry of the system in the edge-on view. . . . 145
7.3 Schematic view of the model parameters α and β added to Figure 7.1. . . . 147
7.4 Equivalent widths and luminosities in low and mid flux states. . . . 148
7.5 Synthesized spectra of `MONACO` and `XSTAR`. . . . 150
7.6 Close-up view of Figure 7.5 around the Fe XXVI Lyα. . . . 150
7.7 Close-up view of Figure 7.5 around the Fe XXV Heα. . . . 151
7.8 Equivalent width obtained with `MONACO`. . . . 152
7.9 Equivalent width obtained with `MONACO` and `XSTAR`. . . . 152
7.10 Equivalent width obtained with `MONACO` for different intrinsic luminosity. 153
7.11 Geometry assumed in `MONACO` and `SKIRT`. . . . 155

7.12 Synthesized spectra simulated by MONACO for the viewing angle of 80–90 degree. . . . 157
7.13 Same with Figure 7.12 but for the viewing angle of 30–40 degree. . . . 157
7.14 Synthesized spectra simulated by MONACO for the viewing angle of 30–40 degree. . . . 158
7.15 Comparison of the diffuse component for different plasma volumes. . . . 159
7.16 Synthesized spectra simulated by SKIRT for the viewing angle of 90 degree. 160
7.17 Synthesized spectra simulated by SKIRT for the viewing angle of 0 degree. 160
7.18 Synthesized spectra simulated by SKIRT for the Fe Heα profile. . . . 160
7.19 Geometry of simulation. . . . 162
7.20 Normalized light curve calculated by SKIRT. . . . 164
7.21 Edge-on view of the partial covering material. . . . 166
7.22 Photoionized plasma simulated with CLOUDY. . . . 168
7.23 Relation between the companion mass and the inclination angle for two selected mass of the compact object. . . . 168
7.24 X-ray flux change of LMXBs. . . . 169
7.25 Estimation of the inclination. . . . 170
7.26 Schematic view of dipping LMXB. . . . 171
7.27 Orbital dependency of the column density due to an accretion stream. . . . 172
7.28 Location of the conventional photoionized plasma. . . . 173
7.29 Schematic view of an accretion ring. . . . 173

List of Tables

3.1 Comparison of the previous studies using the two-blackbody model. . . . 45

4.1 *NICER* observations in the Performance Verification phase and AO1 cycle. 56
4.2 *NICER* Observations in the AO2 cycle. 57
4.3 *NICER* observations in the AO3 cycle. 57
4.4 *NICER* observations in the AO4 cycle. 58
4.5 Observation of Cir X-1 by *Suzaku*. 65
4.6 Observations by *Chandra* HETGS. 70

5.1 Equations for distributions that hold in each equilibrium state. 91
5.2 Symbols used in the descriptions of the physics of `XSTAR`. 110
5.3 Comparison of the two Monte Carlo codes used in this work. 114
5.4 Energy levels and transitions of Mg XII (Foster et al., 2012). 118
5.5 Spectral decomposition. 123

6.1 Best-fit spectral parameters for continuum components observed by *Suzaku* with 90% confidence. 138
6.2 Best-fit spectral parameters for line components observed with *Suzaku* XIS 0. 139
6.3 Characterization of major P Cygni lines using *Chandra* observation (ObsID 1700). 141

7.1 Spectral decomposition. 149
7.2 Setup for the P Cygni profile simulation. 155
7.3 Energy levels and transitions of Fe XXV (Foster et al., 2012). 156

8.1 Revisions 199

Chapter 1

Introduction

Agents for energy redistribution in the Universe: At various levels of the cosmic hierarchy, energy is redistributed through a variety of astrophysical processes. The overall trend is toward the equipartition among the degrees of freedom to reach a thermal equilibrium, but some redistribution occurs away from the equilibrium, preventing the Universe from evolving monotonically toward a thermal death. One of the agents for such redistribution is the accreting compact objects (hereafter, we use the term for black holes and neutron stars). They accumulate matter through accretion from the surrounding environment and emit some fraction of it via jets and outflows. A part of the accumulated energy and angular momentum from the entire accreting mass is redistributed into a small fraction of the outgoing mass, which is a process in the opposite direction of the equipartition. Accreting compact objects are extremely rare; there are only $\mathcal{O}(1)$ supermassive black holes and $\mathcal{O}(100)$ stellar mass black holes and neutron stars in a galaxy. Yet, they are major agents for the energy and angular momentum circulation in the Universe. We want to understand the physical mechanisms of such circulation, which is an essential ingredient to unveil how the Universe has become the one we observe now and how it evolves in the future.

X-ray binaries: We focus on the stellar mass accreting compact objects. They constitute a binary system that hosts a compact object and a star. They are often discovered in X-rays. When the companion is a low-mass star with a mass of $\sim$1 $M_\odot$, they are called low-mass X-ray binaries (LMXBs). When the companion is a high-mass star with a mass of $\sim$10 $M_\odot$, they are called high-mass X-ray binaries (HMXBs). The compact object can be either a black hole or a neutron star. There are about 150 X-ray binaries known in our Galaxy (Liu, Paradijs, and Heuvel, 2001).

There are several advantages to studying X-ray binaries over super-massive black holes in terms of the mass accretion and outflow phenomena. First, the X-ray binaries are much more proximate, enabling us to collect more photons. The brightest X-ray binary (Sco X-1) has an X-ray flux of $\mathcal{O}(10^{-7}$ erg s^{-1} cm$^{-2})$, while the brightest extra-galactic source (3C 273) has $\mathcal{O}(10^{-10}$ erg s^{-1} cm$^{-2})$. Second, X-ray binaries have much shorter time scales of changes, enabling us to identify the accretion states more clearly on a human time scale. Together with the richer photon statistics, we can perform time-resolved spectroscopy. Third, which we think is the most important, is that we can observe the same X-ray binary in changing viewing angles as it rotates around the center of the mass in the binary system, where the accretion and the outflow are definitely nonaxis-symmetric. In contrast, a single extra-galactic source can be observed only in one direction. Fourth, the binary system parameters are constrained using various methods, which include the orbital elements, ephemeris, and viewing angles. Fifth, the properties

of the binary constituents are also constrained using various methods, including the mass, radius, magnetic field strength, and compactness of the object and the spectral type and luminosity class of the companion star. Finally, the gross loss of the mass and angular momentum of the binary is measurable through the change of the binary orbital period.

Circinus X-1: Amongst ∼150 X-ray binaries in our Galaxy, we choose Circinus X-1 (Cir X-1 hereafter) as a target of this study. This might sound like the worst choice; Cir X-1 has always been considered an exception for its anomalous X-ray flux and spectral changes at various time scales unseen in any other X-ray binaries. It started with a misidentification as a black hole binary when it was discovered (Margon et al., 1971) until type I X-ray bursts (Tennant, Fabian, and Shafer, 1986a) and kilo-Hz quasi-periodic oscillations (kilo-Hz QPO) (Boutloukos et al., 2006) were discovered, both of which are signatures of accreting neutron stars. Controversy still remains about whether the binary system is seen in the face-on or edge-on direction and about the origin of the X-ray emission. It is not even classified as the LMXB or HMXB, either of which most other X-ray binaries conclusively belong to.

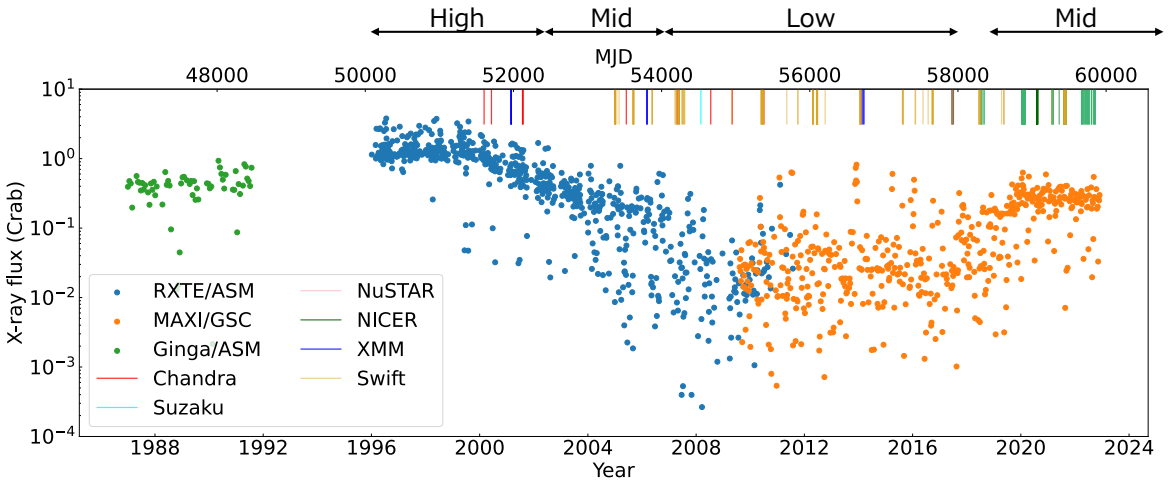

Figure 1.1: The long-term light curve by *Ginga* (green), *RXTE* (blue) and *MAXI* (orange) monitor observations. The vertical color lines show the epochs of pointing observations with various X-ray observatories (Tominaga et al., 2023).

We do, however, believe that Cir X-1 is the ideal target of choice for this study. Due to its brightness, it is one of the few X-ray sources with a record of monitoring for half a century since the dawn of the X-ray astronomy (Figure 1.1). The X-ray flux changed for a few orders, but the faintest state is still above the detection threshold of all-sky X-ray monitors in recent decades. It occasionally exhibits flux "dips" due to materials blocking the line of sight. In terms of the supermassive black holes, Cir X-1 sometimes behaves like a type I AGN out of dips and a type II AGN during dips. It behaves like a low-luminescence AGN during the low-flux state and the normal AGN in the high-flux state. Cir X-1, as a single target, can serve as a proxy to understand a wide range of accreting objects. Another feature unique to this source is its young age of ≈5000 years. Cir X-1 is the only X-ray binary associated with a supernova remnant that gave birth to

the neutron star, based on which its extreme youth was established (Heinz et al., 2013). Dynamical relaxation has not been reached at such a young age, and mass accretion and outflow phenomena may be enhanced in comparison with old systems. In fact, the P Cygni profile, which is strong evidence of outflow, was first discovered in this source in the X-ray band (Brandt and Schulz, 2000).

X-ray spectroscopy: How can we observationally access the mass accretion and outflow phenomena of accreting compact objects? X-ray spectroscopy is the method of choice. As in the name, the X-ray binaries are bright in the X-ray bands. Because of the intense X-ray flux from the vicinity of the compact object, the surrounding materials are often ionized by incident photons, producing a photoionized cloud. They are characterized by strong line emission due to radiative recombination and de-excitation of photoionized and photoexcited matter. Lines carry valuable information in their intensities, wavelengths, and profiles about the geometry, density, and velocity field of the line production and propagation regions.

With the advent of X-ray grating spectroscopy with the *Chandra* and *XMM-Newton* X-ray observatories (Weisskopf et al., 2000; Jansen et al., 2001) in 1999 and X-ray microcalorimeter spectroscopy with the *XRISM* X-ray observatory (Tashiro, 2023) in 2023, X-ray line spectroscopy became feasible with a spectral resolution to resolve the fine structures and even the profile of a line complex. With the two X-ray observing experiments onboard the international space station; *MAXI* (Matsuoka et al., 2009) and *NICER* (Gendreau et al., 2016), we can monitor and perform high-cadence observations of X-ray binaries exploiting their wide fields of view and operational flexibility.

3D radiative transfer: How can we interpret the observed X-ray spectra, in particular the line emission and absorption? Radiative transfer modeling is undoubtedly needed. The photoionized plasma, which provides diagnostics through lines, is far away from the local thermal equilibrium (LTE). Under a strong radiation field made by the compact object, the plasma is in non-local thermal equilibrium (NLTE), forcing us to calculate the charge and level populations of ions consistently with the radiation field; without their population, we cannot interpret the observed line strengths. This requires us to solve the radiative transfer equation with a code that implements all the relevant atomic transitions.

The photoionized plasma typically has a thickness of 10^{22}–10^{24} cm^{-2} in the hydrogen-equivalent column density. For electron scattering, the opacity is $\lesssim 1$. For resonance line scattering, the opacity easily exceeds 10^3. The line profiles are heavily distorted even with a completely symmetric and static cloud with no velocity field. The emission is often absorbed by the plasma itself and a part of the blocking materials in the line of sight. All of these require the radiative transfer calculation in a 3D space.

Goal: The need for the 3D radiative transfer calculation is obvious, yet almost no studies have been made to interpret the observed X-ray spectra of X-ray binaries based on the 3D radiative transfer calculations. The development of the 3D radiative transfer codes is far from satisfactory in comparison to the quality of observational data that we routinely obtain. This will be more serious in the near future as the X-ray microcalorimeter data will be available. Most authors still rely on a 1D radiative transfer code based on a numerical solver that is claimed to overestimate line intensities (Hubeny et al., 2001)

and is designed not to calculate scattering and diffusion over wavelengths. Some 3D radiative transfer codes are available, but their applications to X-rays are limited and not well tested.

These are the reasons for this thesis. It is time to embark on a journey to interpret the high-quality X-ray spectral data based on the 3D radiative transfer to extract vital information. We will demonstrate that this is possible even for one of the most challenging sources, Cir X-1. We will also show limitations of the currently available radiative transfer codes and make some progress. We hope that this thesis will convince the community that the 3D radiative transfer is the way to go in the X-ray microcalorimeter spectroscopy that has just begun. Let's start the journey now.

Chapter 2

Purpose and Structure

Contents

2.1 Purposes **17**
2.2 Structure **20**

Based on the background and goal set up in § 1, we list the purposes of this study (§ 2.1) and present the structure of this thesis (§ 2.2). We will set up the design of this research.

2.1 Purposes

As stated in § 1, our goal is to interpret the X-ray spectral variability of Cir X-1 based on the numerical calculation of the 3D radiative transfer. We take three steps. The goal of each step is as follows.

Purpose 1 To construct the coherent X-ray spectral model through the X-ray observation of Cir X-1 at the highest cadence over an entire binary orbit.

Purpose 2 To construct a 3D geometry of the X-ray emitting and absorbing material of the system.

Purpose 3 To apply the 3D radiative transfer calculation to several selected spectral features in the observations and explore its effectiveness and limitations.

In addition to the three goals in the mainstream above, we will further aim to achieve the following two additional goals.

Purpose 4 To reveal some of the debated parameters of Cir X-1 in comparison to some theoretical studies.

Purpose 5 To compare some numerical radiative transfer codes of different solvers and implementations, to clarify their differences and limitations, and to make some further developments for our purpose.

Each item is elaborated below with the corresponding sections.

Purpose 1 "To construct the coherent X-ray spectral model through the X-ray observation of Cir X-1 at the highest cadence over an entire binary orbit": As we will review in § 3.3 and § 3.4, the interpretation of the X-ray spectrum and variability of Cir X-1 is chaotic. The most critical reason behind this situation is the lack of high-resolution ($E/\Delta E \gtrsim 100$) X-ray spectral observations covering the entire orbit. High-resolution spectra were taken only at selected phases focusing mostly near the periastron, while spectra taken over many orbits were only at low spectral resolution.

What we need is the high-resolution X-ray spectra of uniform quality at a high cadence over an orbit with a spectral resolution capable of isolating major spectral features. This is exactly what we will present in this thesis. We will show 103 well-exposed spectra using *NICER* along the orbital phase with sufficient cadence, energy resolution, and uniform quality (§ 4.1). Such observations were not possible before the launch of *NICER* in 2017, which has the operational flexibility and unprecedented large collecting area with moderate energy resolution.

The observed spectra exhibit a variety of appearances, but we will construct a simple spectral model applicable to all the spectra. This will enable us to identify the components that contribute to the changes of the X-ray flux in different time scales (§ 6.1).

Purpose 2 "To construct a 3D geometry of the X-ray emitting and absorbing material of the system": Observed spectra are the integration of all the emission and absorption in the line of sight. The 3D information is projected into 1D. However, we can reconstruct a 3D geometry by using the spectral variation. An entire coverage of one orbit in our data makes it possible to see the system in 360 degrees in changing azimuthal directions. The cadence of our data set corresponds to the angle resolution of $\sim$3.6 degrees. This result will be presented in § 7.1.

Purpose 3 "To apply the 3D radiative transfer calculation to several selected spectral features in the observations and explore its effectiveness and limitations.": Based on the 3D geometry, we will conduct the radiative transfer calculation. We will synthesize the X-ray spectral models and compare them with the data. We will pick up three remarkable features in the observations to compare with the simulation. We will not "fit" the data though, as the current model is simple and the tools are not mature enough to do so. The three features are the following:

Feature 1 Changes between the line emission and absorption through an orbit (§ 7.2.1).
Feature 2 P Cygni line profile (§ 7.2.2).
Feature 3 X-ray light curve variation over an orbit (§ 7.2.3).

For feature 1, we will use the *NICER* and *Suzaku* data, in which the same lines (e.g, Fe XXV Heα and Fe XXVI Lyα) change between the emission and absorption (§ 6.1.4, 6.2). This should be explained as the relative strength of the incident emission through the photoionized plasma ("transmitted emission") and the emission from the plasma itself ("diffuse emission"). We also need to consider the "scattered emission" of the incident emission by the photoionized plasma. We will run radiative transfer calculations and decompose the synthesized spectra into the transmitted, diffuse, and scattered emission. We will then re-synthesize with different weights to explain the observed changes among *NICER* and *Suzaku* spectra. The changes in the weights reflect the changes of the geometry over both short (on the order of days) and long (spanning decades) time scales.

For feature 2, the P Cygni line profile was observed with *Chandra* when Cir X-1 was in the high flux state (§ 3.4.2). This is direct evidence of the presence of outflow motion of the photoionized plasma. We will perform a radiative transfer calculation of photoionized plasma with an outflow velocity and compare the result with the observations.

For feature 3, the X-ray flux exhibits rapid changes for $\sim$30% of the orbit in our *NICER* data (§ 6.1.2). Our model will explain these changes due to variations of the column density and covering fraction of the material in the line of sight. We will synthesize the X-ray light curve using the 3D radiative transfer code `SKIRT` to compare with the observed light curve. This result will strongly favor the edge-on geometry of the system.

Purpose 4 "To reveal some of the debated parameters of Cir X-1 in comparison to some theoretical studies": To our knowledge, there are no studies of interpreting observed X-ray spectra of X-ray binaries along the orbital phase based on 3D radiative transfer calculations. This will be done for the first time using one of the most complex X-ray binaries, Cir X-1, in this study. We will obtain some novel perspectives about the accretion and outflow phenomena of Cir X-1. These will be compared to theoretical models established for general X-ray binaries. We will unveil some of the defining parameters of this mysterious source (viewing angles, companion mass), which has been under intensive debate for many decades.

Purpose 5 "To compare some numerical radiative transfer codes of different solvers and implementations, to clarify their differences and limitations, and to make some further development for our purpose": Several solvers have been proposed for the numerical calculations of radiative transfer (Peraiah, 2001). The widely used solvers include the accelerated lambda iteration method, the discrete-ray method,

and Monte Carlo method. In the X-ray astronomy, the `XSTAR` code (T. Kallman and Bautista, 2001) is dominantly used, which is an implementation based on a 1D version of the discrete ray method; i.e., two-stream method. Some authors use the `SPEX` code (Kaastra, Mewe, and Nieuwenhuijzen, 1996). Yet another code `CLOUDY` has been most widely used in the optical and infrared band, and started its application to the X-ray band recently (Chakraborty et al., 2020a; Chakraborty et al., 2020b; Chakraborty et al., 2020c; Chakraborty et al., 2021; Chakraborty et al., 2022).

However, these 1D codes have limitations. In particular, the scattering and non-radially symmetric distribution of matter cannot be modeled with the 1D codes. Monte Carlo solver is a prospective approach to 3D problems, but most of the codes are still under development. One of the industry standard codes `SKIRT` (Baes et al., 2003; Baes et al., 2011; Camps and Baes, 2015; Camps and Baes, 2020) started its X-ray application only this year (Vander Meulen et al., 2023) for limited atomic processes. Another code `MONACO` (Watanabe et al., 2003; Watanabe et al., 2006; Odaka et al., 2011) has been used in the X-ray astronomy for some 10 years (Tomaru et al., 2023; Tanimoto et al., 2019; Mizumoto et al., 2019; Hagino et al., 2016), but it is not sufficiently tested for spectral line features. None of the solvers and implementations meet the needs for the interpretation of the observed data. This will be even worse for the higher-quality spectral data to be brought by *XRISM* very soon.

We will make comparisons among three different implementations of the numerical radiative transfer codes, `XSTAR`, `MONACO`, and `SKIRT`. After reviewing the basic physics of the atomic transitions (§ 5.1), radiative transfer (§ 5.2), and photoionized plasma (§ 5.3), we will describe the assumptions and limitations of these implementations (§ 5.4). We will apply these codes for real problems compared to observations (§ 7.2), where we will identify their differences and limitations and discuss how we can work around them with hybrid usages.

The limitations of existing 3D Monte Carlo solvers need to be overcome. What we need is a code that can calculate the NLTE radiative transfer in the X-ray band with flexible 3D geometry construction capabilities. None of the existing tools satisfy this requirement. In this work, we will make an extension to `SKIRT`, so that the NLTE calculation can be done within this tool, based on the recent work by Matsumoto et al. (2023) in the infrared spectroscopy for several molecular lines. In § 5.4.3, we will show how to extend this calculation to all the major atomic species of all charge states for the X-ray spectroscopy.

2.2 Structure

In § 1, we have set up the context and strategy of this study. We clarified (1) what kind of **object** should be studied, (2) what kind of **data** set needs to be assembled, (3) what kind of **physics and tools** are necessary, (4) what kind of **analysis** should be performed, and (5) what kind of features should be **model**ed. The rest of this thesis is organized to address these items: (1) in § 3, (2) in § 4, (3) in § 5, (4) in § 6, and (5) in § 7 to **conclude** in § 8. The logical relationship among them is depicted in Figure 1.

Object (§ 3)

First, a review of Cir X-1 is presented. The source has been studied since the dawn of X-ray astronomy, and there is a wealth of information available. Our review focuses on items that will be used in the discussion of this thesis. We start by elaborating on the binary constituents (§ 3.1) of both the compact object and the companion star. Subsequently, we provide a summary of previous studies on the physical parameters of the binary system (§ 3.2), including ephemeris, orbit, distance, inclination, and age. Next, we review the most remarkable feature of this source, namely X-ray variability (§ 3.3) at different time scales. We finally describe the X-ray spectral features (§ 3.4) and reveal unique features of this source observed in different flux states.

Data (§ 4)

Cir X-1 has been continuously monitored by three generations of all-sky X-ray monitors onboard the *Ginga* and *RXTE* satellites and the *MAXI* experiment placed on the International Space Station (ISS). We used *MAXI* (§ 3.2) for the most recent monitoring. We recognized that a particular flux change pattern over a binary orbit was repeated responsibly (Tominaga et al., 2023), which is quite unusual for this source that is notorious for having irregular variability. We obtained our data set using *NICER* (§ 3.1), another X-ray observing experiment placed on the ISS. Cir X-1 was observed with ∼100 snapshots over the entire orbit. X-ray spectra were obtained at the highest cadence ever, which is the main data set of this thesis. The *NICER* observation was performed when the source was in the mid flux state. X-ray spectra of different states help us establish a physical model of the X-ray emission. Thus, we used the *Suzaku* X-ray observatory (§ 3.3) data in the low flux state and the *Chandra* X-ray observatory (§ 3.4) data in the high flux state.

Physics and Tools (§ 5)

What we will study is the emission from photoionized plasmas (§ 5.3). The photoionized plasma is characterized by numerous and intense emission lines of atomic transitions in the X-ray band. The atomic states in the plasma are heavily influenced by the strong radiation field of the neutron star. We need a basic understanding of both the microscopic and macroscopic views of the photon interaction with matter. The former is the subject of atomic physics (§ 5.1) while the latter is the subject of radiative transfer (§ 5.2). Finally, we will review the numerical solvers for the calculation of radiative transfer and make further developments when necessary (§ 5.4).

Analysis (§ 6)

We will then discuss the data analysis of the mid (§ 6.1), low (§ 6.2), and high (§ 6.3) flux states respectively using *NICER*, *Suzaku*, and *Chandra*.

Model (§ 7)

We select three distinct features of the data: (1) Line change between emission and absorption in the mid and low flux state, (2) P Cygni profile in the high flux state, and (3) X-ray flux variability repeated over an orbit. We start by establishing the geometry of the system (§ 7.1). We will then construct a model to explain the three features based on the calculation of radiative transfer (§ 7.2). Finally, we provide implications obtained by the analysis (§ 7.3).

Conclusion (§ 8)

To conclude, we will summarize the findings of this study in § 8.1 and present future prospects in § 8.2.

Chapter 3

Object — Circinus X-1

Contents

3.1 Binary Constituents 24
3.1.1 Compact object 24
3.1.2 Companion star 24
3.2 System 27
3.2.1 Binary period and ephemeris 27
3.2.2 Eccentricity of orbit 28
3.2.3 Extinction and distance 29
3.2.4 Inclination 29
3.2.5 Age 32
3.3 X-ray Flux Variability 35
3.3.1 Long term variability 35
3.3.2 Orbital variability 36
3.4 X-ray Energy Spectra 44
3.4.1 Continuum emission 44
3.4.2 Line emission in high flux state 45
3.4.3 Line emission in low flux state 47

In this chapter, we review previous observations of Cir X-1. Numerous studies were made across wavelengths for this exceptional source, but we focus on topics that are related to the discussion of this thesis. In particular, we highlight some of the remaining controversies about the nature of this source and how we will resolve them in this thesis.

In § 3.1, an overview of the binary constituents is presented for the compact object (§ 3.1.1) and the companion star (§ 3.1.2). The neutron star nature of the compact object was established. The nature of the companion star remains uncertain with no clear photospheric features observed in the optical and infrared spectra.

In § 3.2, we summarize the representative parameters of the system, which we use in this thesis. Parameters include the binary period and ephemeris (§ 3.2.1), the orbital elements (§ 3.2.2), the extinction and distance to the source (§ 3.2.3), the inclination or the viewing angle to the source (§ 3.2.4), and the age (§ 3.2.5). Cir X-1 is unique among all the X-ray binaries for having the radio jet, X-ray P Cygni profiles, and association with a supernova remnant. These contribute to the constraints of the inclination and age, sometimes with contradictory theories.

We then move on to the X-ray description of the source in its flux variation (§ 3.3) and the spectra (§ 3.4). In the former, we review the long-term variability spanning decades (§ 3.3.1) using the X-ray monitor data for half a century and shot-term variability within an orbital period (§ 3.3.2).

In §3.4, we summarize the X-ray spectral analysis and its interpretations. Before the 2000s, the origin of the continuum emission was at the focus (§ 3.4.1). After the advent of the X-ray grating spectrometers, the interest shifted to line emission. We summarize the finding made during the high flux (§ 3.4.2) and low flux (§ 3.4.3) states. We discuss both continuum and line emission later in this thesis.

3.1 Binary Constituents

3.1.1 Compact object

Cir X-1 has been under study since its discovery by Margon et al. (1971) in the early days of the X-ray astronomy. Initially, it was believed to be a black hole binary due to observational similarities with the black hole candidate Cygnus X-1 discovered at around that time (Toor, 1977).

However, the several pieces of the evidence argued for the neutron star nature. One is the detection of Type I X-ray bursts. Eight bursts were observed in 1984 (Tennant, Fabian, and Shafer, 1986b) and three more in 1985 (Tennant, Fabian, and Shafer, 1986a). The source had been inactive since then, until Linares et al. (2010) detected 15 bursts in 2010. Some of these bursts exhibited typical Type I characteristics, including decaying X-ray flux with a cooling blackbody temperature. Another is the discovery of twin kilohertz QPOs with *RXTE*/PCA during the high-flux states (Boutloukos et al., 2006). This arises from the interaction between the magnetic field of the neutron star and the surrounding disk. Yet another is the typical behavior as a "Z source" (Oosterbroek et al., 1995; Shirey et al., 1998; J. L. Qu, Yu, and Li, 2001), which is the transition in the hardness intensity diagram typical of neutron stars. Together with the lack of coherent pulsation, all these features point to an accreting neutron star with low magnetic fields (Klis, 2006).

3.1.2 Companion star

Despite the primary being conclusively identified as a neutron star, the nature of the companion star is still unknown. Photospheric absorption features of the companion star, which would provide the most conclusive evidence of the dynamical mass, have not been clearly identified. Most features appear in emission, with the exception of absorption in a limited orbital phase in optical and infrared spectra. This suggests that the optical and infrared emission is dominated by materials other than the companion star. Nevertheless, some authors attribute the emission features to the companion star. Others suggest that the emission features are from the accretion disk around the compact object. We will argue differently in § 7.3.1 for the possibility that the optical and infrared emission and absorption features are from the photoionized plasma. Some of the results are summarized below.

Spectral features: In the optical band, the spectra are characterized by the presence of Hα emission line of strongly asymmetric profile (R. Mignani, Caraveo, and Bignami, 1997). H. M. Johnston, Fender, and Wu (1999) and H. M. Johnston et al. (2001) found that this Hα line is highly variable, both within a single orbit and over many years. Jonker, Nelemans, and Bassa (2007) obtained the optical spectra in the I band ranging from 8300–9800Å for an entire orbit. They also detected other spectral features such as diffuse interstellar band absorption, He I line at 8648 Å and Paschen–12 line at 8750 Å.

In the near-infrared (NIR) band, J. S. Clark et al. (2003) identified strong emission lines of H I and He I and weak emission line of Fe II at 2.089 μm. The origin of these emission lines is unknown. Given their difference in the formation temperatures, they are likely produced in various regions within the binary system.

The velocity field around the system has been examined through analysis of the Doppler shift of the spectral lines. R. Mignani, Caraveo, and Bignami (1997) detected a double-peaked profile of the Hα line, which was fitted with a narrow and a broad Gaussian function during observations with HST/FOS in June 1995. The broad component (σ = 11.4 Å) is centered almost at the rest frequency, while the narrow component (σ = 3.32 Å) is red-shifted with a radial velocity of 400 km s^{-1}. As no blue-shifted line was observed, the authors discussed that the observed line originates from a compact region of a highly inclined accretion disk. If the region corresponds to a hot spot interacting between the disk and the accretion stream, it resulted in the observation of either a red-shifted or blue-shifted line depending on the orbital period. It is also possible that only the blue-shifted component was masked from the deep absorption observed in part of the orbital phase in the contemporaneous *ASCA* observations (Brandt et al., 1996).

H. M. Johnston, Fender, and Wu (1999) also observed the Hα line using the Anglo Australian Telescope in January 1997. This observation revealed a redshift of 370 km s^{-1} for the narrow line and a blueshift of 310 km s^{-1} for the broad line. In contrast to R. Mignani, Caraveo, and Bignami (1997)'s interpretation, they proposed that the narrow component was associated with the heated surface of the companion star, while the broad component represented an optically thick, high-velocity outflow driven by super-Eddington accretion onto the neutron star.

Spectral type and luminosity class: If the companion star fills the Roche lobe, and the optical radiation comes from the irradiated companion star, the average density of the companion star should be $\langle\rho\rangle < 0.003$ g cm^{-3} (Paczynski, 1971). However, theoretically, no young stars meets this criterion (H. M. Johnston, Soria, and Gibson, 2016). Therefore, they proposed that the companion star may have been warmed up and puffed by the supernova explosion, leading to a lower surface effective temperature. In this case, the companion star can be a low-mass star that is not fully evolved.

On the one hand, another observation made in the optical I-band suggests a B5–A0 supergiant star with a relatively low magnitude of $M_V = -4.9$ (Jonker, Nelemans, and Bassa, 2007). On the other hand, the NIR K-band observations indicate mid-B supergiant from line features, though the authors caution that the recurrent photometric and spectroscopic variability is unlikely to originate only from the companion star (J. S. Clark et al., 2003).

If the optical radiation originates from the accretion disk instead, the absence of typical stellar photospheric features in the optical and NIR spectra can be explained (H. M. Johnston, Soria, and Gibson, 2016). However, it becomes necessary to assume an asymmetric accretion disk or accretion flow to reproduce the pronounced flux and spectral variations. We will reveal and model such an asymmetry in § 7.2.3. J. S. Clark et al. (2003) speculated that the emission from the companion is obscured by the accretion disk, synchrotron radiation from the jet, or thermal bremsstrahlung from the disk outflow.

The possibility remains that the companion star is a Be-type star, which is a rapidly rotating B-type star with a decretion disk. However, the double-peaked line profile, which is one of the characteristic features of the Be stars, was not detected either in Jonker, Nelemans, and Bassa (2007) or H. M. Johnston, Soria, and Gibson (2016). Also, the orbital period is shorter than other Be/X-ray binaries (Reig, 2011). Although the near-infrared spectra are similar to those of the Be/X-ray binaries, the line flux is only

∼20 % of the predicted value and cannot be conclusively determined (J. S. Clark et al., 2003).

Mass: Assuming that the observed absorption lines and radial velocity curves (Figure 3.1) are attributed to the companion star, Jonker, Nelemans, and Bassa (2007) derived the relationship between the inclination and the companion mass. The companion mass is constrained to be $< 10 M_{\odot}$ for inclinations > 13.7 degrees. For the relatively edge-on assumption, it is considered to be around 0.4 $M_{\odot}$.

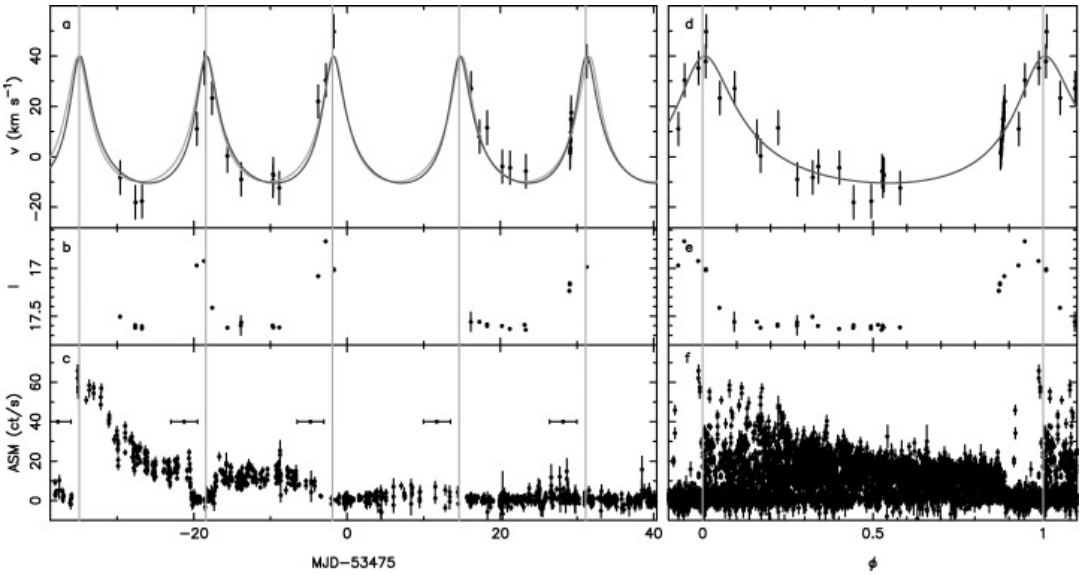

Figure 3.1: Left panels show (a) the radial velocity curve obtained from cross-correlating spectra of Cir X-1, (b) I-band magnitude, and (c) the simultaneous observations of X-ray flux by *RXTE* /ASM. Right panels are folded plots of the left panels (Jonker, Nelemans, and Bassa, 2007).

3.2 System

3.2.1 Binary period and ephemeris

Several ephemerises and characteristic time scales are proposed for the binary system. One is based on radio flux, which exhibits periodic peaks. A long-term data set is used to derive the following ephemeris (Stewart et al., 1991).

$$t(N) = 43076.37 + (16.5768 - 0.0000353 \times N) \times N \text{ MJD} \tag{3.1}$$

This ephemeris requires a large quadratic correction of $\dot{P} = -4.26 \times 10^{-6}$, leading to an estimate of the characteristic time $(P/2\dot{P})$ of ∼5600 years. All the other proposed ephemerises below suggest a very large quadratic correction, hence a very short characteristic time.

The X-ray flux sometimes shows recurrent behavior (for more details, see § 3.3.1). With the use of the phase dispersion minimization technique, as well as the fast Fourier transform analysis, P. M. S. Parkinson et al. (2003) derived the orbital period from the periodogram. They fitted the evolution of P (Figure 3.2), finding the best-fit parameters as $P_0 = 16.6534 \pm 5.6 \times 10^{-3}$ and $\dot{P} = -1.6261 \times 10^{-5} \pm 1.109 \times 10^{-6}$, yielding $(P/2\dot{P})$ of ∼1400 yr.

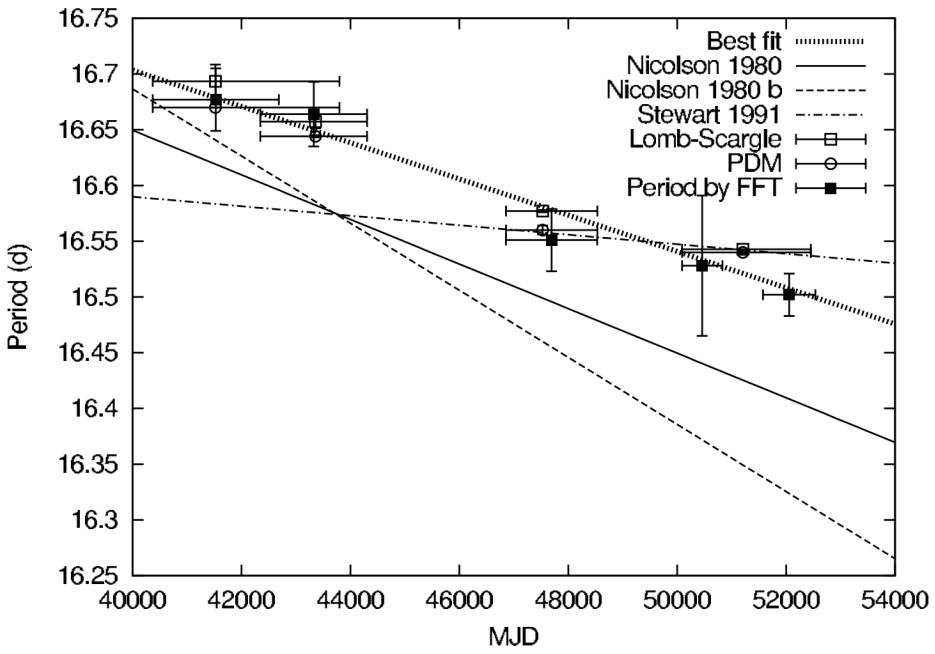

Figure 3.2: Evolution of the orbital period of Cir X-1 (P. M. S. Parkinson et al., 2003).

Clarkson, Charles, and Onyett (2004) also investigated the periodic behavior of Cir X-1, focusing on the X-ray dips rather than the maxima. They utilized the *RXTE*/ASM data for their study and obtained

$$t(N) = 50081.76 + (16.5732 - 0.000215 \times N) \times N \text{ MJD} \ . \tag{3.2}$$

Finally, Nicolson (2007) defined the ephemeris using 21 well-observed radio flares as follows:

$$t(N) = 43076.32 + (16.57794 - 0.0000401 \times N) \times N \text{ MJD}. \tag{3.3}$$

This ephemeris has become the one most widely used in recent studies, which we also adopt in this work. In fact, this ephemeris nicely represents the repeated behavior of the recent data taken with *NICER* (§ 6.1.1).

3.2.2 Eccentricity of orbit

The eccentricity of the binary orbit provides crucial information about the binary evolution, as the orbit tends to become more circular after experiencing sufficient tidal interactions. On the contrary, young binary systems, having not undergone enough angular momentum extraction, often exhibit highly eccentric orbits. The orbital characteristics significantly influence the accretion process.

Murdin et al. (1980) calculated the eccentricity in terms of the morphology of the light curve. They assumed that the luminosity variation is caused by the radiation from the X-ray emitting object being blocked by the stellar wind. They found $e \sim 0.8 \pm 0.1$.

H. M. Johnston, Soria, and Gibson (2016) took the same approach by assuming that the optical light curve variation is caused by the companion star's surface being illuminated by the X-ray emission of the neutron star. The increase or decrease in the fraction of emission is calculated for representative e values and the mass of the companion star based on the positional relationship between the binary star constituents. By comparing the results with optical light curves, they concluded that $e = 0.4$ is the most plausible value.

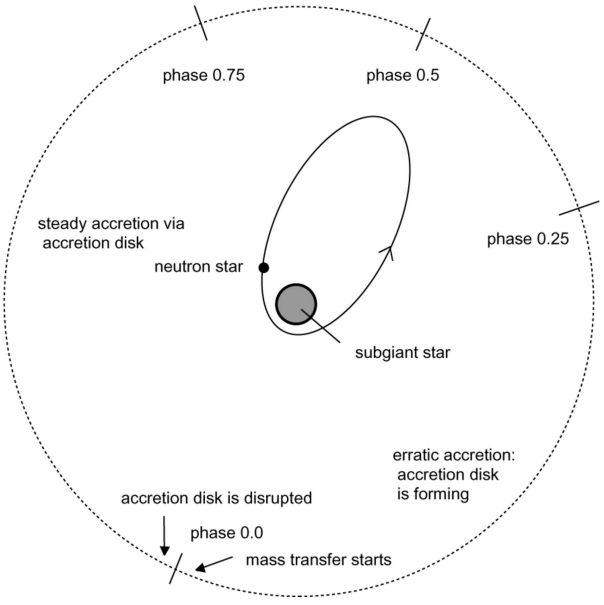

Figure 3.3: Model for Cir X-1 orbit (H. M. Johnston, Fender, and Wu, 1999).

Tauris et al. (1999) calculated the dynamical effects of a supernova with analytical formulae to constrain the kinematic parameters with Monte Carlo simulation. It calculates the changes in momentum caused by supernova explosions. The pre-supernova binary orbit is assumed to be circular. They derived the orbital eccentricity $e = 0.94 \pm 0.04$ under the assumption that the companion is a low-mass star with a mass of $< 4.6 M_{\odot}$.

Jonker, Nelemans, and Bassa (2007) conducted phase-resolved optical spectroscopy and photometry in the I band (Figure 3.4) and discovered numerous Paschen absorption lines throughout almost all phases of the orbital cycle, with the exception of a brief absence around the periastron. By cross-correlating spectra at various orbital phases, they determined the relative radial velocity of the system as $e = 0.45$ and $a \sin i = 16.9$ light seconds. We adopt these values in this work.

3.2.3 Extinction and distance

The interstellar extinction toward Cir X-1 is large for being located in the Galactic plane at $(l, b) = (322.1, 0.038)$. Various authors have employed X-ray observations to determine the interstellar absorption toward the source. D'Aì et al. (2012) proposed a minimum value for the interstellar absorption as $N_{\rm H} \sim 1 \times 10^{22}$ cm^{-2} corresponding to $A_V > 5.6$ mag. It is an upper limit of the interstellar contribution to the total observed absorption, which also includes the circumstellar contribution local to Cir X-1. H. M. Johnston, Soria, and Gibson (2016) inferred an extinction $E(B-V) = 2.44 \pm 0.21$ from the equivalent widths of the diffuse interstellar bands and estimated $A_V = 3.1E(B-V) = 7.6 \pm 0.6$ mag. They also obtained a color excess of 3.39 between the Hα and Hβ lines, resulting in A_V >9.1 mag. Assuming a distance of 9.4 kpc, the absolute magnitude is estimated as $-2.2 < M_V < -0.7$. Jonker, Nelemans, and Bassa (2007) also calculated these values as $9 < A_V < 12$ and $-4.9 < M_V < -2.5$.

An extreme extinction toward Cir X-1 makes it difficult to determine the distance to the source using conventional methods. There had been several competing estimates. A distance of 5.5 kpc was proposed assuming that the source is a run-way binary associated with the SNR G321.9-0.3 (D. H. Clark, J. H. Parkinson, and Caswell, 1975). Another estimate is based on the 21 cm absorption feature observed during a radio outburst. Its velocity extends to -90 km s^{-1}, indicating a tangential point of the spiral arm at 7.9 kpc (Goss and Mebold, 1977). Iaria et al. (2005) computed the visual extinction (Hakkila et al., 1997) and the equivalent hydrogen column (Predehl and Schmitt, 1995) to compare with the $N_{\rm H}$ values obtained from the X-ray spectrum fitting. They argued the distance to be 4.1±0.3 kpc.

In recent years, an improvement was made by the dismissal of attachment to SNR G321.9–0.3 (R. P. Mignani et al., 2002), but a different SNR was found to be related to Cir X-1 in both X-ray and radio observations (Heinz et al., 2013) (§ 3.2.5). In subsequent observations, Heinz et al. (2015) derived 9.4 kpc from a set of X-ray light-echo rings associated with the clouds that emit CO lines. The value is consistent with 7.8–10.5 kpc by Jonker and Nelemans (2004), who used the X-ray luminosity of the Type I bursts showing evidence of the photospheric expansion. In this thesis, we assume 9.4 kpc for the distance to Cir X-1.

3.2.4 Inclination

Regarding the disk inclination of the system, various observations yielded contradicting results between the face-on and the edge-on geometry.

The face-on geometry is mainly advocated on the basis of jet observations. In radio observations, a jet-like structure associated with a radio nebula was detected (Stewart et al., 1993). Fender et al. (2004) characterized the observed arcsec-scale jet with a

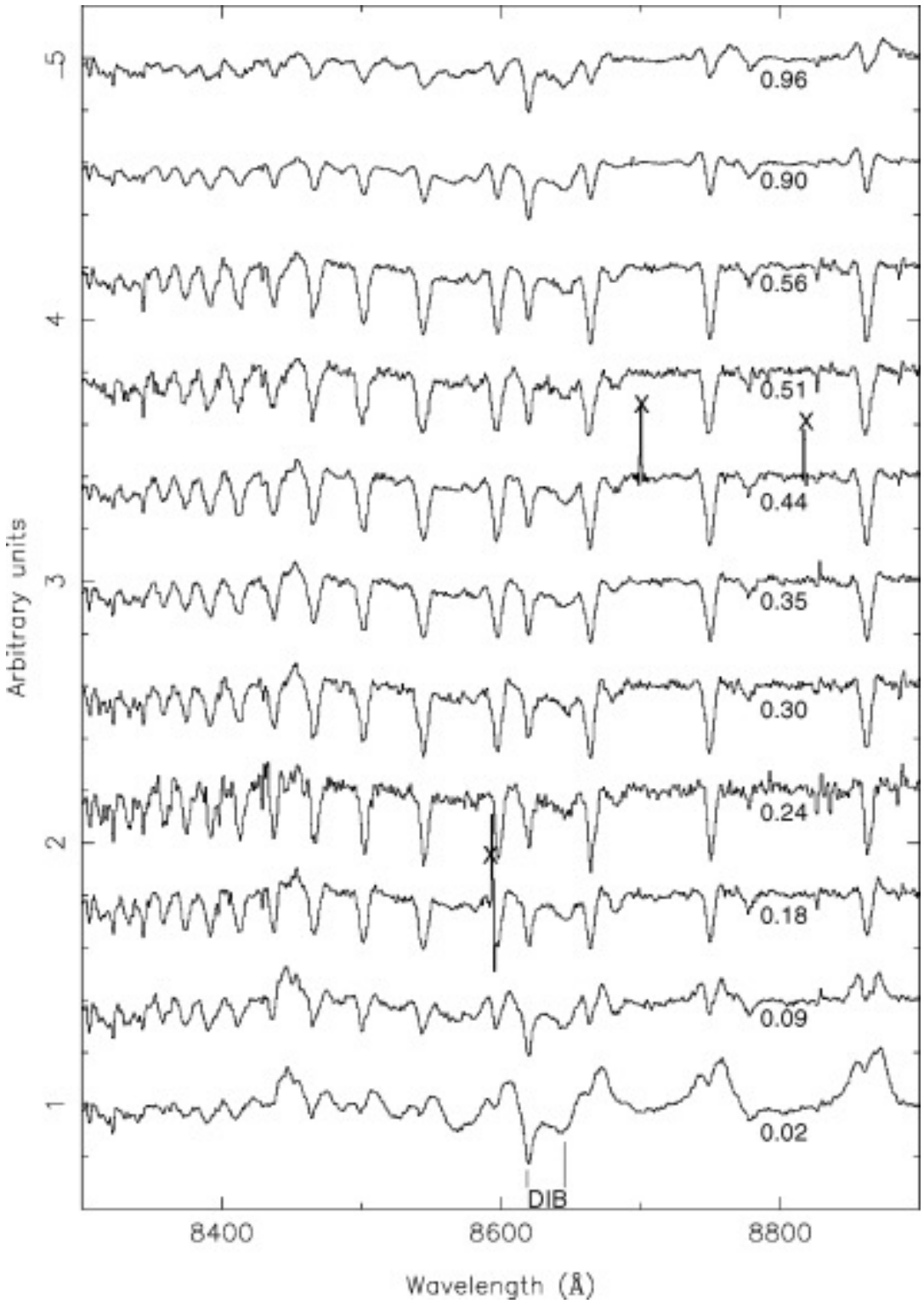

Figure 3.4: Spectra in the 8300 and 8900 Å range for an orbit (Jonker, Nelemans, and Bassa, 2007). The Paschen absorption lines on the right-hand side are observed except for the periastron passage at the bottom, at which the strong emission lines replace the absorption lines. Spectra were folded according to the ephemeris of the equation 3.2.

Lorentz factor $\Gamma > (1-\beta^2)^{-1/2} \sim 10$, where $\beta = v/c$ is the velocity of the jet (v) relative to the speed of light (c). The inclination of the jet was estimated as $\theta < 5°$ from the relation

$$\beta_{\text{apparent}} = \frac{\beta \sin\theta}{(1-\beta\cos\theta)}, \tag{3.4}$$

with the apparent velocity β_{apparent}, which was related to the proper motion of ~400 mas day^{-1} using

$$\beta_{\text{apparent}} \sim \left(\frac{d}{\text{kpc}}\right)\left(\frac{\mu}{170 \text{ mas day}^{-1}}\right). \tag{3.5}$$

The subsequent analysis by Tudose et al. (2008) and the subsequent observations by Calvelo et al. (2012) agreed with the conclusion of a very high jet velocity.

The jet axis was found to be precessing. Coriat et al. (2019) observed the region around Cir X-1 in multiple radio frequencies and noted that the flux contours exhibited a symmetric distribution at each frequency, but different orientations among different frequencies (Figure 3.5). They argued that this is due to interactions with jet and surrounding materials. Alternatively, they also argued that a similar structure could be created if the jet is in precessional motion. The kinetic jet model (Hjellming and K. J. Johnston, 1981) provided the optimal fit, indicating a 5-year precession period with parameters β =0.5 and $\theta = 86°$. Calvelo et al. (2012) also observed structural changes of the jet and interpreted it as an asymmetry in the distribution of surrounding matter or a change in the direction of the outflow due to precessional motion or curvature of the jet.

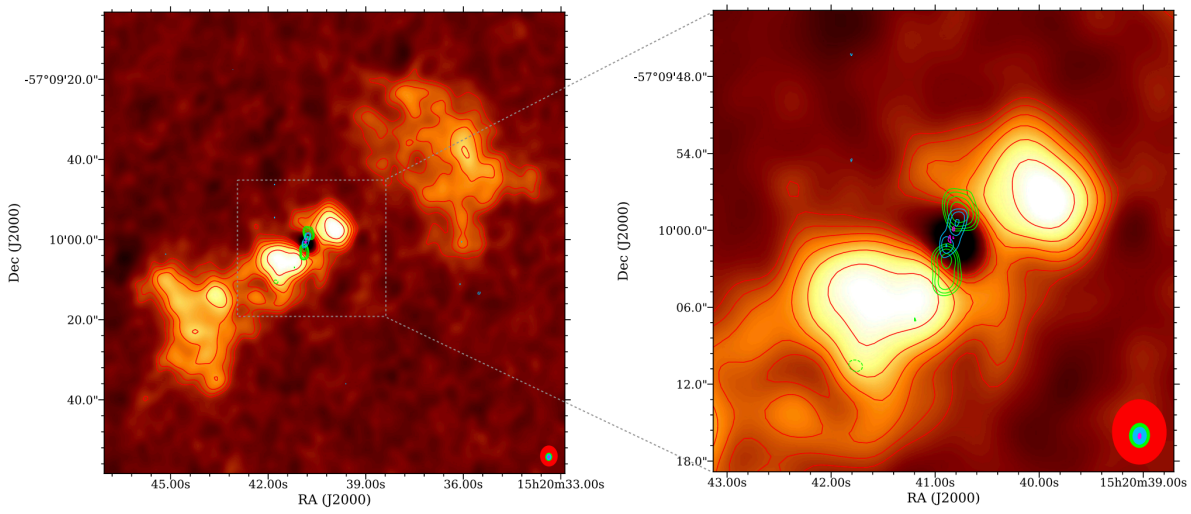

Figure 3.5: Image of Cir X-1 observed at 2.1 GHz with overlaid counters at 2.1 GHz (red), 5.5 GHz (green), 9.0 GHz (blue), and 34 GHz (magenta). The central core source was removed. Taken from Figure 8. in Coriat et al. (2019).

However, X-ray observations consistently advocate the edge-on geometry. Cir X-1 shows X-ray flux dips (Brandt et al., 1996) similar to a class of LMXBs called "dippers" (Díaz Trigo et al., 2006). The dips are caused by intervening material above the accretion disk, and hence are observed only in high inclination systems. Moreover, P Cygni profiles were detected from X-ray binaries for the first time from this source (Brandt and Schulz,

2000), which is attributable to the outflowing material in the edge-on direction. These support the edge-on view of the system.

3.2.5 Age

Heinz et al. (2013) discovered an X-ray nebula extending over 4 arcmin around Cir X-1 using long-exposure observations with *Chandra* (Figure 3.6). Its origin is unlikely to be a dust-scattering halo. The X-ray spectrum of the nebula indicates that it is indeed a supernova remnant (SNR) characterized by emission lines of Mg, Si, and S at a non-ionization equilibrium (Figure 3.7). We note that the emission from the SNR is sufficiently low compared to the one from Cir X-1 itself, and its contribution is not considered in the spectral analysis performed in this thesis. Based on the Sedov self-similar solution of the dynamical evolution of SNRs (Hamilton, Chevalier, and Sarazin, 1983; Borkowski, Lyerly, and Reynolds, 2001), an upper limit was obtained for the age of $< 4600\ (D/8\ \mathrm{kpc})$ years. This is in agreement with a very short characteristic time of $P_{\mathrm{orb}}/\dot{P}_{\mathrm{orb}}$ (§ 3.2.1).

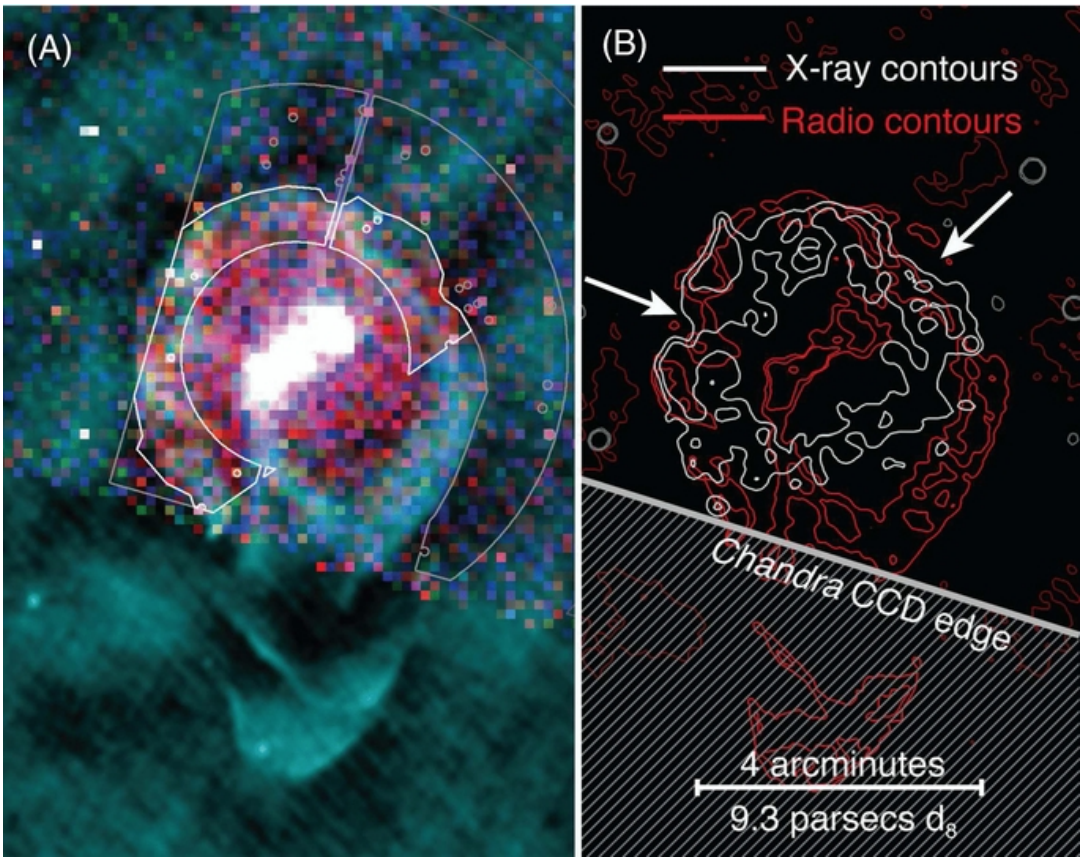

Figure 3.6: Radio and X-ray overlaid image of the SNR around Cir X-1. Left panel (A) shows the X-ray emission in the 1–2 (red), 2–3 (green), and 3–5 (blue) keV. The radio synchrotron emission is overlaid in cyan. Right panel (B) shows the contours of the remnant edge in X-ray (white) and radio (red). Taken from Figure 5 in Heinz et al. (2013).

The only other X-ray binary associated with an SNR is a black hole candidate SS433 (Geldzahler, Pauls, and Salter, 1980), which has an age estimate of 10^4–10^5 years

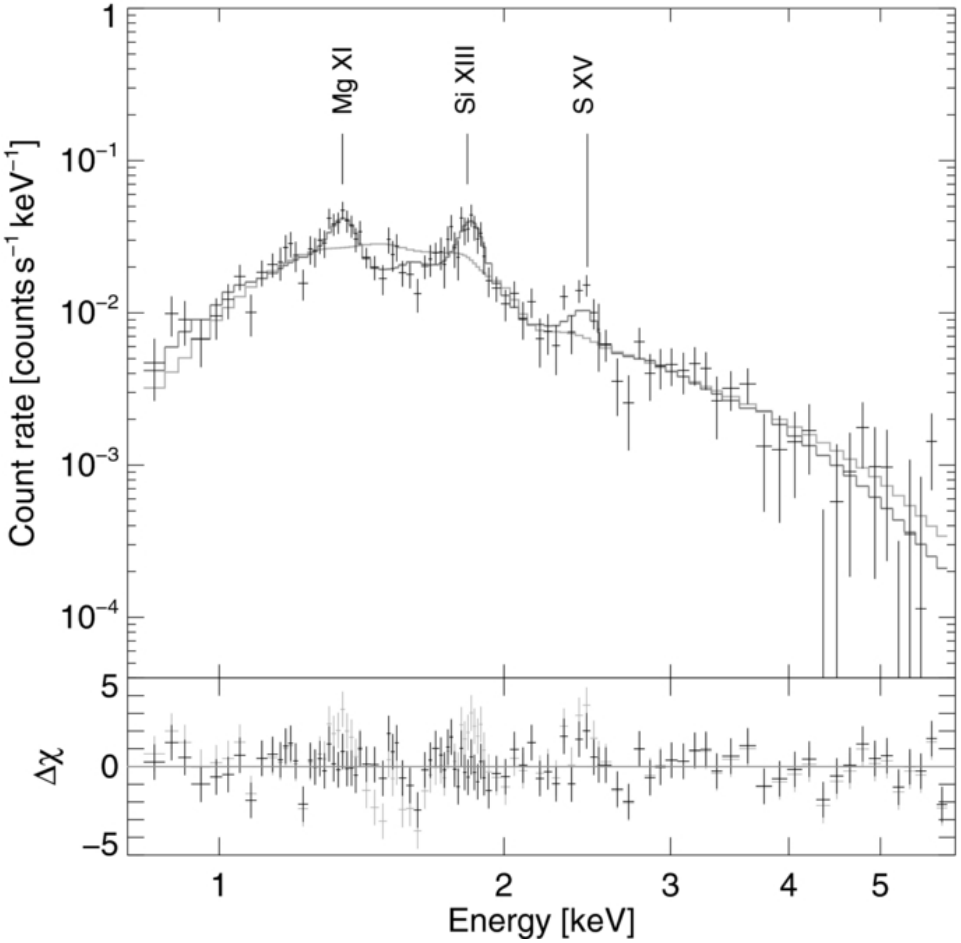

Figure 3.7: X-ray spectrum of the outer part of the SNR (Heinz et al., 2013).

(Goodall, Alouani-Bibi, and Blundell, 2011). Cir X-1 has thus established its status as being the youngest known X-ray binary in our Galaxy.

3.3 X-ray Flux Variability

3.3.1 Long term variability

Cir X-1 exhibits a plethora of flux variations in various time scales. The source has been monitored for the last 50 years, and the long-term flux change was greater than two orders of the magnitudes (Figures 1.1, 3.8). This may be related to being in the early stage of the binary evolution. The X-ray flux went under the detection limit of *RXTE* ASM around 2010, but fortunately *MAXI* started monitoring at that time, which has continued monitoring until today.

In the late 1990s and early 2000s, the observed flux exceeded a Crab (high state), during which P Cygni profiles of highly ionized metallic lines were observed in X-ray grating spectra with *Chandra* (Brandt and Schulz, 2000; Schulz and Brandt, 2002).

The flux decreased to a 10 mCrab level throughout the 2010s (low state), during which emission-dominated spectra were observed (Schulz et al., 2020). Schulz et al. (2008) speculated that the source entered the low state around 2007 because the flux was not high after the periastron passages unlike the previous state. The transition from the high to the low state took 5–10 years, which we call the "medium state".

From around 2018, the flux recovered to a few hundred mCrab at a level similar to that in the 1980s. This happened when repeated *NICER* observations were made in its AO1–4 cycles (green lines in Figure 1.1).

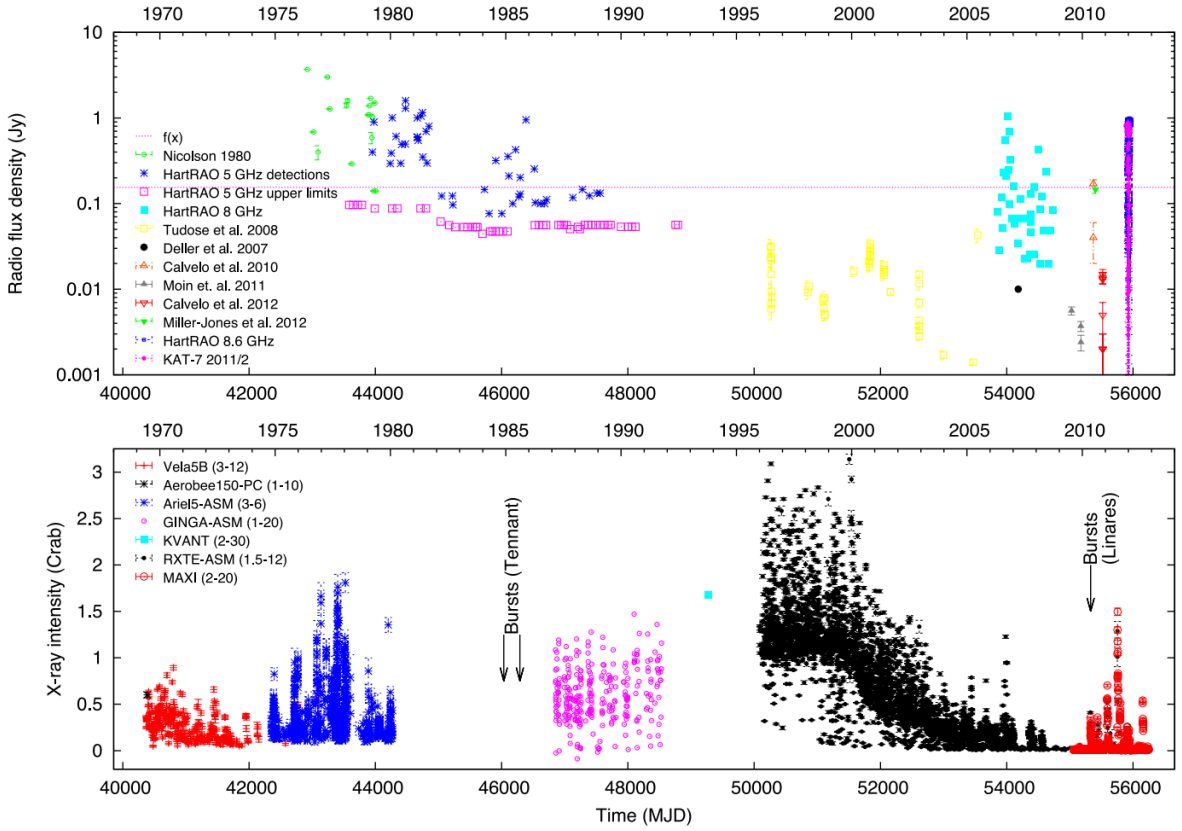

Figure 3.8: Long-term X-ray and simultaneous radio light curves for the last >40 years(Armstrong et al., 2013).

3.3.2 Orbital variability

In this section, we summarize the results obtained at different phases of an orbit at varying flux states in the long-term variations. We put an emphasis on describing the distribution of circumstellar materials and accretion variations, which will be the main focus of the modeling in this study.

3.3.2.1 Periastron

In systems with an elliptical orbit, periastron passages are likely to be very active in mass accretion from the companion star; hence more observational results are available than in the other phase.

Cir X-1 has often shown outbursts. The most widely accepted interpretation for the cause of the outbursts in accreting X-ray binaries is the disk instability model. In this model, the change in the opacity resulting from the ionization of hydrogen causes a drastic change in the viscosity of materials within the disk. This instability propagates in the viscosity time scale (which explains the measured day-long rise time). When viscosity allows rapid mass accretion, an outburst occurs. Since the bright outburst often occurs at the periastron, the instability is probably caused by a sudden change in the surface mass density at the outer region of the accretion disk (D'Aì et al., 2012). The tidal interaction, or a periastron-driven enhanced accretion, may partially disrupt the outer region of the disk.

Asai et al. (2014) studied the relation between the orbital phase and the outburst using X-ray monitoring data with *MAXI*/GSC (Figure 3.9) during the low flux state. They found that most outbursts start in an orbital phase between –0.3 and –0.2. Eleven outbursts lasted until the next periastron. The behavior of the next periastron was classified into three types. First, the outburst continued smoothly to the next orbital cycle after the periastron. The intensity decreased temporarily around the periastron probably due to the intervening absorber. The second type is similar to the first, but the decay profile is not continuous. Additional mass transfer at the next periastron may overwrite the profile of the outburst. Clarkson, Charles, and Onyett (2004) also argued that the second in a series of outbursts at the next periastron would occur by the enhanced mass transfer during the high state in 1996–2000. The third type shows a sudden decrease in intensity around the periastron at phase $\sim$ 0.95. Cir X-1 often exhibits dips from phase $\sim$0.95 to $\sim$1.3, where the intensity is too low for the actual end of the outbursts to be observed. Asai et al. (2014) also pointed out that burst-like data points appeared between the phases –0.05 and 0.05, denoted by arrows in Figure 3.9. They call them "periastron spikes". The spikes are probably caused by a temporary increase in the accretion rate independent of the existence of the accretion disk, such as spherical accretion from the polar directions.

The P Cygni profiles were observed around the periastron (Brandt and Schulz, 2000; Schulz and Brandt, 2002). While it has not been observed in other phases so far, this observation, at the very least, suggests that the material in the outflow is highly ionized at the periastron.

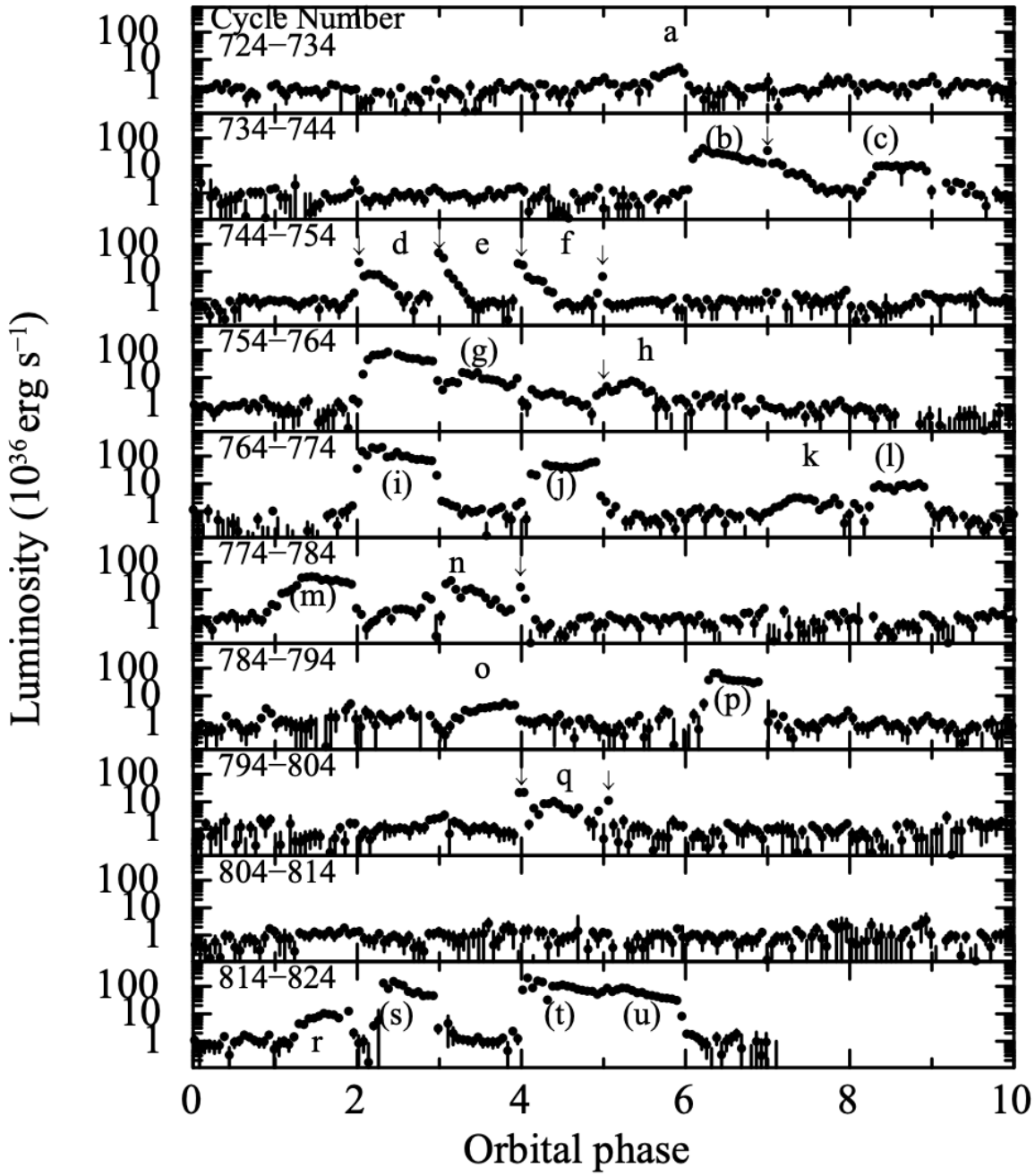

Figure 3.9: One-day averaged light curve of 2–10 keV luminosity as a function of orbital phase assuming a distance of 7.8 kpc. The alphabets (a–u) denote the observed outbursts (Asai et al., 2014).

3.3.2.2 Apastron

Another interesting orbital phase is the opposite phase of the periastron; i.e., the apastron passage. Iaria et al. (2002) obtained a broadband spectrum (1.8–200 keV) with *BeppoSAX* close to an apastron (phase 0.61–0.63) on February 7 and 8, 1999. In comparison to the periastron passage observation (Iaria et al., 2001a) conducted during a different orbital cycle, the presence of an accretion disk was discussed using the partial covering of the surrounding corona. The covering fraction is larger during the periastron than during the apastron. The fact that the temperature of the seed photons of Comptonization is lower and the accretion rate is larger around the periastron requires the seed photons to be produced at a site further than the accretion disk. On the other hand, during the apastron, since the coronal region is smaller, we can observe the blackbody radiation from the uncovered disk. The hard excess could be produced by Comptonization by non-thermal electrons or by synchrotron emission in the jet. The outflowing wind (Brandt and Schulz, 2000) is expected to have some relation to the highly ionized torus-like structure that generates the absorption edge and the flaring activity with magnetic reconnection.

3.3.2.3 Long dip

The dip phase before the periastron (called "long dip" in the literature) is an important period for constraining the geometry of the system. G. Q. Ding, J. L. Qu, and Li (2006) studied the evolution of broadband spectra (3–200 keV) just before the periastron obtained with *RXTE*/PCA. They concluded that a partial covering with a heavy column of $N_{\rm H} > 10^{24}$ cm^{-2} causes the long dip. They discovered a hard power-law component above ∼30 keV, a fluctuating Fe emission line whose parameters vary throughout the orbital cycle, a Comptonized component, and a blackbody component. The most pronounced hard tail, the lowest line energy, and the widest line width of the Fe emission line are observed at the periastron.

The interpretation of the long dip by Brandt et al. (1996) is that an outer bulge in the inner accretion disk obscures the emission from a part of the edge-on disk with different column densities depending on the line of sight. The obscuration occurs as a result of electron scattering or free-free absorption in the corona, produced by the heating of the surface of the disk. If the accretion from the companion star forms a stellar wind rotating at a Keplerian velocity, they may evaporate a part of the disk to form a gaseous envelope, which can produce the partial covering material (G. Q. Ding, J. L. Qu, and Li, 2006).

Besides the work by Iaria et al. (2001a), no X-ray flares or dips were observed in the vicinity of this periastron phase of ∼0.053–0.088. They proposed that the formation of the accretion disk might occur near the periastron passage. Following the periastron passage, mass accretion takes place in a steady manner through the accretion disk, and matter from the disk may accumulate within the accretion disk corona surrounding its inner region, leading to an increase in the optical depth. Subsequent to the apastron passage, the accretion disk and its corona undergo disruption, resulting in a reduction of the optical depth. It is speculated that the covering matter is widely distributed from the surface of the neutron star to the region emitting the iron line within the disk.

3.3.2.4 Short dips

In addition to the long dip, short dips lasting only a few hundred seconds are frequently observed. Some examples can be found in our *NICER* data (orange arrows in Figure 6.1).

Lei et al. (2007) analyzed three long dips ($> 10^4$ s) and two short dips ($< 10^4$ s) using the *RXTE*/PCA data in 1996–2001. They developed a model that incorporates a weak and soft component that is not influenced by the obscuring matter. The argument posited that during periods without dips or in the transition phase to a dip, the emissions from the neutron star and the disk are so intense that the weak component remains undetected in the spectra. The spectra were fitted well with the partially covered Comptonization of two-temperature blackbody components and line emissions. They found a strong correlation between the column density of the partial coverer $N_{\rm H}$ and the ratio of the normalization of the Fe Kα emission line to the normalization of the blackbody component during long dips. This implies that the Fe emission line originates from the absorbing (accreting) matter from the inner region of the accretion disk. Conversely, during the short dips, the line flux remained nearly constant, indicating that the line is likely generated outside of the place where the absorbing matter exits, or the size of the absorbing matter is smaller than that of the line-emitting region. Shirey et al. (1996) also proposed that short-term dips result from absorption due to a bulge in the outer part of the accretion disk.

3.3.2.5 Variation over an entire orbit

In a system like Cir X-1, where the behavior is completely different phases over a long term with a diversity from orbit to orbit, it is necessary to observe the system for a full orbit or to compare similar orbital phases in close orbital cycles.

Some studies have argued that the partial covering materials play a dominant role in changing the observed X-ray spectra. To interpret the differences between the periastron and apastron passages, Iaria et al. (2001b) studied the system along the entire orbit with *ASCA* in 1998 March (Figure 3.10). They distinguished three different X-ray states of the source as a function of the orbital phase; (1) a high accretion rate (super-Eddington) state during phase ∼0.97–1.3 when a shock due to accretion could form in the inner region of the system producing an outflow of ionized matter. The blue-shifted absorption edge at ∼8.7 keV supported this interpretation. They needed no partial coverer implying the absence of neutral matter in the line of sight; (2) a quiet state (sub-Eddington) during the phase ∼0.3–0.7, when the outflow weakened and a hydrogen column is smaller; and (3) a partial covering state at phases ∼0.78–0.97, when the emission from the compact object is partially absorbed by neutral matter with an equivalent hydrogen column of 10^{24} cm^{-2}, which is presumably due to the surface of the companion star and/or the accreting matter. The spectral fitting did not require blackbody emission from the surface of the neutron star or from the inner region of the accretion disk. The observed Comptonized component probably came from the accretion disk corona located at ∼90 km away from the central region where optically thick material is located, which hides the central region if the disk is edge-on.

D'Aì et al. (2012) analyzed the snapshots every few days covering an orbit during an outburst observed in May 2010 with *RXTE*/PCA (3.0–25 keV), *Swift*/XRT (1.0–9.0 keV) observations, and a 20 ks *Chandra*/HETGS observation (1.0–9.0 keV). The observed phenomena include a bright outburst, which decayed over two orbits, followed

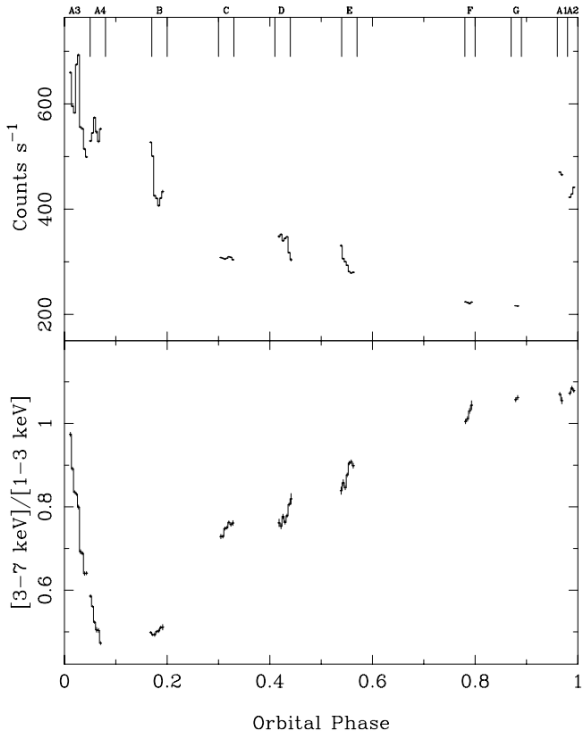

Figure 3.10: Light curve (upper) and hardness radio (lower) along a whole orbit observed with *ASCA* (Iaria et al., 2001b).

by a smaller outburst (Figure 3.11). All spectra were characterized using an optically thick thermal Comptonization model with a variable neutral local absorption component, predominantly needed near the periastron, and interstellar absorption (parameterized with N_{H} fixed at 1×10^{22} cm^{-2}) (Figure 3.12). Fluctuating flares soon after the dip phase imply that accreting matter during the flaring period may also contribute to the dips. The authors suggested that the transition in the accretion state during the dips operates only during the periastron phase and not throughout the entire outburst phase.

Changes in the mass accretion rate along the phase were also studied. Shirey et al. (1996) investigated the mass accretion rate along the orbital phase with *RXTE*/PCA (1.5–12 keV). The flaring state after phase 0 reached 3.3 Crab for 2–5 days, preceded by the dips for 3–20 minutes, which is almost recurrent as shown in the hardness ratio (Figure 3.13 left). The hardness ratio was soft during the flaring phases (∼0–0.2), then hardened while the count rate was almost steady (phase ∼0.2–0.7) as also observed by Tsunemi et al. (1989). They calculated the power spectral density (Figure 3.13 right) during the non-flaring phase (∼0.2–0.7), whose narrow QPO peaks gradually evolved from 1.3 to 12 Hz. There was also a broad QPO at a higher frequency. These QPOs were strongly correlated with the flat-top power level of the PSD, as well as the cut-off frequency. Similar QPOs (low frequency of 5–20 Hz and high frequency of 100–200 Hz) were also observed by EXOSAT for about a day, including phase zero in 1986 (Tennant, 1987). They argued that the high-frequency QPO is not from a pulsar but from lumps in the inner region of the accretion disk. They concluded that spectral hardening, the evolution of the QPOs, and the correlation between the QPOs and flat-top level are caused by the evolution of the accretion disk depletion.

G. Ding, Huang, and J. Qu (2012) studied the orbital modulation of the spectra

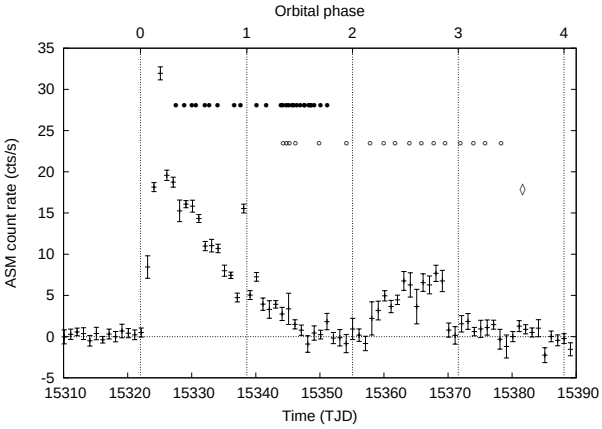

Figure 3.11: Daily-averaged light curve observed with ASM. Filled circles mark the *RXTE*, open circles for *Swift*, and diamond for *Chandra* observations. Grid lines show phase zero. Taken from Figure 1 in D'Aì et al. (2012).

and the mass accretion rate for two orbits using *RXTE*/PCA observations. The spectra were well described with a blackbody, a multi-color blackbody, and a line component. The disk accretion rate was distinguished into three phases; super-Eddington phase ∼0–0.1; decreasing to near-Eddington phase ∼0.1–0.5; and relatively steady reaching the Eddington phase ∼ 0.5–1. The evolution of the disk could be associated with a high orbital eccentricity. The mass accretion to the neutron star is less than that to the accretion disk, which was interpreted to show the existence of outflows from the disk.

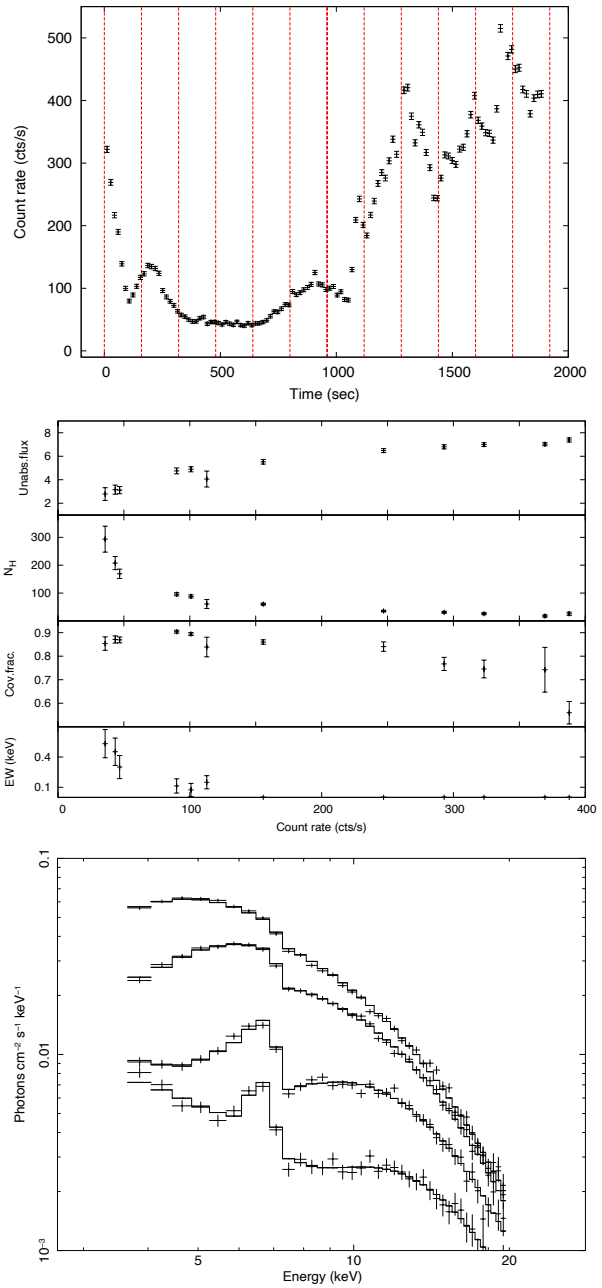

Figure 3.12: Light curve obtained with *RXTE* around the periastron (upper), best fitting spectral results (middle) and unfolded spectra for four segments (bottom). Taken from Figure 9 in D'Aì et al. (2012).

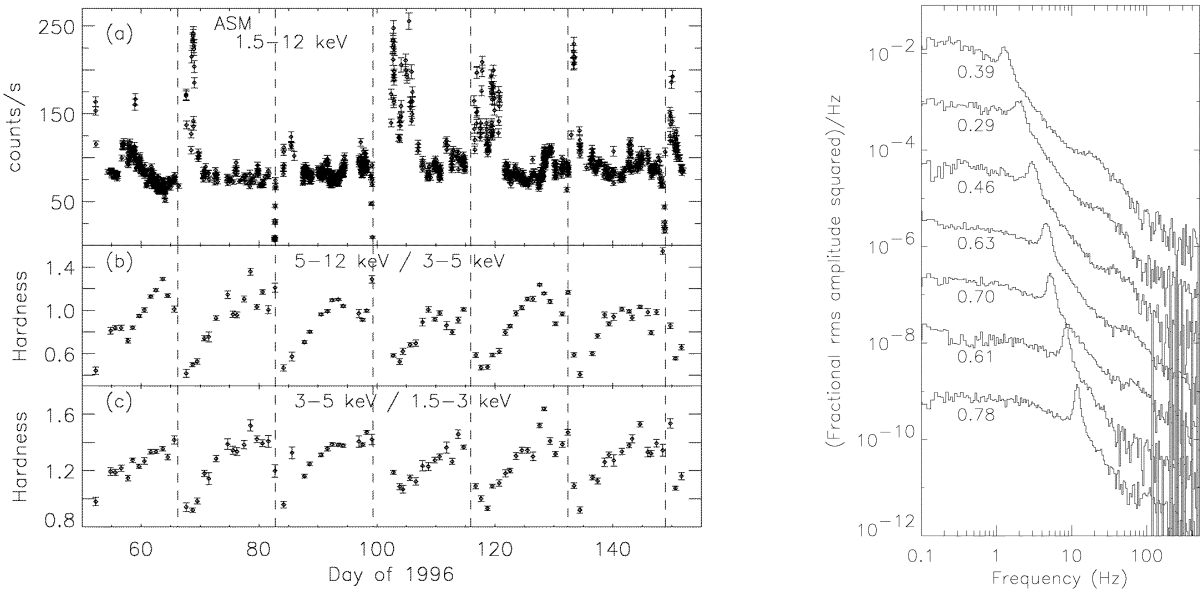

Figure 3.13: Light curve and two hardness ratios obtained from the ASM (left), and power density spectra along the orbital phase (right) taken from Fig 1 & 3 in Shirey et al. (1996).

3.4 X-ray Energy Spectra

3.4.1 Continuum emission

Since 1980's, an intensive debate has been made for the origin of the continuum X-ray emission from LMXBs. Two completing ideas — the so-called "western model" versus "eastern model" — were proposed. The Eastern model (Mitsuda et al., 1984) explains the X-ray spectra using two components: one is the multi-color blackbody emission from an optically thick and geometrically thin accretion disk (we call this as "disk blackbody emission" throughout this thesis) and the other is the Comptonized emission of the blackbody emission from the surface of the neutron star or the disk blackbody emission by the inverse-Compton scattering by the hot corona around the neutron star. On the other hand, the Western model explains the X-ray spectra using two different components: one is the thermal blackbody emission from the surface of the neutron star and the other is the Comptonized emission by the inverse-Compton scattering by the hot corona on the surface of the accretion disk (N. E. White, Stella, and Parmar, 1988). The X-ray continuum spectra are mostly featureless when observed with low-resolution spectrometers. This made it difficult to distinguish the two scenarios.

A similar debate was conducted for Cir X-1. As we review some of them below, many proposals have been made, but none is widely accepted. This is largely due to the lack of X-ray spectra of the same quality taken at multiple epochs. This will be improved significantly in this thesis (§ 4.1). Indeed, we will propose an X-ray continuum spectral model for our data (§ 6.1.2.4) that is simpler and more universal than those in previous works.

Iaria et al. (2001a) analyzed the broadband X-ray energy spectrum (0.1–100 keV) obtained with *BeppoSAX* near the periastron of phase $\sim$ 0.11–0.16 on August 1, 1998. The observation captured the beginning of a flare for $\sim$6 ks. The continuum spectrum was described well with two blackbody emission: the softer one is from the accretion disk and the harder one is from the neutron star surface. However, the radius of the neutron star was derived to be $\sim$30 km, which is too large. They alternatively used the Comptonized component with the seed photons of a $\sim$0.4 keV blackbody and the electron temperature of the corona to be $\sim$0.9 keV. The hard excess emission above 15 keV was additionally fitted by a non-thermal hard tail of the electron velocity distribution. A similar feature was observed in the Z sources (e.g., GX 17 + 2 (Di Salvo et al., 2000), GX 349 + 2 Di Salvo et al. (2001), etc.).

They also detected a strong absorption edge at 8.4–8.7 keV in all the spectra and a Fe XXV emission line during the low count observation. The optical depth corresponds to a hydrogen column density of $\sim$1.5 $\times 10^{24}$ cm^{-2}, which is in agreement with the surrounding highly photoionized torus model argued in Brandt et al. (1996) with an edge-on view. In an entire observation of one orbit made by *ASCA* in 1998, the Comptonization model could be applied over one orbital period, although there are some differences such as the presence of dense material $\sim 10^{24}$ cm^{-2} in the line of sight around the periastron.

Iaria et al. (2002) made observations in the apastron phase ($\sim$ 0.61–0.63) between February 7 and 8, 1999. They modeled the continuum emission with three components: (1) a blackbody of a temperature of $\sim$0.6 keV originating in the inner region of the accretion disk, (2) a Comptonized component of $kT_{\rm seed-photon}$ $\sim$1.2 keV and $kT_{\rm electron}$ $\sim$6 keV

with an electron scattering optical depth of $\tau \sim 1.7$ irradiated from a corona or an outflowing wind around the neutron star, and (3) power-law component needed to model the hard excess above 20 keV, which is probably produced by Comptonization by non-thermal electrons or the synchrotron emission from the jet. Highly photoionized Fe lines are interpreted as an outflowing wind along the disk surface associated with the Comptonized component (2).

Brandt et al. (1996) and G. Q. Ding, J. L. Qu, and Li (2006) analyzed the X-ray spectra taken before (during the dip) and after (out of the dip) the periastron. Both were successful in explaining the two spectra with a common model, which consists of two blackbody components modified by the photoelectric absorption of the interstellar matter and of the partial-covering circumstellar matter. The correlation between the spectral hardness ratio and the flux intensity implied that a cold neutral matter absorbs the emission in the lower energy band. The higher temperature blackbody is suggested to originate from the surface of the neutron star, while the lower temperature blackbody is from the accretion disk. Their results are comparable to each other, especially in the dip phase, which is slightly different probably due to the energy band (Table 3.1).

TABLE 3.1: Comparison of the previous studies using the two-blackbody model.

Study	Brandt et al. (1996)	G. Q. Ding, J. L. Qu, and Li (2006)
Observatory	*ASCA*	*RXTE*/PCA
Energy band	1–10 keV	3–21 keV
Date	1994 Aug. 4–5	1996 Sep. 20–21
Dip phase		
$kT_{\rm lower}$	0.46 keV	0.5–0.61 keV
$kT_{\rm higher}$	1.16 keV	1.80–2.26 keV
$N_{\rm H} \times 10^{22}$ cm^{-2} of the coverer	162	28–362
covering fraction f_{cov}	0.938	0.7–0.896
Non-Dip phase		
$kT_{\rm lower}$	0.59 keV	1 keV
$kT_{\rm higher}$	1.38 keV	2.2 keV
$N_{\rm H} \times 10^{22}$ cm^{-2} of the coverer	123	18–38
covering fraction f_{cov}	0.42	0.239–0.813

3.4.2 Line emission in high flux state

The presence of an outflow can be unveiled through the observation of a P Cygni profile. This profile is typically observed in the ultraviolet band in cataclysmic variables (an accreting binary of a white dwarf and a star) having an outgoing motion. The transmitted emission through the outgoing material has red-shifted absorption features, whereas the scattered emission in the outgoing material has blue-shifted emission. When they are added, the P Cygni profile is formed.

Brandt and Schulz (2000) made the discovery of P Cygni profiles in Cir X-1 using a *Chandra*/HETGS observation on February 29, 2000 (MJD∼51594; ObsID=706 in Table 4.6). This marked the first observation of P Cygni profiles in X-ray binary systems. Their observations included the detection of H-like and He-like Ne, Mg, Si, S, and Fe

lines (Figure 3.14). These lines exhibited broad profiles, extending to approximately ± 2000 km s^{-1}. To account for the material reaching terminal wind velocities at the outflow launch radius of approximately $r_{\rm launch} \approx 10^{10}$ cm, assuming an ionization parameter (Equation 5.145) of $\log \xi < 3$, the density of the material at this radius was estimated to be around $n_{\rm radius} \sim 2 \times 10^{18}$ cm^{-3}. These conditions were too ionized and dense for Hα emission to be formed. It was postulated that the Hα line originates at a larger distance in the outflow or within the accretion disk.

The emission of X-rays from the inner region of the system heated the surface of the accretion disk, giving rise to a corona and a thermally driven wind. In the cases of high luminosity systems, radiation pressure needs to be considered in the calculations. They concluded that the P Cygni profiles emanated from the accretion disk wind, particularly in a region of moderate temperature (approximately $\sim 5 \times 10^6$ K), and that the system is seen in an edge-on direction. In the central region, both the wind and the corona were heated to the Compton temperature, resulting in complete ionization. The study also considered the possibility of clumpy outflowing materials, as mentioned in Iaria et al. (2001a).

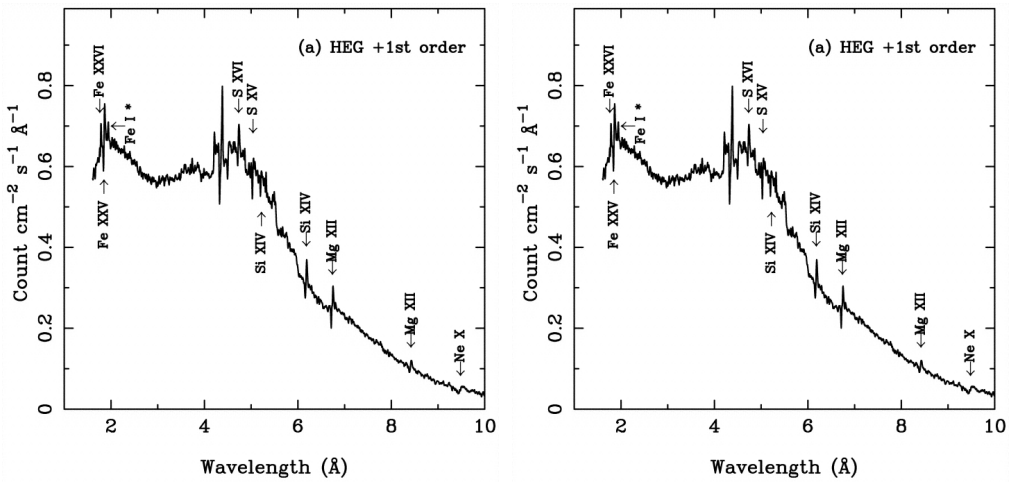

Figure 3.14: X-ray spectra observed with Chandra. P Cygni profiles with more than 5σ significance are marked (Brandt and Schulz, 2000).

In Schulz and Brandt (2002), the P Cygni profile observed in Brandt and Schulz (2000) was compared with the P Cygni profile observed at a different epoch (Figure 3.15) with slightly lower flux, but within a high-flux state in the long run, on 2000 June 8 (MJD$\sim$51703; ObsID=1700 in Table 4.6). The most notable change is that the equivalent widths of the lines are greater in ObsID=1700. This is interpreted as an increase in the proportion of material that obstructs the continuum. The spectrum of ObsID=1700 exhibited the resonance, intercombination, and forbidden lines of the He-like Mg XI triplet, which were used to predict the temperature as $\sim 3.8 \times 10^6$ K (Porquet and Dubau, 2000). The comparison of the ionization structure of the plasma at this temperature shows a new estimate of the ionization parameter $\log \xi \sim 4$ (T. Kallman and Bautista, 2001).

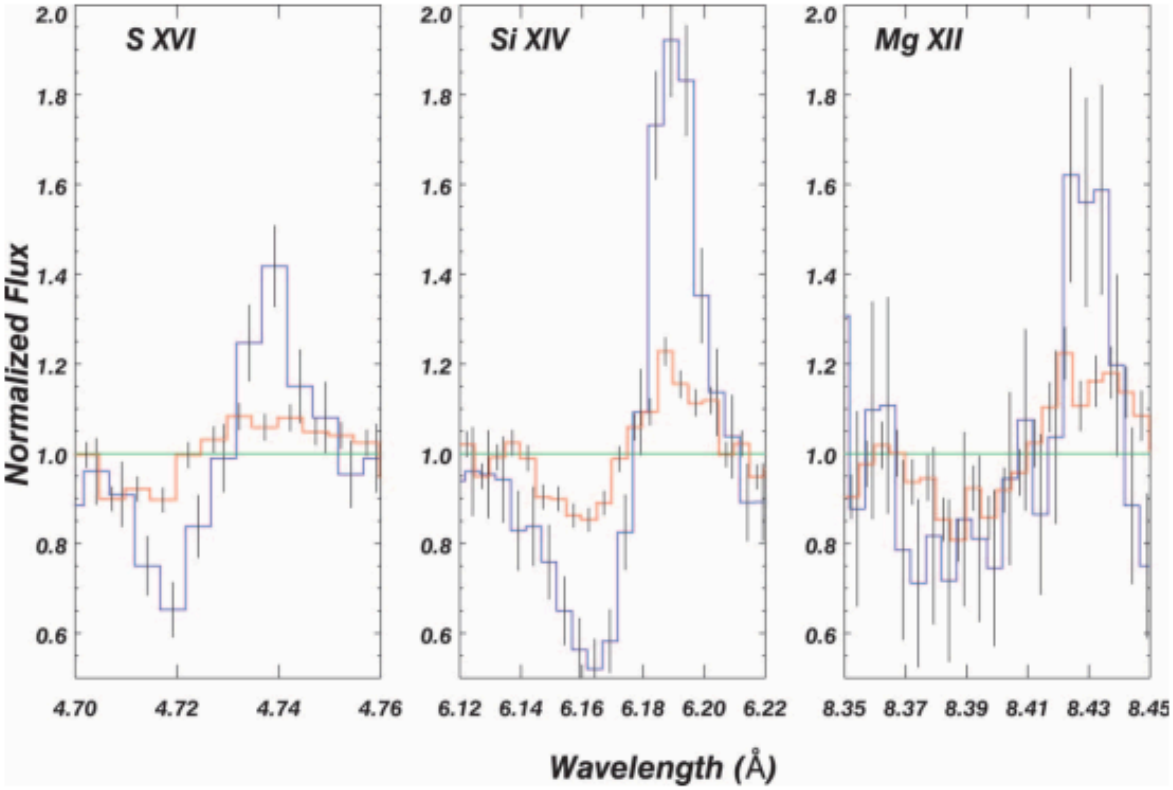

Figure 3.15: P Cygni profiles of the Lyman α in S XVI, Si XIV and Mg XII for ObsID=706 (red) and 1700 (blue) taken from Schulz and Brandt (2002).

3.4.3 Line emission in low flux state

The prolonged lifetime of *Chandra* beyond 20 years enabled the extended studies after Cir X-1 turned into a low flux state around 2008. The *Chandra* HETGS revealed X-ray spectra dominated by emission lines (Iaria et al., 2008; Schulz et al., 2008). The *Suzaku* observation conducted in the same state exhibits the same features, which will be presented in § 6.2. The data are modeled by assuming that these emission lines are from the photoionized plasma. At that time, the continuum emission was low and was often described by a simple phenomenological model such as one or two partially covered power-law components.

Schulz et al. (2008) conducted *Chandra* HETGS observations of Cir X-1 near the periastron during the low-flux state ($L \sim 10^{35}$ erg s^{-1}) in 2005. The X-ray spectra are entirely different from those taken in the high flux state using the same instrument (Schulz and Brandt, 2002). In the low flux state, there are no P Cygni profiles, but numerous emission lines of H-like and He-like Si, S, Ar, Fe, and Ca were identified.

Two observations were made in the pre-zero phase (0.96–0.99) and post-zero phase (1.06–1.10). In the pre-zero phase, only emission lines were observed. In the post-zero phase, the Fe and Ca lines changed to absorption (Figure 3.16). They argued for the presence of two different materials in the line of sight; highly ionized ("hot") and moderately ionized ("warm") absorbers in the line of sight for absorption.

A quantitative assessment was made based on plasma diagnostics. The plasma density was determined to be above 1×10^{13} cm^{-3} using the Mg XI line complex, below the critical density 5×10^{14} cm^{-3} using the Si XIII line complex, and above 10^{15} cm^{-3} using

the Fe XXV line complex. These line complexes of He-like ions contain the allowed and forbidden transitions in the fine structure. The forbidden line relative to the allowed line decreases as the density increases toward the local thermal equilibrium (we review this in § 5.2.2). The line complex was observed with very small photon counts, and hence only a poor constraint was obtained for the plasma density. Other line complexes were not detected[1].

The ionization degree was also constrained using the `photemis` model in `xspec`, yielding $\log \xi \sim 3$. Note that the `photemis` model is a pre-calculated model based on a generic incident spectrum of a power-law form. The incident luminosity required to account for the observed emission measure of the Fe XXV line exceeded 10^{37} erg s^{-1}. This is more than two orders of magnitude greater than the observed luminosity at that time. Two possible explanations emerge; one suggests that the luminosity of the incident emission itself fluctuates rapidly, and the other posits that the incident emission in the line of sight was obscured by the surrounding materials. The additional analysis for the observations in 2008 and 2017 suggested the same results (Schulz et al., 2020). A self-consistent approach for the photoionized plasma emission and the incident emission is the obvious next step, which we will embark on for the first time in this thesis.

[1] These situations will be significantly improved with *XRISM* observations.

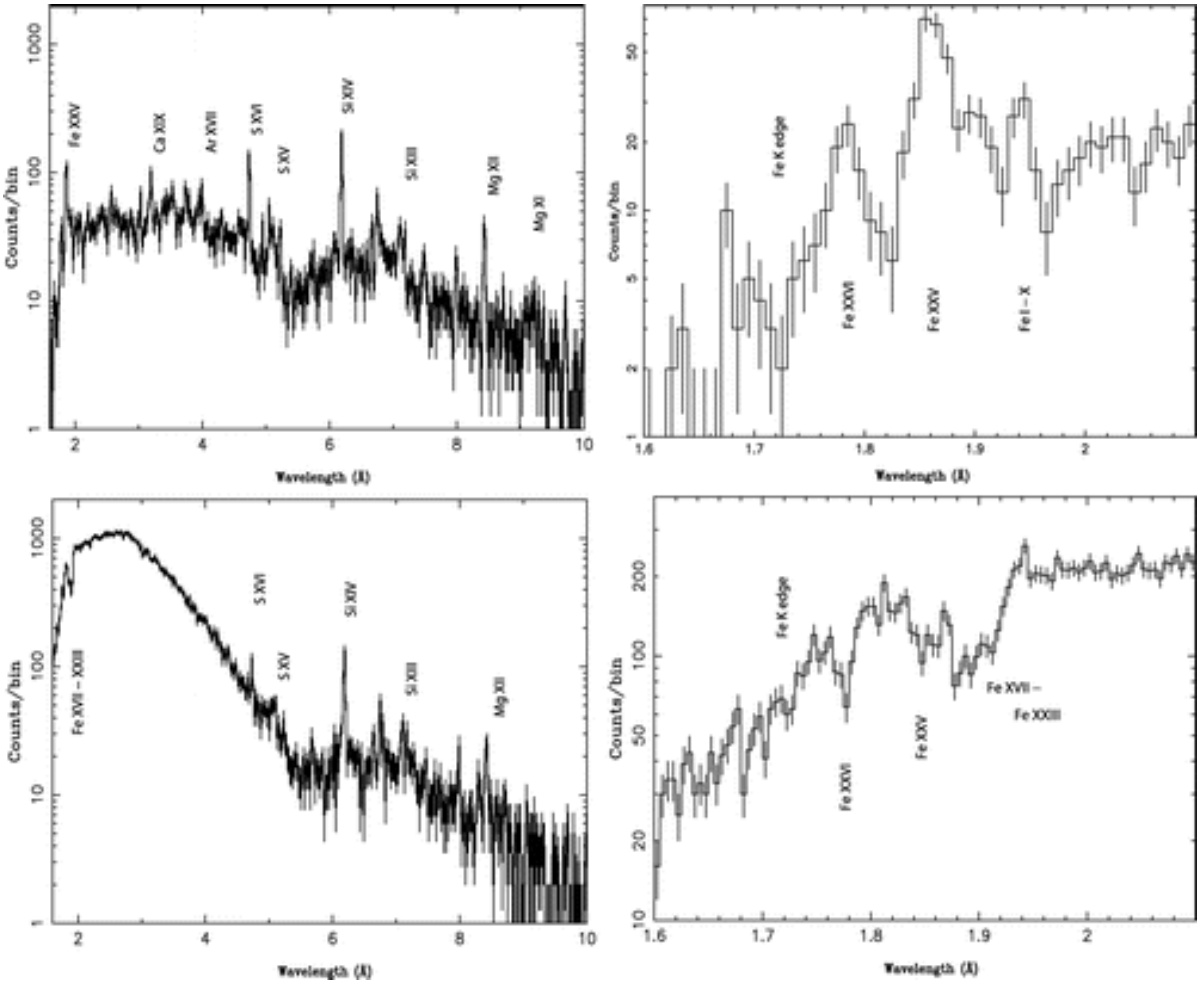

Figure 3.16: X-ray spectra observed with *Chandra* HETGS in the low flux state (Schulz et al., 2008). The top and bottom panels show pre-zero and post-zero phase spectra, respectively. The left and right panels show the entire band and a close-up view around Fe K features.

Chapter 4

Instruments & Observations

Contents

4.1 *NICER* 51
4.1.1 Mission & Operation 51
4.1.2 Instruments 51
4.1.3 Observations 54
4.1.4 Data reduction 55
4.2 *MAXI* 59
4.2.1 Mission & Operation 59
4.2.2 Instruments 59
4.2.3 Observations 60
4.2.4 Data reduction 60
4.3 *Suzaku* 61
4.3.1 Mission & Operation 61
4.3.2 Instruments 61
4.3.3 Observations 64
4.3.4 Data reduction 64
4.4 *Chandra* 66
4.4.1 Mission & Operation 66
4.4.2 Instruments 66
4.4.3 Observations 70
4.4.4 Data reduction 70

In this chapter, we describe the instruments and observations for each observatory and experiment; *NICER* (§ 4.1), *MAXI* (§ 4.2), *Suzaku* (§ 4.3), and *Chandra* (§ 4.4). For each of them, we describe their mission and operation (§ 4.1.1, § 4.2.1, § 4.3.1, § 4.4.1) and instruments (§ 4.1.2, § 4.2.2, § 4.3.2, § 4.4.2) as well as observations (§ 4.1.3, § 4.2.3, § 4.3.3, § 4.4.3) and the data reduction (§ 4.1.4, § 4.2.4, § 4.3.4, § 4.4.4). We particularly emphasize the kinds of technological advances that have made it possible to obtain the unique data sets presented in this thesis.

4.1 *NICER*

4.1.1 Mission & Operation

The Neutron Star Interior Composition Explorer (*NICER*; Gendreau et al. 2016) is an experiment onboard the International Space Station (ISS) at an altitude of ∼400 km above the Earth. *NICER* was launched on a SpaceX Falcon 9 rocket on June 3, 2017.

The primary goal of the mission is to address the fundamental astrophysical question of "How large are neutron stars?" It aims to explore the exotic states of matter within neutron stars through spin-phase-resolved X-ray spectroscopy. The capabilities of *NICER* are unparalleled, in particular, for fast timing and spectroscopy, low background noise, and high throughputs. In addition to its scientific pursuits, *NICER* facilitates the first-ever space demonstration of pulsar-based spacecraft navigation through the Station Explorer for X-ray Timing and Navigation Technology (SEXTANT) enhancement, funded by NASA's Space Technology Mission Directorate's Game-Changing Development program.

The X-ray timing instrument (XTI) is the instrument onboard *NICER*. It employs high-heritage components. At its core, the instrument utilizes as many as 56 sets of X-ray "concentrator" optics (XRC) and the silicon drift detector (SDD). Each XRC collects X-rays from a relatively large sky region (∼30 arcmin^2) and focuses them on a small SDD. The SDD detects individual photons, recording their energies with a spectral resolution of a few percent and their arrival times with unprecedented precision in the 0.2–12 keV X-ray range. *NICER* usually observes many targets with short snapshots of approximately 500 s during one ISS orbit of 90 minutes. These features are particularly suited for X-ray binaries, in which fast variability of up to a few kilohertz and orbital flux changes are commonly observed. Every year, an announcement of opportunity (AO) is made for observation proposals, through which guest observer programs are selected and executed.

A star tracker is used for the pointing system for the XTI to accurately point to and track celestial targets across nearly a full hemisphere. The pointing system's design accommodates the ISS's vibrational and contamination environments. In conjunction with *NICER*'s GPS-based absolute timing, it supports the high-precision pulsar light-curve measurements through extended exposures spanning up to 18 months.

4.1.2 Instruments

4.1.2.1 Overview

The mechanical system of *NICER* is comprised of the XTI structure, the Deploy and Pointing System (DAPS), and the adapter plate, through which *NICER* is connected to the Active Flight Releasable Attachment Mechanism (A-FRAM) and to the Passive counterpart (P-FRAM) of the ISS (Figure 4.1). The adapter plate support has a launch-lock mechanism that secures the XTI during the launch and releases it after *NICER* is installed in the ISS.

4.1.2.2 XRC

The X-ray Concentrator (XRC) is an epoxy-replicated, thin aluminum foil X-ray mirror with a single-stage parabolic grazing incidence optics designed to concentrate X-rays

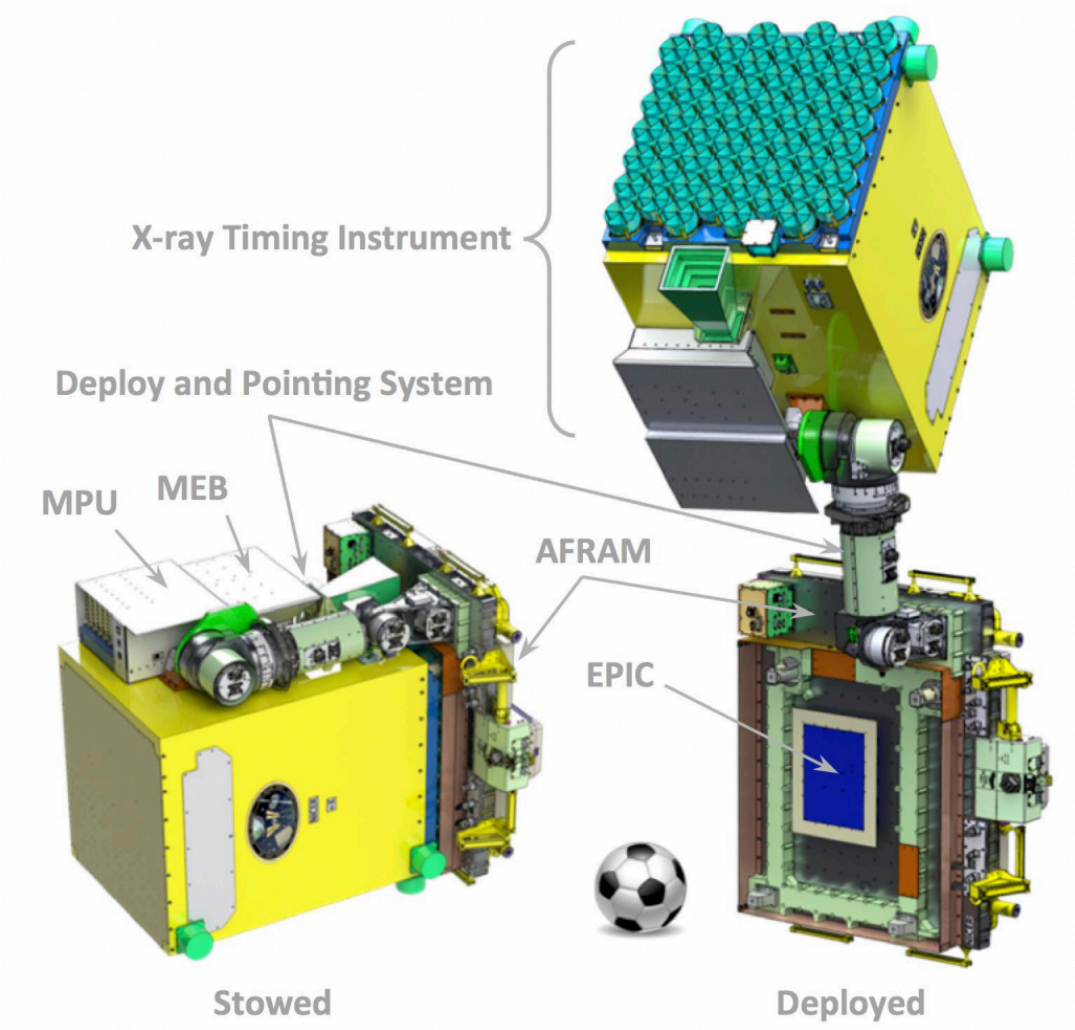

Figure 4.1: *NICER* in its stowed and deployed configurations (Gendreau et al., 2016).

onto the non-imaging detector. The XRC comprises 24 shells with diameters ranging from 30 to 103 mm and a focal length of 1.085 m. At the seam of each shell, there is a 0.5 mm gap intentionally left open in the support structure (Figure 4.2).

The effective area of the 56 flight XRCs was determined by measurements using a CCD camera and a proportional counter. An example of an X-ray image focused by an XRC is presented in Figure 4.3 along with the encircled energy function (EEF). On average, the XRC directs approximately 91 % of the X-ray beam into a 2 mm diameter detector aperture. The 56 XRCs were installed on the XTI's optical bench. Taking into account thermal shield transmission, the estimated total effective area combining the XRC is 2276 cm^2 at 1.5 keV (Figure 4.4 left). The complete effective area that includes the transmission of the detector filter, quantum efficiency, event filtering losses, contamination, etc, is 1793 cm^2 (Figure 4.4 right). This is larger than *XMM-Newton* (Jansen et al., 2001) at ∼1 keV, which had been the X-ray observatory of the largest effective area with X-ray optics.

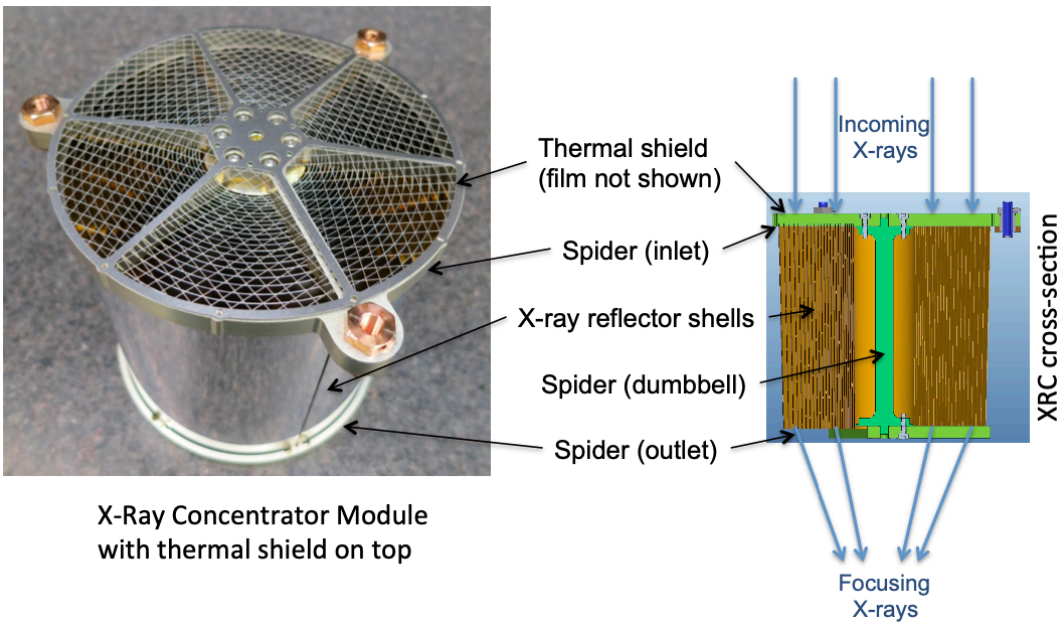

Figure 4.2: Photo of an XRC unit (left) and a schematic view of the cross-section (right) (Okajima et al., 2016).

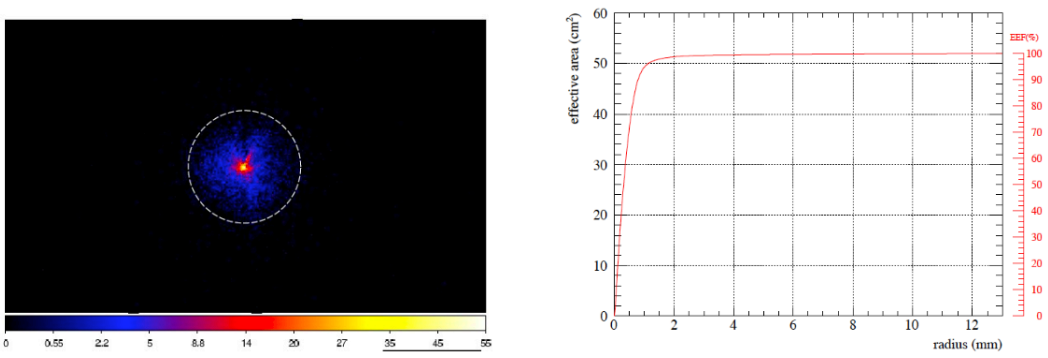

Figure 4.3: An X-ray image measured at 1.5 keV with XRC 43 (left) and an encircled energy function from the image (right) (Okajima et al., 2016).

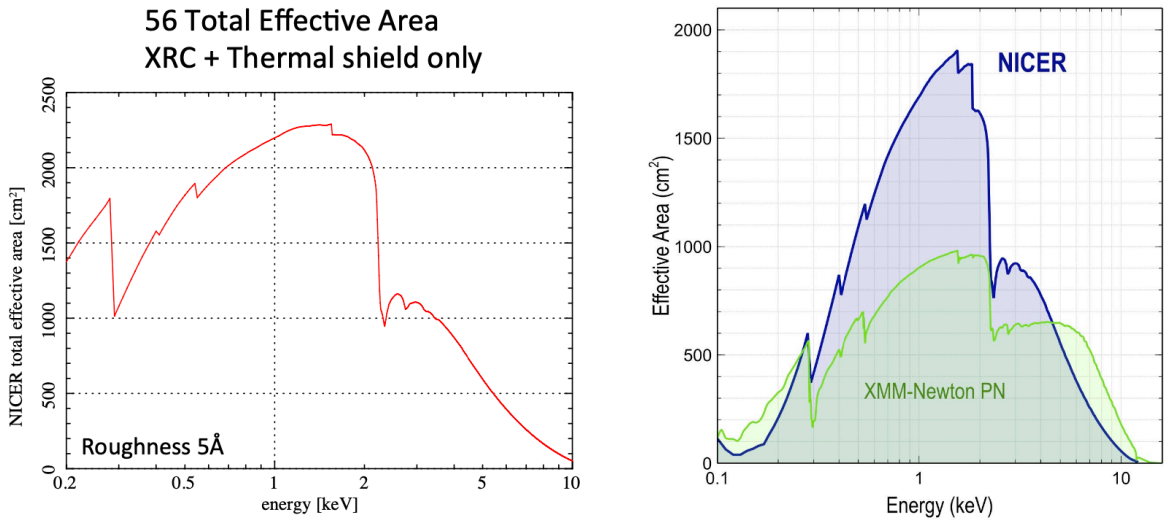

Figure 4.4: Total effective area of the 56 XRCs only with the thermal shield transmission taken from Figure 7 (Okajima et al., 2016) (left) and anticipated effective area compared with the XMM-*Newton* telescope's timing-capable PN camera taken from Figure 2 (Arzoumanian et al., 2014).

4.1.2.3 SDD

X-rays concentrated by the XRCs reach the Focal Plane Module (FPM) where 56 Silicon Drift Detectors (SDDs) are arranged (Prigozhin et al., 2012). The SDDs are off-the-shelf Amptek XR100SDDs 25 mm^2 detectors. Each detector is located on a Thermo Electric Cooler (TEC) for cooling the detectors to a low temperature of –55.0 °C. Both the silicon chip and the TEC are housed within a hermetically sealed metal can contained in a TO-8 package.

The package includes a very thin custom-made entrance composed of a 40 nm silicon nitride film covered with 30 nm of aluminum, effectively blocking visible light. These windows exhibit high transmission (∼30% at 200 eV). To utilize the SDD as a timing sensor, the active detector surface area is intentionally reduced to maintain a relatively narrow range of the drift times. The active area is shielded by an internal multilayer collimator. This design prevents incoming X-rays from arriving at unpreferred collection areas located away from the detector's central region. The X-ray optics placed in front of the SDD exhibit a point spread function smaller than this collimator's aperture.

FPMs are connected to a Measurement/Power Unit (MPU) for signal processing, which has fast and slow chains that analyze the same signal from the detector in parallel. By using the difference in their response times, it is possible to screen out events occurring outside the 2 mm diameter of the detector collimator as background.

4.1.3 Observations

NICER observed Cir X-1 numerous times every year up to the AO4 cycle so far. Among them, we had successful observation proposals for the AO2 and AO4 cycles. In AO2, we observed Cir X-1 with 103 snapshots over its orbital period, with an orbital phase ranging from $\phi = 0.54$ to 1.48, at a similar cadence from August 1, 2020, to August 16, 2020 (MJD = 59062–59078). The AO4 observations focused on a particular phase

in many orbits. In AO1 and AO3, different groups made observations of the source for different reasons. The setup of these observations is the same.

4.1.4 Data reduction

We retrieved the level 2 products from the archive, reprocessed them with the latest `CALDB` (calibration database), and produced the level 3 products. We used `HEAsoft` version 6.32.1 and `CALDB` version 20221001. The level 3 products include X-ray light curves and spectra, along with redistribution matrix functions (RMF), auxiliary response files (ARF), and background spectra.

The background spectra consist of both the non-X-ray background and the X-ray background. The former is caused by local particle environment, while the latter is caused by the foreground emission, cosmic X-ray background, etc. In general, the non-X-ray background varies as a function of time, whereas the X-ray background varies as a function of position in the sky. *NICER* offers the SCORPEON model for the non-X-ray background, which includes the following parameterized components; South Atlantic Anomaly (S), Cosmic Rays (COR), Polar and Precipitating Electrons (PE), cOnstant terms (O), and Noise peak (N). We used the SCORPEON background model throughout this work.

Figure 4.5 depicts the phase-folded light curve with ephemeris (Equation 3.3) derived from all *NICER* observations. Given the repeatable behavior in flux changes across phases among different cycles, we concentrate on the AO2 data that most uniformly covers the entire phase.

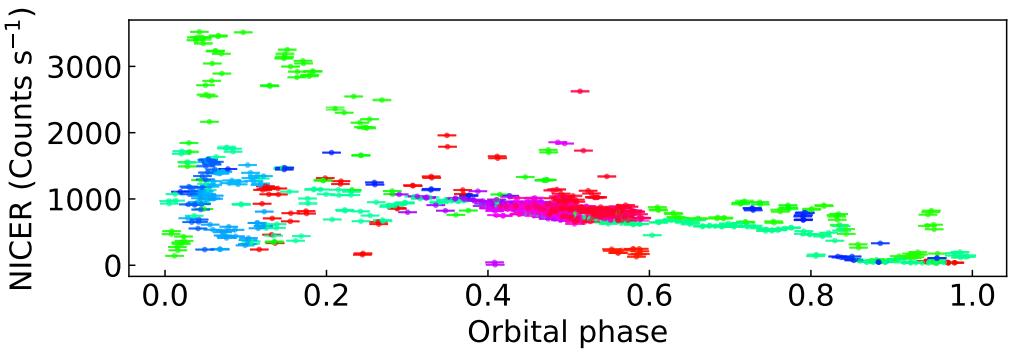

Figure 4.5: *NICER* light curves phase folded based on the ephemeris, with different colors for each orbital cycle. Time progresses from red to blue.

TABLE 4.1: *NICER* observations in the Performance Verification phase and AO1 cycle.

ObsID	Date	Time (UT)	Orbital phase	Exposure (s)
1050050101	2018-07-13	13:22:30	0.12	5832.01
1050050102	2018-07-14	04:44:43	0.16	2326.0
1050050103	2018-07-15	05:31:00	0.22	1633.0
1050050104	2018-07-16	00:00:19	0.27	2047.0
1050050105	2018-07-17	02:14:59	0.33	2559.0
1050050106	2018-07-18	10:44:34	0.41	613.5
1050050107	2018-07-27	05:55:35	0.94	2133.0
1050050108	2018-08-22	19:09:20	0.56	1682.0
1050050109	2018-08-22	23:47:20	0.57	3722.0
2050050103	2020-01-16	12:06:43	0.56	159.0
2050050104	2020-01-17	07:45:00	0.61	1032.0
2050050105	2020-01-18	02:22:05	0.66	1145.0
2050050106	2020-01-19	03:06:00	0.72	1195.0
2050050107	2020-01-20	11:40:24	0.80	879.0
2050050108	2020-01-21	00:02:51	0.83	2582.0
2050050109	2020-01-22	05:30:10	0.91	4239.0
2050050110	2020-01-23	00:01:40	0.95	1622.0
2050050111	2020-01-24	00:54:40	0.02	6377.0
2050050112	2020-01-25	06:20:00	0.10	259.0
2050050113	2020-01-26	03:57:40	0.15	1708.0
2050050114	2020-01-27	04:53:41	0.21	987.0
2050050115	2020-01-28	04:14:02	0.27	81.0
2050050116	2020-01-31	14:05:41	0.48	1075.0
2050050117	2020-02-09	22:40:43	0.05	149.0
2050050118	2020-02-10	00:13:43	0.05	102.0
2050050119	2020-02-11	08:45:07	0.13	921.0
2050050120	2020-02-12	11:05:02	0.20	1361.0
2050050121	2020-02-13	01:12:20	0.23	2187.0
2050050122	2020-02-15	04:37:00	0.36	834.0
2050050123	2020-02-16	00:37:20	0.41	1558.0
2050050124	2020-02-16	23:55:20	0.47	1771.0
2050050127	2020-02-21	01:03:27	0.72	855.0
2050050128	2020-02-22	00:18:41	0.77	188.0
2050050129	2020-02-23	01:07:25	0.84	1230.0
2050050130	2020-02-24	23:39:22	0.95	409.0
2050050131	2020-02-26	05:07:26	0.03	69.0
2050050132	2020-02-27	22:56:20	0.14	316.0

Table 4.2: *NICER* Observations in the AO2 cycle.

ObsID	Date	Time (UT)	Orbital phase	Exposure (s)
3578010101	2020-07-31	02:32:20	0.48	4643.0
3578010201	2020-08-01	01:47:00	0.54	3310.0
3578010301	2020-08-02	02:33:28	0.60	2791.0
3578010401	2020-08-03	00:12:56	0.65	2446.0
3578010501	2020-08-04	01:04:08	0.72	2252.0
3578010601	2020-08-05	01:50:20	0.78	2117.0
3578010701	2020-08-06	02:37:00	0.84	1066.0
3578010801	2020-08-07	00:27:40	0.89	2835.0
3578010901	2020-08-08	01:10:20	0.96	5108.0
3578011001	2020-08-09	01:34:24	0.02	4112.0
3578011101	2020-08-10	02:46:48	0.09	2681.0
3578011501	2020-08-10	22:56:20	0.14	330.0
3578011201	2020-08-11	00:27:57	0.14	2628.0
3578011301	2020-08-12	00:44:43	0.20	4424.0
3578011401	2020-08-13	01:33:20	0.26	4259.0
3578011502	2020-08-14	03:54:09	0.33	3196.0
3578011601	2020-08-15	00:18:40	0.38	3090.0
3578011701	2020-08-16	02:23:40	0.45	5240.0
3668010101	2021-02-23	04:41:09	0.03	5081.0
3668010102	2021-02-24	00:50:19	0.08	2360.0
3668010201	2021-03-11	22:49:42	0.05	1738.0
3668010202	2021-03-12	02:08:20	0.05	3636.0
3668010203	2021-03-13	02:42:32	0.12	2038.0
3668010301	2021-06-02	04:55:14	0.03	8844.0

Table 4.3: *NICER* observations in the AO3 cycle.

ObsID	Date	Time (UT)	Orbital phase	Exposure (s)
4050050101	2021-08-03	08:25:40	0.79	595.0
4050050102	2021-08-04	07:42:15	0.85	801.0
4050050105	2021-08-08	00:04:10	0.08	541.0
4050050108	2021-08-11	00:25:40	0.26	559.0
4050050109	2021-08-12	04:21:15	0.33	1151.0
4050050110	2021-08-13	19:05:12	0.43	403.0
4050050111	2021-08-18	18:39:40	0.73	1151.0
4050050112	2021-08-19	19:36:00	0.79	723.0
4050050113	2021-08-20	12:46:38	0.84	537.0
4050050114	2021-08-21	08:42:46	0.89	985.0
4050050117	2021-09-05	07:44:57	0.79	324.0
4050050118	2021-09-06	08:33:17	0.86	591.0

TABLE 4.4: *NICER* observations in the AO4 cycle.

ObsID	Date	Time (UT)	Orbital phase	Exposure (s)
5571010101	2022-03-30	08:29:00	0.28	820.0
5571010102	2022-03-31	01:26:31	0.33	2776.0
5571010103	2022-04-01	00:39:59	0.38	4069.0
5571010104	2022-04-01	23:53:39	0.44	2884.0
5571010105	2022-04-17	14:36:21	0.39	671.0
5571010106	2022-04-17	23:54:28	0.41	4103.0
5571010107	2022-04-19	00:44:19	0.48	570.0
5571030101	2022-05-04	04:39:53	0.39	2023.0
5571030102	2022-05-05	00:46:20	0.45	2357.0
5571040101	2022-05-21	06:05:56	0.43	1900.0
5571040102	2022-05-22	00:40:40	0.48	1358.0
5571050101	2022-06-06	07:46:37	0.40	4171.0
5571050102	2022-06-07	02:24:45	0.45	4757.0
5571060102	2022-06-23	00:30:18	0.42	4346.0
5571060103	2022-06-24	01:16:20	0.48	2331.0
5571070101	2022-07-09	11:37:28	0.41	1351.0
5571070102	2022-07-10	00:00:00	0.44	1837.0
5571070103	2022-07-11	00:26:21	0.51	501.0
5571090101	2022-08-11	15:59:40	0.42	1147.0
5571090102	2022-08-12	01:15:40	0.45	3669.0
5571090103	2022-08-13	01:49:34	0.51	311.0
5571110101	2022-09-13	19:22:27	0.43	1487.0
5571110102	2022-09-14	01:34:00	0.45	2019.0
5571110103	2022-09-15	02:54:40	0.51	3418.0
5571110104	2022-09-16	03:04:00	0.57	446.0
5571120101	2022-09-30	09:35:20	0.44	889.0
5571120102	2022-10-01	00:50:27	0.48	1799.0
5571120103	2022-10-02	00:04:26	0.54	16.0
5571140102	2023-01-07	00:21:57	0.42	14.5
5571140103	2023-01-08	01:04:20	0.48	352.5
5571140104	2023-01-09	00:21:20	0.54	212.5
5571160101	2023-02-10	00:14:20	0.48	10783.0
5571160102	2023-02-11	01:12:40	0.54	4748.0
5571170101	2023-02-26	14:18:48	0.48	2152.0
5571170102	2023-02-27	01:03:08	0.51	5729.0
5571170103	2023-02-28	00:23:40	0.57	479.0

4.2 *MAXI*

4.2.1 Mission & Operation

The Monitor of All-sky X-ray Image (*MAXI* ; Matsuoka et al. 2009) is a mission dedicated for all-sky X-ray monitoring. The mission objectives of *MAXI* include alerting transient X-ray events to the community, monitoring long-term behaviors of bright X-ray sources, facilitating multi-wavelength observations of variable sources, generating unbiased X-ray source catalogs, and observing diffuse cosmic X-ray emission.

The instrument was launched by the Space Shuttle Endeavor on July 16, 2009 and was placed in the Japanese Experiment Module (Kibo) onboard the ISS. *MAXI* takes an all-sky image by scanning the entire sky by the orbital motion of the ISS. *MAXI* employs two semicircular arc-shaped X-ray slit cameras with a wide field of view (FOV). Throughout the 92-minute orbit of the ISS, *MAXI* captures a 360-degree image of the sky.

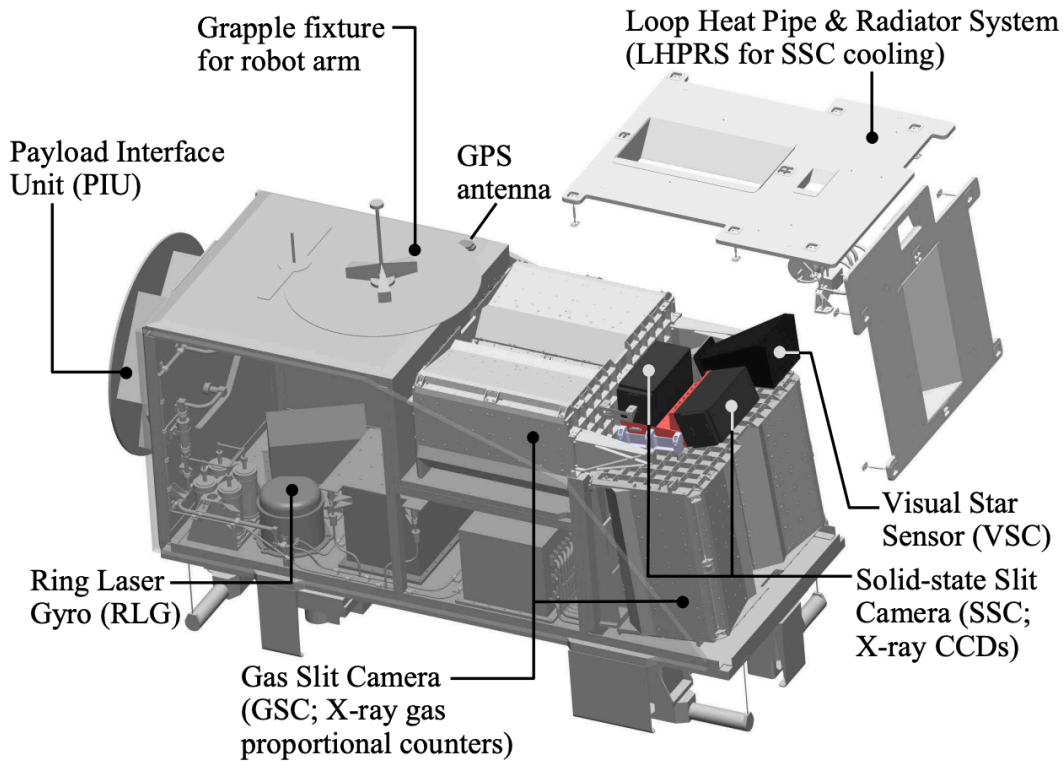

Figure 4.6: Schematic view of *MAXI* (Matsuoka et al., 2009).

4.2.2 Instruments

The schematic view of *MAXI* is shown in Figure 4.6. It has two payloads; the Solid-state Slit Camera (SSC; Tomida et al., 2011) and the Gas Slit Camera (GSC; Mihara et al., 2011).

The SSC employs X-ray CCD detectors, which are sensitive to the energy range of 0.7–7 keV with moderate energy resolution. Due to performance degradation, SSC is no longer used for observations after 2021. We do not use SSC data in this work.

The GSC uses the gas proportional counters, which are sensitive to the energy range of 2–20 keV. It has an energy resolution of 18 % at 5.9 keV. GSC is good at detecting transient objects thanks to its large effective area and high observation efficiency. The GSC comprises six units of conventional slit camera. Each unit contains two one-dimensional proportional counters, as well as the slit and slat collimators (Figure 4.7). The 12 proportional counters provide the total detection area of 5350 cm^2.

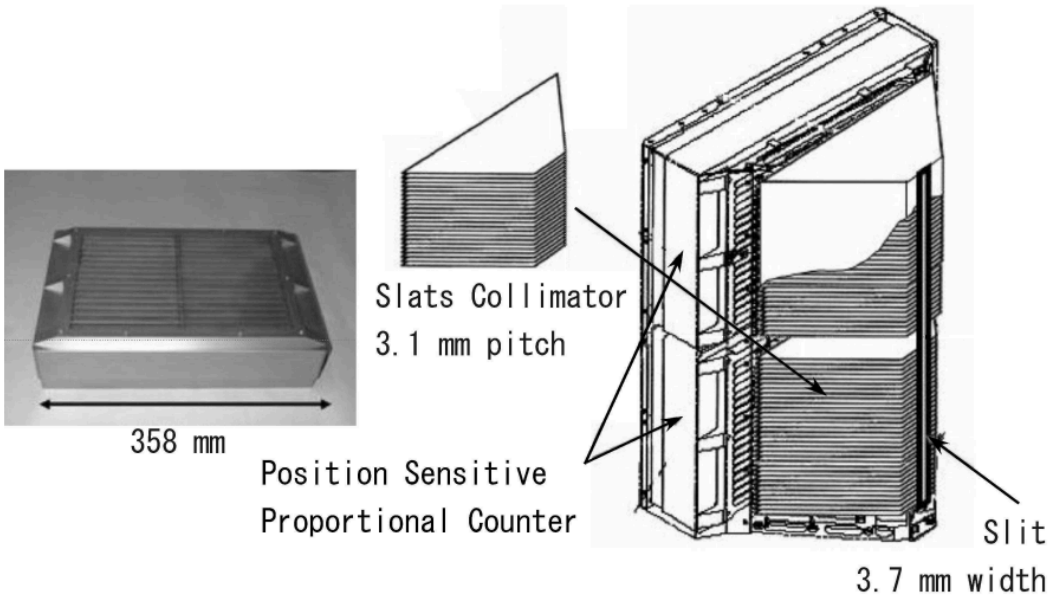

Figure 4.7: Schematic view of one GSC unit among six; a unit consists of two gas-proportional counters, and slit & slat collimators (Matsuoka et al., 2009).

4.2.3 Observations

We used all the available GSC data of *MAXI* since its operation to investigate the long-term behavior of Cir X-1.

4.2.4 Data reduction

MAXI offers several methods for retrieving the data. Among them, we used the on-demand data service[1]. We obtained the level 3 equivalent products for the X-ray light curve binned by a day or by an ISS orbit.

[1] http://maxi.riken.jp/mxondem/index.html

4.3 *Suzaku*

4.3.1 Mission & Operation

Suzaku (Figure 4.8; Mitsuda et al. 2007) is the X-ray observatory built by the Institute of Space and Astronautical Science (ISAS) of the Japan Aerospace Exploration Agency (JAXA) in cooperation with the U.S. National Aeronautics and Space Administration (NASA) Goddard Space Flight Center (GSFC) and several other organizations. The mission was dedicated to studying high-temperature plasmas in the X-ray to gamma-ray bands. The main goals include the investigation of the structure and evolution of the universe and spectroscopic observations of black hole binaries and active galactic nuclei in a wide energy band.

Suzaku was launched by the M-V rocket from the Uchinoura Space Center on July 10, 2005. It was injected into the orbit with an altitude of 570 km, an inclination of 31°, and an orbital period of 96 minutes. It has three scientific instruments. One is the X-ray Imaging Spectrometers (XIS; Koyama et al. 2007) with four X-ray CCD detectors, three of which use the front-illuminated chips (FI; energy range of 0.4–12 keV) and the remaining one uses the back-illuminated chip (BI; energy range of 0.2–12 keV). They are mounted on the focal plane of the four X-ray Telescopes (XRT; Serlemitsos et al. 2007). The second is the non-imaging collimated Hard X-ray Detector (HXD; Takahashi et al. 2007) covering an energy range of 10–600 keV. The third is the X-ray Spectrometer (X-ray Spectrometer; XRS; Kelley et al. 2007) using an X-ray micro-calorimeter detector. The XRS lost its super-liquid He before scientific observations and was not operational. *Suzaku* conducted scientific observations for 10 years, well beyond its design life of two years, and ended its operation in 2015.

4.3.2 Instruments

We focus on the description of the XRT+XIS, which are used in this thesis.

4.3.2.1 XRT

XRTs are X-ray telescopes that use grazing-incidence reflecting optics consisting of thin foil conical mirror shells that are densely nested. The small thickness of the reflectors makes it possible to place many nested structures in a limited space. As a result, a large effective area and moderate imaging resolution are realized in the energy range of 0.2–12 keV. Of the five units of XRTs, four (XRT-I0–I3) are used for XIS (Figure 4.9). The angular resolution of the XRTs ranges from 1.8–2.3 arcmin for the half-power diameter. The effective area is typically 440 cm^2 at 1.5 keV and 250 cm^2 at 8 keV per telescope. The focal length is 4.75 m for XRT-Is. The optical axes of each XRT are located within 2 arcmin of each other. The field of view of XRT-Is is about 17 arcmin at 1.5 keV and 13 arcmin at 8 keV. Figure 4.10 shows the effective area of the four XRT-I's, including detector efficiency, compared with that of *XMM-Newton* and *Chandra*.

4.3.2.2 XIS

XIS is equipped with X-ray CCDs operated in the photon-counting mode as in *Chandra* ACIS (§ 4.4.2). X-ray CCDs convert an incident X-ray photon into a charge cloud. The

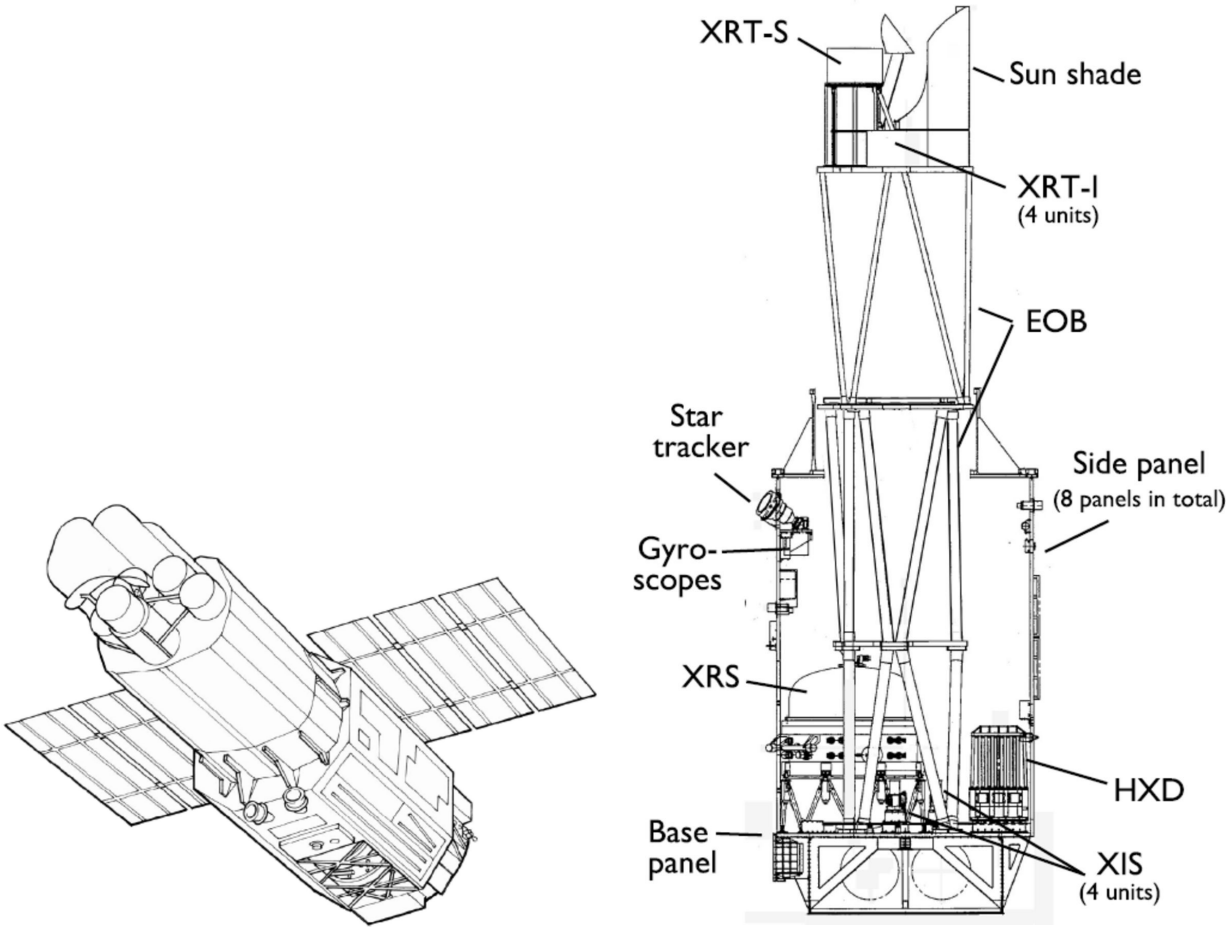

Figure 4.8: Schematic view (left) and the side view of *Suzaku* with the internal structures (right) (Mitsuda et al., 2007).

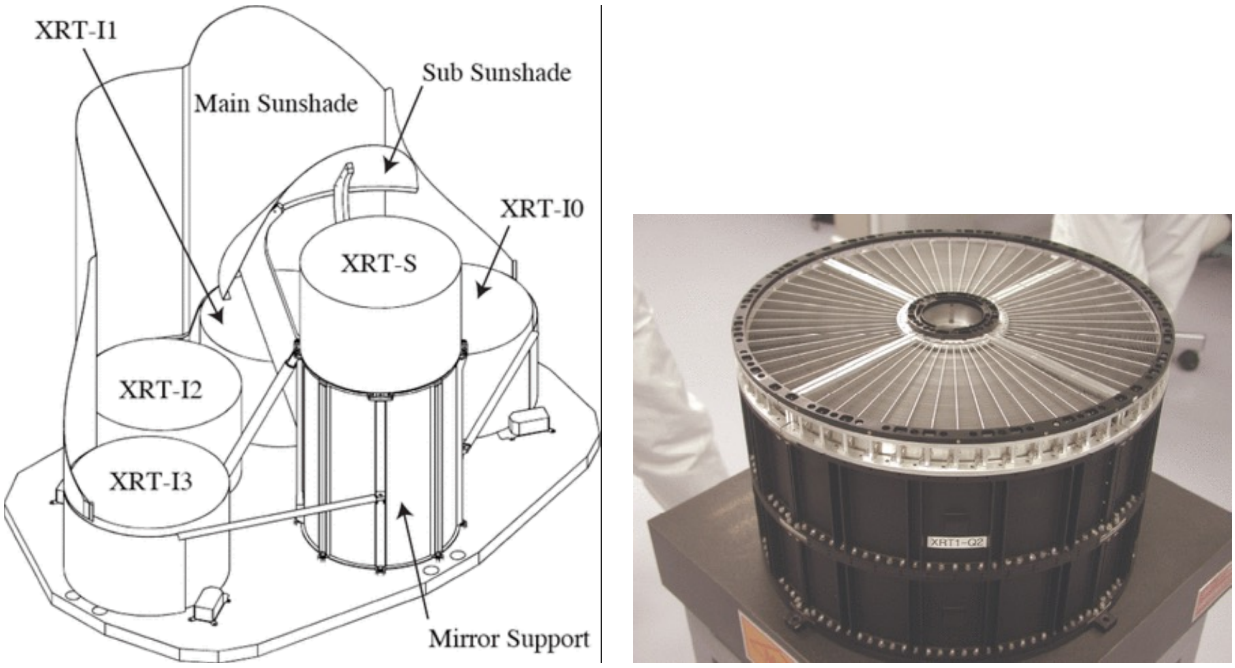

Figure 4.9: Schematic view of XRT mounted on the top plate of the Extensible Optical Bench (EOB) (left) and a photo of the XRT-I1 (Serlemitsos et al., 2007).

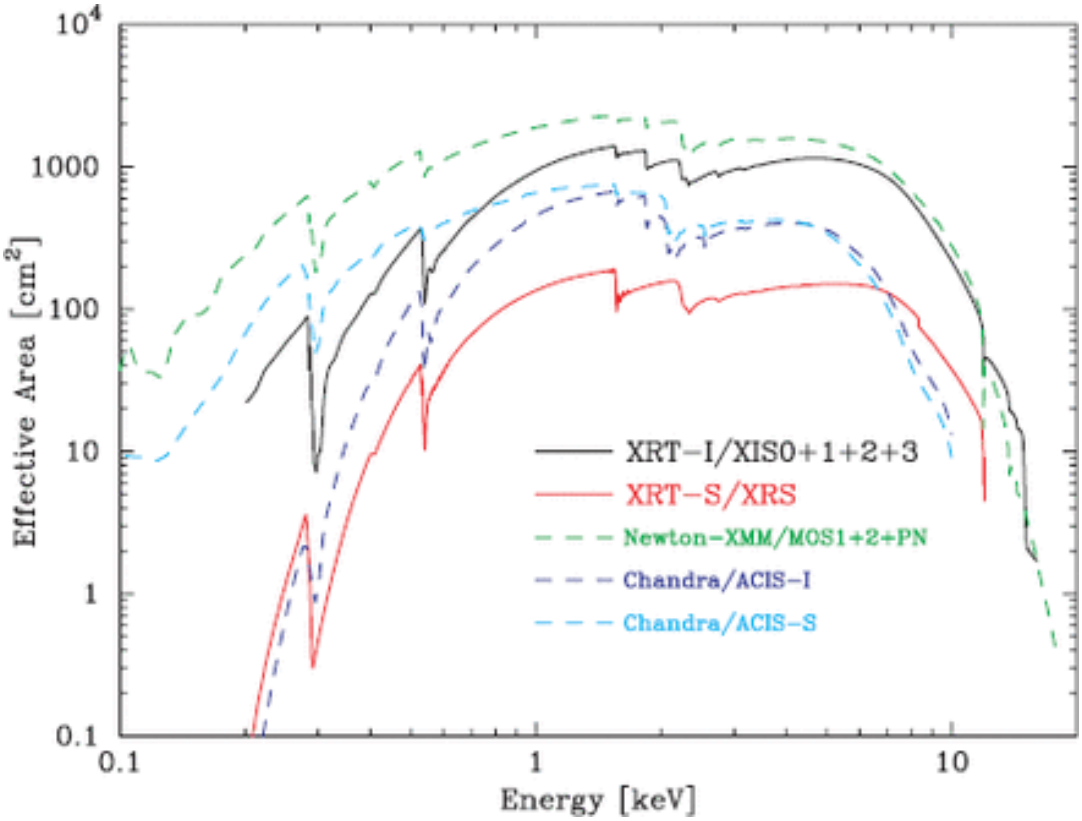

Figure 4.10: Effective area of XRT+XIS system, for FI (XIS0, 2, 3) and BI (XIS1)(Serlemitsos et al., 2007).

amount of the charge is proportional to the energy of the absorbed X-ray. The charges are transferred and read out pixel by pixel through a clock pattern of time-varying electrical potential. This enables the X-ray imaging observations with a large format array.

The four sets of XIS named XIS 0–3 are located on the focal plane of the X-ray Telescopes called XRT-I0–3. Each CCD camera has one CCD chip with an array of 1024×1024 pixels covering 17.8×17.8 arcmin^2 region. Each pixel has a size of 24×24 μm^2, and the size of the array is 25×25 mm^2. The energy resolution of XISs is shown in Figure 4.11. The entire XIS2 was lost in 2006 due to a micrometeorite hit, which was not used in this thesis.

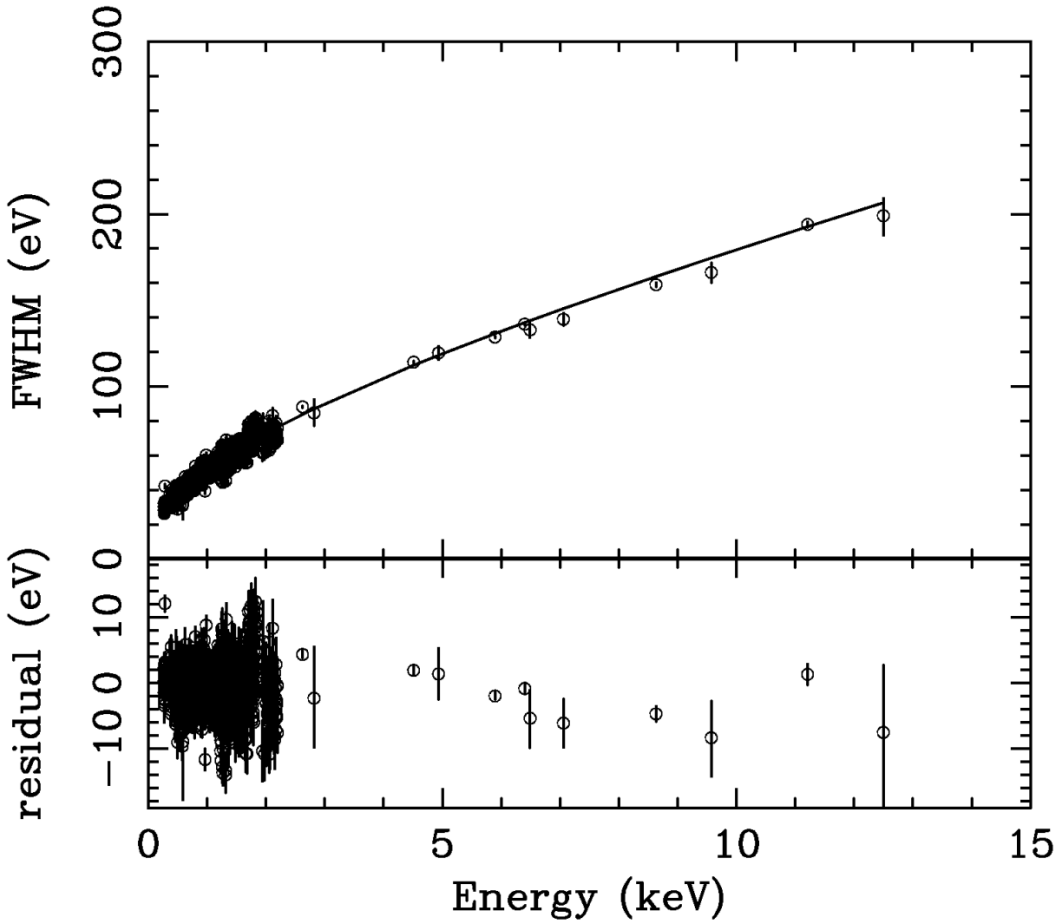

Figure 4.11: The energy resolution as a function of energy for the FI (XIS 2 segment C) (Koyama et al., 2007).

4.3.3 Observations

One observation of Cir X-1 was conducted by *Suzaku* as shown in Table 4.5. The observation was made with the XIS in the normal clocking mode with no window or burst options.

4.3.4 Data reduction

We used `HEAsoft` version 6.31.1 for the data reduction. The events in the 3×3 and 5×5 editing modes were combined for each of the observations with XIS0, 1, and 3. The

TABLE 4.5: Observation of Cir X-1 by *Suzaku*.

ObsID	Date	Time (UT)	Orbital phase	Exposure (ks)
402070010	2008-03-05	04:41:16	0.07	46.4

source region was chosen within a 1.2 arcmin circle around the center of the object. The background region was chosen as a concentric circle of a $\sim$1.7 arcmin radius excluding the source region. We created RMF with `xisrmfgen` and ARF with `xissimarfgen`. For the spectral fitting, we re-binned the spectra so that each bin contains more than 50 counts.

4.4 *Chandra*

4.4.1 Mission & Operation

The *Chandra* X-ray observatory (Figure 4.12; Weisskopf et al. 2002; see also Chandra-IPI-Teams 2022[2]), formerly known as NASA's Advanced X-ray Astrophysics Facility (AXAF), was launched with the Space Shuttle Columbia on July 23, 1999. *Chandra* is the third mission of NASA's Great Observatories and is designed to measure the X-rays emitted by various celestial objects. Its high spatial resolution makes it possible to study extremely faint point-like sources even in crowded fields.

It was put into an elliptical high-altitude orbit, with a perigee and an apogee altitude of ∼10,000 and ∼140,000 km and the orbital period of ∼64 hours to enable uninterrupted exposures of celestial objects longer than 170 ks. The satellite and its instruments were developed and built by the Smithsonian Astrophysical Observatory (SAO), NASA's Marshall Space Flight Center (MSFC), Massachusetts Institute of Technology (MIT), the Space Research Institute of the Netherlands (SRON), the Max-Planck Institut für extraterrestrische Physik (MPE) and the University of Kiel. SAO provides support for the *Chandra* X-ray Center (CXC) and general mission support.

Two focal plane science instruments, the Advanced CCD Imaging Spectrometer (ACIS; Garmire et al., 2003) and the High Resolution Camera (HRC; Murray et al., 2000) are well suited to capture the sharp images formed by the mirror and provide information about the incoming X-rays, including their position, energy, and time of arrival. They are placed in the focal plane of the telescope and can be switched by the mechanical moving module.

The grating spectroscopy is possible using one of the two grating instruments; the Low Energy Transmission Grating (LETG; Brinkman et al., 2000) and the High Energy Transmission Grating (HETG; Canizares et al., 2005). The attitude of the satellite is controlled and determined by the Pointing Control and Aspect Determination (PCAD) system with a higher accuracy than the spatial resolution of ∼0.5 arcsec at the optical on-axis position.

4.4.2 Instruments

We focus on HRMA (mirrors; § 4.4.2.1), HETGS (grating; § 4.4.2.2), and ACIS (detector; § 4.4.2.3), with which the data used in this work were taken.

4.4.2.1 HRMA

The X-ray telescope is called the high-resolution mirror assembly (HRMA; Figure 4.13). It consists of four units of the grazing-incidence Wolter-I type mirror. The outer mirror is number 1, and, progressing inwards, 3, 4, and 6 (the original design had six mirror units but numbers 2 and 5 were eliminated). The diameters range from about 0.65–1.23 m. The distance from the center of the Central Aperture Plate (CAP) to the HRMA focus point is 10.0548 m, varying slightly around this value for each mirror pair. On-axis X-ray photons enter each mirror and are reflected twice by the paraboloids and the hyperboloids, then they converge at the focus for the imaging.

[2] https://cxc.cfa.harvard.edu/proposer/POG/html/index.html

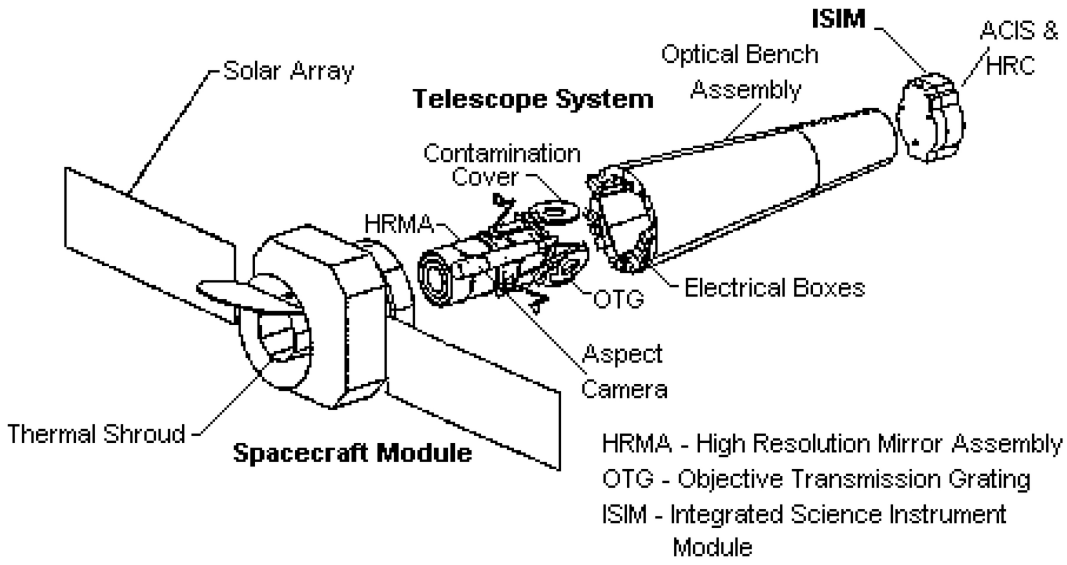

Figure 4.12: Schematic view of the *Chandra* satellite and sub-systems (Weisskopf et al., 2002).

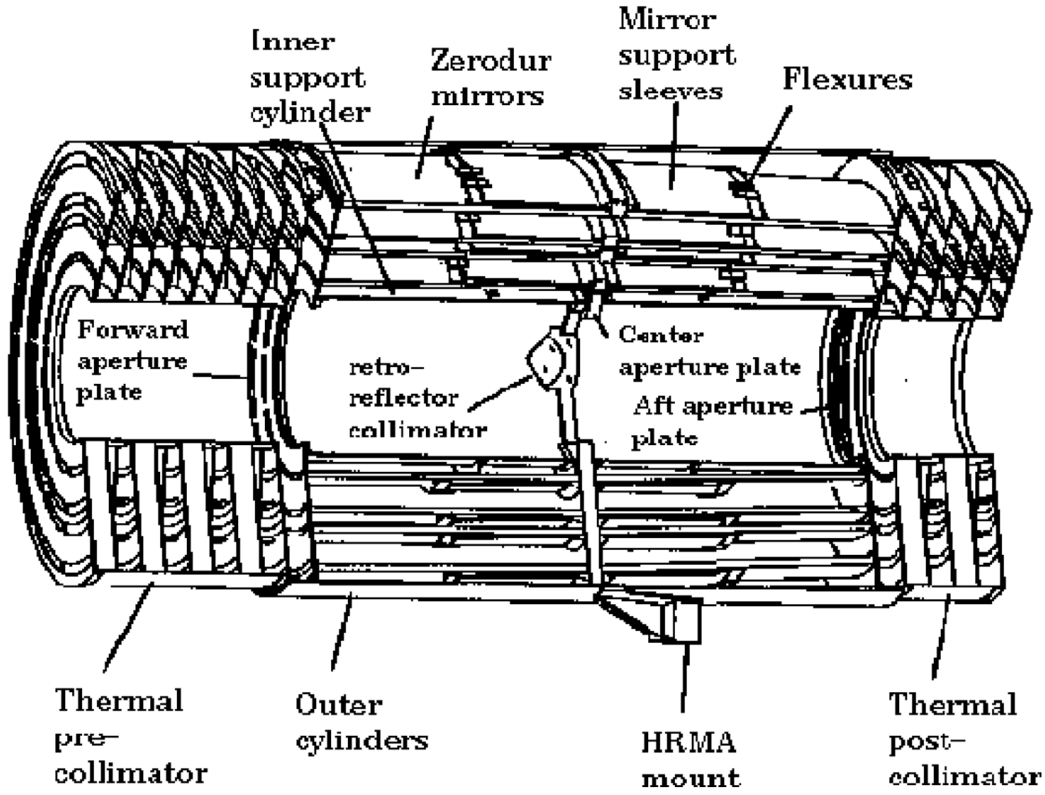

Figure 4.13: Schematic view of HRMA (Chandra-IPI-Teams, 2022).

The geometric aperture of HRMA is 1145 cm^2. Since the reflectivity of the mirror optics depends on the photon energy as well as the grazing angle, the HRMA throughput varies as a function of them. The on-axis effective area is ~800 cm^2 at 0.25 keV, which decreases to 100 cm^2 at 8 keV. The effective area combined with the focal plane instruments is shown in Figure 4.14. The effective area also decreases with increasing off-axis angles.

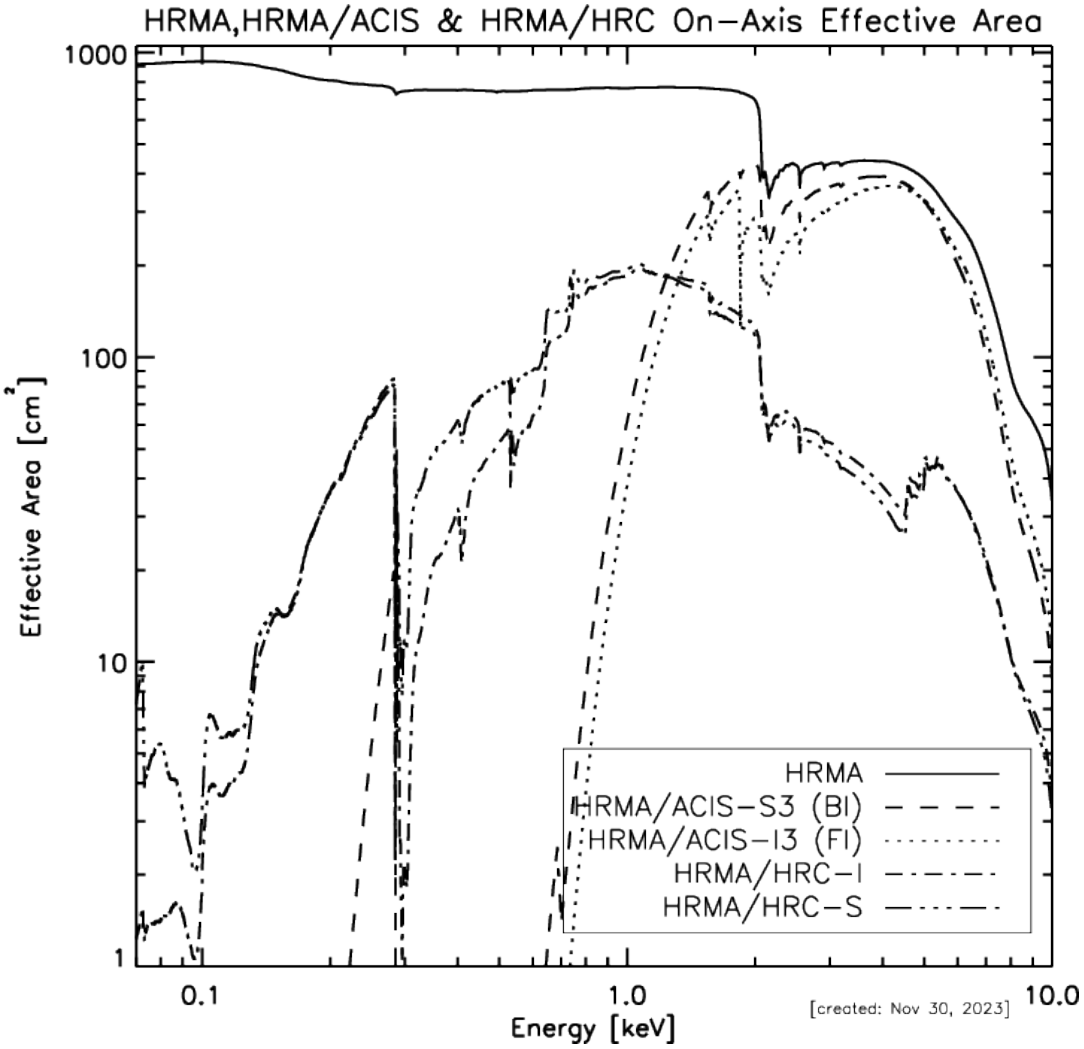

Figure 4.14: Effective area of HRMA, HRMA+HRC, and HRMA+ACIS (Chandra-IPI-Teams, 2022).

4.4.2.2 HETG

HETG stands for the High-Energy Transmission Grating (Figure 4.15; Canizares et al. 2005). When used with an HRMA and a focal plane instrument (either HRC or ACIS), the instrument is called the High-Energy Transmission Grating Spectrometer (HETGS). The HETG is designed for use mainly with ACIS-S, but other detectors can be used depending on specific applications.

HETGS can be used to obtain grating spectra of point sources and slightly extended (~a few arcsec) sources, providing high-resolution spectra ($E/\Delta E$ up to 1000) in the energy range of 0.4–10.0 keV. The HETG itself consists of two sets of gratings. One is

the Medium Energy Grating (MEG), which intercepts X-rays from the outer shell of the HRMA and is optimized for the medium energy range (0.4–5.0 keV). The other is the High Energy Grating (HEG), which intercepts X-rays from the two inner shells and is optimized for high energy (0.8–10.0 keV). Both are mounted on a single support structure so that they can be used simultaneously. The two sets of gratings are mounted at different angles so that the dispersive images from the HEG and MEG form a shallow "X" shape centered at the non-dispersive (zero-order) position (Figure 4.16). The combination of the diffraction efficiency of HETG, the effective area of HRMA, and the detector efficiency of ACIS-S yields the effective area of the system as a function of energy (Figure 4.17).

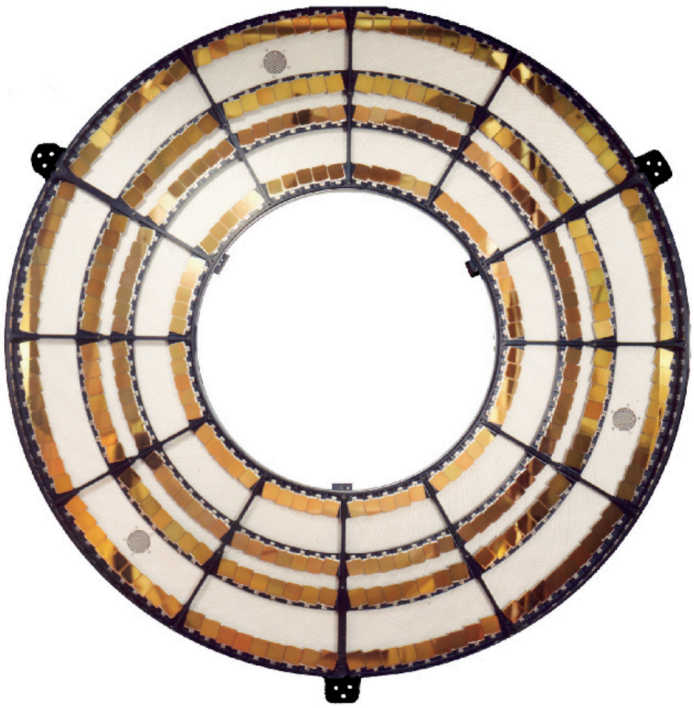

Figure 4.15: Photo of the HETG (Canizares et al., 2005).

4.4.2.3 ACIS

ACIS (Garmire et al., 2003) is a sub-system for imaging, spectroscopy, and temporal studies of astronomical X-ray sources. It consists of 10 X-ray CCD chips, each of which has a format of 1024×1024 pixels (Figure 4.18). Each CCD covers an 8.4 arcmin×8.4 arcmin on the celestial sphere with a plate scale of 0.492 arcsec/pixel, which is compatible with the on-axis performance of the telescope of 0.5 arcsec. Four CCDs are arranged in a 2×2 array (ACIS-I) used for imaging, and the other six are arranged in a 1×6 array (ACIS-S) used either for imaging or for grating spectroscopy. Two CCDs are back-illuminated (BI) optimized for soft X-rays and eight are front-illuminated (FI). In principle, any combination of up to 6 CCDs can be operated simultaneously.

Because CCDs are sensitive to optical light as well as X-rays, an optical blocking filter (OBF) is placed above the CCD. The filter is made of polyimide (polycarbonate plastic) sandwiched between two thin aluminum layers. The filter and gate structure of the CCDs absorb low-energy X-rays, resulting in the edges in the effective area (Figure 4.14).

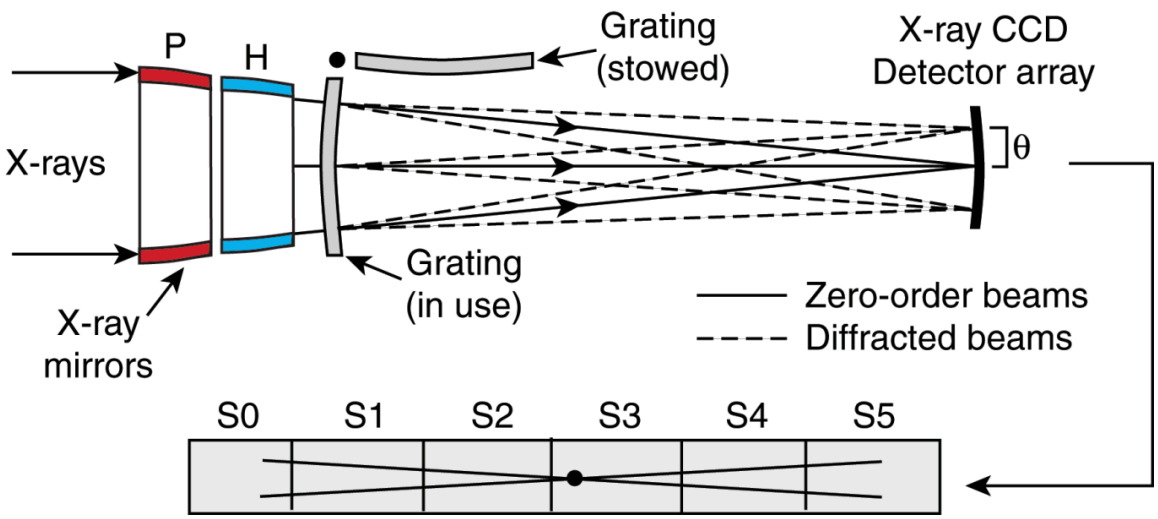

Figure 4.16: Schematic view of HETGS. It is used by the combination of HRMA, HETG, and the ACIS-S detector (Canizares et al., 2005). The outer two rings of gratings are MEGs and intercept rays from the HRMA shells 1 and 3. The inner two rings are HEGs working with HRMA shells 4 and 6.

4.4.3 Observations

The observations conducted by *Chandra* HETGS are summarized in Table 4.6 and Figure 4.19. All observations were made with ACIS-S.

Table 4.6: Observations by *Chandra* HETGS.

ObsID	Date	Time (UT)	Orbital phase	Exposure (s)
706	2000-02-29	22:08:46	0.04	27950.0
1700	2000-06-08	04:11:58	0.04	15320.0
1905	2001-08-01	09:27:01	0.39	8160.0
1906	2001-08-05	17:32:05	0.65	8130.0
1907	2001-08-09	14:27:33	0.89	8210.0
5478	2005-06-02	08:34:54	0.14	52650.0
6148	2005-01-03	01:13:49	0.05	25070.0
8993	2008-07-16	07:57:55	0.13	33720.0
12235	2010-07-04	05:04:05	0.58	20080.0
18990	2017-06-17	12:35:21	0.43	13620.0
20093	2017-06-17	22:00:54	0.45	10100.0
20094	2017-07-05	06:50:07	0.50	36470.0

4.4.4 Data reduction

CXC (*Chandra* X-ray Center) provides the data analysis software package called the *Chandra* Interactive Analysis of Observations (CIAO; Fruscione et al. 2006) and CALDB. We used `CIAO` version 4.15 and `CALDB` version 4.10.2 in this study.

We retrieved the level 1 products and reprocessed them using the `chandra_repro` task to create the level 2 products. We extracted the source and background spectra

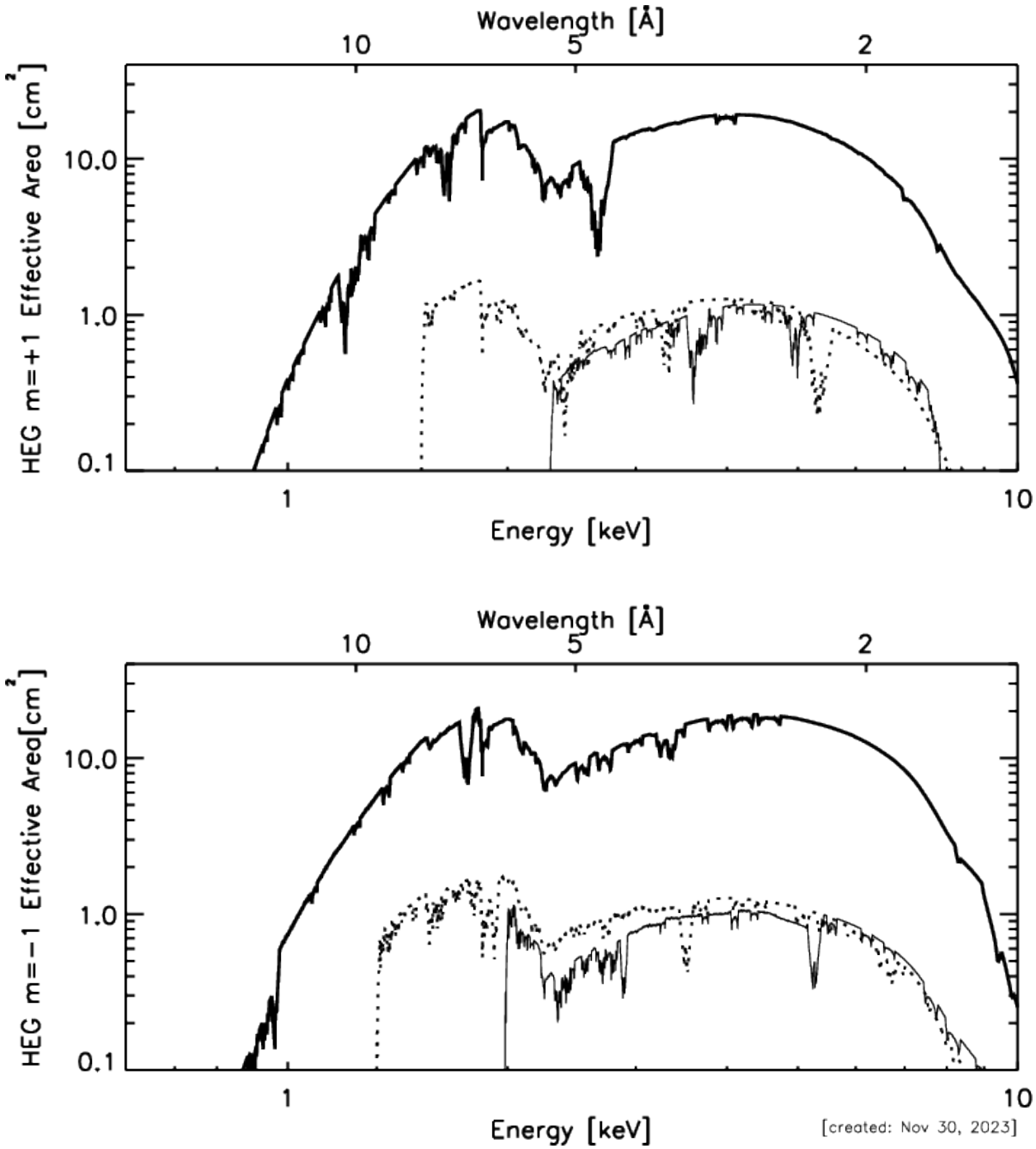

Figure 4.17: Effective area integrated over the PSF of HETGS HEG (Chandra-IPI-Teams, 2022). The m =+1, +2, +3 orders (top) and the m =–1, –2, –3 orders (bottom) are shown as thick solid lines, the dotted line, and thin solid lines, in order.

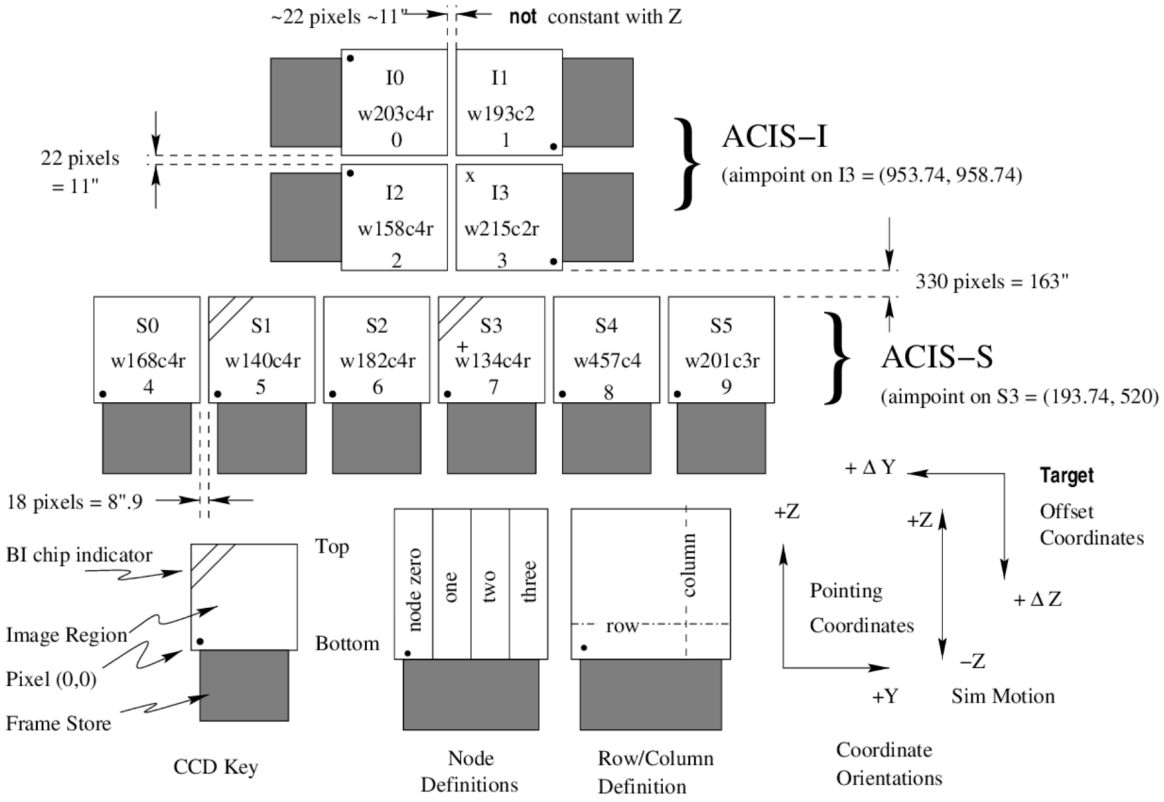

Figure 4.18: Schematic view of the ACIS focal plane (Chandra-IPI-Teams, 2022).

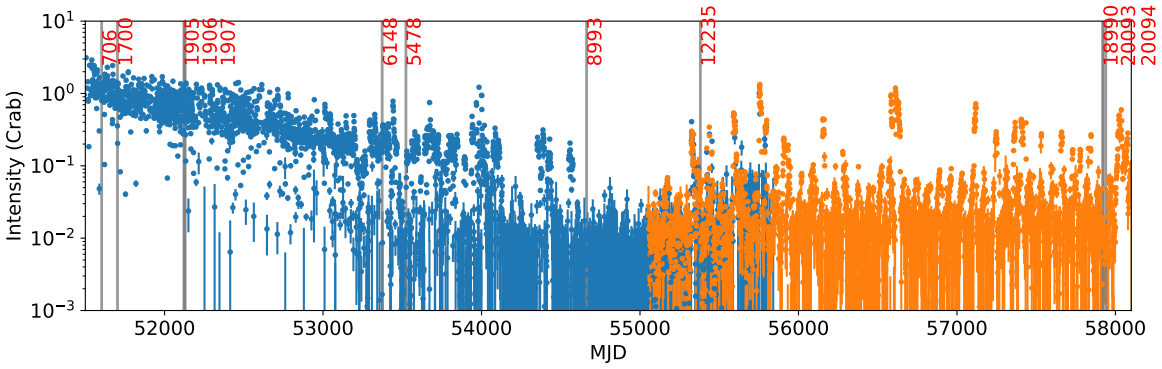

Figure 4.19: Epochs of *Chandra* observations (vertical lines and numbers). The blue data points were taken by *RXTE* and the orange ones by *MAXI*.

using the `tgextract` task separately for each grating part (HEG and MEG) and order. We used the positive and negative first-order grating datasets both for MEG and HEG. The background spectra were extracted.

We created the ARF and RMF files with the `mktgresp` task. For the spectral fitting, we combined the positive and negative spectral data for HEG and MEG with the `combine_grating_spectra` task. The resultant spectra are shown in Figure 4.20.

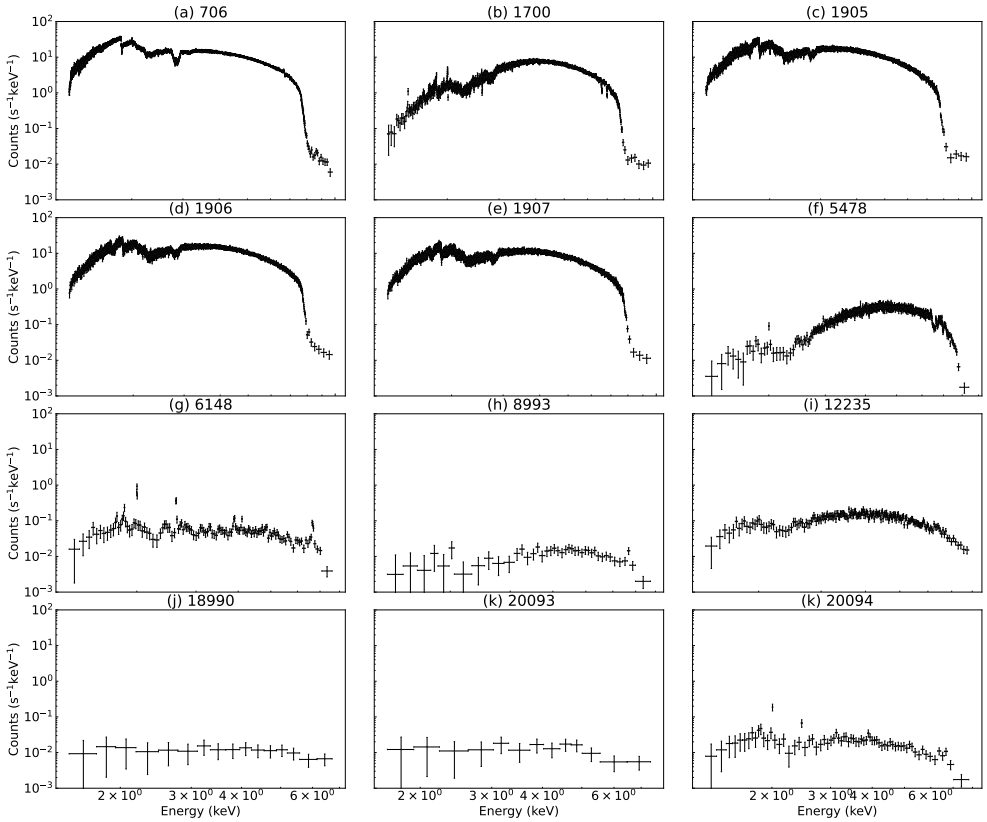

Figure 4.20: Spectra observed with *Chandra*/HETGS. We only show HEG data in each panel with ObsID.

Chapter 5

Physics & Tools

Contents

5.1 Atomic Physics 75
5.1.1 Atomic structure 75
5.1.2 Photon-atom interactions 79
5.2 Radiative Transfer 87
5.2.1 Concept 87
5.2.2 Detailed balance and equilibrium states 90
5.2.3 Line formation, profile, and strength 94
5.3 Photoionized Plasma 101
5.3.1 Nebular approximation 101
5.3.2 Ionization parameter 103
5.3.3 Balances 104
5.4 Radiative Transfer Codes 110
5.4.1 Two-stream solver 110
5.4.2 Monte Carlo Solvers 114
5.4.3 Further Development 117

This chapter delves into the basic principles of physics and the computational tools that underpin our study of the photoionized plasma and its emission. This chapter is described referring to Pradhan and Nahar (2011), Osterbrock and Michael Shull (1989), Rybicki and Lightman (1985), Takayanagi (2009), Umemura, Fukue, and Nomura (2016), and Nakamura et al. (2022).

In § 5.1, we start with an introduction to the atomic physics, beginning with an exploration of the atomic structure (§ 5.1.1), followed by a discussion of interactions between atoms and photons (§ 5.1.2). We omit a discussion of interactions between atoms and electrons, which plays a minor role in the presented data interpretation. This section provides a microscopic view of the interaction of photons and matter.

We then go into radiative transfer in § 5.2. This section provides a macroscopic view of the interaction of photons propagating through matter. We introduce the basic equations of radiative transfer (§ 5.2.1), delve into the detailed balance and representative equilibrium states (§ 5.2.2), and discuss the process of line formation and its profile and strength (§ 5.2.3).

Based on the two bases of physics (atomic physics and radiative transfer), we describe the physics of the photoionized plasma in § 5.3. Under the nebular approximation (§ 5.3.1), we define the ionization parameter (§ 5.3.2) and elucidate three balances achieved in stable photoionized plasmas (§ 5.3.3).

In § 5.4, we proceed to discuss the numerical radiative transfer codes to calculate the synthesized X-ray spectra from photoionized plasmas. Several different solvers and implementations are described; two-stream solver `XSTAR` in § 5.4.1 and Monte Carlo solver `MONACO` and `SKIRT` in § 5.4.2. We also make an extension to the codes in § 5.4.3.

5.1 Atomic Physics

5.1.1 Atomic structure

5.1.1.1 Wave equations

When examining the atomic states, the system's energy is obtained by solving the wave equation. This equation encompasses both the kinetic energy and the Coulomb potential energy among the nuclei and the electrons that constitute an atom.

Schrödinger equation (non-relativistic case): The wave function of an atom in the non-relativistic case is described by the Schrödinger equation

$$\mathcal{H}\psi = i\hbar\frac{\partial\psi}{\partial t}, \tag{5.1}$$

where the Hamiltonian $\mathcal{H}$ is described as

$$\mathcal{H} = -\frac{\hbar^2}{2M}\nabla_X^2 - \frac{\hbar^2}{2m_e}\sum_i \nabla_{x_i}^2 - \sum_i \frac{Ze^2}{4\pi\epsilon r_i} + \sum_{i,j}\frac{e^2}{4\pi\epsilon r_{ij}} \tag{5.2}$$

with the Coulomb potential among the nucleus and electrons.

Analytical solutions can be obtained for single-electron systems (H and H-like ions). For multielectron systems, approximations are required due to the complex interactions introduced by the Coulomb forces among multiple electrons. Iterative methods, such as perturbation or variation methods, are often used. In the perturbation method, for example, the eigenstates of the atoms are determined by neglecting the Coulomb interaction term among electrons for the zeroth order solution. Then, a correction term is computed as a perturbation for a higher-order solution.

Dirac equation (relativistic case): For simplicity, we deal with the equation of a free electron. Since time and space should be described equally to comply with Einstein's relativity theory, Dirac revised the Hamiltonian as

$$\mathcal{H} = c\boldsymbol{\alpha}\cdot\boldsymbol{p} + m_e c^2\beta \tag{5.3}$$

where $\boldsymbol{\alpha}$ is a vector, and its three components α_k $(k = x, y, z)$ are operators represented by matrices. The specific forms of $\boldsymbol{\alpha}$ and β are expressed as follows.

$$\boldsymbol{\alpha} = \begin{pmatrix} 0 & \boldsymbol{\sigma} \\ \boldsymbol{\sigma} & 0 \end{pmatrix} \tag{5.4}$$

$$\beta = \begin{pmatrix} 1 & 0 & 0 & 0 \\ 0 & 1 & 0 & 0 \\ 0 & 0 & -1 & 0 \\ 0 & 0 & 0 & -1 \end{pmatrix} \tag{5.5}$$

where $\boldsymbol{\sigma}$ is the Pauli matrix,

$$\sigma_x = \begin{pmatrix} 0 & 1 \\ 1 & 0 \end{pmatrix} \tag{5.6}$$

$$\sigma_y = \begin{pmatrix} 0 & -i \\ i & 0 \end{pmatrix} \tag{5.7}$$

$$\sigma_z = \begin{pmatrix} 1 & 0 \\ 0 & -1 \end{pmatrix}. \tag{5.8}$$

The wave function ψ also has four components

$$\psi = \begin{pmatrix} \psi_1 & \psi_2 & \psi_3 & \psi_4 \end{pmatrix}^{\boldsymbol{T}}. \tag{5.9}$$

The energy of the electrons should satisfy

$$E^2 = \boldsymbol{p}^2 c^2 + m_e^2 c^4. \tag{5.10}$$

To obtain a steady-state solution, we assume

$$\psi = \chi(\boldsymbol{r}) e^{-iEt/\hbar}, \tag{5.11}$$

and an equation without t as

$$E\chi(\boldsymbol{r}) = [c\boldsymbol{\alpha} \cdot \boldsymbol{p} + m_e c^2 \beta]\chi(\boldsymbol{r}). \tag{5.12}$$

When the coordinate system is chosen so that the momentum is oriented in the z direction, four independent solutions are obtained

$$\chi_1 \propto \begin{pmatrix} 1 \\ 0 \\ \frac{E_p - m_e c^2}{cp} \\ 0 \end{pmatrix}, \quad \chi_2 \propto \begin{pmatrix} 0 \\ 1 \\ 0 \\ \frac{E_p - m_e c^2}{cp} \end{pmatrix}, \quad \chi_3 \propto \begin{pmatrix} -\frac{E_p - m_e c^2}{cp} \\ 0 \\ 1 \\ 0 \end{pmatrix}, \quad \chi_4 \propto \begin{pmatrix} 0 \\ \frac{E_p - m_e c^2}{cp} \\ 0 \\ 1 \end{pmatrix}, \tag{5.13}$$

where $E_p = \sqrt{m_e^2 c^4 + \boldsymbol{p}^2 c^2}$. Here, χ_1 and χ_2 represent the states in which the spins are oriented in the $\pm z$ directions, respectively, and the energy is $+E_p$. On the other hand, χ_3 and χ_4 correspond to the states with the spin oriented in the $\pm z$ direction and an energy of $-E_p$. In this manner, concepts of the spin and the positron are inherently embedded in the Dirac equation.

5.1.1.2 Quantum numbers

Schrödinger equation (non-relativistic case): The Schrödinger equation for a single electron atom is solved analytically by introducing a position vector for the center of mass and a relative position vector. By focusing on the former for the relative motion ($\boldsymbol{r}$), we separate variables as

$$\psi(\boldsymbol{r}) = R(r)Y(\theta, \phi). \tag{5.14}$$

For the non-radial part, we can describe $Y(\theta, \phi)$ using the spherical harmonic function

$$Y_{lm}(\theta, \phi) = i^{|m|+m}\sqrt{\frac{(2l+1)(l-|m|)!}{2(l+|m|)!}}P_l^{|m|}(\cos\theta)\frac{e^{im\phi}}{\sqrt{2\pi}} \tag{5.15}$$

with the associated Legendre function $P_l^{|m|}(x)$ of the azimuthal quantum number l and the magnetic quantum number m.

For the radial part, we can describe $R(r)$ using the associated Laguerre polynomials. The energy, denoted as E, is calculated as

$$E = -\frac{\mu e^4 Z^2}{2n^2(4\pi\epsilon_0)^2\hbar^2} \tag{5.16}$$

with the principal quantum number n. The wave function is described with the three quantum numbers (n, l, and m). For H-like ions, the energy levels are degenerate for l and m, thus n only determines the energy. For multi-electron ions, the energy levels are degenerate for m, therefore, a combination of (n, l) is necessary to specify the energy level of an electron orbit.

It has been known from experiments that the electron has a degree of freedom called spin with two quantum states, which is not included in the Schrödinger equation. The spin angular momentum (s) is manually added. For the azimuthal quantum number of l, we have $2l+1$ states. In analogy with this, the spin angular momentum s should have $2s+1$ states of 2, thus $s = \frac{1}{2}$.

Dirac equation (relativistic case): In the Schrödinger theory, the angular momentum $\boldsymbol{l}\hbar$ commutes with the Hamiltonian; thus, a quantum state can be specified with its absolute value l and its projection m in one direction. In Dirac's theory, in contrast, the angular momentum $\boldsymbol{l}\hbar = \boldsymbol{r} \times \boldsymbol{p}$ and the Hamiltonian do not commute.

$$[\mathcal{H}, \boldsymbol{l}\hbar] = -i\hbar c\boldsymbol{\alpha} \times \boldsymbol{p} \tag{5.17}$$

The spin angular momentum and the Hamiltonian do not commute either.

$$[\mathcal{H}, \boldsymbol{s}\hbar] = i\hbar c\boldsymbol{\alpha} \times \boldsymbol{p} \tag{5.18}$$

However, when they are added, $\boldsymbol{j} = \boldsymbol{l} + \boldsymbol{s}$ commutes with the Hamiltonian as

$$[\mathcal{H}, (\boldsymbol{l} + \boldsymbol{s})\hbar] = 0. \tag{5.19}$$

Thus, the quantum state can be specified by j.

5.1.1.3 Energy levels and labeling

LS coupling: For the Schrödinger equation of multi-electron atoms, $\boldsymbol{l_i}$ and $\boldsymbol{s_i}$ of individual electrons (i) vary due to the electron-electron interactions. However, their sums

$$\boldsymbol{L} = \sum_i \boldsymbol{l_i} \tag{5.20}$$

$$\boldsymbol{S} = \sum_i \boldsymbol{s_i} \tag{5.21}$$

remain constant with time as they are commutable with the non-relativistic Hamiltonian ($[\mathcal{H}, \boldsymbol{L}]$=0, $[\mathcal{H}, \boldsymbol{S}]$=0). This is called the "LS coupling" or Russell-Saunders coupling, and $\boldsymbol{L}$ and $\boldsymbol{S}$ can be used to specify the energy levels.

***j*-*j* coupling:** For atoms of a large Z, the relativistic effects cannot be ignored. The spin-orbit interaction of an electron becomes significant. Their sum for an electron $\boldsymbol{j_i} = \boldsymbol{l_i} + \boldsymbol{s_i}$ varies as they interact with other electrons, but their sum

$$\boldsymbol{J} = \sum_i \boldsymbol{j_i} \tag{5.22}$$

remains constant with time. This is called the j-j coupling and $\boldsymbol{J}$ is the quantum number to specify the energy levels.

Term Symbol: The LS and j-j couplings are limiting cases at low and high Z atoms. For a wide range of Z, both LS and j-j couplings hold to some extent, which is called the intermediate coupling scheme. The commonly used energy labeling is based on this scheme, in which L, S, and J are used to specify energy levels as

$$^{2S+1}L_J \tag{5.23}$$

where $L = 0, 1, 2, 3$ are denoted by the letters S, P, D, F, and so on. We use this notation throughout this thesis.

Transitions: The electron orbits are referred to as K-shell, L-shell, M-shell, and so on, corresponding to the principle quantum number $n = 1, 2, 3, ...$ respectively. Transitions with $\Delta n = 1, 2, 3, ...$ are denoted as $\alpha, \beta, \gamma,$, etc. For example, the photon emitted when the electron transitions from $n = 2$ to $n = 1$ is called the Kα line, and the transition from $n = 3$ to $n = 1$ is known as the Kβ line. Conventionally, transitions of inner-shell electrons are labeled as Kα, Kβ, etc, while those of outer-shell electrons are labeled as Lyα, Lyβ, etc, for H-like ions. We use this notation throughout this thesis.

5.1.2 Photon-atom interactions

The atoms and ions described above interact with photons, which we use for spectroscopy. The amount of interaction depends on the photon energy and the atomic states, which are characterized by the cross section. By the interaction with a photon, an atom or an ion makes transitions between two energy levels. These transitions are categorized into "bound-free" (§ 5.1.2.1), "bound-bound" (§ 5.1.2.2), and "free-free" (§ 5.1.2.3) transitions, depending on whether the electrons in the state are bound to or free from the atom or ion potential.

5.1.2.1 Bound-free interactions

We start with the bound-free cross section, which we derive from the semi-classical theory. The non-relativistic Hamiltonian of an electron in an external electromagnetic field is

$$\mathcal{H} = \frac{1}{2m_e}\left(\boldsymbol{p} - \frac{e\boldsymbol{A}}{c}\right)^2 + e\phi = \frac{p^2}{2m_e} - \frac{e}{m_e c}\boldsymbol{A}\cdot\boldsymbol{p} + \frac{e^2\boldsymbol{A}^2}{2m_e c^2} + e\phi, \tag{5.24}$$

with the electron mass m_e, the vector potential $\boldsymbol{A}$, and the scalar potential ϕ. The photon interaction is calculated by assuming that the photon is represented by a plane-parallel electromagnetic field of

$$\boldsymbol{A}(\boldsymbol{r}, t) = \boldsymbol{A}(t)e^{i\boldsymbol{k}\cdot\boldsymbol{r}}. \tag{5.25}$$

Assuming that the $\boldsymbol{A}^2$ term is negligible compared to the $\boldsymbol{A}$ term,

$$\mathcal{H} \sim \frac{p^2}{2m_e} + e\phi - \frac{e}{m_e c}\boldsymbol{A}\cdot\boldsymbol{p}, \tag{5.26}$$

where the former two terms are time-independent ($\equiv \mathcal{H}^0$), while the latter term is time-dependent. We treat the latter as the perturbation term ($\equiv \mathcal{H}^1$) and calculate the transition rate between the two states. With the non-perturbed state wave function ϕ_k and the energy eigenvalue E_k, the solution of the wave function derived from the time-dependent Schrödinger equation is written as

$$\psi(t) = \sum a_k(t)\phi_k \exp\{(-iE_k t/\hbar)\}. \tag{5.27}$$

When an electron is ejected from the initial bound state (i) to the final ionized free state (f), and the transition rate γ_{fi} during the time interval from t =0 to $t = T$ is,

$$\gamma_{fi} = \frac{4\pi^2}{\hbar^2 T}|\mathcal{H}^1_{fi}(\omega_{fi})|^2, \tag{5.28}$$

where

$$\mathcal{H}^1_{fi}(\omega) \equiv \frac{1}{2\pi}\int_0^T \mathcal{H}^1_{fi}(t)e^{i\omega t}dt \tag{5.29}$$

$$\mathcal{H}^1_{fi}(t) = \int \phi^*_f \mathcal{H}^1 \phi_i d^3x \tag{5.30}$$

$$\omega_{fi} \equiv \frac{E_f - E_i}{\hbar}. \tag{5.31}$$

For a multi-electron atom, we can write $\mathcal{H}^1$ as

$$\mathcal{H}^1 = -\frac{e}{m_e c}\sum \boldsymbol{A}\cdot\boldsymbol{p}_j = \frac{ie\hbar}{m_e c}\boldsymbol{A}\cdot\sum\nabla_j. \tag{5.32}$$

With the plane parallel electromagnetic wave, the transition rate is

$$\gamma_{fi} = \frac{4\pi^2 e^2}{m_e^2 c^2 T}\frac{I(\omega_{fi})}{\omega_{fi}^2}|\left\langle f\right| e^{i\boldsymbol{k}\cdot\boldsymbol{r}}\boldsymbol{e}\cdot\boldsymbol{\nabla}\left|i\right\rangle|^2 \tag{5.33}$$

with the electromagnetic wave intensity

$$I(\omega) = \frac{c|\boldsymbol{E}(\omega)|^2}{T} = \frac{\omega^2}{cT}|\boldsymbol{A}(\omega)|^2 \tag{5.34}$$

and a unit vector $\boldsymbol{e}$.

When the ionized electron has kinetic energy ranging between p to $p+dp$, the differential transition rate is described as

$$d\gamma = \frac{4\pi^2 e^2}{m_e^2 c^2}\frac{I(\omega_{fi})}{\omega_{fi}^2}|\left\langle f\right| e^{i\boldsymbol{k}\cdot\boldsymbol{r}}\boldsymbol{e}\cdot\boldsymbol{\nabla}\left|i\right\rangle|^2\left(\frac{dn}{dpd\Omega}dpd\Omega\right). \tag{5.35}$$

Thus, the differential cross section for the bound-free emission is

$$\frac{d\sigma_{\mathrm{bf}}}{d\Omega} = \frac{\alpha v V}{2\pi\omega}|\left\langle f\right| e^{i\boldsymbol{k}\cdot\boldsymbol{r}}\boldsymbol{e}\cdot\boldsymbol{\nabla}\left|i\right\rangle|^2, \tag{5.36}$$

with $v = p/m_e$ and $\alpha = e^2/\hbar c$.

When a hydrogen-like ion with a nuclear charge Z in the ground state absorbs a photon with a frequency of ω that is large enough to ionize the atom (13.6 eV for H), the differential cross section is

$$\frac{d\sigma_{\mathrm{bf}}}{d\Omega} = \frac{32\alpha\hbar}{m_{\mathrm{e}}\omega}\left(\frac{Z}{a_0}\right)^5\frac{q(\boldsymbol{e}\cdot\boldsymbol{q})^2}{[(Z/a_0)^2+q^2]^4} \tag{5.37}$$

with $\boldsymbol{q} = \boldsymbol{p}/\hbar$. When the electron energy is much larger than the ionization energy,

$$\frac{d\sigma_{\mathrm{bf}}}{d\Omega} \approx \frac{32\alpha\hbar}{m_{\mathrm{e}}\omega}\left(\frac{Z}{a_0}\right)^5\frac{q(\boldsymbol{e}\cdot\boldsymbol{q})^2}{q^7} \tag{5.38}$$

and the total cross section is

$$\sigma_{\mathrm{bf}} = \int\frac{d\sigma_{\mathrm{bf}}}{d\Omega}d\Omega = \frac{32\alpha\hbar}{m_{\mathrm{e}}\omega}\left(\frac{Z}{a_0}\right)^5\frac{4\pi}{3q^5} \approx \frac{(2\alpha)^{9/2}\pi Z^5 c^{7/2}}{3a_0^{3/2}\omega^{7/2}}. \tag{5.39}$$

The total cross section for an atom at an energy level of (n,l) is written as

$$\sigma_{\mathrm{bf}} = \frac{512\pi^7 m_e e^{10} Z^4}{3^{3/2}ch^6n^5}\frac{g_{bf}(\omega,n,l,Z)}{\omega^3} = \frac{64\pi^4 m_e e^{10}Z^4}{3^{3/2}ch^6n^5}\frac{g_{bf}}{\nu^3}, \tag{5.40}$$

where $g_{bf}(\omega,n,l,Z)$ is Gaunt factor for bound-free transition. Figure 5.1 shows an example of numerical calculations.

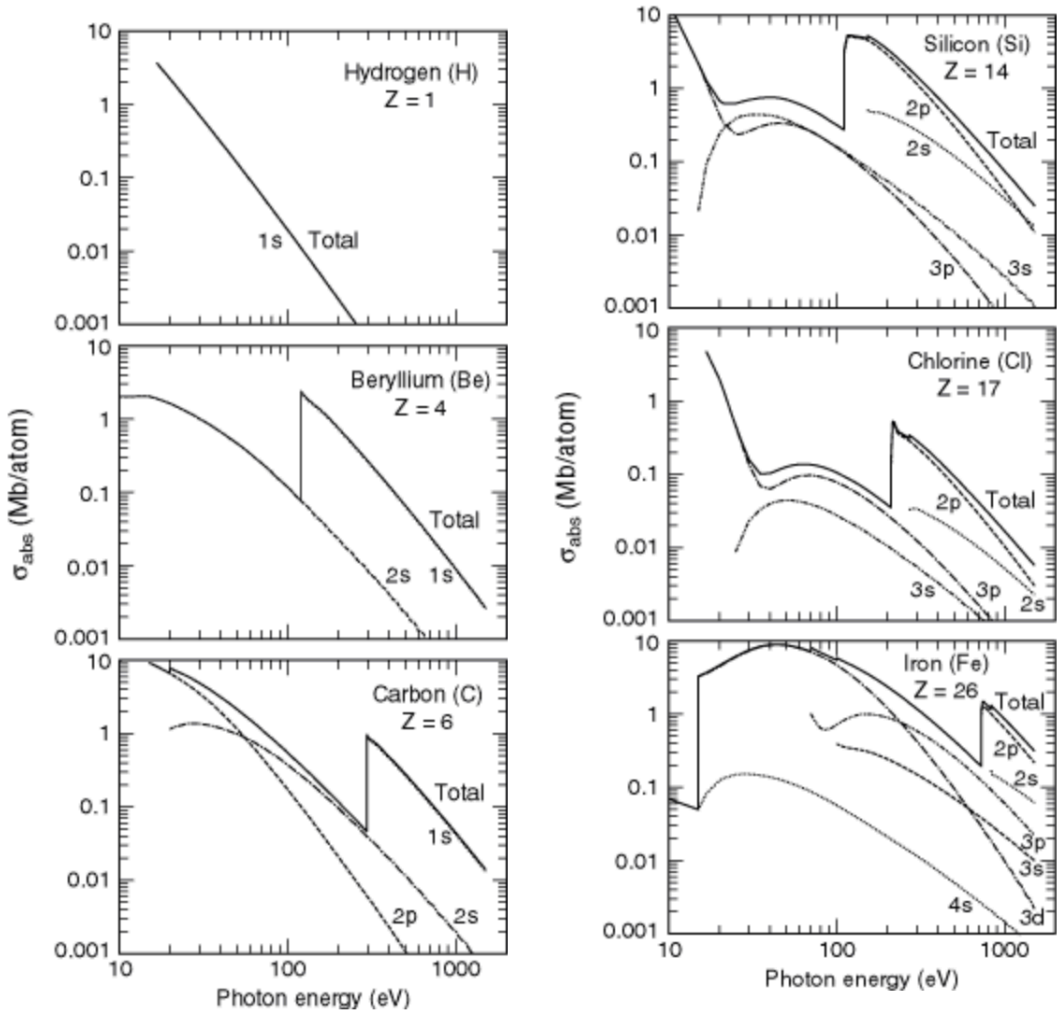

Figure 5.1: Sub-shell photoionization cross sections for H, Be and C (left) and for Si, Cl and Fe (right) calculated with the Hartree-Fock-Slater one-electron central potential model (Yeh and Lindau, 1985).

5.1.2.2 Bound-bound interactions

When an electron makes a transition from an initial bound state (i) to another bound state (j), the transition rate γ_{ij} is described similarly with Equation 5.33 as,

$$\gamma_{ij} \propto |\langle i| e^{i\boldsymbol{k}\cdot\boldsymbol{r}}\boldsymbol{e}\cdot\boldsymbol{\nabla}|j\rangle|^2. \tag{5.41}$$

Under $\boldsymbol{k}\cdot\boldsymbol{r} \ll 1$, by using the following expansion formula and approximation

$$e^{i\boldsymbol{k}\cdot\boldsymbol{r}} = 1 + i\boldsymbol{k}\cdot\boldsymbol{r} + ... \approx 1, \tag{5.42}$$

the following term in Equation 5.41 is approximated as

$$\langle i| e^{i\boldsymbol{k}\cdot\boldsymbol{r}}\boldsymbol{e}\cdot\boldsymbol{\nabla}|j\rangle \sim \boldsymbol{e}\cdot\langle i|\boldsymbol{\nabla}|j\rangle = \boldsymbol{e}\cdot -\frac{m_\mathrm{e}}{\hbar}\omega_{ij}\boldsymbol{r}_{ij}. \tag{5.43}$$

Therefore,

$$|\langle i|\boldsymbol{e}\cdot\boldsymbol{\nabla}|j\rangle|^2 = \left(\frac{m_\mathrm{e}}{\hbar}\omega_{ij}\right)^2|\boldsymbol{e}\cdot\boldsymbol{r}_{ij}|^2. \tag{5.44}$$

This is called the dipole approximation. Such electric dipole transitions with non-zero transition rates are called the allowed transition. On the other hand, a transition for which this value is zero is called the forbidden transition, which means that the first term in Equation 5.41 does not contribute, and the true transition rate can be obtained by considering the higher order terms.

Oscillator strength: When describing the transition rates considered so far, it is convenient to introduce the oscillator strength defined as

$$f_{ij} = \frac{2m_\mathrm{e}(E_j - E_i)}{3\hbar^2 g_i}|\langle i|\boldsymbol{r}_{ij}|j\rangle|^2, \tag{5.45}$$

which is a dimensionless value to describe the cross section in the unit of the dipole approximation cross section. For $E_i < E_j$, f_{ij} is called the absorption oscillator strength and f_{ji} is called the emission oscillator strength. The oscillator strength is defined as the mean and sum of the initial and final state, respectively, when they have multiplicity g_i and g_j, thus

$$g_i f_{ij} = g_j f_{ji}. \tag{5.46}$$

In practice, the "gf–value" is often stored in atomic databases, so as not to be confused between f_{ij} and f_{ji}.

Selection Rule: Assuming the LS coupling, electric dipole transitions are allowed when all the following conditions are met:

$$\Delta S = 0 \tag{5.47}$$

$$\Delta L = 0, \pm 1 \tag{5.48}$$

$$\Delta J = 0, \pm 1 \tag{5.49}$$

except for $J = 0 \to 0$. The Grotrian diagram (Figure 5.2) shows the possible level transitions of Ne-like Fe ion (Fe XVII) as an example.

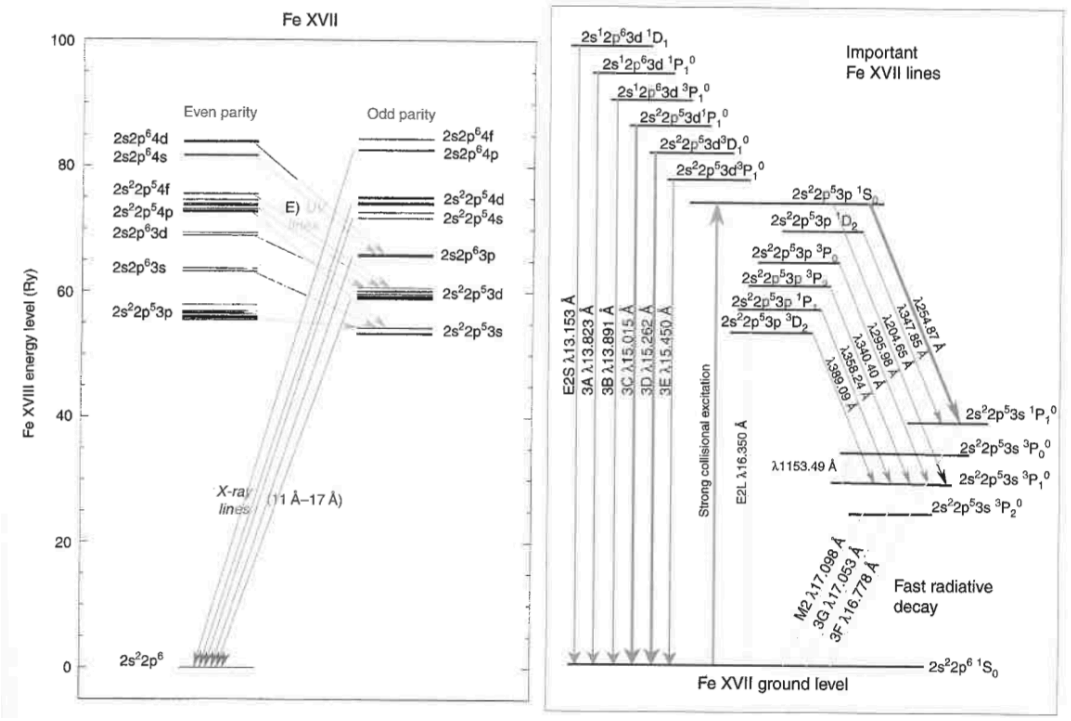

Figure 5.2: Grotrian diagram of Fe XVII energy level and transitions (Pradhan and Nahar, 2011; Chen, Pradhan, and Eissner, 2003).

5.1.2.3 Free-free interactions and scattering

Photons interact with electrons either they are free or bound. In addition, electrons interact with other charged particles to emit photons. They are scattering processes, which we describe here all together.

Photon scattering by free electron

Thomson scattering: If the incident photon energy is much smaller than the rest mass energy of electrons (511 keV) and the electrons are non-relativistic; i.e.,

$$h\nu \ll m_e c^2, \quad m_e v^2/2 \ll m_e c^2, \tag{5.50}$$

we can assume that the photon-electron interaction does not change the energy of both but the direction of incoming and outgoing photon. In this context, we treat the incident photon as an electromagnetic wave and the free electron as a charged particle within the classical treatment. Let's assume that an electric field

$$\boldsymbol{E} = \boldsymbol{E_0} \cos(\omega t - kz) \tag{5.51}$$

is injected in the z direction for an electron placed at the origin. The equation of motion for the electron is described by

$$m_e \ddot{\boldsymbol{r}} = -e\boldsymbol{E_0} \cos \omega t, \tag{5.52}$$

and the dipole moment is $\boldsymbol{d} = -e\boldsymbol{r}$, thus

$$\ddot{\boldsymbol{d}} = \frac{e^2}{m_\mathrm{e}} \boldsymbol{E_0} \cos \omega t. \tag{5.53}$$

The intensity of the dipole radiation P emitted by this dipole oscillator within a solid angle $d\Omega$ is given by

$$\frac{dP}{d\Omega} = \frac{1}{4\pi c^3} (\ddot{\boldsymbol{d}} \times \boldsymbol{n})^2 = \frac{e^4 E_0^2}{8\pi m_\mathrm{e}^2 c^3} \sin^2 \Theta \tag{5.54}$$

$$P = \frac{e^4 E_0^2}{3 m_\mathrm{e}^2 c^3}, \tag{5.55}$$

where $\boldsymbol{n}$ is the unit vector in the radial direction, and Θ is the angle between $\boldsymbol{d}$ and $\boldsymbol{n}$. Since the time-averaged magnitude of the Poynting vector of the electromagnetic wave $\boldsymbol{s}$ is

$$\langle s \rangle = \frac{c}{8\pi} E_0^2, \tag{5.56}$$

the relation between the angular distribution of the output energy and the differential cross section of the emitted photons is written as

$$\frac{dP}{d\Omega} = \langle s \rangle \frac{d\sigma}{d\Omega}. \tag{5.57}$$

Let $\theta = \pi/2 - \Theta$ be the angle of the emitted photon relative to the incident photon, then

$$\frac{d\sigma}{d\Omega} = r_\mathrm{e}^2 \cos^2 \theta \tag{5.58}$$

with the classical electron radius

$$r_\mathrm{e} \equiv \frac{e^4}{m_\mathrm{e}^2 c^4}. \tag{5.59}$$

Therefore, the total cross section is

$$\sigma_\mathrm{T} = \int \frac{d\sigma}{d\Omega} d\Omega = \frac{8\pi}{3} r_\mathrm{e}^2, \tag{5.60}$$

which is called the Thomson scattering cross section. This is independent of the incident photon energy $h\nu$ and has a value of 6.65×10^{-25} cm^2. The electron column density of 1.5×10^{24} cm^{-2} makes the Thomson optical depth to be unity, which is an important criterion as the photoionized plasma that we study often goes below or above this value.

When the electromagnetic wave is unpolarized, it can be considered as the average of multiple polarizations distributed uniformly over the polarization angles. The angle between the direction of incidence and the direction of scattering θ leads $\cos\Theta = \sin\theta \cos(\phi - \alpha)$. By taking the average over α,

$$\frac{d\sigma}{d\Omega} = \frac{1}{2} r_\mathrm{e}^2 (1 + \cos^2 \theta) = \frac{3}{16\pi} \sigma_\mathrm{T} (1 + \cos^2 \theta). \tag{5.61}$$

Compton scattering: When the incident photon energy is comparable to the rest mass energy of electrons, the energy exchange between the photon and electron cannot

be ignored, and the photon needs to be treated as a particle, rather than like a field in the case of Thomson scattering.

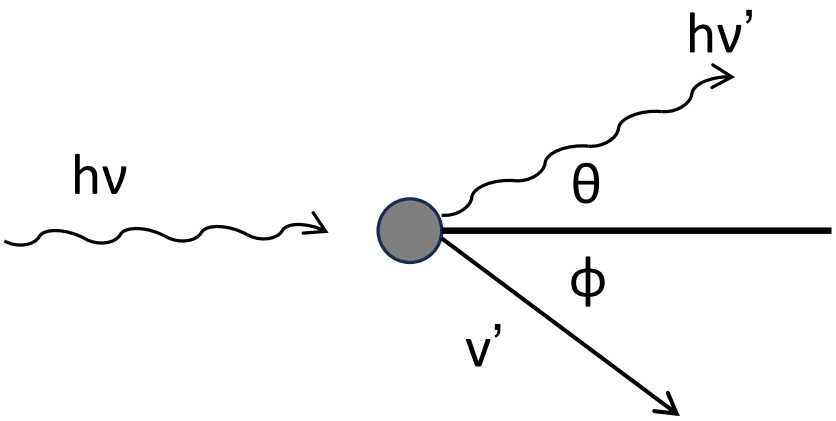

Figure 5.3: Compton scattering.

By applying the law of conservations of momentum before and after the interaction, we obtain

$$\frac{m_e c^2}{h\nu'} - \frac{m_e c^2}{h\nu} = 1 - \cos\theta \tag{5.62}$$

$$\nu' = \frac{\nu}{1 + \frac{h\nu}{m_e c^2}(1 - \cos\theta)}. \tag{5.63}$$

This scattering is important in the hard X-ray band since the cross section of the Compton scattering surpasses that of photoionization above ∼10 keV.

When relativistic effects come into play, the scattering cross section also undergoes changes and becomes smaller than the Thomson scattering cross section. The effective scattering cross section is given as the Klein–Nishina's formula (Klein and Nishina, 1929),

$$\frac{d\sigma}{d\Omega} = \frac{3\sigma_T}{16\pi}[C^3 + C - C^2 \sin^2\theta] \tag{5.64}$$

with the photon energy $x = E/m_e c^2$, the Thomson cross section σ_T, and the Compton factor,

$$C = C(\theta, x) = \frac{1}{1 + x(1 - \cos x)}. \tag{5.65}$$

The total cross section is derived by the integration as

$$\sigma = \frac{3\sigma_T}{4}\left[\frac{1+x}{(1+2x)^2} + \frac{2}{x^2} + \left(\frac{1}{2x} - \frac{x+1}{x^3}\right)\ln(2x+1)\right]. \tag{5.66}$$

This value approaches to the Thomson cross section for $x \to 0$, and it declines as the photon energy increases.

Photon scattering by bound electron: For bound electrons, the scattering processes are classified into three: the Rayleigh scattering without changing the final state from the initial state,

$$X_{+i} + h\nu \to h\nu + X_{+i}, \tag{5.67}$$

the Raman scattering leaving the final state into an excited state,

$$X_{+i} + h\nu \rightarrow h\nu' + X^*_{+i}, \tag{5.68}$$

and the Compton scattering leaving the final state into an ionized state

$$X_{+i} + h\nu \rightarrow h\nu' + X_{+i-1} + e^-. \tag{5.69}$$

Bremsstrahling: Photon radiation resulting from the two-body scattering of electrons and ions is referred to as "bremsstrahlung". When electrons follow a thermal (Maxwellian) distribution, the emission is specifically called the thermal bremsstrahlung. The total emission per unit time per unit volume per unit frequency is described as

$$\frac{dW}{dVdtd\nu} = \frac{2^5\pi e^6}{3mc^{7/2}} \left(\frac{2\pi}{3k}\right)^{1/2} T^{-1/2} Z^2 n_{\mathrm{e}n_i} e^{-h\nu/kT} \bar{g}_f f \tag{5.70}$$

with a Gaunt factor

$$g_f f = \frac{\sqrt{3}}{\pi} \log\left(\frac{b_{\max}}{b_{\min}}\right) \tag{5.71}$$

and the impact parameter b.

5.2 Radiative Transfer

5.2.1 Concept

5.2.1.1 Basic equation

The radiative transfer equation describes the change of the light ray intensity I erg s^{-1} cm^{-2} str^{-1} along a light path s as a function of time and position. We hereafter use the notation X_ν as the value of X at a specific frequency ν. The change of the specific intensity dI_ν while passing a medium across ds increases by the radiation from the medium and the scattering into the light path, and decreases by the absorption by the medium and the scattering out of the light path, thus

$$\frac{dI_\nu}{ds} = -\alpha_\nu \left(I_\nu - \frac{\eta_\nu}{\alpha_\nu} \right) - \beta_\nu (I_\nu - \Phi_\nu) \tag{5.72}$$

Below, we define the parameters in this equation.

Emission coefficient: The emission of photons from the medium per unit volume, per unit time, per unit solid angle radiated per unit frequency is referred to as the emission coefficient denoted by η_ν erg cm^{-3} s^{-1} Hz^{-1} str^{-1}. The emission coefficient is also represented by other parameters with a different unit as

$$\eta_\nu = \epsilon_\nu \rho = \frac{j_\nu}{4\pi} \rho, \tag{5.73}$$

where ϵ_ν erg g^{-1} s^{-1} Hz^{-1} str^{-1} is mass emissivity and j_ν erg g^{-1} s^{-1} Hz^{-1} is angle-averaged emissivity. Here, ρ is mass density of the medium.

Absorption coefficient: We consider a medium with a number density n and a photon absorption cross section ζ_ν. As photons pass through this absorber, the intensity of the radiation decreases as,

$$dI_\nu = -n\zeta_\nu I_\nu ds = -\alpha_\nu I_\nu ds = -\kappa_\nu \rho I_\nu ds. \tag{5.74}$$

Here, $\alpha_\nu = n\zeta_\nu$ cm^{-1} represents the absorption coefficient and κ_ν cm^2 g^{-1} represents the mass absorption coefficient, also known as the opacity.

Scattering coefficient: When photons pass through a scattering medium, the decrease in the intensity is described as,

$$dI_\nu = -\beta_\nu I_\nu ds = -\sigma_\nu \rho I_\nu ds, \tag{5.75}$$

where β_ν cm^{-1} is the scattering coefficient and σ_ν cm^2 g^{-1} represents the scattering opacity. This phenomenon is akin to the absorption for the intensity decrease, and the sum is called extinction. We introduce the extinction coefficient defined as

$$\chi_\nu = \alpha_\nu + \beta_\nu, \tag{5.76}$$

where α_ν denotes the absorption coefficient.

It is important to note that scattered photons can go out of or into the direction of interest. In the former case, dI_ν decreases. In the latter case, dI_ν increases. We define

$$\Phi_\nu \equiv \int \phi_\nu(\boldsymbol{l}, \boldsymbol{l'}) I_\nu(\boldsymbol{l'}) d\Omega', \tag{5.77}$$

in which $\phi_\nu(\boldsymbol{l}, \boldsymbol{l'})$ is the scattering probability function. It describes the possibility that the photons in the direction $\boldsymbol{l}$ is scattered into the direction $\boldsymbol{l'}$. It satisfies the following relation:

$$\int \phi_\nu(\boldsymbol{l}, \boldsymbol{l'}) d\Omega' = \int \phi_\nu(\boldsymbol{l}, \boldsymbol{l'}) d\Omega = 1. \tag{5.78}$$

5.2.1.2 Related quantities

Optical depth: The optical thickness, or optical depth, across s is defined as

$$\tau_\nu(s) \equiv \int_{s_0}^{s} \kappa_\nu \rho ds' = \int_{s_0}^{s} \alpha_\nu(s') ds'. \tag{5.79}$$

The optical depth τ_ν is more useful than the physical distance (s) in radiative transfer. For example, the probability of photons propagating through an optical thickness of τ_ν is given by $P_\nu = \exp(-\tau_\nu)$. At the entry, $\tau_\nu = 0$ and $P_\nu = 1$. When $\tau_\nu \ll 1$ and $\tau_\nu \gg 1$, we refer to the medium as "optically thin" and "optically thick", respectively.

The optical depth depends strongly on the photon frequency ν. Therefore, the same medium of the same physical distance can be optically thin at a certain ν and optically thick in another ν. This often happens in the photoionized plasma under the scope of this work.

Mean free path: The mean free path characterizes the average physical distance of interactions between photons and the matter. Using the interaction cross section of the medium against the photon (σ_ν), the number density n, the mass density ρ, and the opacity κ_ν, the mean free path is given by

$$l_\nu = \frac{1}{\sigma_\nu n} = \frac{1}{\kappa_\nu \rho}. \tag{5.80}$$

Photon destruction probability and single scattering albedo: From the absorption and scattering coefficients, we can estimate the probability that a photon is absorbed or scattered within one mean free path. We define the fraction of photons to be absorbed as the photon destruction probability, denoted as ϵ_ν

$$\epsilon_\nu \equiv \frac{\kappa_\nu}{\kappa_\nu + \sigma_\nu}. \tag{5.81}$$

with the mass absorption coefficient κ_ν cm^2 g^{-1} and the opacity σ_ν cm^2 g^{-1}. The complement is the fraction of photons to be scattered, which is the single scattering albedo defined as

$$\omega_\nu \equiv 1 - \epsilon_\nu = \frac{\sigma_\nu}{\kappa_\nu + \sigma_\nu}. \tag{5.82}$$

Effective optical depth: We consider a situation in which a photon passes through the medium of a thickness τ_ν with scattering as random walk. After N'th scattering, the mean square displacement is

$$l_* = \sqrt{N} l_\nu \sim \frac{l_\nu}{\sqrt{\epsilon_\nu}} = \frac{1}{\sqrt{\kappa_\nu(\kappa_\nu + \sigma_\nu)}\rho}. \tag{5.83}$$

This is called the "effective mean free path". In a system with the scale L, the effective optical depth is

$$\tau_* \equiv \frac{L}{l_*} = \sqrt{\kappa_\nu \rho L(\kappa_\nu \rho L + \sigma_\nu \rho L)} = \sqrt{\tau_{\rm abs}(\tau_{\rm abs} + \tau_{\rm sca})}. \tag{5.84}$$

by defining the optical depth for the absorption and the scattering across the system with $\tau_{\rm abs}$ and $\tau_{\rm sca}$, respectively.

5.2.1.3 Formal solution

We define the source function as

$$S_\nu \equiv \frac{\eta_\nu}{\alpha_\nu} = \frac{j_\nu}{4\pi\kappa_\nu}. \tag{5.85}$$

Using it, the radiative transfer equation is rewritten in a more simple form as

$$\frac{dI_\nu}{ds} = -\alpha_\nu \left(I_\nu - \frac{\eta_\nu}{\alpha_\nu} \right) - \beta_\nu (I_\nu - \Phi_\nu) = -(\alpha_\nu + \beta_\nu)(I_\nu - S_\nu). \tag{5.86}$$

The second equality assumes the isotropic scattering ($\Phi_\nu = J_\nu$).

With emission: When only the emission is considered, the radiative transfer equation is simplified as

$$\frac{dI_\nu}{d\tau_\nu} = S_\nu. \tag{5.87}$$

The intensity at the optical depth $\tau_\nu = \alpha_\nu s$ is solved formally as

$$I_\nu(\tau_\nu) = I_\nu(0) + \int_0^{\tau_\nu} S_\nu(\tau'_\nu) d\tau'_\nu. \tag{5.88}$$

With emission and absorption: When considering both emission and absorption, the equation becomes

$$\frac{dI_\nu}{d\tau_\nu} = -I_\nu + S_\nu. \tag{5.89}$$

The formal solution in this case is written as

$$I_\nu(\tau_\nu) = I_\nu(0) e^{-\tau_\nu} + \int_0^{\tau_\nu} e^{-(\tau_\nu - \tau'_\nu)} S_\nu(\tau'_\nu) d\tau'_\nu. \tag{5.90}$$

In the optically thick limit ($\tau_\nu \to \infty$), it approaches the source function ($I_\nu \to S_\nu$), and for optically thin ($\tau_\nu \ll 1$) and $I_\nu(0)$ is small, $I_\nu \to S_\nu \tau_\nu$.

With emission, absorption, and scattering: We redefine the optical depth as

$$d\tau_\nu \equiv (\alpha_\nu + \beta_\nu)ds = \chi_\nu ds = (\kappa_\nu + \sigma_\nu)\rho ds. \tag{5.91}$$

and the source function as

$$S_\nu \equiv \frac{\eta_\nu + \beta_\nu \Phi_\nu}{\alpha_\nu + \beta_\nu} = \epsilon_\nu \frac{\eta_\nu}{\alpha_\nu} + (1 - \epsilon_\nu)\Phi_\nu. \tag{5.92}$$

Then, the radiative transfer equation apparently becomes the same as Equation 5.89.

These are formal solutions. In practice, we need to know the source function S_ν to calculate the scattering Φ_ν and vice versa. They are not known a priori, so we need to rely on numerical iterative methods, which will be described in § 5.4.

5.2.2 Detailed balance and equilibrium states

From the microscopic point of view, the transitions between two levels (u and l) of an atom is balanced as

$$n_l B_{lu} J_{\nu,ul} + n_e n_l C_{lu} = n_u A_{ul} + n_u B_{ul} J_{\nu,ul} + n_e n_u C_{ul} \tag{5.93}$$

for time-constant situations. Here, $J_{\nu,ul}$ is the radiation field strength at the frequency corresponding to the energy difference between the two levels, and n_u and n_l are the level population of the upper and lower levels, respectively, which implicitly include the multiplicity g_u and g_l. Out of the five terms, three represent the radiative process (interaction with photons) and two represent the collisional process (interaction with matter). The collisional process mostly takes place against electrons in the application of our interest, so we hereafter consider electrons as the collision partner of atoms.

The three radiative terms are related to the Einstein coefficients:

- Spontaneous emission (A_{ul}). This process represents the rate of transition from the upper level to the lower level per second due to the spontaneous emission of a photon $h\nu_{ul}$ corresponding to the energy difference between the two levels.
- Stimulated emission (B_{ul}). In this process, an incoming photon $h\nu_{ul}$ induces the transition from the upper to the lower level. The transition rate is thus proportional to the radiation field strength $J_{\nu,ul}$.
- Absorption (B_{lu}). This process is the reverse of the stimulated emission and its transition rate is also proportional to $J_{\nu,lu}$.

The other two terms represent the collisional processes. C_{lu} for the collisional excitation and C_{ul} for the collisional de-excitation. The rates are proportional to the density product of the colliding particles $n_u n_e$ or $n_l n_e$, where n_e is the electron density. The electron velocity distribution for the energy integral is usually assumed to be Maxwellian.

In general, the detailed balance (Equation 5.93) needs to be solved for a given radiation and electron velocity distributions to derive the level populations, so that we can synthesize the radiated photon spectrum to be compared with observations. This is very challenging but needs to be done in this work. In most astrophysical applications, however, simplifying assumptions are made (Table 5.1), which we describe below.

TABLE 5.1: Equations for distributions that hold in each equilibrium state: thermodynamic equilibrium (TE), the local thermodynamic equilibrium (LTE), and non-local thermodynamic equilibrium (NLTE).

Distribution	Equation	TE	LTE	NLTE
Photon energy	Planck	yes	no	no
Level population	Boltzmann	yes	yes	no
Charge population	Saha	yes	yes	no
Electron energy	Maxwell	yes	yes	yes

5.2.2.1 Thermodynamic equilibrium (TE)

In TE, the radiation field and the matter are completely coupled at an equilibrium, including charge and level populations, and is characterized by a single temperature T.

Maxwell distribution for particle energy distribution: At TE, the velocity distribution of particles is described by the Maxwell distribution,

$$f(v) = 4\pi v^2 \left(\frac{m}{2\pi kT}\right)^{3/2} \exp\left(-\frac{mv^2}{2kT}\right). \tag{5.94}$$

Planck distribution for photon energy distribution: Photon energy distribution at TE follows the Planck distribution,

$$J_\nu = B_\nu(T) = \frac{2h\nu^3}{c^2}\frac{1}{e^{h\nu/kT}-1}. \tag{5.95}$$

Boltzmann distribution for level population: At TE, the level populations in atoms satisfy the Boltzmann distribution. With an excitation energy ϵ_i and the statistical weight g_i, the fraction of atoms (p_i) at the energy level i is given by

$$\frac{p_i}{p} = g_i e^{-\epsilon_i/kT}, \tag{5.96}$$

where p is a normalization constant. Between the level u and l, the population density at each level n_u and n_l are related by

$$\frac{n_u}{n_l} = \frac{g_u}{g_l} e^{-h\nu_{ul}/kT}, \tag{5.97}$$

where h is the Planck constant, k is the Boltzmann constant, g_i represents the statistical weight, and ν_{ul} is the frequency between the two levels.

Saha distribution for the charge population: At high temperatures, atoms become ionized and reach an ionization equilibrium. We define the number of neutral atoms and their statistical weight at the ground level as N_0 and g_0, respectively, and for singly ionized atoms as N_0^+ and g_0^+. The ionization potential is denoted as χ, the electron's mass as m_e, its velocity as v, and its momentum as $p = m_\mathrm{e}v$. The probability

that an ejected electron after ionization has a velocity between v and $v + dv$ is derived as

$$\frac{dN_0^+(v)}{N_0} = \frac{g_0^+}{g_0} \exp\left[-\frac{1}{kT}\left(\chi + \frac{1}{2}m_e v^2\right)\right] \frac{2}{h^3}\, d^3x\, d^3p, \tag{5.98}$$

which can be further simplified to

$$\frac{N_0^+ N_e}{N_0} = \left(\frac{2\pi m_e kT}{h^2}\right)^{3/2} \frac{2g_0^+}{g_0} \exp\left(-\frac{\chi}{kT}\right). \tag{5.99}$$

Between the two adjacent ionization stages i and $i+1$, the Saha equation holds at TE as

$$\frac{N^{i+1} N_e}{N^i} = \left(\frac{2\pi m_e kT}{h^2}\right)^{3/2} \frac{2U^{i+1}}{U^i} \exp\left(-\frac{\chi}{kT}\right), \tag{5.100}$$

with the partition function

$$U^i \equiv \sum_s g_s^i e^{-\chi_s^i/kT}. \tag{5.101}$$

Saha-Boltzmann distribution: The population distribution between a specific level i and the charge state c is derived from the combination of Saha and Boltzmann distributions as

$$\frac{N^c N_e}{N^i} = \frac{(2\pi m_e kT)^{3/2}}{h^3} \frac{2g^c}{g^i} \exp\left(-\frac{\chi_{ci}}{kT}\right), \tag{5.102}$$

with the total population density at level i as N^i, the number of ions at the ionization level c as N^c. The ionization energy from level i to the charge state c is

$$\chi_{ci} = \chi_n - \chi_{n,i} + \chi_{n+1,c} = h\nu. \tag{5.103}$$

In TE with an intense radiation field, in which collisional processes can be ignored, the detailed balance (Equation 5.93) becomes

$$n_u A_{ul} + n_u B_{ul} J_{\nu,ul} = n_l B_{lu} J_{\nu,lu}. \tag{5.104}$$

For TE, we know the relation between the populations of the two levels, thus the Einstein coefficients are related as

$$g_l B_{lu} = g_u B_{ul}, \tag{5.105}$$

$$A_{ul} = \frac{2h\nu_{ul}^3}{c^2} B_{ul}. \tag{5.106}$$

As they are equations among atomic properties independent of external conditions such as T, and J, the relations hold regardless of whether the TE conditions are met or not.

5.2.2.2 Local thermodynamic equilibrium (LTE)

In the Local Thermodynamic Equilibrium (LTE), collisions between particles take place sufficiently frequently to reach a Maxwell distribution, but the interaction between particles and photons is insufficient to reach a Planck distribution. Collisions within a local region control the energy redistribution among particles, while photons can escape a

long distance with fewer interactions. In LTE, a TE is achieved at each location, and the Boltzmann and Saha equations hold for the level and charge populations.

In LTE with a weak radiation field, in which terms proportional to J_ν can be ignored, the detailed balance (Equation 5.93) becomes

$$n_u A_{ul} + n_e n_u C_{ul} = n_e n_l C_{lu}. \tag{5.107}$$

On the left hand side, if the collisional de-excitation rate (C_{ul}) surpasses the spontaneous emission rate (A_{ul}) at a high density, we have

$$\frac{n_l}{n_u} = \frac{g_l}{g_u} \exp\left(-\frac{h\nu_{ul}}{kT}\right), \tag{5.108}$$

and

$$\frac{C_{lu}}{C_{ul}} = \frac{g_u}{g_l} \exp\left(-\frac{h\nu_{ul}}{kT}\right). \tag{5.109}$$

This implies that the population of the excited state of the particle follows the Boltzmann distribution. This is called the LTE limit.

On the contrary, if the spontaneous emission rate (A_{ul}) surpasses the collisional de-excitation rate (C_{ul}) at a low density,

$$\frac{n_l}{n_u} = \frac{g_l}{g_u} \frac{A_{ul}}{n_e C_{lu}}. \tag{5.110}$$

This is called the coronal limit. The boundary between the two limits takes place at the critical density for n_e at

$$n_{\rm cr} = \frac{A_{ul}}{C_{ul}}. \tag{5.111}$$

5.2.2.3 Non-local thermodynamic equilibrium (NLTE)

Non-Local Thermodynamic Equilibrium (NLTE) is, unlike LTE, a state in which the radiation field cannot be ignored, but affects the level and charge populations. Note that NLTE is not "non-LTE" (complementary set of LTE) but "non-local TE" (a form of equilibrium). As the radiation field deviates from the Planck distribution, the level and charge populations deviate from the Boltzmann and Saha distributions. Still, we assume that the particle energy distribution follows the Maxwell distribution.

At NLTE, we need to solve the level and charge population from the detailed balance including B instead of C in Equation 5.93. At the same time, the radiative field needs to be solved, which deviates from the Planck distribution. In such a case, the radiative transfer equation needs to be solved fully, incorporating all the atom-photon interactions described in § 5.1.2. This is the situation of interest in this work. The solution can be obtained only numerically in practice using numerical solvers and implementations.

5.2.3 Line formation, profile, and strength

5.2.3.1 Line formation

We describe how the emission or absorption lines are formed through the radiative transfer. For a homogeneous medium with a constant source function, the radiative transfer equation solves as

$$I_\nu(\tau_\nu) = I_\nu(0)e^{-\tau_\nu} + S_\nu(1 - e^{-\tau_\nu}). \tag{5.112}$$

When the plasma is optically thick $\tau_\nu \gg 1$ (Figure 5.4 a),

$$I_\nu(\tau_\nu) \approx S_\nu, \tag{5.113}$$

regardless of the incident emission to the plasma $I_\nu(0)$. When it is optically thin $\tau_\nu \ll 1$ and no incident emission (Figure 5.4 b), emission lines are formed.

$$I_\nu(\tau_\nu) \approx \tau_\nu S_\nu, \tag{5.114}$$

If the incident emission is not null $I_\nu(0) > 0$, hence

$$I_\nu(\tau_\nu) \approx I_\nu(0) + \tau_\nu[S_\nu - I_\nu(0)], \tag{5.115}$$

there are two possibilities. One is that $I_\nu(0)$ is larger than the source function of the medium S_ν. The medium absorbs photons from the incident emission at specific ν, resulting in the formation of absorption lines (Figure 5.4 d). The other is that the incident emission is smaller than the source function. In this case, emission lines are formed (Figure 5.4 c).

5.2.3.2 Line profile

Next, we examine the line profile. Lines are broadened for several reasons, resulting in different profiles. We list some of them below.

Lorentz profile: The natural line width stems from the uncertainty principle $\Delta E \Delta t > \hbar$, where Δt represents the lifetime of the upper-level particles, resulting in an energy uncertainty of ΔE. We calculate the line profile in the context of the classical oscillator with a damping term. The equation of motion reads

$$m_e\ddot{x} + \Gamma\dot{x} + \omega_0^2 x = 0, \tag{5.116}$$

where $\Gamma \equiv 2e^2\omega_0^2/3m_ec^3$ is the classical damping constant and ω_0 is the angular frequency corresponding to the energy level difference. The solution is $x = x_0 e^{-\Gamma t/2 \pm i\omega_0 t}$, which includes the exponentially decaying lifetime of $e^{-\Gamma t/2}$. Since the amplitude of the electromagnetic wave is proportional to $\ddot{x}$,

$$E(t) = E_0 e^{-\Gamma t/2 \pm i\omega_0 t}, \tag{5.117}$$

and the energy spectrum has a Lorenzian profile of

$$E(\omega) = \frac{x_0^2}{2\pi} \frac{1}{(\omega - \omega_0)^2 + (\Gamma/2)^2}. \tag{5.118}$$

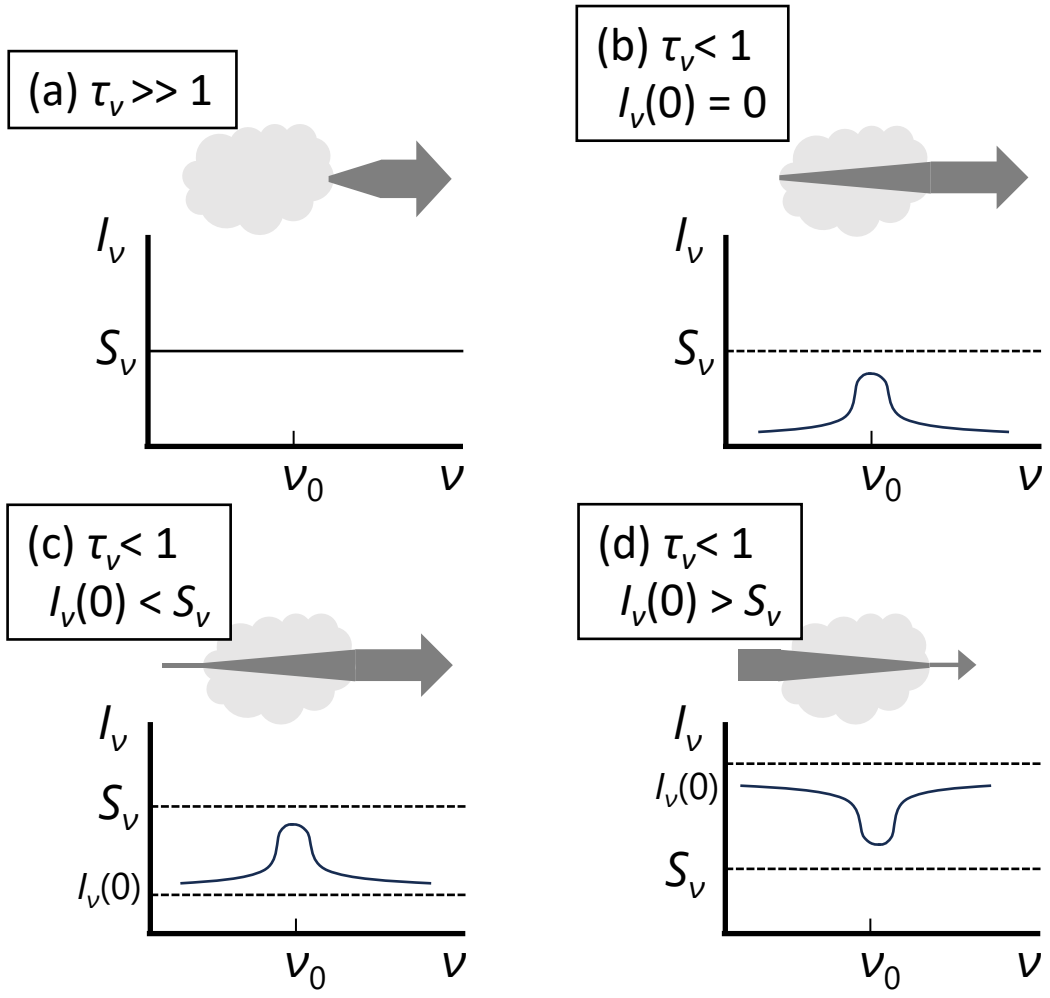

Figure 5.4: Line formation for different optical depth and source function.

The normalized line profile function is given as

$$\phi(\nu) = \frac{\Gamma/4\pi^2}{(\nu-\nu_0)^2 + (\Gamma/4\pi)^2}. \tag{5.119}$$

Other causes for the line-broadening, e.g. collisional (pressure) broadening by other particles altering the lifetime, also result in the Lorentz profile.

Gauss profile: When particles are distributed according to the Maxwell distribution at a given temperature, the line profile becomes a Gauss function. Assuming that the particle has a velocity of v, the photon frequency observed by the particle becomes $\nu - \nu_0 = (v/c)\nu_0$. The distribution of v is

$$f(v)dv = \left(\frac{m}{2\pi kT}\right)^{1/2} \exp\left[-\frac{v^2}{v_{\rm th}^2}\right] dv. \tag{5.120}$$

Here, $v_{\rm th}$ represents the most probable velocity of the Maxwellian distribution given by $\sqrt{\frac{2kT}{m}}$, and m is the particle mass. We define the Doppler width as $\Delta\nu_{\rm D} \equiv \frac{v_{\rm th}}{c}\nu_0 = \frac{\nu_0}{c}\sqrt{\frac{2kT}{m}}$. The line profile is then

$$\phi(\nu) = \frac{1}{\Delta\nu_{\rm D}\sqrt{\pi}} \exp\left[-\frac{(\nu-\nu_0)^2}{\Delta\nu_{\rm D}^2}\right]. \tag{5.121}$$

Voigt profile: Various broadening occurs at the same time. As a result, the line profile becomes a convolution of the Gaussian and Lorentzian profiles known as the Voigt profile, which is given as

$$\phi(\nu) = \frac{1}{\Delta\nu_{\rm D}} \frac{H(a,x)}{\sqrt{\pi}} \tag{5.122}$$

where $H(a,x)$ is the Voigt function

$$H(a,x) \equiv \frac{a}{\pi} \int \frac{e^{-y^2}}{(x-y)^2 + a^2} dy, \tag{5.123}$$

in which $a \equiv \frac{\Gamma}{4\pi}\frac{1}{\Delta\nu_{\rm D}}$, $x \equiv \frac{\nu-\nu_0}{\Delta\nu_{\rm D}}$, and $y \equiv \frac{\Delta\nu}{\Delta\nu_{\rm D}}$.

Figure 5.5 shows the normalized Voigt profile for $H(a = 0.1)$ and $H(a = 2)$. The central part dominated by the Gauss profile is called the Doppler core, while the wing part dominated by the Lorentz profile is called the damping wing for the classical oscillator model with a damping term (Equation 5.116). The damping constant a is the relative strength of the two. The resulting optical depth sometimes differs by many orders of magnitude between the core and the wing.

Harrington and Dijkstra profiles: The profiles above are for optically thin limits. For optically thick cases, the line profiles are often distorted. This is particularly the case for resonance scattering, which is the absorption and immediate subsequent emission that occur for lines with a large oscillator strength, such as Lyα lines. This behaves like scattering, thus was named so.

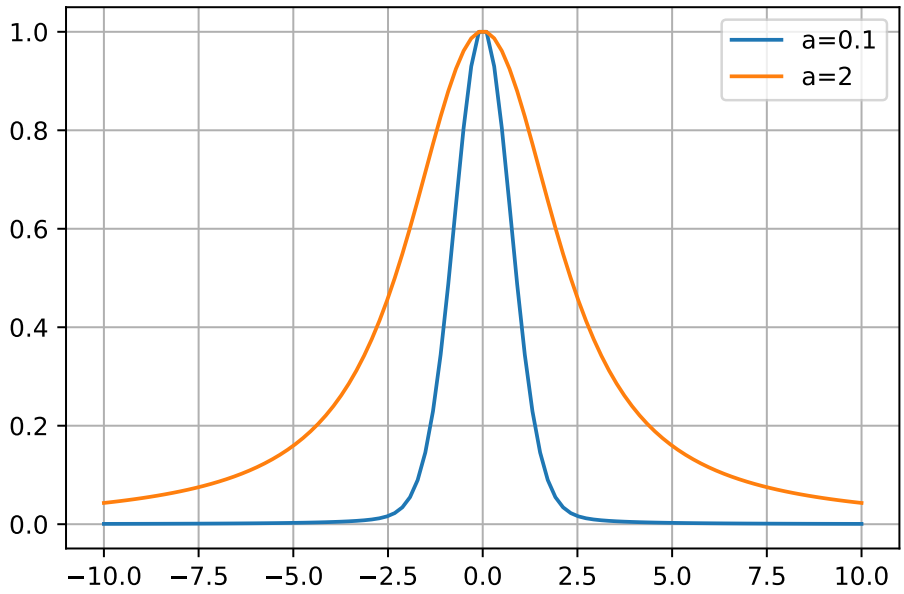

Figure 5.5: Normalized Voigt profile for different damping constant (a).

Because the optical depth at the line center is very large, photons are virtually trapped in the medium. The velocity of the atoms has some distributions due to thermal motion, bulk motion, or micro-turbulence. Therefore, in every resonance scattering, the photon energy changes. In short, photons diffuse not in space but in wavelengths.

Consider a medium with no turbulent or bulk motion. During repeated resonance scattering, a photon can be re-emitted with an energy in the damping wing part of the profile. The optical depth becomes very small, and the photon can escape from the medium in a single long flight. In this case, the line profile is double-peaked around the center. The analytical solution is obtained for a plane-parallel (Harrington, 1973; Neufeld, 1991) and spherical (Dijkstra, Haiman, and Spaans, 2006) geometry of a uniform density. The Dijkstra profile is

$$J(x) = \frac{\sqrt{\pi}}{\sqrt{24}a\tau_0}\left(\frac{x^2}{1+\cosh\left[\sqrt{\frac{2\pi^3}{27}}\frac{|x^3|}{a\tau_0}\right]}\right). \tag{5.124}$$

In the radiative transfer calculations, we need to consider the redistribution of emission line photons over wavelengths at each resonance scattering. Although this is done in Monte Carlo solvers, it is often approximated in other solvers. The often used approximation is the escape probability method. Escape probability refers to the probability that a photon at a given location in the medium can escape from the system without being absorbed or scattered. This rate is a function of the optical depth from the position to the boundary of the medium $\tau_\nu(\boldsymbol{l})$,

$$\beta_\nu(\boldsymbol{l}) = e^{-|\tau_\nu(\boldsymbol{l})|} \tag{5.125}$$

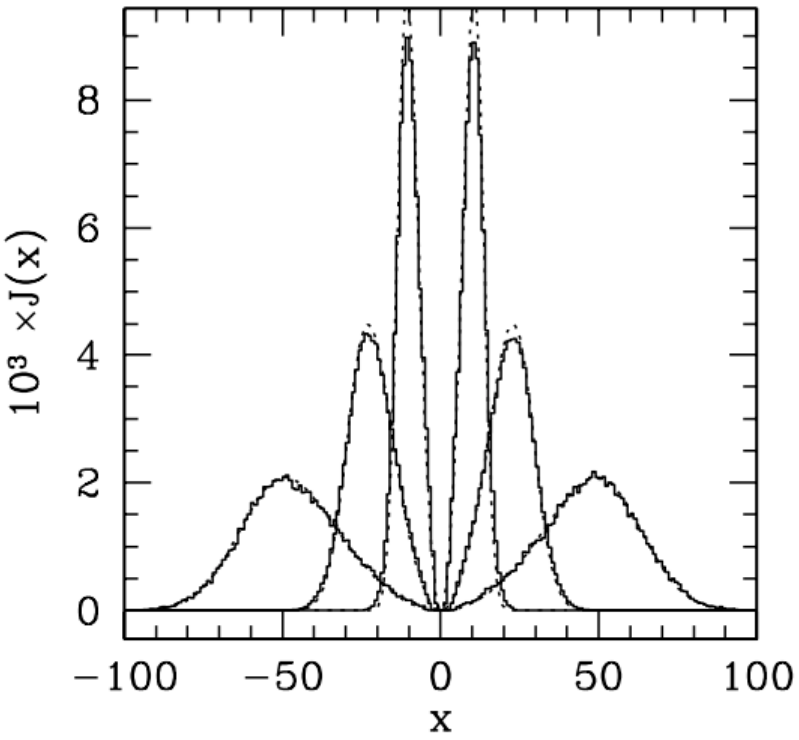

Figure 5.6: Emergent spectra obtained with Monte Carlo simulation for the central optical depth from 10^5 as the narrowest to 10^7 as the broadest profile as solid lines. Analytical solutions are overplotted with dotted lines. Cited from (Dijkstra, Haiman, and Spaans, 2006).

Sobolev condition: Consider a medium with a bulk motion with a uniform velocity gradient across the space. The Sobolev condition

$$v_{\rm th} \ll |\boldsymbol{\nabla v}| L, \tag{5.126}$$

is often met in the winds from accreting binaries, where the bulk velocity gradient over a typical spatial scale L of the medium is much larger than the thermal velocity $v_{\rm th}$. In this case, the resonance scattering photons at the line center can escape easily from the system. The escape probability then becomes

$$\beta = \frac{1 - e^{-\tau_{\rm S}}}{\tau_{\rm S}}, \tag{5.127}$$

where

$$\tau_{\rm S} = \frac{2 v_{\rm thermal} \alpha_{\rm L}}{|\boldsymbol{\nabla v}|} \tag{5.128}$$

and

$$\alpha_{\rm L} = \int \alpha_\nu d\nu. \tag{5.129}$$

5.2.3.3 Line strength

Oscillator strength: The cross section is conveniently described as a dimensionless value multiplied by the cross section of the dipole transition as

$$\sigma(\nu) = \frac{\pi e^2}{m_e c} f \phi(\nu), \tag{5.130}$$

in which e represents the elementary charge, m_e is the electron's mass, c denotes the speed of light, and $\phi(\nu)$ is the normalized line profile such that $\int \phi(\nu) d\nu = 1$. The multiplier f is called the oscillator strength with a value between 0 and 1, which describes the strength of the transition between two energy levels in an atom or ion.

The Einstein coefficient A can be described with the oscillator strength as,

$$A_{ij} = \frac{\alpha^3}{\tau_0} \frac{g_i}{g_j} \frac{(E_j - E_i)^2}{Ry^2} f_{ij} = 8.032 \times 10^9 \frac{g_i}{g_j} \frac{(E_j - E_i)^2}{Ry^2} f_{ij} \tag{5.131}$$

Here, α is the fine-structure constant, τ_0 is the mean lifetime of the excited state, g_i and g_j are the statistical weights of the levels i and j, respectively, E_i and E_j are the energies of the levels i and j, respectively, and $Ry = e^2/(2a_0)$ is the Rydberg constant with $a_0 = \hbar/(me^2)$.

Equivalent width: The emission or absorption line strength in comparison to the continuum is characterized by the equivalent width (W). It is defined as the width of a hypothetical rectangular line profile that would have the same total area as the observed line profile (F_ν) normalized by the local continuum level (F_c) as

$$W_\nu = \int \frac{F_c - F_\nu}{F_c} d\nu \tag{5.132}$$

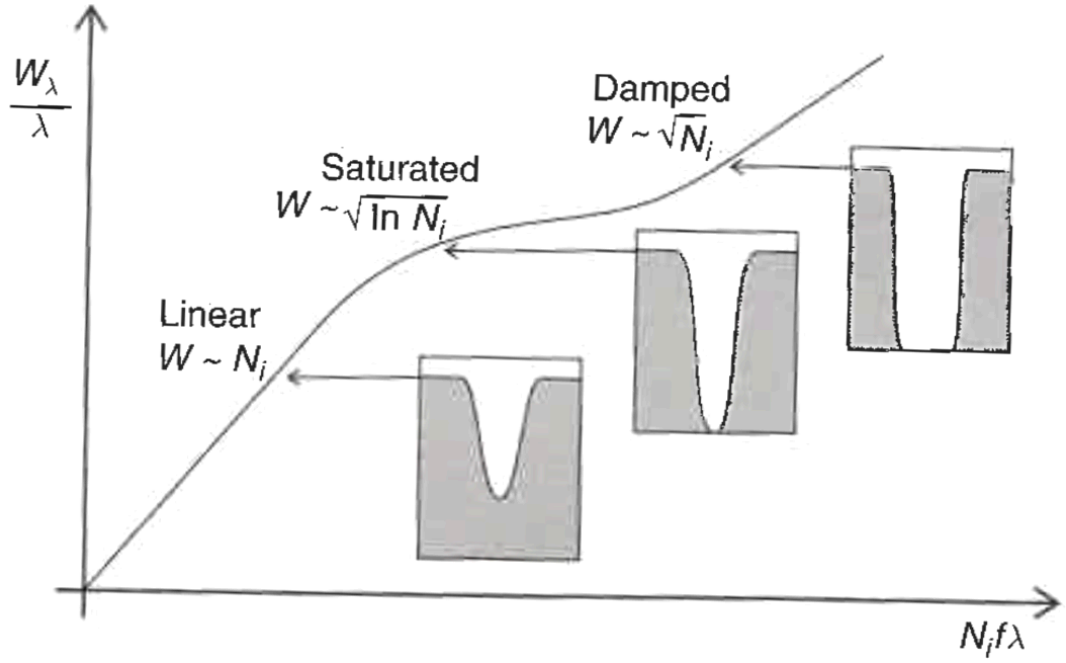

Figure 5.7: Schematic view of the curve of growth and the relations with line shapes (Pradhan and Nahar, 2011).

for a given line. The same definition applies to the absorption and emission lines. In general, $W_\nu > 0$ for absorption, while $W_\nu < 0$ for emission. In X-ray astronomy, the reverse sign is often used.

Curve of growth: The curve of growth is the evolution of W_ν as the column density increases. The column density in the line of sight is given by

$$N = \int n ds, \tag{5.133}$$

where n is the volume number density of the absorbing matter.

By converting ν to λ using $\nu = c/\lambda$, the curve of growth is calculated as

$$W_\lambda = \frac{\lambda^2}{c} \int (1 - e^{-\tau_\nu}) d\nu, \tag{5.134}$$

where

$$\tau_\nu = \left(\frac{\pi e^2}{m_e c} \right) N_i f_\nu \phi(\nu) \tag{5.135}$$

with the column density of the ion N_i.

Figure 5.7 shows an example of the curve of growth. For a small τ_ν, $W \sim \lambda^2/c \int \tau_\nu d\nu \propto N_\mathrm{i}$, which is the linear part of the curve of growth. For an intermediate τ_ν, the line center becomes completely opaque but the Doppler wing does not. The equivalent width increases by absorbing the Doppler broadening part of the profile, resulting in a slow increase of $W \propto \sqrt{\ln N_\mathrm{i}}$. For a large τ_ν, the entire Doppler core is saturated. The equivalent width increases by absorbing the damping wing part of the profile, resulting in $W \propto \sqrt{N_\mathrm{i}}$.

5.3 Photoionized Plasma

5.3.1 Nebular approximation

Interactions between the photons and plasma, i.e., atoms, ions, and electrons, have upward and downward transitions among different energy levels of different charge states (Figure 5.8). They occur both collisionally and radiatively. In the photoionized plasma, which is the subject of this thesis, radiative processes dominate. The approximation to neglect the collisional processes is called the nebular approximation.

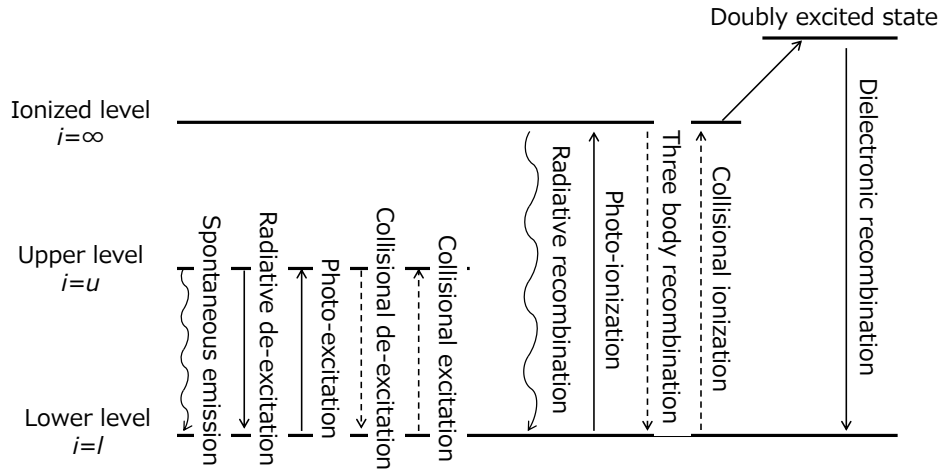

Figure 5.8: Overview of the atomic processes. Below, we will explain the processes drawn with the solid lines, except the collisional processes.

5.3.1.1 Photoionization and recombination

Photoionization is the process in which a photon is absorbed by an atom or an ion, followed by an ejection of a bound electron or electrons into an unbound state. The inverse process is called radiative recombination, in which an unbound electron is captured by a positively charged ion, followed by the emission of a photon. They are bound-free processes, and the observed spectral features are continuous.

The photoionization process is described as

$$X_{+i} + h\nu \rightarrow X_{+(i+1)} + e^{-}, \tag{5.136}$$

The electron e^{-} ejected from the atom or ion X is called the photoelectron. The photoelectron has a kinetic energy equivalent to the differences between the input photon energy and the ionization potential $E_{\rm IP}$ as

$$\frac{1}{2}mv^2 = h\nu - E_{\rm IP}. \tag{5.137}$$

The photoionization cross section $\sigma_{\rm bf}$ is given by

$$\sigma_{\rm bf} = \frac{64\pi^4 m_e e^{10} Z^4}{3^{3/2} c h^6 n^5} \frac{g_{\rm bf}}{\nu^3}, \tag{5.138}$$

with the Gaunt factor $g_{\rm bf}$ of an order of 1.

The inverse process is the radiative recombination. The radiative recombination rate depends on the electron velocity distribution or the temperature. Radiated photons have a continuum spectrum called the "radiative recombination continuum (RRC)". The RRC spectrum has a minimum energy, which is called the RRC edge. When an electron is captured in an excited state, the radiative de-excitation follows, leading to line emission (Figure 5.11 b). The presence of RRC and numerous emission lines are prime signatures of the photoionized plasma.

The discussion above implicitly assumes that the processes involve a single electron. There are also processes in which two electrons are involved both for the ionization and recombination. They occur through a doubly excited state

$$X^{+i} + h\nu \longleftrightarrow X^{+i^{**}} \longleftrightarrow X^{(+i+1)^*}. \tag{5.139}$$

When a photon is absorbed, multiple electrons are excited. The doubly excited state X^{**} is unstable, and one of the two electrons receives all the excited energies to go unbound. This is called dielectronic recombination.

A photon in the X-ray band often photoionizes an electron in the inner shell of an atom or an ion. This leaves the atom or the ion in a highly excited state of multiple electrons. This decays quickly either by the emission of a photon (photons) or an electron (electrons). The former is called the fluorescence emission, while the latter is called the Auger electrons.

$$X^*_{+i} \rightarrow X_{+i} + h\nu \tag{5.140}$$

$$X^*_{+i} \rightarrow X_{+i-1} + e^- \tag{5.141}$$

The fluorescence and the Auger process are competing, and the probability of the fluorescence (fluorescence yield, the complement of the Auger yield) increases as the atomic number increases.

5.3.1.2 Photoexcitation and stimulated/spontaneous emission

Photoexcitation is a process in which a photon is absorbed by an atom or an ion, followed by the excitation of a bound electron into another bound state of a higher energy level. The electron at a higher energy level decays into a lower energy level by emitting a photon by spontaneous or stimulated emission. The latter is referred to as the radiative de-excitation. They are bound-bound processes, and the observed spectral features are lines.

Photoexcitation is described as

$$X_{+i} + h\nu \rightarrow X^*_{+i}, \tag{5.142}$$

where a photon is absorbed by an atom or an ion, which are excited. After the process, the excited atom or ion decays to a lower energy level with the emission of a photon.

$$X^*_{+i} \rightarrow X_{+i} + h\nu \tag{5.143}$$

The cross section of photoexcitation has a peak at the energy corresponding to the difference of the initial and final state i to j as

$$\sigma_{ij}(E) = \sqrt{\pi}\frac{e^2}{m_e c^2}\frac{f_{ij}}{\Delta\nu_{\rm D}}H(a,E) \tag{5.144}$$

with the Voigt profile $H(a,x)$ (§ 5.2.3).

5.3.2 Ionization parameter

In the nebular approximation, it is known that the physical state of the nebula, or the photoionized plasma, is described by a single parameter called the ionization parameter (Tarter, Tucker, and Salpeter, 1969). Consider a medium with a density n that uniformly surrounds an incident source of a luminosity L, and let r be the distance from the source, the ionization parameter ξ erg cm s^{-1} is defined as

$$\xi = \frac{L}{nr^2}. \tag{5.145}$$

Alternatively,

$$\Xi = \frac{L}{4\pi c r^2 p}, \tag{5.146}$$

is also used, in which p is a constant pressure across the medium. For a specific ξ (the radiation field strength), the charge and level populations are determined. An example of the charge population is shown in Figure 5.9.

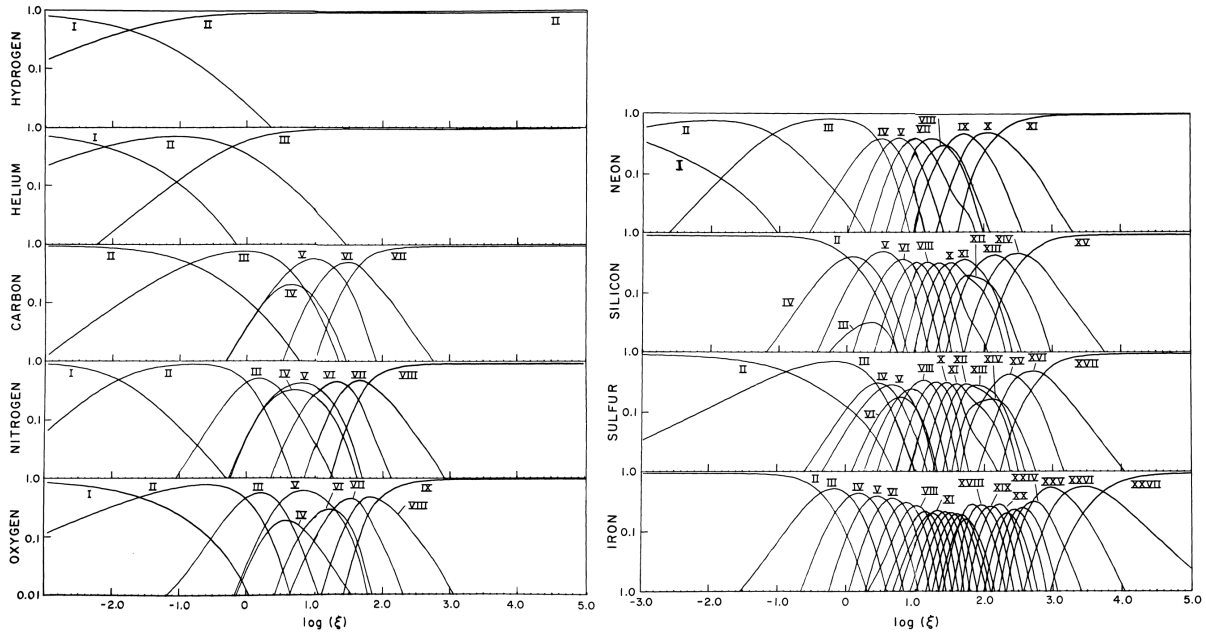

Figure 5.9: Charge population for representative atoms for $-3 < \log\xi < 5$ assuming a particular geometry of the plasma and incident spectrum(T. R. Kallman and McCray, 1982).

5.3.3 Balances

Physical conditions of the photoionized plasmas are determined by three types of the balance; the thermal balance (§ 5.3.3.1) the ionization balance for the charge population (§ 5.3.3.2), and the excitation balance for the level population (§ 5.3.3.3). We explain each of them below. For our application, the time scale to reach a balance is sufficiently short compared to the time of the change in the incident flux, thus we only discuss the static cases.

5.3.3.1 Thermal balance

In a static photoionized plasma, the temperature is determined by the equilibrium between heating and cooling. Heating is provided by photoionization, photoexcitation, and Compton scattering by electrons. Cooling is provided by recombination, radiative deexcitation, inverse Compton scattering, and bremsstrahlung (free-free radiation). Collisional processes by charged particles in addition to electrons are assumed to be negligible. We explain the details of energy gain and loss with photoionization and recombination by taking H as an example.

Heating by photoionization: At a specific point in the photoionized medium, the energy input per unit volume per unit time is

$$G(\mathrm{H}) = n(\mathrm{H}^0) \int_{\nu_0}^{\infty} \frac{4\pi J_\nu}{h\nu} h(\nu - \nu_0) a_\nu(\mathrm{H}^0) d\nu, \tag{5.147}$$

in which $\alpha_\nu(\mathrm{H}^0)$ is the photoionization cross section and $n(\mathrm{H}^0)$ is the density of H^0.

Cooling by recombination: The loss of kinetic energy of electrons on average by recombination per unit volume per unit time is

$$L_R(\mathrm{H}) = n_e n_p kT \beta_\mathrm{A}(\mathrm{H}^0, T), \tag{5.148}$$

where

$$\beta_\mathrm{A}(\mathrm{H}^0, T) = \sum_{n=1}^{\infty} \sum_{l=0}^{n-1} \beta_{nl}(\mathrm{H}^0, T) \tag{5.149}$$

and

$$\beta_{nl}(\mathrm{H}^0, T) = \frac{1}{kT} \int_0^{\infty} v \sigma_{nl}(\mathrm{H}^0, T) \frac{1}{2} m v^2 f(v) dv, \tag{5.150}$$

where n and l are the principal and angular quantum numbers. Here, when the subscript is R, both direct radiative recombination (RR) and dielectronic recombination (DR) are included.

Cooling by free-free radiation: Free electrons emit free-free radiation or bremsstrahlung by the interaction with atoms or ions (§ 5.1.2.3). This process takes place in photoionized plasmas. Its contribution to the cooling rate is small in our application of interest, but it is important as it radiates the continuum spectrum even in a pure H medium.

For ions of a charge Z, the cooling rate is approximated as

$$L_{ff}(Z) = 4\pi j_{ff} = \frac{2^5 \pi e^6 Z^2}{3^{3/2} hmc^3} \left(\frac{2\pi k T^{1/2}}{m} \right) g_{ff} n_e n_+, \tag{5.151}$$

where n_+ is the number density of the ion. Due to the dominant abundance, we only consider H^+ and He^+ by $n_+ = n_p + n_{He+}$. The mean Gaunt factor $g_{ff} \approx 1.3$ is generally used.

Cooling and heating by the Compton scattering: For high-energy photons, the cross section of photoionization decreases rapidly as the energy increases and is taken over by the Compton scattering. This change happens at ≈10 keV. In the energy balance, we need to take into account the Compton scattering.

When a photon is scattered by an electron, a part of its momentum and energy is transferred to the electron. The wavelength shift is

$$\lambda - \lambda_0 = \frac{h}{m_e c}(1 - \cos\theta). \tag{5.152}$$

When the mean energy of the electrons is larger than the photons, $kT > h\nu$, the photons gain energy by the collision, which is called the inverse Compton scattering. The net gain of the heating and cooling is calculated by integrating Equation 5.152 over the energy distribution of photons and electrons as

$$H_{\rm Comp} = \frac{4\pi n_e}{mc^2} \left(\int \sigma_T J_\nu h\nu d\nu - 4kT \int \sigma_T J_\nu d\nu \right), \tag{5.153}$$

with σ_T being the Thomson scattering cross section. This is for the non-relativistic and weak radiation field limit.

S curve: A thermal equilibrium is reached when the heating and cooling rates, as described above, are balanced. The plot illustrating the equilibrium temperature for each ionization parameter is known as the "S curve" (Figure 5.10). On the left side of the curve, cooling exceeds heating and on the right side, heating exceeds cooling. In the branch of the S curve with a positive slope, the photoionized plasma is thermally stable. This is because a small upward perturbation in temperature increases cooling, and a small downward perturbation in temperature increases heating, constituting a negative feedback. In contrast, in the branch with a negative gradient, the photoionized plasma is thermally unstable.

5.3.3.2 Ionization balance

The ionization balance determines the charge population; i.e., the fraction of ions in a particular charge state. The cross section of radiative recombination, which is the inverse process of photoionization (Figure 5.11 a), is derived from the detailed balance between the bound-free and free-bound transitions.

Milne Relations: We derive the relationships between $\sigma_{\rm fb}$ and $\sigma_{\rm bf}$, which are cross sections of recombination and photoionization, respectively. We assume the TE condition,

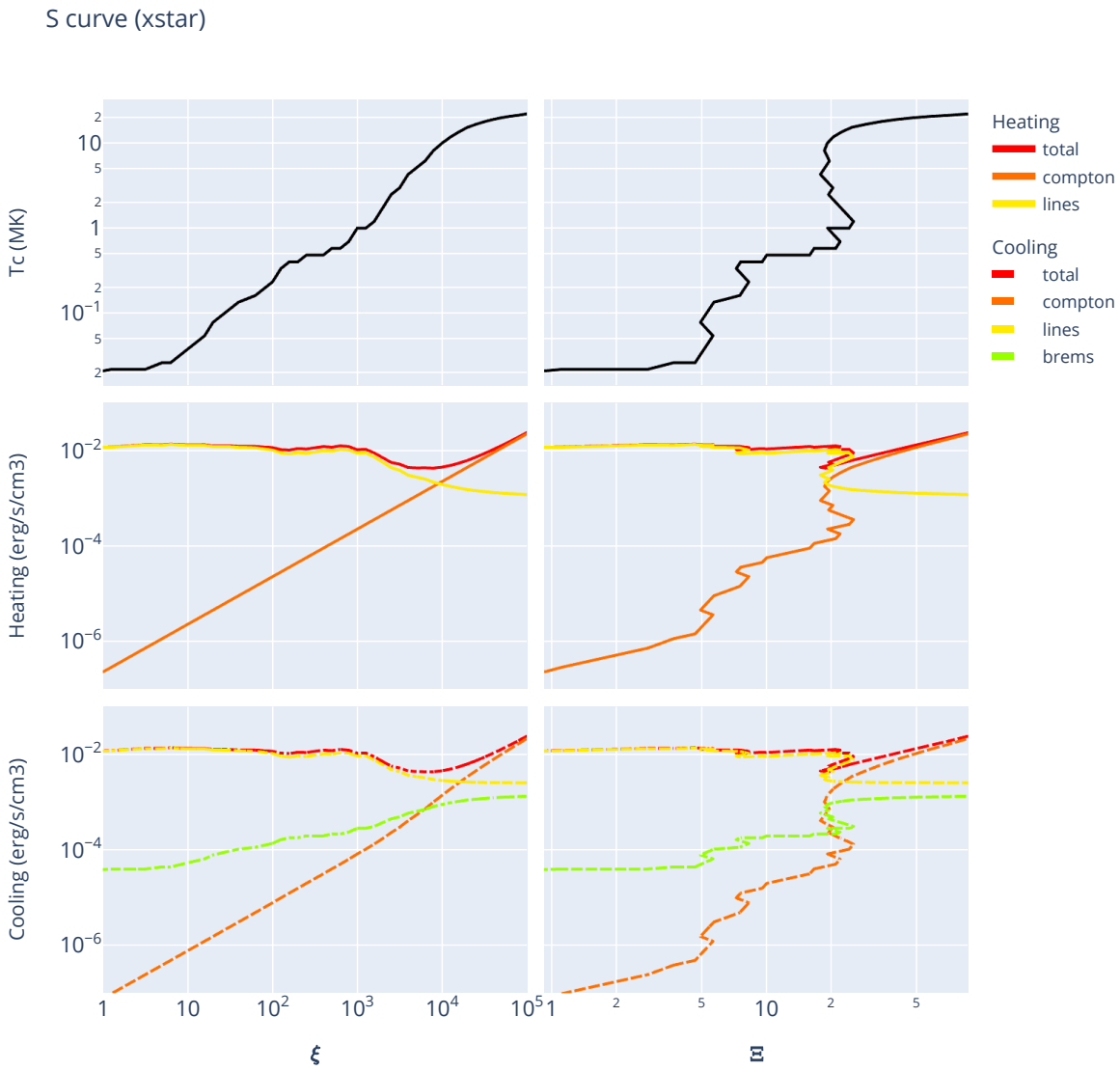

Figure 5.10: Thermal equilibrium temperature (top), heating rate (middle), and cooling rate (bottom) as a function of the ionization parameter ξ (left) or Ξ (right). The so-called "S-curve" is on the top right. The result is calculated by `XSTAR` for $N_{\mathrm{H}} = 10^{18}$ cm^{-2} and $n_{\mathrm{H}} = 10^{10}$ cm^{-3}.

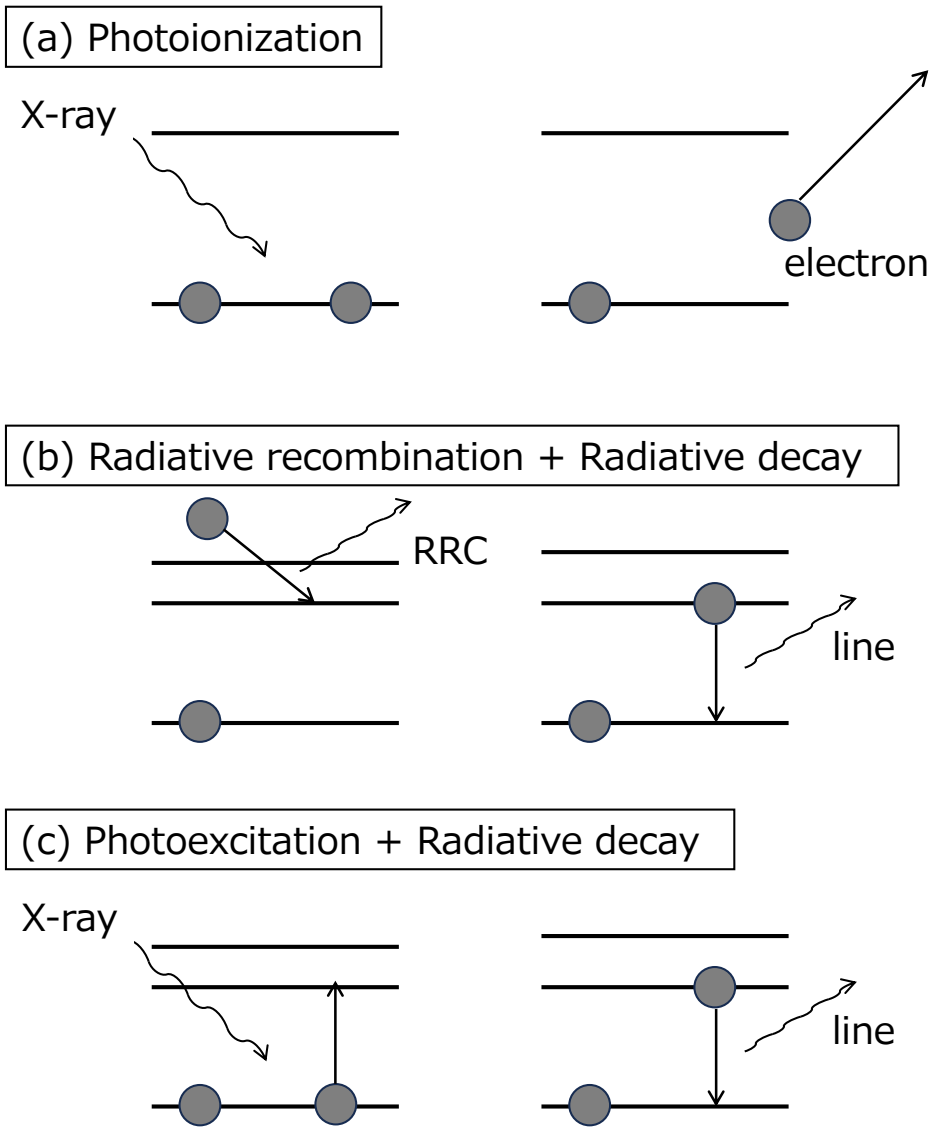

Figure 5.11: Various radiative transitions.

in which the electrons follow the Maxwell distribution as

$$f(v) = \frac{4}{\sqrt{\pi}} \left(\frac{m}{2kT}\right)^{3/2} \exp\left(-mv^2/2kT\right) \tag{5.154}$$

and the radiation field follows the Planck distribution (i.e., blackbody radiation B_ν). The number of photoionizations per unit volume per unit time is

$$\frac{4\pi}{h\nu} n_i \sigma_{\rm bf} (1 - e^{-h\nu/kT}) B_\nu d\nu, \tag{5.155}$$

where n_i is the number density of the capturing ion. The subtracion in the parentheses is for the effective photoionization rate when considering the stimulated recombinations.

The number of recombinations per unit volume per unit time is

$$n_{i+1} n_e \sigma_{\rm fb} f(v) dv. \tag{5.156}$$

When they are balanced, the ratio of the cross sections is

$$\frac{\sigma_{\rm bf}}{\sigma_{\rm fb}} = \frac{n_{i+1} n_e}{n_i} e^{h\nu/kT} \frac{f(v) c^2 h}{8\pi m_e \nu^2} = \frac{m_e^2 c^2 v^2}{\nu^2 h^2} \frac{g_{i+1}}{g_i}, \tag{5.157}$$

which is called the Milne relation. In the second equation, we used the Saha equation for the n_{i+1}/n_i value for the TE condition. In this manner, we can derive the recombination cross section from the photoionization cross section (§ 5.1.2.2). As the Milne relation is among the atomic quantities, it holds more generally beyond the TE condition.

Charge population: We continue the simple example of the pure H medium with no radiation loss from the medium. The thermal balance equation is written as

$$G(\mathrm{H}) = L_R(\mathrm{H}), \tag{5.158}$$

in which $G(\mathrm{H})$ is the heating rate by the photoionization and $L_R(\mathrm{H})$ is the cooling rate by the recombination. This translates to

$$n(\mathrm{H}^0) \int_{\nu_0}^{\infty} \frac{4\pi J_\nu}{h\nu} a_\nu d\nu = n_p n_e \sum_{n,l} \int_0^\infty v \sigma_{nl}(\mathrm{H}^0, v) f(v) dv, \tag{5.159}$$

in which $\sigma_{nl}(\mathrm{H}^0, v)$ is the recombination cross section to capture an electron of a velocity v into the (n, l) state. Then, $\beta_{nl}(\mathrm{H}^0, T)$ is the effective kinetic energy averaged over the Maxwellian velocity distribution of the electron.tion. Since the recombination cross section is almost proportional to v^{-2}, electrons of a lower kinetic energy are easier to be captured, leading to an averaged kinetic energy smaller than $\frac{3}{2}kT$.

For general atoms, the balance equation is written as

$$\int_{\nu_0}^{\infty} \frac{4\pi J_\nu}{h\nu} n(X^Z) \sigma_{\rm PI} d\nu = \sum_j n_e n(X^{Z+1}) \alpha_{\rm R}(X_j^Z; T), \tag{5.160}$$

where $\alpha_{\rm R}(X_j^Z; T)$ is the recombination rate coefficient into level j for an electron temperature T. All the electron recombinations into possible levels are summed. The left-hand

side is the photoionization rate Γ_Z. The populations among the three adjacent charge states are balanced as

$$n(X^{Z-1})\Gamma_{Z-1} + n_e n(X^{Z+1})\alpha_Z = n(X^Z)[\Gamma_Z + n_e\alpha_{Z-1}]. \tag{5.161}$$

In this manner, photoionizationaion cross sectiontion and the recombination rate coefficients provide the charge state distribution of all the elements with all the charges.

5.3.3.3 Excitation balance

Excitation balance determines the level population; i.e., the fraction of ions of a particular charge state in a particular energy level. The photoexcitation turns an ion from a lower level to an upper level, and the radiative de-excitation is the reverse. Their strength is given by the Einstein A and B coefficients (§ 5.1.2.1). The bound-bound transition produces line emissions (Figure 5.11 c).

5.4 Radiative Transfer Codes

We give an overview of the radiative transfer codes that we use in this work. Among various solvers, we use the two-steam solver (§ 5.3.1) and the Monte Carlo solver (§ 5.3.2). The goal of this section is to describe how the radiative transfer calculations are implemented and what approximations and assumptions are adopted in each code.

5.4.1 Two-stream solver

We introduce a code based on the two-stream solver, `XSTAR`, here.

5.4.1.1 XSTAR

The `XSTAR` code (T. Kallman and Bautista, 2001) is a simulation framework solving the radiative transfer equation for NLTE conditions for the charge and level populations in the photoionized plasma. We use version 2.59b. The symbols defined in Table 5.2 are used in the following description.

There are three important assumptions; (1) two-stream (only radially inward or outward) radiations considered in the geometrically symmetric spherical cloud, (2) steady-state cloud, and (3) use of the escape probability approximation. Due to the 1D nature of the framework, it cannot handle scattering processes in a 3D space.

TABLE 5.2: Symbols used in the descriptions of the physics of `XSTAR`.

Symbol	Description
L_ϵ	Specific continuum luminosity at the cloud boundary in units of erg s^{-1}.
$L_\epsilon^{(\mathrm{inc})}$	Incident radiation field at the inner edge of the cloud.
L_i	Specific line luminosity at the cloud boundary in units of erg s^{-1}.
$L_{\mathrm{line},\epsilon}^{(\mathrm{in/out})}$	Binned specific line luminosity in the inward/outward direction.
$\tau_{\mathrm{cont}}(R,\epsilon)$	Continuum optical depth from radius R to the outer boundary of the shell.
$\tau_{\mathrm{cont}}^{(\mathrm{tot.})}$	Total continuum optical depth through the cloud.
$\tau_{\mathrm{cont}}^{(\mathrm{in/out})}(\epsilon)$	Continuum optical depth in the inward/outward direction.
$\tau_i^{(\mathrm{in/out})}(R)$	Line optical depths in the inward/outward direction.
$j_\epsilon(R)$	Local continuum emissivity at the radius R.
$\kappa_{\mathrm{cont}}(\epsilon)$	Continuum opacity.
κ_i	Line center opacity.
$P_{\mathrm{esc,cont}}^{(\mathrm{in/out})}(R)$	Escape probability in the inward/outward direction for the continuum.
$P_{\mathrm{esc,line}}^{(\mathrm{in/out})}(R)$	Escape probability in the inward/outward direction for the line.

Two-stream approximation: Radiative transfer equation is calculated in concentric spherical shell divided into a small optical depth. In each shell, the balances of heating/cooling, ionization/recombination, and excitation/de-excication are calculated. The incident photon upon the innermost shell is the source spectrum. The emergent photon from the outermost shell is the emitted spectrum from the photoionized plasma. The calculation is iterated for an odd number of iterations; the first from the innermost shell

to the outermost, the second in the opposite direction, the third in the outward direction again, and so on.

Continuum transfer: Continuum photons interact with the matter via the bound-free process, such as photoionization and its reverse process, radiative recombination. `XSTAR` further incorporates the free-free (Bremsstrahluung) emission by electrons interacting with ions, which is often ignored in Monte Carlo solvers. On the other hand, because of the 1D nature of `XSTAR`, it cannot calculate the scattering. Indeed, Thomson (electron) scattering is incorporated as "Thomson absorption". Thomson scattering is relevant for the cloud column density of $\gtrsim 10^{23}$ cm^{-2}. When the column density is $\gtrsim 10^{24}$ cm^{-2}, multiple scattering and Comptonization dominate the interactions, for which `XSTAR` is not applicable.

The equation for the continuum photon is

$$\frac{dL_\epsilon^{(1)}}{dR} = -\kappa_{\rm cont}(\epsilon) L_\epsilon^{(1)} + 4\pi R^2 j_\epsilon(R), \tag{5.162}$$

which corresponds to Equation 5.89. The diffuse emission emerging from a shell is calculated by

$$L_\epsilon = \int_{R_{\rm in}}^{R_{\rm out}} 4\pi R^2 j_\epsilon(R) e^{-\tau_{\rm cont}(R,\epsilon)} dR. \tag{5.163}$$

The incident emission attenuated by the matter in the shell is calculated by

$$L_\epsilon^{(2)} = L_\epsilon^{(\rm inc)} \times e^{-\tau_{\rm cont}^{(\rm tot.)}}, \tag{5.164}$$

where the total optical depth of the absorption is given by

$$\tau_{\rm cont}^{(\rm tot.)} = \int_{R_{in}}^{R_{out}} \kappa_{\rm cont}(\epsilon) dR. \tag{5.165}$$

The total continuum radiations in the inward and outward directions are described as

$$L_\epsilon^{(3)} = \int_{R_{in}}^{R_{out}} 4\pi R^2 j_\epsilon(R) e^{-\tau_{\rm cont}^{(\rm in)}(\epsilon)} P_{\rm esc,cont}^{(\rm in)}(R) dR \tag{5.166}$$

$$L_\epsilon^{(4)} = \int_{R_{in}}^{R_{out}} 4\pi R^2 j_\epsilon(R) e^{-\tau_{\rm cont}^{(\rm out)}(\epsilon)} P_{\rm esc,cont}^{(\rm out)}(R) dR. \tag{5.167}$$

Here, the escape probability $P_{\rm cont}^{(\rm in/out)}(R)$ is controlled by a simulation parameter C (covering fraction; see below).

Line transfer: Similarly to the continuum emission, the luminosity for the line emission in the inward $L_i^{(1)}$ and outward $L_i^{(2)}$ directions are given by

$$\frac{dL_i^{(1)}}{dR} = -\kappa_{\rm cont}(\epsilon) L_i^{(1)} + 4\pi R^2 j_i(R) P_{\rm esc,line}^{(\rm in)}(R) \tag{5.168}$$

$$\frac{dL_i^{(2)}}{dR} = -\kappa_{\rm cont}(\epsilon) L_i^{(2)} + 4\pi R^2 j_i(R) P_{\rm esc,line}^{(\rm out)}(R), \tag{5.169}$$

where i is the label for individual lines.

The optical depth of lines in the inward and outward directions is described as

$$\tau_i^{(\mathrm{in})}(R) = \int_{R_{in}}^{R} \kappa_i(R')dR' \tag{5.170}$$

$$\tau_i^{(\mathrm{out})}(R) = \int_{R}^{R_{out}} \kappa_i(R')dR'. \tag{5.171}$$

Sum of continuum and line: The line emission and opacity in the unit of erg s^{-1} need to be binned so that they can be added to the continuum emission and opacity in the unit of erg s^{-1} erg^{-1}. Binning is performed across the line profile $\phi(\epsilon - \epsilon_i)$, which includes the natural, thermal Doppler, and turbulence broadening. For the emission,

$$L_{\mathrm{line},\epsilon}^{(\mathrm{in/out})} = \sum_{|\epsilon_i - \epsilon| \le \Delta\epsilon} \frac{L_i^{(1/2)}\phi(\epsilon - \epsilon_i)}{\Delta\epsilon}. \tag{5.172}$$

By adding this to the continuum emission, the total emitted specific luminosity in the inward $L_\epsilon^{(6)}$ and outward $L_\epsilon^{(7)}$ directions is

$$L_\epsilon^{(6/7)} = L_\epsilon^{(3/4)} + L_{\mathrm{line},\epsilon}^{(\mathrm{in/out})}. \tag{5.173}$$

Similarly, the line opacity is binned as

$$\kappa_{\mathrm{line}}(\epsilon) = \sum_{|\epsilon_i - \epsilon| \le \Delta\epsilon} \kappa_i \phi(\epsilon - \epsilon_i), \tag{5.174}$$

and added to the continuum opacity to derive the total opacity as

$$\tau^{(\mathrm{tot.})}(\epsilon) = \int_{R_{in}}^{R_{out}} (\kappa_{\mathrm{cont}}(\epsilon) + \kappa_{\mathrm{line}}(\epsilon))dR. \tag{5.175}$$

The total transmitted specific luminosity $L_\epsilon^{(5)}$ is

$$L_\epsilon^{(5)} = L_\epsilon^{(\mathrm{inc})} e^{-\tau^{(\mathrm{tot.})}(\epsilon)}. \tag{5.176}$$

In the output of `XSTAR`, $L_\epsilon^{(\mathrm{inc})}$ is labeled as "incident", $L_\epsilon^{(5)}$ as "transmitted", $L_\epsilon^{(6)}$ as "emit_inward" and $L_\epsilon^{(7)}$ as "emit_outward".

Steady state assumption: The gas density and incident flux are assumed to be steady, of which the timescales of their variation are usually much longer than those of the atomic processes and photon propagations. The only assumption is the Maxwell distribution of the particle energy distribution as NLTE. The thermal, ionization, and excitation balances (§ 5.3.3) are calculated from a given gas density and radiation field.

For the thermal balance of the plasma, the heating terms include the photoionization, photoexcitation, and Compton heating, while the cooling terms include the radiative recombination, radiative deexcitation, inverse Compton, and bremsstrahlung.

Line profile and escape probability: Within a spectral line, as a photon undergoes repeated absorption and emission, its frequency (energy) undergoes slight changes due to, e.g., thermal motion of the gas, collision probability, and quantum mechanical effects; this is called the redistribution. This requires a radiation transfer solution over a grid of wavelengths fine enough to resolve a spectral line profile, which is computationally too expensive. Indeed, `XSTAR` does not calculate the diffusion across the wavelengths, and the lines always have the Voigt profile.

The escape probability is an approximation to decouple the source function and the radiation field in the radiative transfer equation, which would otherwise require an iterative calculation (Hubeny et al., 2001). It is defined as the probability that a line photon escapes from the system in a single long flight. In `XSTAR`, the escape probability $P_{\rm line}(\tau_{\rm line})$ is expressed (Kwan and Krolik, 1981) as

$$P_{\rm line}(\tau_{\rm line}) = \frac{1}{\tau_{\rm line}\sqrt{\pi}(1.2+b)} \tag{5.177}$$

for the optically thick case, and

$$P_{\rm line}(\tau_{\rm line}) = \frac{1-e^{-2\tau_{\rm line}}}{2\tau_{\rm line}} \tag{5.178}$$

for the optically thin case, in which

$$b = \frac{\sqrt{\log \tau_{\rm line}}}{1+\tau_{\rm line}/10^5}. \tag{5.179}$$

In `XSTAR`, the escape probability is controlled by a simulation parameter C (the covering fraction), which takes any values between 0 and 1. $C = 0$ is for the open configuration, in which photons can escape both in the inward and outward directions. $C = 1$ is for the closed configuration, in which photons can only escape in the outward direction.

Using the C parameter, the escape probabilities for the continuum in the inward and outward directions are given as

$$P^{\rm (in)}_{\rm cont}(\epsilon)(R) = \frac{1-C}{2}, \tag{5.180}$$

$$P^{\rm (out)}_{\rm cont}(\epsilon)(R) = \frac{1+C}{2} \tag{5.181}$$

and those for lines as

$$P^{\rm (in)}_{\rm line}(\epsilon)(R) = (1-C)P_{\rm line}(\tau_i^{\rm (in)}), \tag{5.182}$$

$$P^{\rm (out)}_{\rm line}(\epsilon)(R) = \frac{C}{2}P_{\rm line}(\tau_i^{\rm (in)}) + (1-\frac{C}{2})P_{\rm line}(\tau_i^{\rm (out)}). \tag{5.183}$$

Contribution of the radiative excitation (known as continuum pumping) and the Thomson scattering is also controlled by the C parameter, in which $(1-C)$ is applied to the contribution of the radiative excitation and the Thomson scatteering. For the closed configuration ($C = 1$; the default value), no Thomson scattering and no radiative excitation are included.

5.4.2 Monte Carlo Solvers

In the Monte Carlo solvers, photons are tracked in the microscopic point of view, instead of solving the radiative transfer equations. One of the benefits of this solver is that it is free from those assumptions often required in other solvers, including a 1D geometry, escape probability, etc. The drawback is that it requires massive computational resources. We use two codes `MONACO` (§ 5.4.2.1) and `SKIRT` (§ 5.4.2.2) in this work. The available physical processes, features, and benefits of each code are summarized in Table 5.3.

TABLE 5.3: Comparison of the two Monte Carlo codes used in this work.

Code	MONACO	SKIRT
Version	1.6	9
Physics:		
Photon-neutral atom interactions (free-bound; photoionization and fluorescence)		
	yes[a]	yes
Photon-ion interactions (free-bound; photoionization and radiative recombination)		
1 or 2 electrons (H- & He-like)	yes[b]	no
more electrons (Li-like & more)	no	no
Photon-ion interactions (bound-bound; photoexcitation and radiative de-excitation)		
1 or 2 electrons (H- & He-like)	yes[b]	no
more electrons (Li-like & more)	no	no
Photon-electron interactions (free-free)		
free elec. scat.	yes	yes
bound elec. scat.; coherent (Rayleigh)	yes	yes
bound elec. scat.; incoherent (Raman, Compton)	yes	yes
Photon-dust interactions	no	yes
Geometry:	limited	flexible
Acceleration technic:	no	yes
Public availability:	no	yes

[a] Only for K-shell and L-shell atoms.
[b] Only for major elements (C, N, O, Ne, Mg, Si, S, Ar, Ca, & Fe).

5.4.2.1 MONACO

`MONACO` (MONte Carlo simulation for Astrophysics and Cosmology) is a Monte-Carlo simulation framework dedicated to calculating the photon-matter interactions mainly in the X-ray wavelengths (Odaka et al., 2011). It utilizes the `Geant4` toolkit (Agostinelli et al., 2003; Allison et al., 2006)[1] to track photon trajectories and to build 3D geometries. The treatment of X-ray reprocessing is based on the original version of the simulation developed by Watanabe et al. (2003) and Watanabe et al. (2006), which was re-written by Odaka et al. (2011). The code is widely used in X-ray astrophysical applications (e.g., Tomaru et al., 2023; Tanimoto et al., 2019; Mizumoto et al., 2019; Hagino et al., 2016; Tsujimoto et al., 2024).

The concept of the simulation is illustrated in Figure 5.12. The user defines the geometry and physical parameters of the matter (density, velocity, elemental abundance,

[1] https//geant4.web.cern.ch/

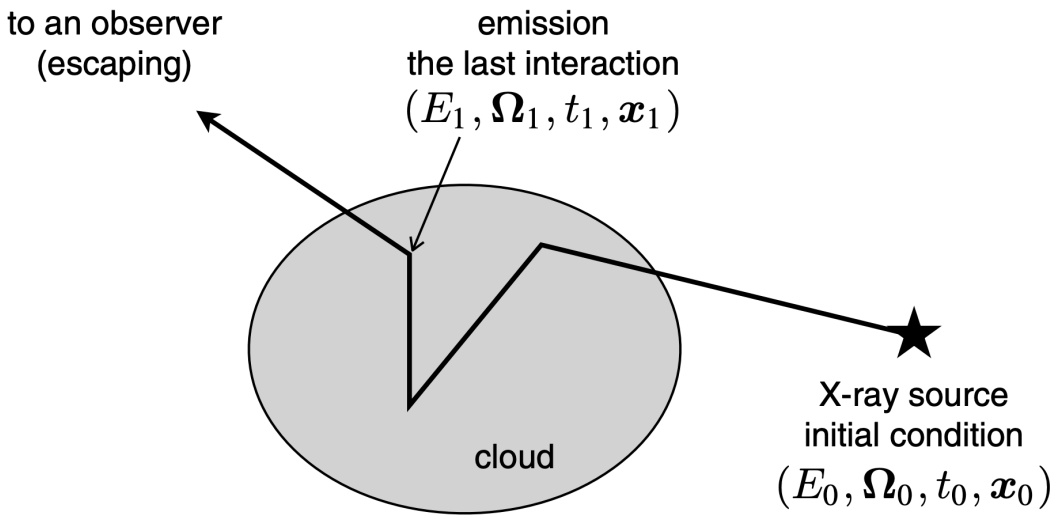

Figure 5.12: Concept of the Monte-Carlo simulation (Odaka et al., 2011).

charge populations, but not level populations) as well as the incident source spectrum. A photon with an energy E_0, randomly selected from an analytical function or a histogram of the source spectrum, is emitted in the direction $\mathbf{\Omega}_0$ from the position $\boldsymbol{x}_0$ at the time t_0. The simulation records the information on every interaction of photons and the matter.

The simulation work using `MONACO` consists of two parts; (1) calculations of charge population and plasma temperature by `XSTAR` and (2) Monte Carlo radiative transfer calculation by `MONACO`. In the first step, a self-consistent charge and level populations are calculated. The information of the charge population (but not the level population) is given as an input to the `MONACO` setup. `MONACO` calculates the level population using the flexible atomic code (FAC)[2] for a given plasma density and temperature by assuming that level populations are dominated by collisional excitation/de-excitation. This is not completely self-consistent and the line enhancement by the continuum pumping (radiative excitation) under the strong radiation field is not taken into account.

5.4.2.2 SKIRT

`SKIRT` (Stellar Kinematics Including Radiative Transfer) [3] is another Monte Carlo radiative transfer code developed mainly to calculate stellar kinematics of dusty galaxies (Baes et al., 2003; Baes et al., 2011; Camps and Baes, 2015; Camps and Baes, 2020). It enables the composition of arbitrary distributions of matter, supported as "built-in" geometries of wide astrophysical interests. Based on the user-defined 3D geometry, it computes the temperature distribution of the plasma irradiated by the central source and calculates the reprocessed emissions.

[2] https://www-amdis.iaea.org/FAC/
[3] https//skirt.ugent.be/root/_home.html

In addition to the flexibility in the geometry setup, the computation speed of SKIRT has been optimized using state-of-the-art acceleration techniques. These methods assign a weight, denoted as W, to each photon. W represents the fraction of the luminosity of the central source carried by each photon, which corresponds to the number of photons (see Steinacker, Baes, and Gordon, 2013, for a review). The initial photon emitted in one run is called a photon packet. One of the notable techniques employed in SKIRT is the peel-off (Yusef-Zadeh, Morris, and R. L. White, 1984), which enables that all photons directly contribute to the observed images or spectra by weighting the photons emitted from the central source and scattered along the trajectories towards the observer

$$W = p(\boldsymbol{n}_{\rm obs})e^{-\tau_{\rm obs}}, \tag{5.184}$$

where $\tau_{\rm obs}$ is the optical depth from the emission point and $p(\boldsymbol{n}_{\rm obs})$ is the probability that the direction of the photon is toward the observer. Other techniques, such as the forced scattering, continuous absorption, and composite biasing, are also implemented in SKIRT (e.g., Baes et al., 2016). Furthermore, SKIRT adopts multi-threading and multi-processing schemes to enable efficient calculations in high performance computing systems. Hierarchical octree algorithms allow efficient gridding even with complex geometries (Saftly et al., 2013).

Recently, some processes relevant to X-ray astrophysics have been implemented in SKIRT to handle continuum radiative transfer in the energy range of 0.1–500 keV (Vander Meulen et al., 2023). This includes photon and electron interactions (scattering by free and bound electrons), photon and atom interactions (photoelectric absorption and fluorescence), and photon and dust interactions. The implementation of these features has been verified by comparing with other X-ray radiative transfer codes. However, the current version does not include photon and ion interactions, which is most relevant for the radiative transfer calculation of the photoionized plasmas.

Matsumoto et al. (2023) made another extension of SKIRT for the NLTE line radiative transfer calculations to incorporate two atoms and four molecules (C, C^+, CO, OH, H_2, and HCO^+) to model the dusty AGN torus in the infrared band. Based on Baes, Camps, and Matsumoto (2022), which introduced a modified Monte Carlo radiative transfer scheme that explicitly handles negative opacity due to absorption and stimulated emission, self-consistent calculations of NLTE line transfer was achieved. The emissivity, opacity, and line profiles of the target atoms or molecules are provided as a database.

The new algorithm updates the temperatures of the dust (media), solves the detailed balance equations (equation 5.93 for all levels), and iterates through these two main steps. It begins by setting input parameters, including the incident source flux, physical properties of the media such as the densities of atom and collision partners, kinetic temperature, and turbulent velocity. After launching primary emission photon packets from the incident source to estimate the radiation field, the level populations of atoms are computed under the LTE assumption to start with. Subsequently, secondary emission photon packets are launched through the media to account for the secondary emission process. The radiation field is estimated as the sum of the primary and secondary emission

$$J_\lambda = J_\lambda^{\rm p} + J_\lambda^{\rm s} \tag{5.185}$$

and the mean intensity of the line is

$$\bar{J}_{\rm line} = \int J_\lambda \phi_{\rm line}(\lambda) d\lambda. \tag{5.186}$$

SKIRT assumes that the equilibrium transitions in the level populations converge more rapidly than the dynamical timescale, enabling us to solve the detailed balance equation effectively. It then obtains the updated level populations and temperature, and iterate through the aforementioned calculations until the convergence criteria are met. The criteria can be defined according to their specific needs.

5.4.3 Further Development

5.4.3.1 NLTE calculation in the X-rays

As reviewed in § 5.4.1 and § 5.4.2, none of the existing codes is sufficient to achieve our goals. The two-stream solver (XSTAR) is incapable of modeling in 3D, while the Monte Carlo solvers lack flexible geometry modeling and acceleration technique (MONACO) or the photon-ion interactions (SKIRT). We thus make an extension to SKIRT so that we can include photon-ion interactions in a flexible 3D Monte Carlo solver for the first time in this work. We present the development and verification here.

We utilize the recent extension by Matsumoto et al. (2023), who implemented NLTE line radiation transfer in the infrared bands. We extended their database so that lines in the X-ray band can be calculated in the same algorithm. Note that the extension by Matsumoto et al. (2023) and our modification solve the detailed balance for the level population under a given radiation field, but not the charge population.

First, the following database files are generated for ions with an atomic number $Z \leq 30$ and the ionization degree $C \leq Z$:

1. Energies and degeneracy of the quantum levels.
2. Einstein A coefficient between two levels of the interest.
3. Collisional excitation coefficients for some selected temperatures.
4. List of temperature grid for the collisional excitation.
5. Atomic mass.

For the energy levels and the Einstein A coefficients, we used the `get_data` task in the `pyAtomDB` package (Foster and Heuer, 2020) and retrieved the data type of "LV (energy levels)" for file 1 and "LA (radiative transition data)" for the file 2 in the list above. For the collisional excitation coefficient, we assume that the collision takes place between the ions and electrons only. We used the `return_line_emissivity` task for the collisional ionization equilibrium object `spectrum.CIESession()` constructed for given temperatures. We selected 100 temperatures in a logarithmic spacing in the range of $1 \times 10^{4-9}$ K, so that we can describe their temperature dependence. For the null value of the emissivity, we adopted a very small value of 1×10^{-20} cm^3 s^{-1} for the stabilization of the calculation.

5.4.3.2 Benchmarking

We benchmark the result of our SKIRT extension for a simple geometry against the XSTAR simulation and the back-of-envelope calculation.

Target: We use H-like Mg (Mg^{11+}) as an example. The energy levels of interest are shown in Table 5.4. The charge state distribution of Mg as a function of the ionization parameter is shown in Figure 5.13. The emissivity of Mg^{11+} by electron collision is given in Figure 5.14. The cosmic abundance of Mg is $A_{Mg} = 3.5 \times 10^{-5}$ (Grevesse, Noels, and Sauval, 1996).

TABLE 5.4: Energy levels and transitions of Mg XII (Foster et al., 2012).

Index	Energy (keV)	Config	Term	Trans [a]	Name	Degeneracy	A coeff (s^{-1})[b]
0	0.0	1s1	$^2S_{1/2}$	(ground)	—	2	—
1	1.47172	2s1	$^2S_{1/2}$	M1		2	2.5×10^{7}
2	1.47169	2p1	$^2P_{1/2}$	E1	Lyα^2	2	1.3×10^{13}
3	1.47264	2p1	$^2P_{3/2}$	E1	Lyα^1	4	1.3×10^{13}
4	1.74457	3s1	$^2S_{1/2}$			2	0
5	1.74456	3p1	$^2P_{1/2}$	E1	Lyβ^2	2	3.5×10^{12}
6	1.74484	3p1	$^2P_{3/2}$	E1	Lyβ^1	4	3.5×10^{12}
7	1.74484	3d1	$^2D_{3/2}$	M1		4	1.8×10^{9}
8	1.74493	3d1	$^2D_{5/2}$	M1		6	1.8×10^{9}
9	1.84003	4s1	$^2S_{1/2}$			2	0

[a] Transition to the ground state. E1 for electric dipole (allowed), M1 for magnetic dipole (forbidden), E2 for electric quadruple (forbidden) transitions. [b] Einstein A coefficient to the ground state.

Geometry: We assume a geometry depicted in Figure 5.15. As the incident source flux, we assumed a 2 keV blackbody emission with an integrated flux $L_x = 1.88 \times 10^{37}$ erg s^{-1} in the energy range of 0.013605–13.605 keV (1–1000 Ry). The incident source is point-like placed at the center of a spherically symmetric shell of the photoionized cloud. The cloud has a thickness equivalent to the hydrogen column density $N_H = 1 \times 10^{24}$ cm^{-2}. It has a density profile $n(r) \propto r^{-2}$ with the innermost density of $n_H = 1 \times 10^{15}$ cm^{-3}. It also has a turbulent velocity of 50 km s^{-1}.

The ionization parameter $\log \xi = 2$ was set, at which the H-like Mg population is close to the peak (Figure 5.13). From these values, $r_{in} = (L_x/\xi n_e)^{1/2} \sim 1.37 \times 10^{10}$ cm and $r_{out} = 1/(1/r_{in} - N_H/n_e r_{in}^2) = 1.48 \times 10^{10}$ cm are derived.

`XSTAR` run: We ran the `XSTAR` calculation for the geometry in Figure 5.15. The covering fraction was set to 1. The resultant radial profiles of the ionization parameter, density, and the thermal equilibrium temperature are given in Figure 5.16. The temperature has an unphysical jump, which is often found in `XSTAR` simulations. Fortunately, this does not affect the benchmarking, as the collisional excitation is negligible for electrons of such low temperatures.

`SKIRT` run: We ran the `SKIRT` calculation for the same geometry in Figure 5.15. This geometry is available as a built-in geometry of `SKIRT`. For the sake of time, we composed the cloud solely of Mg^{11+}. Its column density across the cloud is derived as

$$N_{Mg^{11+}} = N_H \times A_{Mg} \times f_{Mg^{11+}} \sim 7 \times 10^{18} [cm^{-2}], \tag{5.187}$$

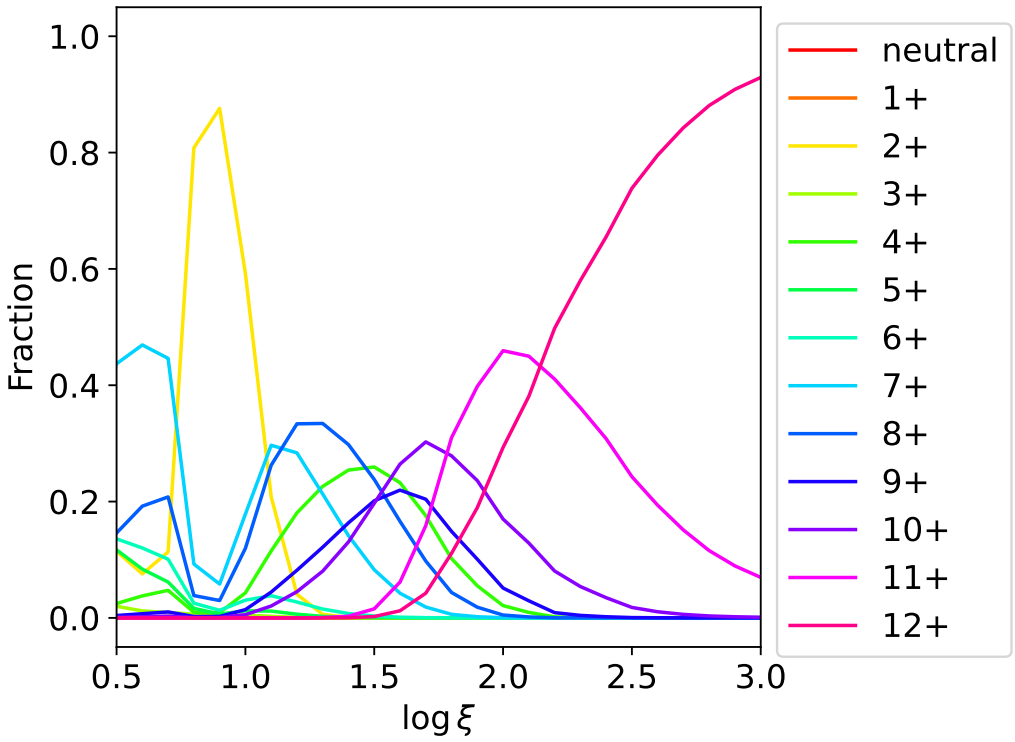

Figure 5.13: Charge state distribution of Mg calculated by `XSTAR`.

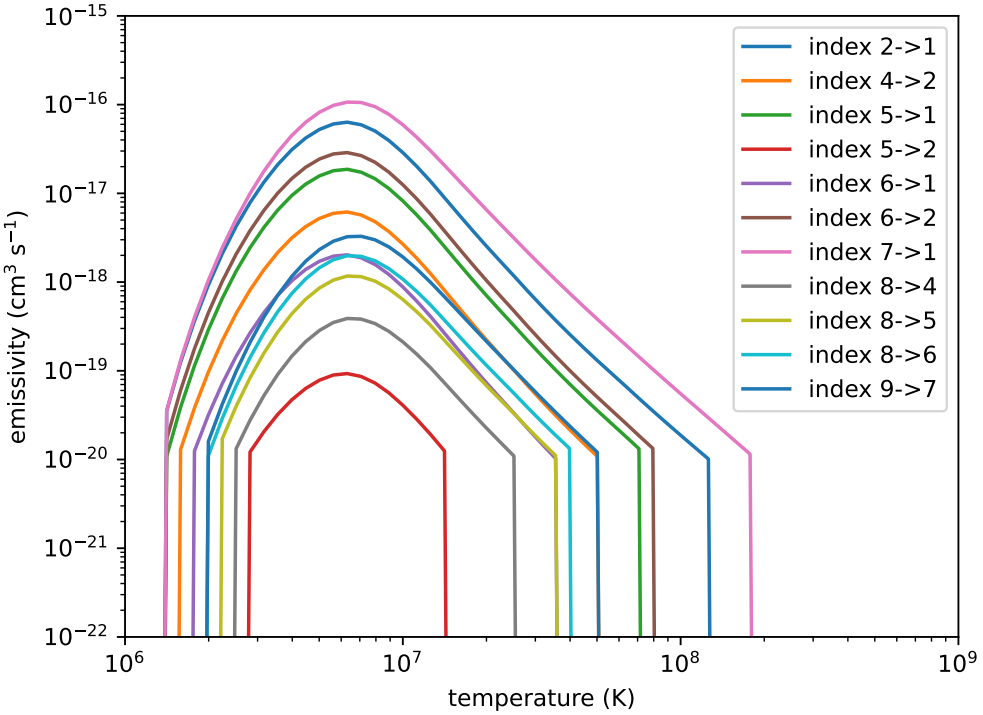

Figure 5.14: Emissivity of Mg XII by electron collisions retrieved from `PyAtomDB` at 10^6 K. See Table 5.4 for the index.

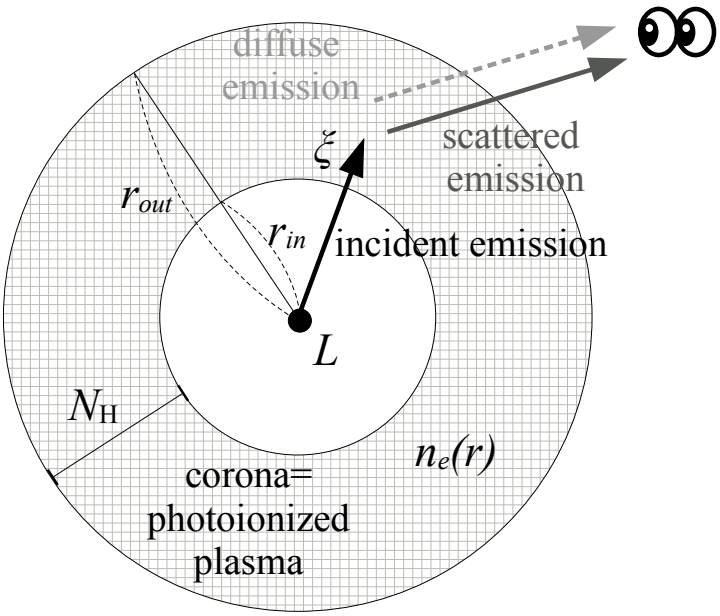

Figure 5.15: Geometry for the benchmarking.

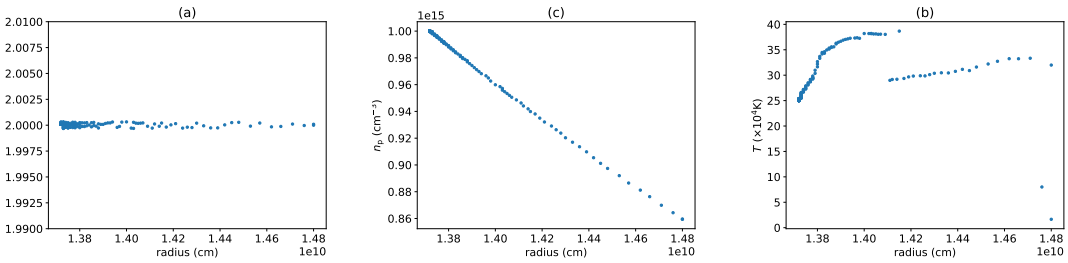

Figure 5.16: Radial distribution of (a) ionization parameter $\log \xi$, (b) electron density n_e and (c) electron temperature T_e calculated by `XSTAR`.

in which $A_{\rm Mg}$ is the Mg abundance relative to H and $f_{\rm Mg^{11+}} = 0.2$ is the charge population of $\rm Mg^{11+}$ (Figure 5.13). We assumed electrons to be the only collision partner for $\rm Mg^{11+}$. Instead of the electron density $n_{\rm e}$ itself, SKIRT requires the ratio $n_{\rm e}/n_{\rm Mg^{11+}} \sim N_{\rm H}/N_{\rm Mg^{11+}} \sim 1 \times 10^6$. The electron temperature profile as an output of XSTAR was provided as an input of SKIRT. The number of the photon packets is 1×10^6.

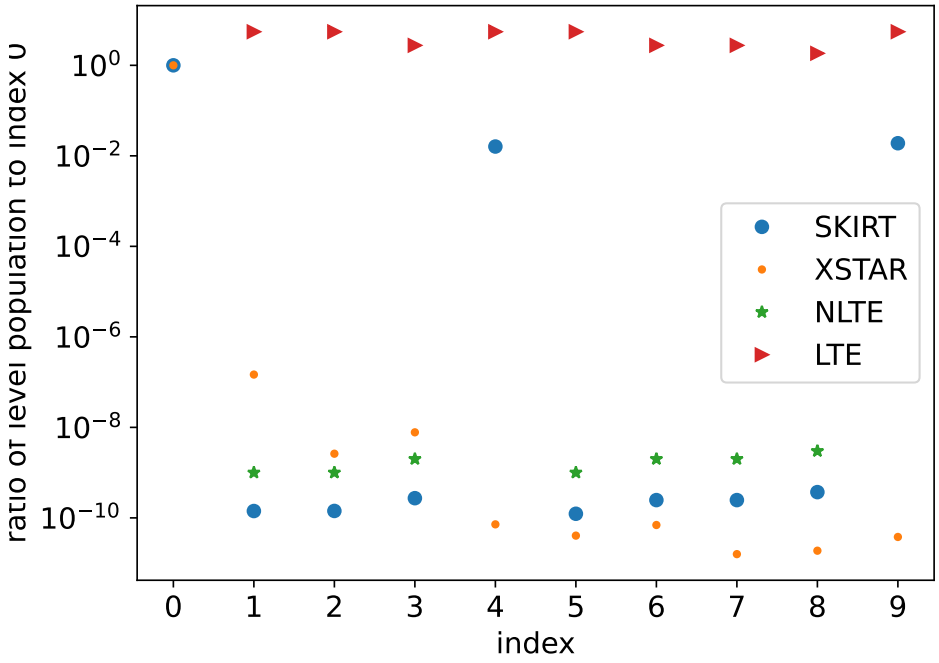

Figure 5.17: Resultant level populations calculated using the XSTAR and SKIRT simulations and those calculated by hand for the LTE (10^7 K) and NLTE (nebular conditions). The index number corresponds to levels in Table 5.4. The population is normalized at the ground state (index 0).

Comparison (1) Level population: We now compare the XSTAR and the SKIRT calculation. First, we examine the level populations, which are available as the output products of the both simulations. The levels are specified by the numbers in Table 5.4. The resultant level populations by the XSTAR and SKIRT are shown in Figure 5.17. We also plot the level population of the LTE and NLTE (nebular conditions) by solving the detailed balance equations between the excited levels (1–9) and the ground level (0). For the LTE, $C_{ul}n_u = C_{lu}n_l$ was solved. For the nebular (NLTE) approximation, $A_{ul} + B_{ul}J_\nu = B_{lu}J_\nu$ was solved.

This comparison provides insights into how the level population changes as it departs from the LTE conditions under a strong radiation field. The most prominent changes occur in the indexes 1, 2, 3, 5, 6, 7 and 8, the population of which is much smaller than that expected for the LTE. As a result, the population of the ground state (level 0) increases. This is because the Einstein A coefficient is large for the transitions between these levels and the ground state, so that they de-excite radiatively very rapidly to the ground state. In contrast, the radiative de-excitation from the index 4 and 9 to the index 0 is weak, thus their level populations remain relatively large in comparison to the others. A discrepancy remains against the result with XSTAR.

We verify if the nebular approximation holds for the present application. We take the transition from index 2 to index 0 as an example. We estimate the values of each term in the detailed balance equation. First, the radiative coefficient (Einstein A coefficient) is $A_{ul} = 1.3 \times 10^{13}$ s^{-1}. From Equation 5.106,

$$B_{ul} = \frac{f^2 c^2}{2E^3} A_{ul} = 2.0 \times 10^7 \ [\mathrm{cm^2\ str\ Hz\ erg^{-1}}]. \tag{5.188}$$

The radiation field strength J_ν is calculated from the incident flux $f^{\mathrm{inc.}}$ [$\times 10^{38}$ erg s^{-1} erg^{-1}] from an output of `XSTAR` as

$$\begin{aligned} J_\nu &= \frac{f^{\mathrm{inc.}} \times 10^{38}\ [\mathrm{erg\ s^{-1}\ erg^{-1}}]}{6.242 \times 10^8} \frac{1}{4\pi r_{\mathrm{in}}^2} \frac{1}{4\pi} \frac{c\ dE}{12.4 \times 10^{-10} [\mathrm{keV\ A}]} \\ &\sim 6.64 \times 10^{-4} [\mathrm{erg\ s^{-1}\ cm^{-2}\ str^{-1}\ Hz^{-1}}]. \end{aligned} \tag{5.189}$$

The collisional excitation coefficient with electrons is very low and was set to the lower limit of 1×10^{-20} cm^3 s^{-1}. Based on the coefficients above, the values are estimated as $A_{ul} \sim 1.3 \times 10^{13}$ s^{-1} for the spontaneous emission, $B_{ul} J_\nu \sim 1.3 \times 10^4$ s^{-1} for the stimulated emission, and $C_{ul} n_{\mathrm{e}} \sim 1 \times 10^{-5}$ s^{-1} for the collisional de-excitation. The spontaneous emission overwhelms the other de-excitation processes, justifying the application of the nebular approximation.

Comparison (2) Spectra: Next, we compare the resultant spectra. We convert the units of the output spectrum that is different between the two solvers. `XSTAR` gives flux f in the unit of $\times 10^{38}$ erg s^{-1} erg^{-1}. Therefore, $f_{\mathrm{XSTAR}}(E)$ [s^{-1} keV^{-1}] is obtained as

$$f_{\mathrm{XSTAR}} = f \times 10^{38} \frac{6.242 \times 10^8\ [\mathrm{keV\ erg^{-1}}]}{E\ [\mathrm{keV}]} \frac{1}{6.242 \times 10^8\ [\mathrm{keV\ erg^{-1}}]}. \tag{5.190}$$

On the other hand, in `SKIRT`, the observed flux (f') at a distance of $D = 10$ kpc is provided in the unit of s^{-1} cm^{-2} keV^{-1}. The converted flux $f_{\mathrm{SKIRT}}(E)$ is given by

$$f_{\mathrm{SKIRT}} = f' \times 4\pi D^2. \tag{5.191}$$

The resultant spectra are shown in Figure 5.18. The incident emission is a 2 keV blackbody emission. In `XSTAR`, we obtain the transmitted spectrum (incident photons attenuated by the cloud) and the diffuse spectrum (emission from the cloud). In `SKIRT`, we obtain differently decomposed spectra, but their arithmetic sum yields components to be directly compared to those of `XSTAR` (Table 5.5). Note that some fluctuations of the `SKIRT` spectra are due to Monte Carlo noise.

Finally, we examine the line intensity taking the level 2 $\rightarrow$ 0 transition of Mg XII (Lyα^2). Assuming that the radiative transition is dominant, the line luminosity can be estimated by

$$L_{\mathrm{line}} = n_u\ A_{ul} \frac{4\pi}{3} (r_{\mathrm{out}}^3 - r_{\mathrm{in}}^3) \sim 6.2 \times 10^{34}\ [\mathrm{erg\ s^{-1}}], \tag{5.192}$$

which is a few percent of the total incident luminosity.

To compare with the simulation, we extracted the diffuse component and derived the line luminosity by integrating in the range of 1.467–1.478 keV. `XSTAR` yielded $\sim 2.2 \times 10^{35}$ erg s^{-1} and `SKIRT` yielded $\sim 7.6 \times 10^{32}$ erg s^{-1}. The diffuse emission without

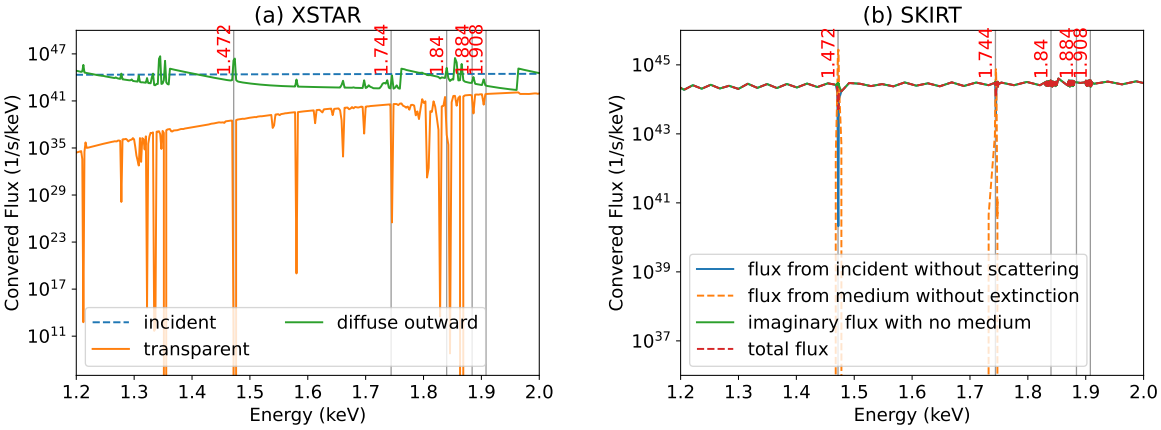

Figure 5.18: Simulated spectra with (a) `XSTAR` and (b) `SKIRT` for different components. The gray vertical lines represent the transitions of a large A value with their energy (keV) in red. We used a fine energy grid around the transitions and a coarse grid otherwise for `SKIRT`, while the grid is constant in `XSTAR`.

TABLE 5.5: Spectral decomposition.

Component	`XSTAR`	`SKIRT`
Incident	`incident`	`transparent`
Transmitted	`transmitted`	`direct primary`
Diffuse	`emit_outward`	`direct secondary`[a]
Scattered	Not available	`scttered primary/secondary`

[a] This component includes the self-absorption in the media. The pure diffuse emission with no self-absorption is provided as `transparent secondary`.

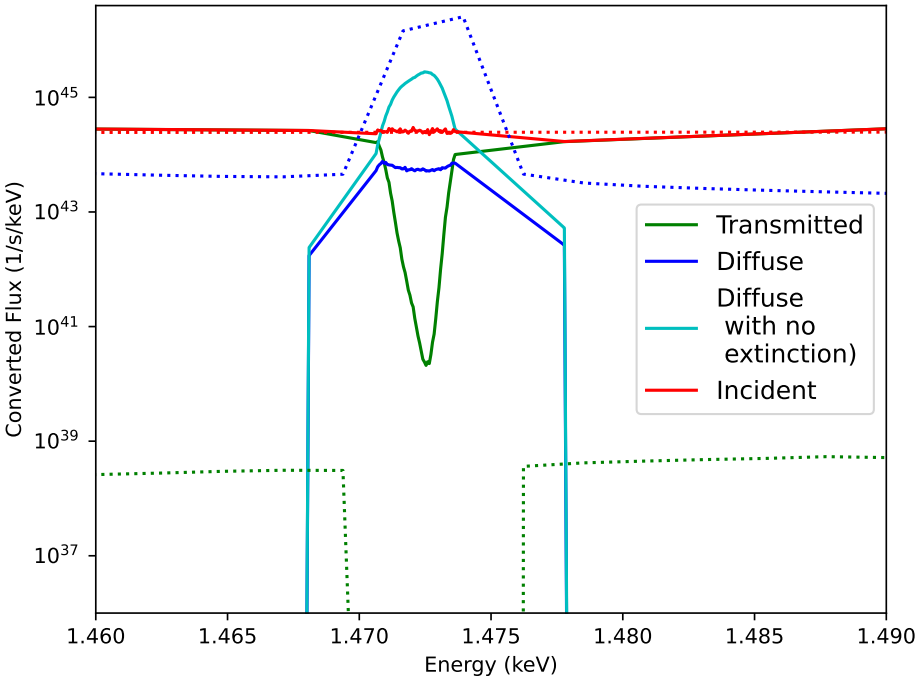

Figure 5.19: Spectra around Mg XII Lyα^2 (index 2 $\rightarrow$0). The solid and dotted lines represent the `SKIRT` and `XSTAR` components, respectively. Note that the cyan component is available only for `SKIRT`.

self-absorption in `SKIRT` yielded $\sim 1.1 \times 10^{34}$ erg s^{-1}, which is closed to the calculated value above. In this manner, the line luminosity varies a lot depending on the codes due to many differences in assumptions and implementations. We will see a similar discrepancy in the comparison between `XSTAR` and `MONACO` in § 7.2.1. This needs to be fixed in the future. For now, we pay attention to the possible systematic errors in the simulation results.

Chapter 6

Analysis

Contents

6.1 Mid Flux State with *NICER* 126
6.1.1 Definition of phases 126
6.1.2 Spectral modeling 127
6.1.3 Continuum emission 132
6.1.4 Line emission 133
6.2 Low Flux State with *Suzaku* 138
6.3 High Flux State with *Chandra* 140

We now move on to the analysis of the data described in § 4. Cir X-1 exhibits variations of different time scales over the long term (§ 3.3.1). Among them, we focused on the behavior since 2018, when the light curve folded by $P_{\rm orb}$ became repeatable in the mid-flux state. To investigate changes within one orbit, we proposed observing the source 103 times over a single orbit with *NICER*, which was accepted and carried out in AO2. Cir X-1 was observed once every less than 4 hours, which is the highest cadence observation made to date (§ 4.1). Our strategy is to use this unique data set intensively to construct a fiducial model to explain the spectral changes within one orbit and apply the model to other data sets in different flux states.

First, in § 6.1, we explore the *NICER* AO2 data set taken in the mid flux state. We start by defining phases during an orbit based on the flux and hardness changes in § 6.1.1, then choosing some representative spectra to estimate the X-ray spectral model in § 6.1.2. The obtained model is then applied to all the data in the orbit, and the changes of the continuum (§ 6.1.3) and line (§ 6.1.4) components are described. The content of this section is based on Tominaga et al. (2023).

In § 6.2, we use the *Suzaku* data set taken in the low flux state, in which we show that the X-ray spectra are dominated by emission lines. In § 6.3, we use the *Chandra* data set taken in the high flux state, in which we show that the emission lines exhibit P Cygni profiles. The goal of these sections is to characterize the X-ray spectra of these flux states.

6.1 Mid Flux State with *NICER*

6.1.1 Definition of phases

Figure 6.1 shows the light curve of the *NICER* AO2 data set. This pattern is repeated as shown with the *MAXI* light curves of the neighboring cycles (Figure 6.2). Some typical patterns are distinctively seen in the light curve, based on which we define phases within one orbit.

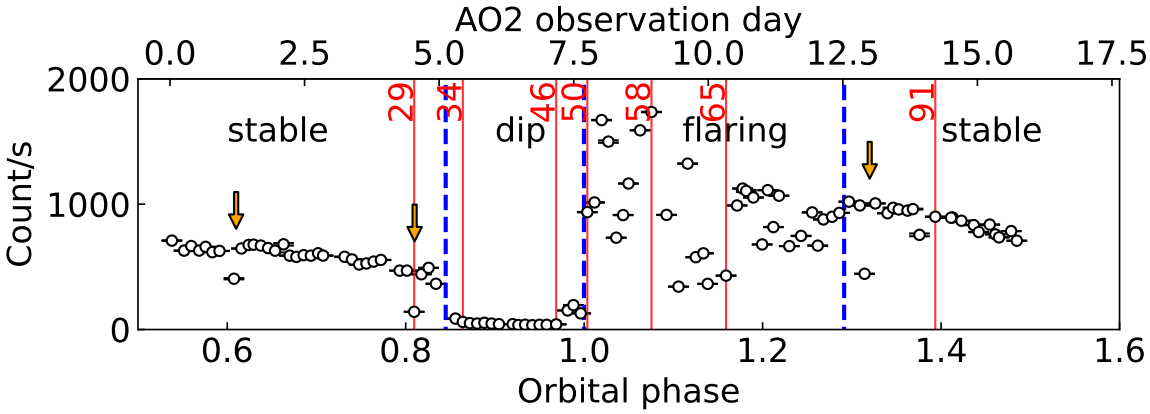

Figure 6.1: Light curve over an orbit observed with *NICER* in AO2 observations (Tominaga et al., 2023). Blue dashed lines represent the phase boundaries derived in § 6.1.1. Orange arrows show short dips described in § 6.1.1. Red lines show the snapshots and their sequential number analyzed in § 6.1.2.

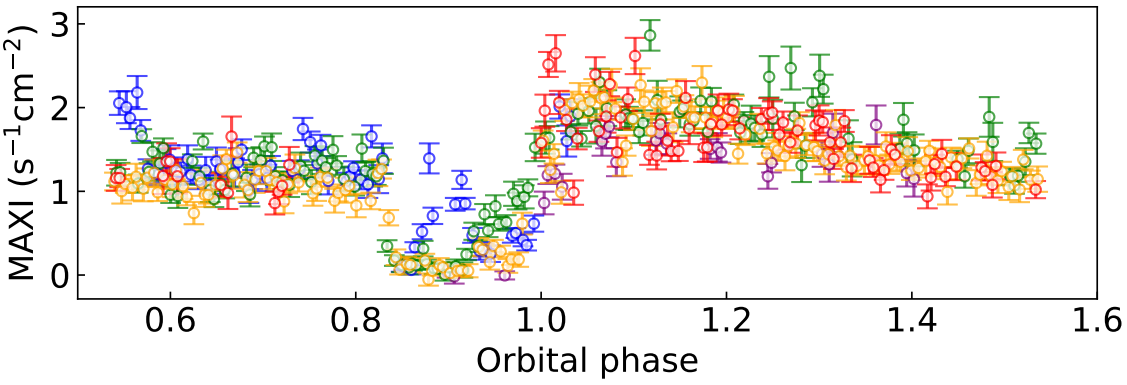

Figure 6.2: Light curve observed by *MAXI* for the last five orbits including the observation by *NICER* shown in Figure 6.1. The colors represent individual orbits (Tominaga et al., 2023).

First, a qualitative description of the light curve is as follows. Before the periastron ($\phi = 1.0$), the flux drops by an order of magnitude for $\Delta\phi \sim 0.15$. This is often called "long dips" in the literature (e.g., Asai et al., 2014). After the periastron, the flux suddenly increases and becomes unstable. The flux then gradually decreases. Our *NICER* data reveal these features with higher significance and finer temporal resolution

than any previous data. Abrupt fluctuations at ϕ =0.83 and 0.97, sharp fluctuations at ϕ =1.0–1.3, and small dips ("short dips") at ϕ =0.61, 0.81, and 1.32 were detected.

The three phases are then defined more quantitatively. Bayesian blocking method (Scargle et al., 2013) was applied to the *NICER* light curves of the count rates and the two hardness ratios. The result of the blocking is shown in Figures 6.1 and 6.3. In the following, we refer to these phases as "dip" (ϕ ∼0.84–1.0), "flaring" (ϕ ∼1.0–1.29), and "stable" (ϕ ∼0.54–0.84 and 1.29–1.48). This division is consistent with the *ASCA* result (Iaria et al., 2001a), in which three (dips, flaring, and stable) phases are recognized at ϕ = 0.78–0.97, 0.93–0.3, and 0.3–0.7 based on observations covering one orbit in March 1998.

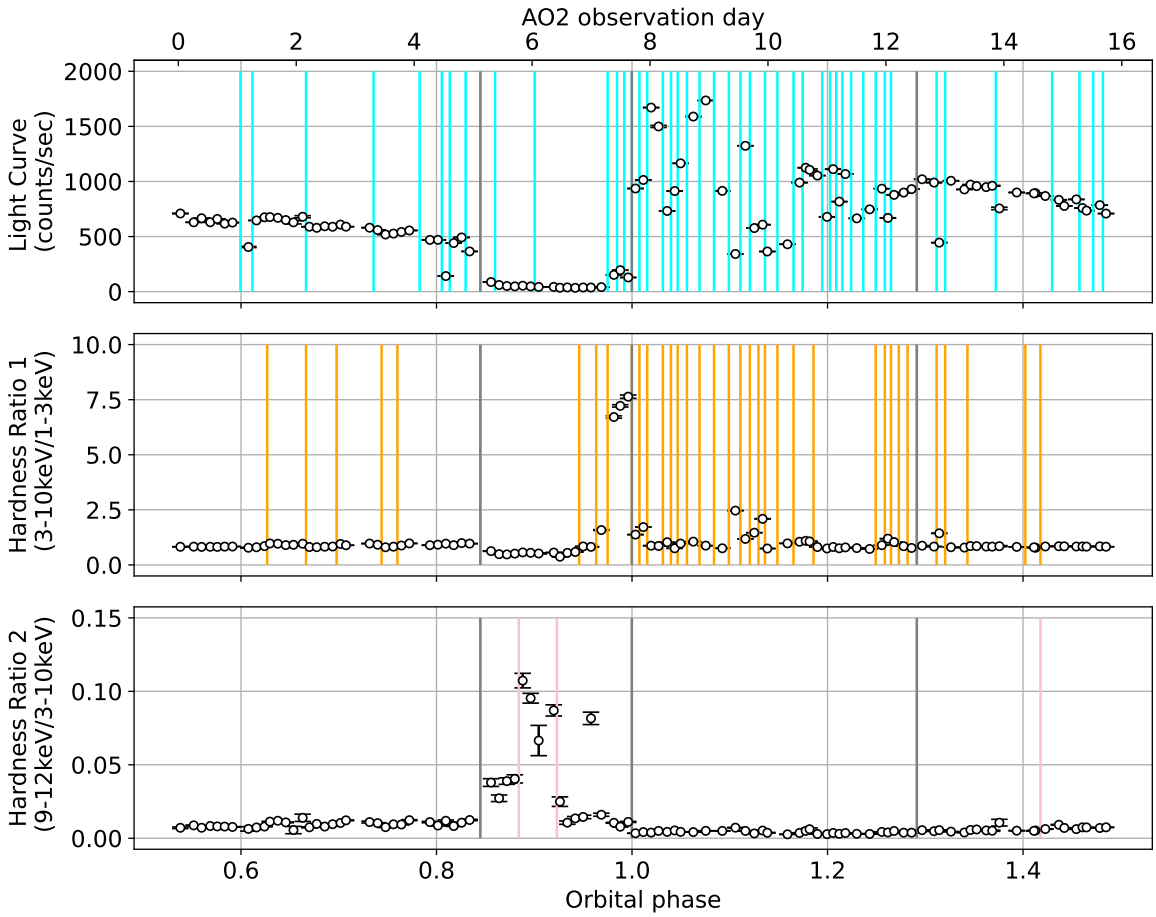

Figure 6.3: Light curves (top), hardness ratios (medium and bottom) of the *NICER* AO2 observation covering the orbital phase. The Bayesian-blocked phase boundaries are shown with cyan, orange, and pink lines, respectively. The common boundaries of the three are shown with grey lines.

6.1.2 Spectral modeling

NICER observation for one day is assigned a unique ObsID. We further sub-divided each ObsID to create 103 "snapshots" in total to cover the entire orbital period. We set the intervals between the two snapshots longer than 10,000 s.

For each of the 103 snapshots, X-ray spectra were constructed in the energy range of 0.9–10.5 keV. This energy range was chosen to ensure a high signal-to-noise ratio given the instrument background and the effective area of the telescope. The spectra were rebinned to achieve a minimum of 30 counts per energy bin. Thanks to the large effective area of *NICER* , well-exposed spectra were obtained in a very high cadence.

We first selected several representative spectra in each phase to construct spectral models. All spectral modeling includes the interstellar photoelectric absorption with the cross section by Verner et al. (1996) and the elemental abundance by Wilms, Allen, and McCray (2000).

6.1.2.1 Stable phase

We first analyzed the simplest spectrum in the stable phase, which includes occasional short dips. During this phase, the spectral shape remains stable except for a gradual decrease in flux.

We show the data from snapshot 91 in Figure 6.4 (a). The continuum emission comprises the multi-temperature blackbody component `diskbb` (Mitsuda et al., 1984; Makishima et al., 1986), which are parameterized by normalization and the innermost disk temperature $T_{\rm in}$. It is partially absorbed by neutral matter described with two parameters (covering factor $f^{(\rm cov)}$ and H-equivalent column density $N_{\rm H}^{(\rm cov)}$), and by the interstellar absorption with a column density of 2×10^{22} cm^{-2}, which was fixed. Because the ionization degree of the absorber could not be discerned, we assumed it to be neutral. Additionally, a Gaussian component was added to account for the observed 6.4 keV Fe K fluorescence line.

The snapshot 29 in Figure 6.4 (b), showing a short dip, can be fitted with the same model, but by increasing the hydrogen column density and the covering fraction of the partial absorber.

6.1.2.2 Dip phase

We next investigated the dip phase, during which a noticeable change in the spectral shape occurred. In the first 10 data points of this phase (hereafter referred to as the "early dip" phase), the spectral shape exhibited a single peak, as exemplified by snapshot 34 (Figure 6.5 a). In contrast, in the following six data points (hereafter referred to as the "late dip" phase), the spectral shape exhibits two peaks, represented by the snapshot 46 (Figure 6.5 b). Despite this distinction, both can be described using different parameters of the same model. Specifically, the two peaks are reproduced by the uncovered and covered components of the blackbody radiation emanating from the accretion disk.

Moreover, the spectrum during this phase is characterized by numerous emission lines, particularly in highly ionized Fe but also in lighter elements such as Mg, Si, and S. These emission lines most likely arise from a photoionizing plasma, which should be associated with the continuum radiation within the spectral bands. Indeed, we observed excess in the soft-energy band of the spectrum, which was phenomenologically represented by a power-law model.

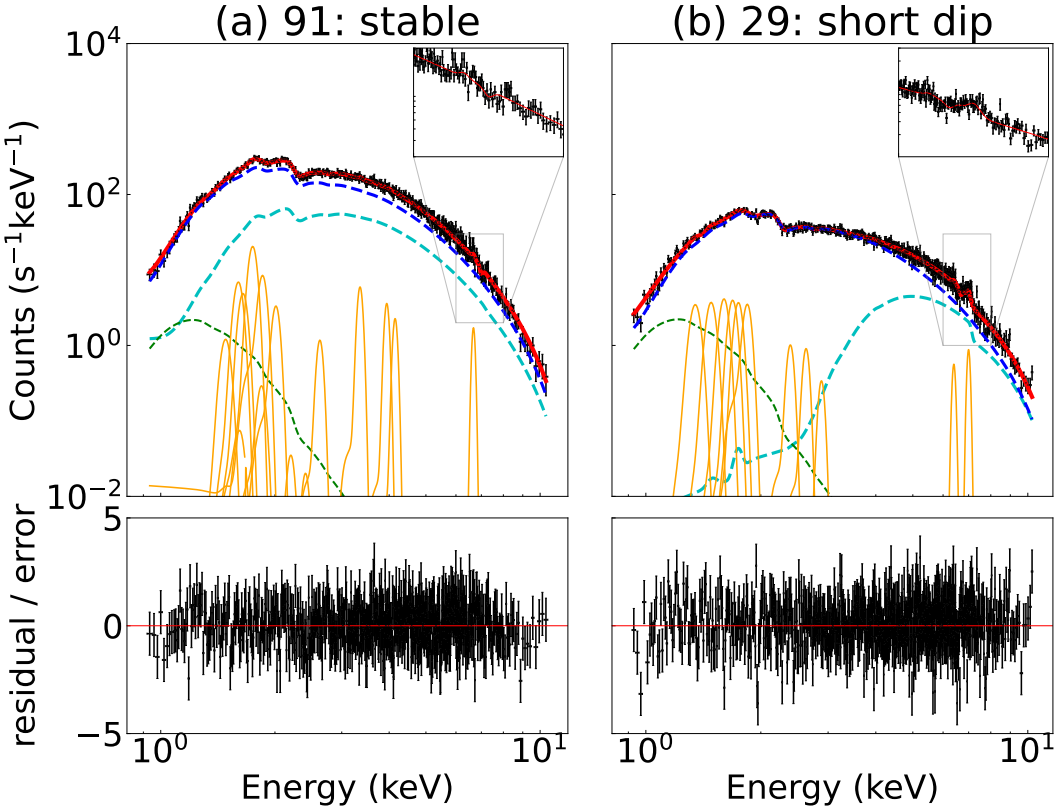

Figure 6.4: Spectra (black) and the best-fit models in the top panels and the residuals of the fits in the bottom panels for the two snapshots (a) 91 and (b) 29, both representing the stable phase. The snapshot 29 (b) was taken during a short dip. Different colors are used for different model components; red for total, cyan for covered disk blackbody, blue for uncovered disk blackbody, orange for Gaussian models, and green for soft excess. The insets give a close-up view of the energy bands with apparent spectral line features.

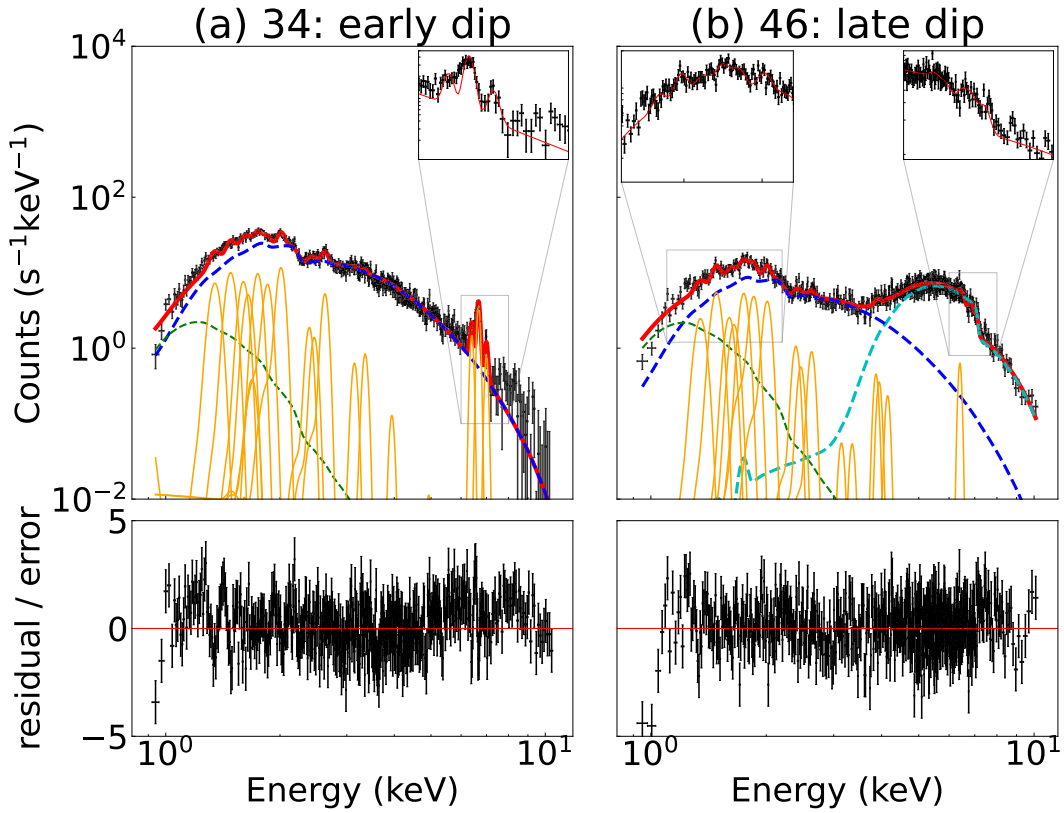

Figure 6.5: Two snapshot spectra representing the early dip (a) and the late dip (b) phase. Colors are used in the same manner as in Figure 6.4.

6.1.2.3 Flaring phase

The flux undergoes rapid changes during the flaring phase. To capture variations in high, mid, and low flux, we selected three snapshots (snapshots 58, 50, and 65, respectively; Figure 6.6). The flux changes by a factor >5. Nevertheless, we applied the same model successfully; the blackbody emission with partial covering described all the spectra with different parameters mostly of the covering fraction and the column density of the partial absorber. In addition, emission or absorption features were observed, which we modeled using several positive and negative Gaussian lines, respectively.

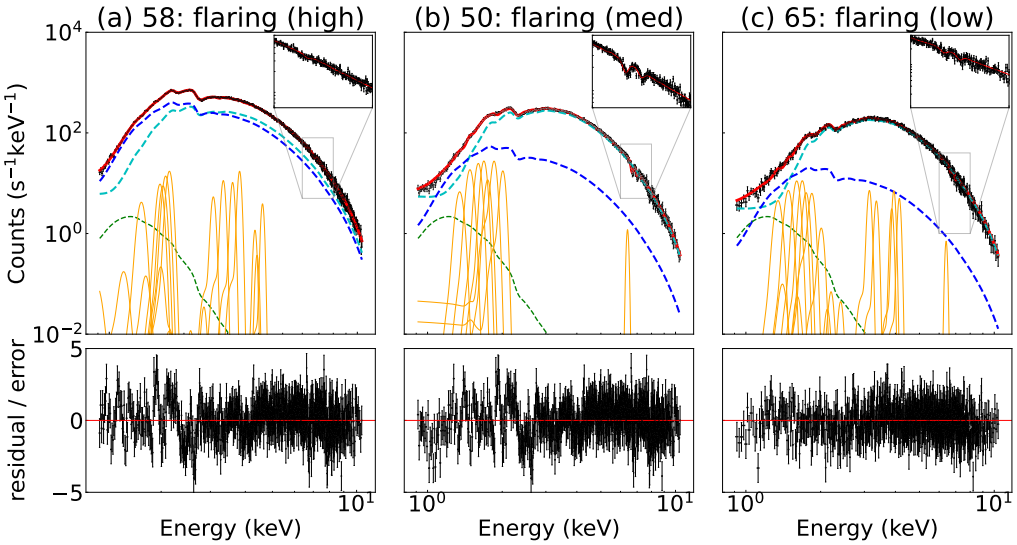

Figure 6.6: Three snapshot spectra representing the flaring phase with high (a), mid (b), and low flux (c). Colors are used in the same manner as in Figure 6.4

6.1.2.4 All the phases

To summarize the aforementioned results, the spectra from the seven selected snapshots were effectively described using the same approach, despite significant variations in the spectral shapes. The continuum emission is described as the disk blackbody emission, which is partially absorbed by neutral clouds and fully covered by photoelectric absorption from the interstellar medium. Minor distinctions remain, such as the necessity for soft excess emission during the late dip phase and the presence of Gaussian lines in different phases, either in emission or absorption.

We next constructed a common model that accommodates these minor differences. While the soft excess was necessary only during the dip phase, we held its parameters constant at values derived from the dip phase and included this component in all the phases. In the other phases, the soft excess is surpassed by the disk blackbody emission, and as a result, it has no impact on the fitting. We incorporated Gaussian lines at energies corresponding to the Lyα and Heα transitions of H-like and He-like ions of Mg, Si, S, and Fe. We also added Fe I Kα fluorescence line. Here, the Heα line encompasses all unresolved lines stemming from (1s)(2p) or (1s)(2s) $\rightarrow$ $(1s)^2$ transitions, while the Lyα line pertains to the (2p) $\rightarrow$ (1s) transition. To account for both emission and

absorption, we allowed both positive and negative values in the fits. Since no significant Doppler shift or broadening was detected in any of the lines, we fixed the energy shift and line width at zero. The best-fit model depicted in Figures 6.4–6.6 show the results of applying this unified model.

In previous studies of Cir X-1, X-ray continuum spectra were frequently interpreted as a combination of multiple spectral components, including blackbody, disk blackbody, and Comptonized emission (e.g., Shirey, Levine, and Bradt, 1999; Iaria et al., 2005; D'Aì et al., 2012). However, we contend that a single disk blackbody component is adequate to account for the spectral diversity within our dataset. The presence of the partial covering on the disk blackbody component results in the appearance of two spectral peaks in the regions that are covered and uncovered.

It is worth noting that we did not find it necessary to include an additional blackbody component for any of the spectra over the entire orbit. It is important to recognize that, while we utilize a single disk blackbody component in our model, the actual emission possibly arises from a combination of multiple optically thick components, including the neutron star surface, the boundary layer, and the accretion disk.

6.1.3 Continuum emission

The common spectral model, derived from the seven selected snapshots, was consistently applied to analyze the spectra of all the 103 snapshots. While the fitting may not be the best for some individual spectra, this approach enables us to capture the overall trends in spectral parameters across the entire orbital period. The phase-dependent changes in the spectral model parameters for the continuum component are represented by the green symbols in Figure 6.7. The free parameters are the innermost temperature $T_{\rm in}$ and the normalization for the disk blackbody emission, as well as the covering fraction $f^{(\rm cov)}$ and the column density $N_{\rm H}^{(\rm cov)}$ for the partial covering material. To address possible parameter degeneracy, we initially conducted a fit using only data above 4 keV with the model to obtain the best fit, then fixed $T_{\rm in}$. Subsequently, the model was refitted using data spanning the entire energy range.

In the stable phase, the parameters for the disk blackbody emission exhibit gradual changes. When partial covering was not required, we fixed both $N_{\rm H}^{(\rm cov)}$ and $f^{(\rm cov)}$ at 0.

During the flaring phase, we observed significant variations in the fitting results. Notably, the parameter representing the normalization of the entire disk exhibited abrupt changes. Given that it is unlikely to change suddenly over a short measurement interval of approximately 4 hours, we restricted to a long-term variation only, which was derived by fitted the data using a single exponential function of time, as indicated by the red symbols in Figure 6.7 (b). The shot-term variation was then primarily attributed to changes in the covering fraction.

When we attempted to extrapolate the normalization trend back to the late dip phase, we obtained an acceptable fit. However, this extrapolation method did not work effectively for the early dip phase. This discrepancy arises from the distinct spectral shapes as illustrated in the spectra of the snapshots 34 and 46 (Figure 6.5). In the late dip phase, we observe both blackbody emissions from the partially covered and uncovered parts of the disk. In contrast, during the early dip phase, we only observe the uncovered component. This situation leaves us with two potential scenarios; (1) a large, presumably fully opaque, partially covering column or (2) a small covering column with

a small disk normalization. In the scenario (2), we would expect significant variations in the disk blackbody parameters ($T_{\rm in}$ and normalization) of the disk, which only affect the orbital variations in mass accretion rate. We thus opted for the scenario (1) and constrained the partial covering column density to be greater than 10^{24} cm^{-2}. This choice led to a larger error estimate in the early dip phase of Figure 6.7. Unfortunately, the *NICER* data do not provide sufficient information to precisely track the trend of the disk blackbody parameters during the early dip phase.

6.1.4 Line emission

We show the phase-dependent variations in the normalized parameters of the line components fitted with the Gaussian model in Figure 6.8. H-like and He-like ions are distinguished by different colors and are separately represented for Mg, Si, S, and Fe. For Mg, Si, and S, emission lines were detected in almost all the snapshots. Especially during the dip phase, emission lines were found for both H-like and He-like ions, and the normalization decreased as the phase progressed.

For Fe, we obtained more stringent constraints, revealing transitions between emission and absorption. Lines appear as emissions in the early dip phase, but the normalization of these lines decreased. Subsequently, the lines changed from emission to absorption, and the absorption continued until the flaring phase. The absorption reverted back to emission in the stable phase.

To determine the ionization parameter, we used the emission or absorption line features fitted with Gaussians and calculated the intensity ratios for each element when both Lyα and Heα lines are detected. These intensity ratios provide valuable information for characterizing the ionization state of the material emitting or absorbing these lines. Emission line pairs were observed during the dip phase for Mg and consistently throughout the orbit for Fe, whereas absorption line pairs were detected from the late dip phase to the flaring phase for Fe.

To estimate the expected line ratios for this pair, we employed the `XSTAR` code (§ 5.4.1.1). As `XSTAR` is designed for one-dimensional geometry, we approximated the photoionized plasma as a plane parallel slab. This slab is assumed to be static, uniform, and optically thin with respect to the electron scattering. It is assumed to have a hydrogen density of $n_{\rm H} = 3 \times 10^{14}$ cm^{-3} and a column density of $N_{\rm H} = 1 \times 10^{18}$ cm^{-2}. As the incident flux for the photoionization, we utilized the representative parameters of the unabsorbed disk blackbody component obtained from the spectral model fitting (S 6.1.3). The flux provides a baseline for the incident radiation.

The Fe emission lines of H-like Lyα and He-like Heα primarily originate from recombination cascades of Fe^{26+} and Fe^{25+}. The Lyα to Heα ratio is highly sensitive to the ionization parameter ξ defined as $\xi = L/(n_{\rm e} r^2)$ (§ 5.3.2). Here, r is the distance from the incident source to the slab. We accounted for the effect of radiative excitation induced by the incident emission. This effect can modify the line strengths when a substantial fraction of the incident emission lies outside the beam (Kinkhabwala et al., 2002), as is the case during the dip phase. To estimate the expected line ratio, we calculated it as a function of $\log \xi$ (in erg s^{-1} cm) with an increment of 0.1, ranging from 0 to 5. Subsequently, we selected the ξ values that are most consistent with the observed line ratio.

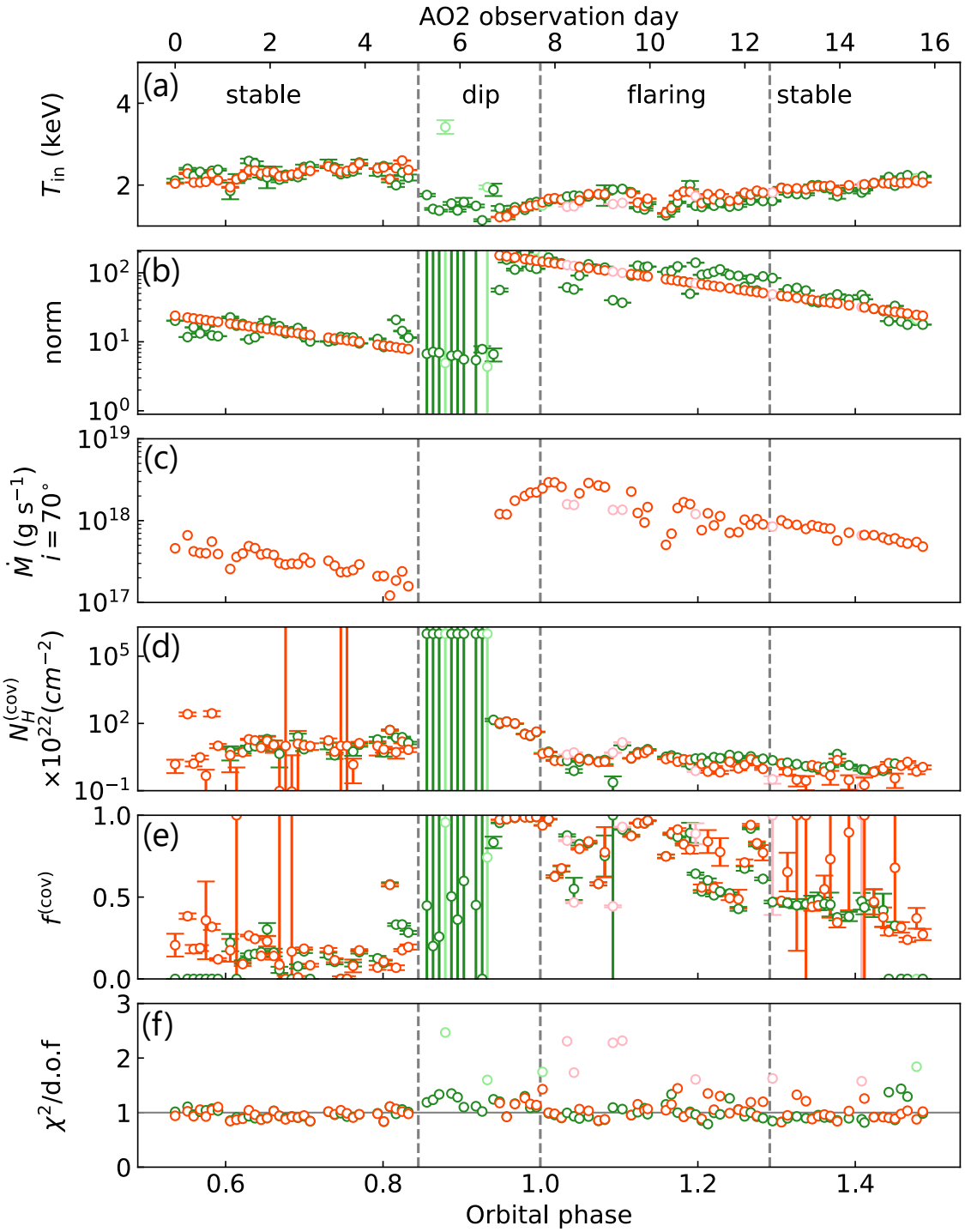

Figure 6.7: Phase-dependent changes in the best-fit parameters of the continuum model (revised version of Tominaga et al. 2023). (a) $T_{\rm in}$ (innermost disk temperature) and (b) normalization for the disk blackbody emission. (c) $\dot{M}$ (mass accretion rate) is calculated from the description $R_{\rm in}^3 T_{\rm in}^4 = GM_1\dot{M}/8\pi\sigma$, assuming the normalization (b) is $(R_{\rm in}/D_{10\ \rm kpc})^2\cos\theta$. (d) $N_{\rm H}^{(\rm cov)}$ (H-equivalent column density for partial coverage) and (e) $f^{(\rm cov)}$ (coverage factor) for partially covering material. (f) Decreased values of χ^2 due to the fitting are also depicted. Green symbols indicate results with unfrozen normalized parameter values, whereas red symbols represent cases with normalized parameter values fixed along the global trend, except for the early dip period. Light-colored symbols are used where χ^2 decreased by more than 1.5.

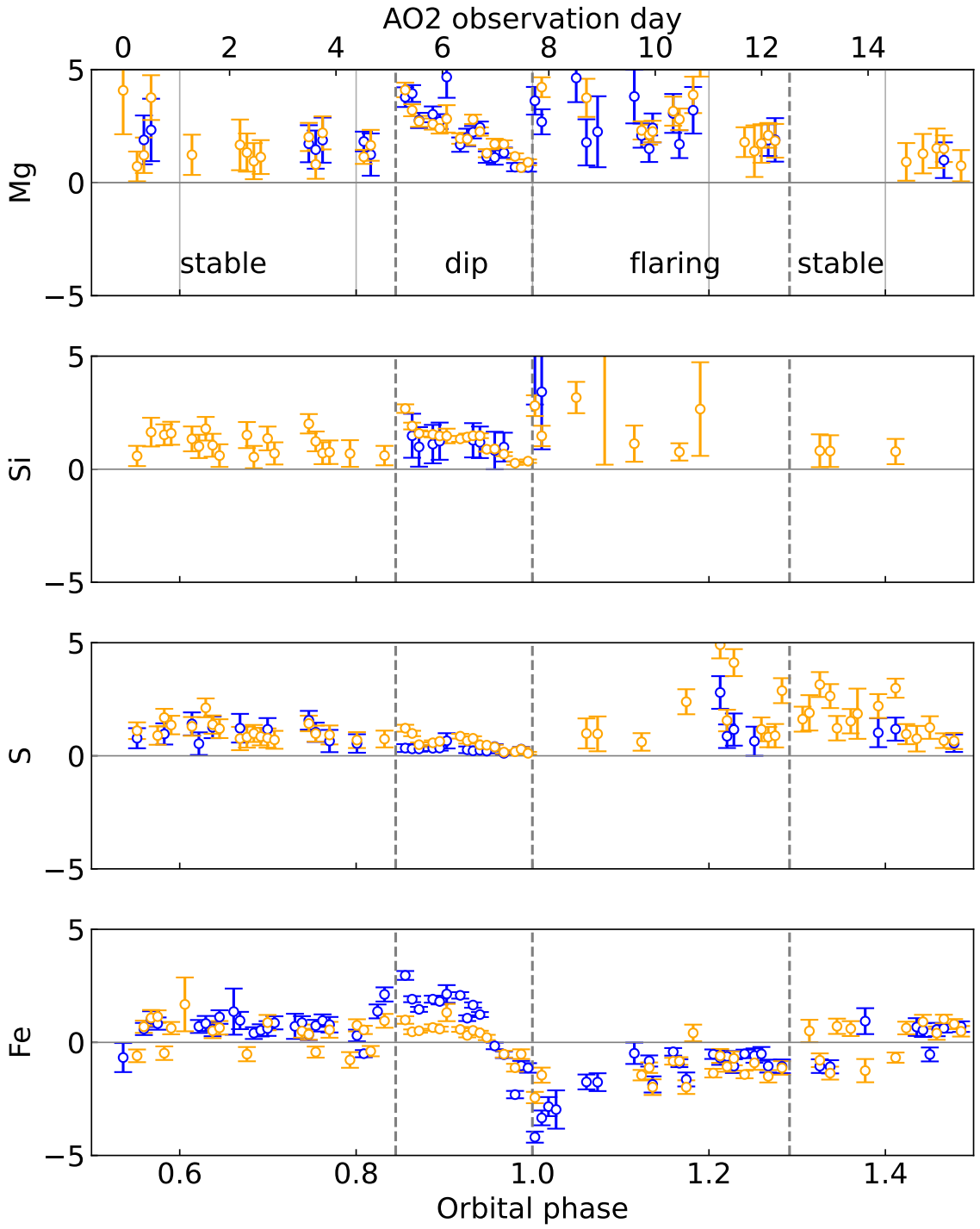

Figure 6.8: Normalization ($\times 10^{-3}$ s^{-1} cm^{-2}) for He-like (blue) and H-like (orange) ions using Heα and Lyα lines for Mg, Si, S and Fe. Snapshots where the reduced χ^2 is greater than 1.5 or the line normalization is consistent with zero were omitted (Tominaga et al., 2023).

For the Lyα and Heα absorption lines, we applied a similar procedure to estimate the column densities of Fe^{25+} and Fe^{24+} within the absorbing slab. This slab intercepts the incident light at each transition energy, resulting in the observed absorption lines. These column densities can be related to the equivalent widths observed in the spectra through the use of the curve of growth (§ 5.2.3.3).

The results are shown in Figure 6.9. The calculated ξ values using emission pairs of Mg, Si, S, Fe, and absorption pairs of Fe display mean values and standard deviations of approximately 1.9 ± 0.02, 2.1 ± 0.04, 2.5 ± 0.02, 3.4 ± 0.04, and 3.7 ± 0.08, respectively. These findings indicate that the actual photoionized plasmas exhibit a stratified ionization structure with varying ξ. However, these variations appear to be relatively stable across different orbital phases. This stability suggests that the photoionized plasma undergoes minimal changes throughout the orbital period. The ξ values derived from Fe emission and absorption features align well, and any differences are likely attributable to variations in the viewing geometry and the incident X-ray flux, rather than intrinsic changes in the photoionized plasma itself.

It is important to note that during the dip phase, the Fe line pair makes a transition from emission to absorption around $\phi \sim 0.95$. Since the emission from the photoionized plasma is considered to be stable over an orbit, this transition is likely caused by an increase in the fraction of incident emission that passes through the photoionized plasma and contributes to the absorption lines. This increase can be caused by the increase of the normalization of disk blackbody emission and/or by the decrease of the line of sight partial coverage.

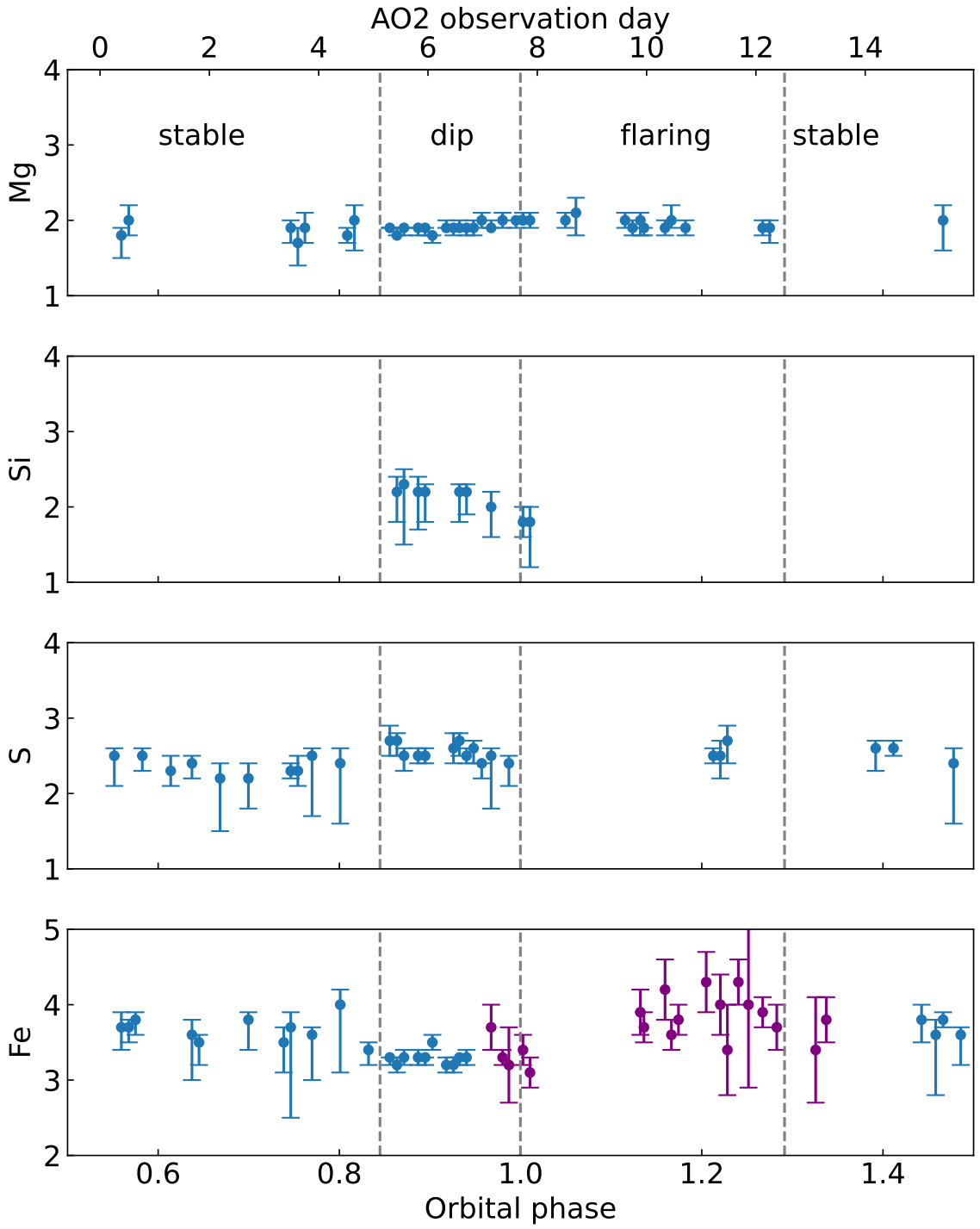

Figure 6.9: Best-fit ionization parameters (ξ) determined by comparing the observed line ratios of Lyα and Heα with the simulated line ratios. Blue symbols represent values obtained using emission line pairs, while purple symbols represent values obtained using absorption line pairs.

6.2 Low Flux State with *Suzaku*

The observed spectra by *Suzaku* in the low flux state (§ 4.4.3) are shown in Figure 6.10. The continuum spectrum was modeled in the same manner with *NICER* as described in § 6.1.3, except for the soft excess component. The best-fit parameters are shown in Table 6.1. Emission lines detected in XIS0 were fitted using Gaussian functions as denoted in Table 6.2.

TABLE 6.1: Best-fit spectral parameters for continuum components observed by *Suzaku* with 90% confidence.

XIS	$f^{(\mathrm{cov})}$	$N_{\mathrm{H}}^{(\mathrm{cov})} \times 10^{22}$ (cm^{-2})	T_{in} (keV)	norm
0	$0.70\ ^{+0.05}_{-0.05}$	$16.8\ ^{+3.1}_{-3.0}$	$1.41\ ^{+0.08}_{-0.08}$	$0.42\ ^{+0.20}_{-0.13}$
1	$0.61\ ^{+0.08}_{-0.09}$	$14.5\ ^{+3.7}_{-3.5}$	$1.43\ ^{+0.12}_{-0.11}$	$0.36\ ^{+0.22}_{-0.13}$
3	$0.70\ ^{+0.05}_{-0.06}$	$19.6\ ^{+4.0}_{-3.7}$	$1.40\ ^{+0.09}_{-0.08}$	$0.44\ ^{+0.22}_{-0.14}$

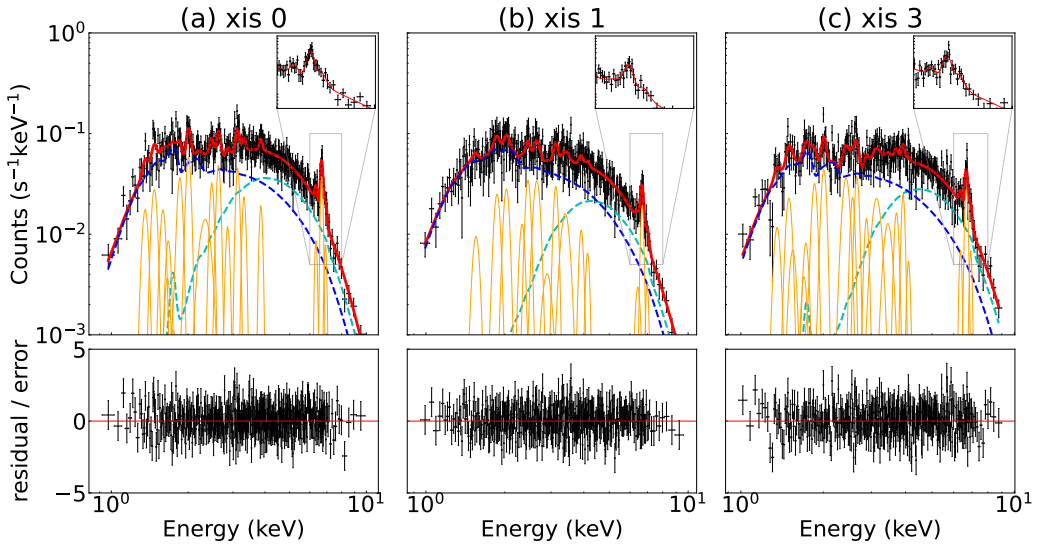

Figure 6.10: Spectra observed with *Suzaku* (a) XIS0, (b) XIS1, and (c) XIS3. Colors are used in the same manners as in Figure 6.4

TABLE 6.2: Best-fit spectral parameters for line components observed with *Suzaku* XIS 0.

Ion, transition	Energy [keV][a]	Centroid [keV]	Width [σ keV]	Flux [$\times 10^{-5}$photon s^{-1} cm^{-2}]
Mg XI He-like triplet	1.343	1.4 $\pm$ 0.72	0 (fixed)	4.5 $\pm$ 2.1
Mg XII H-like Lyα	1.473	1.5 $\pm$ 0.37	$7.0\times10^{-4} \pm 6.4\times10^{-1}$	4.9 $\pm$ 4.0
Si XIV H-like Lyα	2.006	2.0 $\pm$ 0.067	0.0 $\pm$ 1.3×10^{-1}	7.7 $\pm$ 1.6
Si XIV H-like Lyβ	2.376	2.3 $\pm$ 0.11	$9.15\times10^{-2} \pm 1.1\times10^{-1}$	4.9$\pm$ 5.8
S XV He-like triplet	2.460	2.5 $\pm$ 0.25	$6.0\times10^{-7} \pm 9.0\times10^{-1}$	4.4 $\pm$ 2.9
S XVI H-like Lyα	2.621	2.6 $\pm$ 0.16	$2.8\times10^{-7} \pm 3.6\times10^{-1}$	5.8$\pm$ 1.2
S XV He-like	2.876	2.8 $\pm$ 0.034	0 (fixed)	3.1 $\pm$ 1.1×10^{-1}
Fe XXV He-like triplet	6.697	6.7 $\pm$ 0.076	$8.6\times10^{-7} \pm 2.8\times10^{-1}$	4.8 $\pm$ 5.1×10^{-1}
Fe XXVI H-like Lyα	6.973	6.9 $\pm$ 0.17	0.0 $\pm$ 2.2×10^{-1}	1.1 $\pm$ 4.9×10^{-1}

[a] Theoretical energy.

6.3 High Flux State with *Chandra*

This section pertains to data obtained in the high flux state using *Chandra* HETG, where the prominent feature of the P Cygni profile was observed. In particular, as discussed in Schulz and Brandt (2002), conspicuous P Cygni profiles were detected in ObsID 1700. Spectra around the H-like Lyα lines for four different elements are depicted in Figure 6.11. In the case of Fe, the P Cygni profile was observed in the He-like line too. A fluorescence line at 6.4 keV was also identified. In order to characterize the lines, the energy ranges including each line are fitted with the phenomenological power law spectral model in `xspec`. For the remaining residuals, the emission was modeled with a positive Gaussian model, while the absorption was accounted for using a negative Gaussian model. With the energy resolution of the current data set, we could only employ Gaussian models. Nonetheless, the successful fitting with a Gaussian model, as opposed to, for instance, a trapezoidal model, enables us to make certain predictions regarding the distribution of the velocity field. The results of these fits are summarized in Table 6.3.

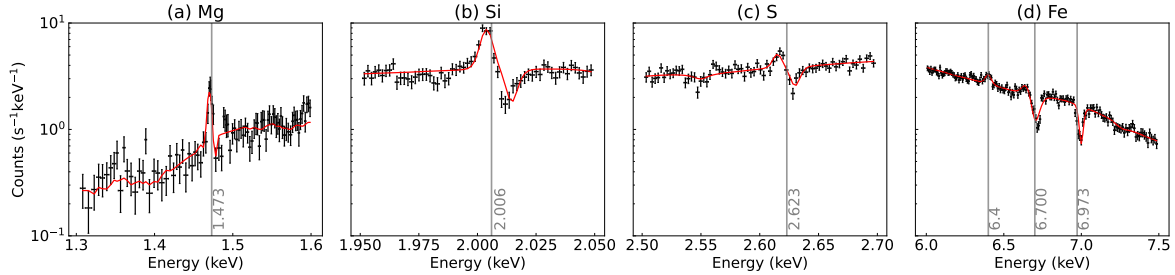

Figure 6.11: P Cygni profiles of (a) Mg, (b) Si, and (c) S H-like Lyα and (d) Fe H-like Lyα and He-like Heα lines. Grey vertical lines show the rest energy of each line. The features of each line are shown in Table 6.3. We used MEG dataset for the left three panels (a,b,c) and HEG for Fe in the remaining panel (d).

TABLE 6.3: Characterization of major P Cygni lines using *Chandra* observation (ObsID 1700).

Ion, transition	Energy[b] (keV)	Emisison [keV] Absorption [keV]	velocity [km s^{-1}][a]	Sigma [keV]	photons [cm^{-2} s^{-1}] Line depth [keV]
Fe XXVI Lyα	6.973	$6.93 \pm 4.22\times10^{-2}$	1.99×10^{3}	$0.161\pm3.67\times10^{-2}$	$7.83\times10^{-3}\pm1.40\times10^{-3}$
		$6.99\pm7.46\times10^{-3}$	-9.03×10^{2}	$1.11\times10^{-2}\pm3.12\times10^{-3}$	$6.55\times10^{-2}\pm1.51\times10^{-2}$
Fe XXV Heα	6.700	$6.68\pm2.25\times10^{-2}$	9.40×10^{2}	$2.35\times10^{-2}\pm3.45\times10^{-3}$	$6.08\times10^{-3}\pm1.05\times10^{-3}$
		$6.72\pm6.58\times10^{-3}$	1.79×10^{2}	$1.35\times10^{-2}\pm2.46\times10^{-3}$	$4.48\times10^{-2}\pm4.66\times10^{-3}$
S XVI Lyα	2.623	$2.62\pm6.27\times10^{-3}$	9.14×10^{2}	$1.31\times10^{-3}\pm2.58\times10^{-3}$	$5.987\times10^{-4} \pm 1.34\times10^{-4}$
		$2.63\pm5.37\times10^{-3}$	-8.00×10^{2}	$2.48\times10^{-}\pm1.57\times10^{-3}$	$6.12\times10^{-3}\pm1.19\times10^{-3}$
Si XIV Lyα	2.006	$2.00\pm1.33\times10^{-3}$	2.99×10^{2}	$1.33\times10^{-3}\pm4.10\times10^{-4}$	$8.90\times10^{-4}\pm6.95\times10^{-5}$
		$2.02\pm3.86\times10^{-3}$	-1.35×10^{3}	$1.52\times10^{-3}\pm7.78\times10^{-4}$	$6.40\times10^{-3}\pm2.08\times10^{-3}$
Mg XII Lyα	1.473	$1.47\pm3.49\times10^{-3}$	6.11×10^{2}	$3.14\times10^{-3}\pm4.94\times10^{-4}$	$1.63\times10^{-4}\pm1.57\times10^{-5}$
		$1.47\pm6.83\times10^{-3}$	4.07×10^{2}	0.01 (fixed)	$9.18\times10^{-3}\pm5.88\times10^{-3}$

[a] Calculated from the best-fit of the line center.
[b] Theoretical energy.

Chapter 7

Discussion

Contents

7.1 Proposed Geometry 143
7.1.1 Schematic view 143
7.1.2 Rationale 143
7.1.3 System scales 144
7.2 Radiative Transfer Modeling 147
7.2.1 Changes between line emission and absorption 147
7.2.2 P Cygni line profile 154
7.2.3 X-ray light curve changes over an orbit 161
7.3 Implications 167
7.3.1 Mass of the companion star 167
7.3.2 Inclination angle 169
7.3.3 Location of the photoionized plasma 173

The observation data were characterized in § 6. We now move on to radiative transfer modeling based on the physics and tools described in § 5.

For the modeling, we need to establish the geometry, which will be presented in § 7.1 based on our high-cadence and whole-orbit X-ray spectroscopic observations with *NICER*. We propose a schematic view of the system (§ 7.1.1), which is different from conventional views of the photoionized plasma of accreting compact objects. We list the rationale for the proposal (§ 7.1.2) and derive their system scales (§ 7.1.3).

Next, we choose three most distinctive features of the X-ray spectra of Cir X-1 and interpret them based on radiative transfer modeling (§ 7.2): (1) Change of Fe lines between absorption and emission found in the *NICER* and *Suzaku* observations, (2) P Cygni profie in the *Chandra* observations, and (3) Rapid X-ray flux changes over an orbit in the *NICER* observations. We will show that the radiative transfer calculation based on the proposed picture above explains these distinctive features well. We will also show strengths and limitations of the current radiative transfer codes.

Finally, in § 7.3, we discuss three of the most important unsettled parameters of Cir X-1 based on our new results and references to theoretical work. In § 7.3.1, we argue for the LMXB nature of the source as opposed to HMXB. In § 7.3.2, we make a case for the edge-on view as opposed to the face-on view. In § 7.3.3, we argue that the photoionized plasma exists radially outward of the accretion disk as opposed to the surface of the accretion disk.

7.1 Proposed Geometry

7.1.1 Schematic view

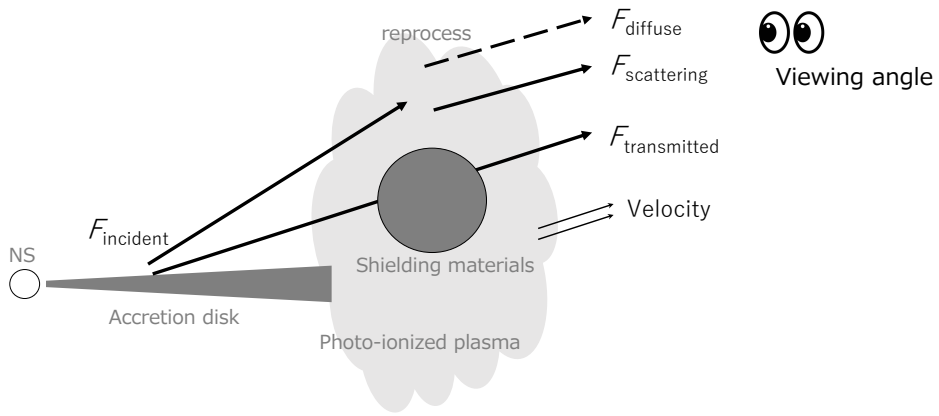

Figure 7.1: Schematic view of physical parameters related to Cir X-1.

We start with the geometry that we propose in Figure 7.1. An accretion disk is formed around the neutron star. The shielding material is located close to the edge of the accretion disk. The photoionized plasma is outside of the blocking material, which has a certain height, and is illuminated by the X-rays from the neutron star and inner part of the accretion disk. The system is observed close to the edge-on.

As for shielding materials, we postulate the presence of a local, geometrically-flared, and optically-thick structure outside the accretion disk, which is sometimes referred to as a "bulge" in the literature and partial covering materials. Bulge has been suggested observationally and theoretically (e.g., Groot, Rutten, and Paradijis, 2001; Hynes et al., 2001; Hellier, 1996; Casares et al., 2003).

We label the flux from the neutron star's surface and the surrounding accretion disk as $F_{\rm incident}$. The incident flux is transmitted through the photoionized plasma with $F_{\rm transmitted}$. The diffuse emission emanates from the photoionized plasma either by scattering the incident flux ($F_{\rm scattering}$) or radiative recombination and de-excitation as well as free-free emission from the plasma ($F_{\rm diffuse}$). The flux in the line of sight changes as the system rotates. The photoionized plasma may have an outward velocity v.

This picture differs from previous work in several points. The first is the position of the photoionized plasma. In the conventional view, the accretion disk corona is typically assumed to be present on the surface of the accretion disk (e.g., Jimenez-Garate, Raymond, and Liedahl, 2002). In our proposed geometry, the plasma is outside the accretion disk. Another difference is that the viewing angle should be close to edge-on (§ 3.2.4).

7.1.2 Rationale

There are five key findings that support our proposed model. The first is the persistence of disk blackbody emission. Throughout the entire orbital period, we consistently observed disk blackbody emission. Importantly, the parameters characterizing this emission change only gradually over the orbital time scale. The variations in apparent flux are primarily attributed to the presence of the covering matter located radially outside

of the disk blackbody emission region, which undergoes changes within the time scale of an orbit.

The second finding is the dip and flaring phases in mid flux state. These phases suggest the presence of a local covering matter with varying density and a covering fraction that depends on the azimuthal angle of the disk. This arrangement results in changes in the line of sight as a function of the orbital phase. The dip in X-ray flux commences when the densest part of the covering medium comes into the line of sight. Subsequently, the total covering column gradually decreases, leading to spectral changes between the early and late dip phase (Figure 6.5). As this dense material disperses in the tail, it transforms into partial covering materials, causing an abrupt flux change during the flaring phase (Figure 6.6).

The third significant result is the appearance of Fe lines as either emission or absorption features (Figure 6.8). These features are generated by highly ionized Fe in the photoionized plasma. When they appear as absorption lines, the incident disk blackbody emission transmitted through the photoionized plasma surpasses the diffuse emission from the plasma. In contrast, when they appear as emission lines, the transmitted emission is not significant because it is blocked in the line-of-sight direction, and the dominant contribution comes from the diffuse emission emitted by the plasma.

The fourth result is the stability of the emission line intensities relative to the total flux. Despite a significant decrease in total flux by an order of magnitude during the dip phase (Figure 6.1), the emission lines do not exhibit a corresponding reduction (Figure 6.8). This suggests that a substantial portion of the photoionized plasma is not obstructed by the blocking material, unlike the blackbody emission from the disk.

The fifth result is the relatively constant ionization degree (ξ) of the photoionized plasma through the orbit. The ξ value was obtained using the Lyα and Heα pairs of Mg, Si, S, and Fe. In Fe, the ξ value was obtained either using emission or absorption features. The constant ξ indicates that the incident emission seen by the photoionized plasma does not change through the orbit (Figure 6.9).

In summary, the proposed model, as illustrated in Figure 7.2, provides a coherent explanation for these findings for the observed features with *NICER* in the mid flux state. Panels (a), (b), and (c) represent the edge-on view for the early dip, late dip + flashing, and stable phase, respectively. We do not know whether the same geometry holds for the low and high flux states. We hypothesize that it does and apply our model to explain the observed features in these flux states in § 7.2.

7.1.3 System scales

Based on the proposed geometry, we constrain the system scale for the radiative transfer simulation setup. The system scale can be estimated by assuming the electron density $n_{\rm e}$. Since the *NICER* data do not provide a constraint on this value, an upper limit estimate from grating spectroscopy of the triplet lines of He-like ions (10^{15} cm^{-3}) was utilized (Schulz et al., 2008; Schulz et al., 2020). The estimated size of the photoionized plasma is calculated as $r_{\rm in} = \sqrt{L_{\rm X}/(\xi n_{\rm e})} \sim 10^{10}$ cm for the best-fit $\log \xi$ parameter for Fe emission and the observed disk luminosity of $L_{\rm X}$. It is important to note that this value of $r_{\rm in}$ serves as a lower limit because we employed the upper limit for $n_{\rm e}$.

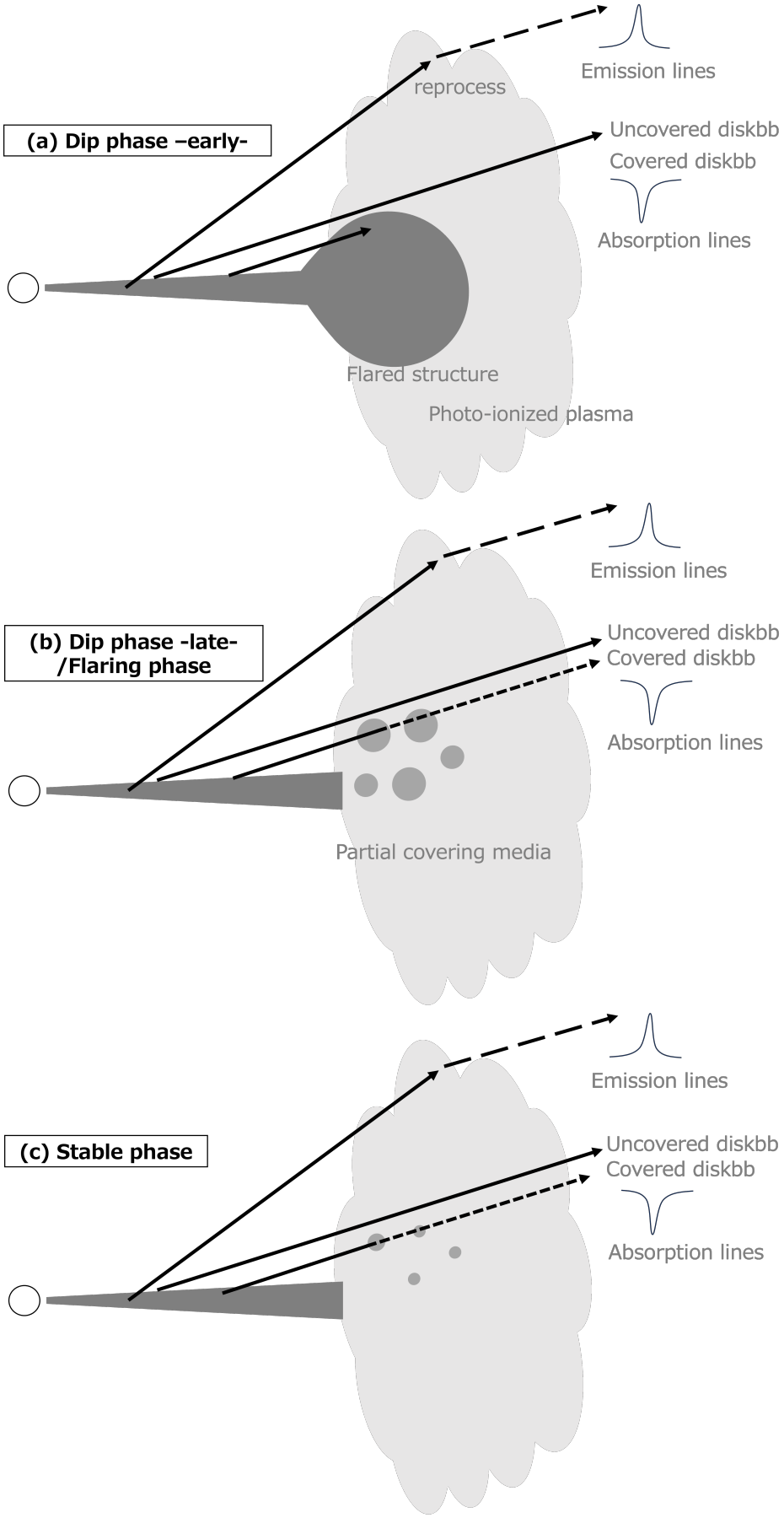

Figure 7.2: Proposed geometry of the system in the edge-on view during the (a) early dip, (b) late dip/flaring, and (c) stable phases, respectively. The flared structure (local blocking medium) has spatial structures depending on the disk azimuth.

The outer radius ($r_{\rm out}$) can be constrained on the basis of the maximum total amount of observed Fe absorption columns by

$$N_{{\rm Fe}i+} \sim f_{{\rm Fe}i+} A_{\rm Fe} n_{\rm H} (r_{\rm out} - r_{\rm in}), \tag{7.1}$$

where $N_{{\rm Fe}i+}$ represents the observed absorption column of Fe^{i+} ions ($i \in \{24, 25\}$), $f_{{\rm Fe}i+}$ is the fraction of Fe with the charge i among all Fe atoms, $A_{\rm Fe}$ is the solar abundance of Fe relative to H, and $n_{\rm H}$ is the hydrogen density, which is approximated as $n_{\rm e}$. The Fe columns were derived from the observed equivalent widths using the curve of growth analysis. The charge fractions and the curve of growth were obtained from simulation, in which the slab's column density $\log N_{\rm H}$ cm^{-2} was varied incrementally from 15 to 25 for a given ionization parameter $\log \xi = 3.5$ erg s^{-1} cm. We used snapshots 50 and 65, where Fe absorption was strong (Figure 6.5 b and c) as representative values. As a result, the value $r_{\rm out} - r_{\rm in}$ is between 10^9 and 10^{10} cm both for H-like ion ($i = 25$) and He-like ion ($i = 24$). The photoionized plasma should have structures for different values of ξ for each element. The part that contributes to the Fe features is relatively thin with $r_{\rm out}/r_{\rm in} = 1.1 - 2$.

With this configuration, strong emission lines can still be obtained from the plasma. In `XSTAR` calculations, Fe XXV Heα is 6–120 $\times 10^{36}$ erg s^{-1} for $N_{\rm H} = 10^{24-25}$ cm^{-2}, which is much larger than the observed value of 1.7×10^{35} erg s^{-1}. This indicates that the volume filling factor of the photoionized plasma is likely smaller compared to the assumption of a spherical medium or that the plasma density is significantly smaller than what is assumed (10^{15} cm^{-3}).

Furthermore, the comparison between the inner and outer radii of the photoionized plasma ($r_{\rm in}$ and $r_{\rm out}$) and the radius of the accretion disk ($R_{\rm in}$ and $R_{\rm out}$) reveals interesting insights. In spectral analysis, the normalized blackbody emission of the accretion disk is related to $(R_{\rm in}/0.94)^2 \cos\theta$. For a perfect edge-on orientation ($\theta = 0$) and a normalized value of $\sim$100 (the maximum of the trend in Figure 6.7 b when most of the disk is exposed), we obtain $R_{\rm in} \sim 10^6$ cm. This $R_{\rm in}$ is close to the typical value of the neutron star radius, since the accretion disk is considered to extend inward almost to the neutron star surface (e.g., J. Frank, A. King, and Raine, 2002). We cannot constrain $R_{\rm out}$ from the present data. However, it must be smaller than the binary's effective Roche lobe radius, which is approximately 10^{10} cm (Eggleton, 1983). Assuming that the typical value for low-mass X-ray binary stars, $R_{\rm out} \sim 10^{9-10}$ cm (Jimenez-Garate, Raymond, and Liedahl, 2002), which is applicable to Cir X-1, we have $r_{\rm in} \gtrsim R_{\rm out}$, suggesting that the photoionized plasma is located radially outside the accretion disk.

7.2 Radiative Transfer Modeling

7.2.1 Changes between line emission and absorption

7.2.1.1 Purpose

One of the most remarkable features discovered in the *NICER* AO2 observations is the change of spectral lines from emission to absorption and vice versa over an orbit (Figure 6.8). This is most evident for the Fe XXV Heα and Fe XXVI Lyα lines. As reviewed in § 5.2.3, the difference of emission or absorption is explained whether the incident source intensity I_ν in the line of sight is smaller or larger than the source function S_ν of the photoionized plasma. This suggests a change in the relative strength of the reprocessed emission and the transmitted emission through the photoionized plasma in Figure 7.2. The absolute strength also matters so that we can also explain the observed continuum flux.

We need at least two parameters. We parameterize with α and β as shown in Figure 7.3; $\alpha = 0 - 1$ is multiplied to the reprocessed emission and represents the fractional strength of its maximum. The maximum is obtained when the photoionized plasma subtends the entire 4π str with a given column density around the incident source. This value is a response to the incident flux and is independent from the incident flux for the zero'th order approximation. $\beta = 0 - 1$ is multiplied to the incident emission and represents the fractional strength of its maximum. We assume that the strength decreases by being partially blocked by thick material in the line of sight.

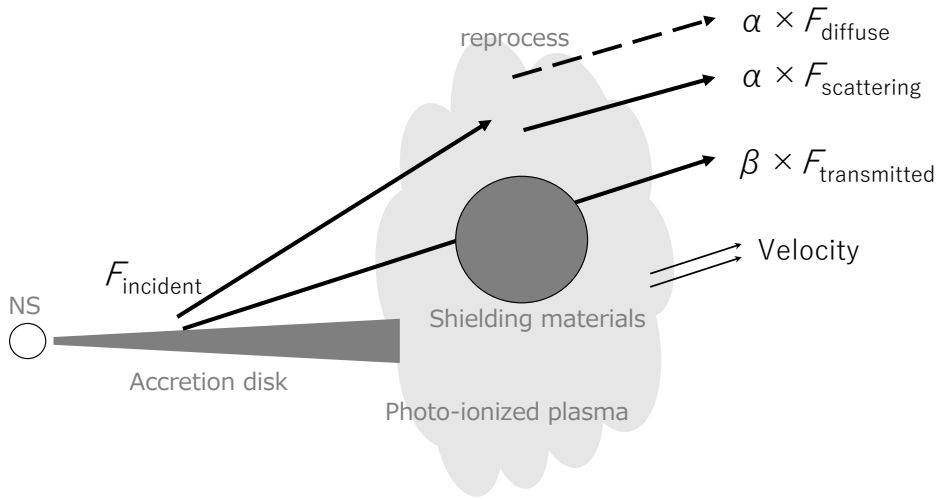

Figure 7.3: Schematic view of the model parameters α and β added to Figure 7.1.

We used three data sets. Two sets are taken from the *NICER* AO2 observation during the mid flux state in the dip phase (snapshot=39) and the flaring phase (snapshot=66), in which the Fe features were observed in emission and absorption, respectively. In addition, we used the *Suzaku* data in the low flux state, in which the X-ray spectrum was dominated by the emission lines including Fe (§ 6.2). The spectrometers onboard the *NICER* and *Suzaku* (XTI and XIS, respectively) have a similar spectral resolution, so they are easy to compare. The observed equivalent width is shown in Figure 7.4. The purpose of the simulation is to investigate how these changes are made by the change of

α and β. As the equivalent width changes among *NICER* dip and flaring and *Suzaku* are similar between Fe XXVI Lyα and Fe XXV Heα, we focus on the latter for simplicity.

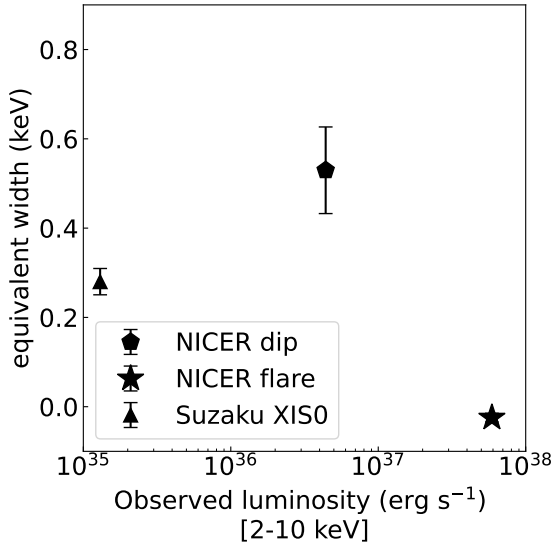

Figure 7.4: Equivalent widths and observed integrated flux obtained from *Suzaku* observations in the low-flux state and *NICER* observations in the mid-flux state during the dip (ObsID=39) and flaring (ObsID=66) phases.

7.2.1.2 Setup

Incident source: We used the spherically symmetric geometry as shown in Figure 5.15. At the center, the incident source is placed with an X-ray luminosity of 1×10^{38} erg s^{-1} and the spectral energy distribution described by the disk blackbody emission of the innermost temperature of 2 keV. The ionization parameter was fixed at $\log\xi = 3.5$, which best explains the observed Fe features with *NICER* (§ 6.1.4).

Photoionized plasma: Photoionized plasma surrounds the incident source. The plasma is assumed to have a density of $n_{\rm H} = 1\times10^{15}$ cm^{-3} and a varying column density of $N_{\rm H} = 1\times10^{22}, 1\times10^{23}, 1\times10^{24}$ cm^{-2}. From ξ, $n_{\rm H}$, and $N_{\rm H}$, the inner and outer radius of the photoionized plasma ($r_{\rm in}$ and $r_{\rm out}$) are uniquely determined.

Solvers: We used two solvers for numerical simulation. The two-stream solver (`XSTAR`; § 5.4.1) was used with the covering fraction of 0 to fully incorporate the radiative excitation of lines.

The Monte Carlo solver (`MONACO`; § 5.4.2) was used based on the radial distribution of the change population and electron temperature calculated by `XSTAR`. To increase the efficiency of the Monte Carlo simulation, we limited the energy band of the incident source to 6–9 keV. The electron temperature calculated by `XSTAR` is $\mathcal{O}(10^5)$ K. The inverse-Compton scattering of photons with lower energies into the band of interest is negligible. Note that the current version of `MONACO` is incapable of calculating the inverse Compton scattering if it is not. Furthermore, we used a flat input spectrum, and the output spectrum was corrected for the 2 keV disk blackbody input spectrum. Note that

the correction needs to be done based on the incident photon energy, not on the output photon energy. This alleviates the weakness of the Monte Carlo solver, in which the dynamic range of the calculation is small compared to other solvers. Note that the weighted input spectrum is implemented in `SKIRT`, but not in `MONACO`, therefore, users must perform the calculation by hand.

Choice of solvers: The reason we chose `MONACO` over `SKIRT` for this simulation is as follows. To achieve the purpose of the simulation, we need to calculate both the reprocessed continuum and line emission in the X-ray band. In `SKIRT`, the former can be achieved with the extension by Vander Meulen et al. (2023), while the latter can be achieved by the extension in this work (§ 5.4.3). However, they cannot be turned on at the same time in the current version.

The reason we used two solvers `XSTAR` and `MONACO` is that the synthesized spectra are often inconsistent among different solvers of numerical radiative transfer stemming from different assumptions (Tsujimoto et al., 2024). The escape probability approach employed in most two-stream solvers including `XSTAR` is speculated to overestimate line intensities (Hubeny et al., 2001; Dumont et al., 2003). `XSTAR` does not calculate electron scattering; it is included only as continuum absorption. On the other hand, the Monte Carlo solvers often ignore emission induced by electrons such as free-free emission. `MONACO` does not fully consider radiative excitation, which is considered important for enhancing the line intensity (Kinkhabwala et al., 2002; Chakraborty et al., 2021) in diffuse emission in the photoionized plasmas. There is no numerical transfer code that incorporates all of them. Line intensity tends to be overestimated by `XSTAR` and underestimated by `MONACO`. We speculate that the reality is somewhere in between.

Components: We need to decompose the synthesized spectra into (i) incident emission transmitted through the photoionized plasma, (ii) diffuse emission from the photoionized plasma, and (iii) scattered emission of the incident emission by the electrons in the photoionized plasma. `XSTAR` and `MONACO` produces each component differently and we decompose them as shown in Table 7.1.

Table 7.1: Spectral decomposition.

Component	`XSTAR`	`MONACO`
Incident	`incident`	Not available
Transmitted	`transmitted`	Events with process = `NoneNoInt`
Diffuse	`emit_outward`	Events with last process other than the two [a]
Scattered	Not available	Events with the last process = `ComptonByFreeElectron`[a]

[a] As the decomposition is based on the last process before escaping from the system, it is not perfect. A single emitted photon experiences multiple interactions (resonance scattering, electron scattering, etc.).

7.2.1.3 Results

Synthesized spectra: The output spectra are shown in Figure 7.5. The solid lines represent components obtained with `MONACO`, while the dotted lines with `XSTAR`. For `MONACO`,

the transmitted, scattered, and diffuse emission components are shown. For `XSTAR`, the incident, transmitted, and diffuse emission components are shown (Table 7.1). The output of `MONACO` and `XSTAR` is normalized using the transmitted component, which is the only component available in both with dominant continuum emission. The spectrum expanded around the Fe XXVI Lyα and Fe XXV Heα lines is shown in Figures 7.6 and 7.7, respectively.

Comparison with varying $N_{\rm H}$: The scattered component, which is a distinctive advantage of the `MONACO` simulation, becomes more prominent as $N_{\rm H}$ increases. The number of photons that escape from the system without any interaction decreases almost irrespective of the photon energy. This is reasonable as the electron scattering opacity increases as $\tau_{\rm es} = N_{\rm H}\sigma_{\rm es}(E)$, where $\sigma_{\rm es}(E)$ is the electron scattering cross section of a weak energy dependence (§ 5.1.2.3). For $N_{\rm H} = 1 \times 10^{24}$ cm^{-2}, $\tau_{\rm es} = 0.66$.

For line emission, as speculated above, `MONACO` tends to underestimate the intensity, while `XSTAR` tends to overestimate it. The discrepancy increases as the density of the column increases.

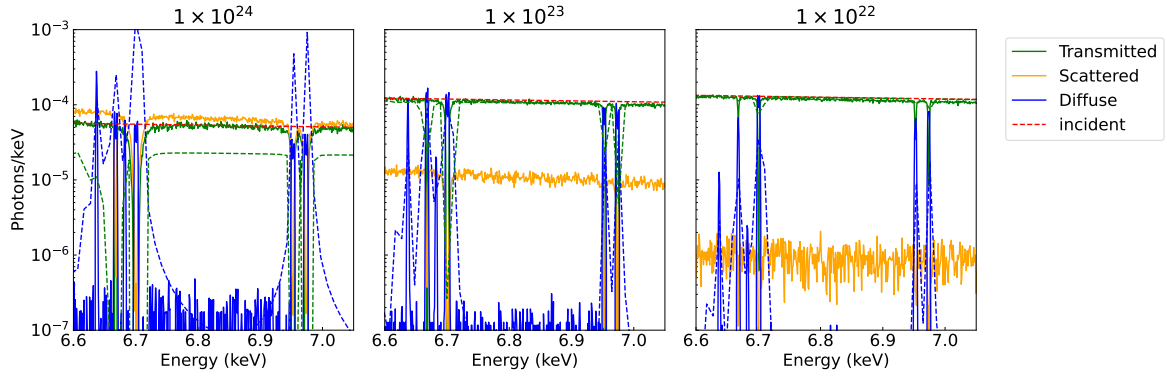

Figure 7.5: Synthesized spectra of `MONACO` (solid) and `XSTAR` (dashed) for the transmitted, scattered, diffuse, and incident emission component. The three panels show different column densities of the photoionized plasma of $N_{\rm H}$ =1×10^{24} (left), 1×10^{23} (middle), 1×10^{22} (right) cm^{-2}. The incident component (red) is only available with `XSTAR`, whereas the scattered component (orange) is only with `MONACO`.

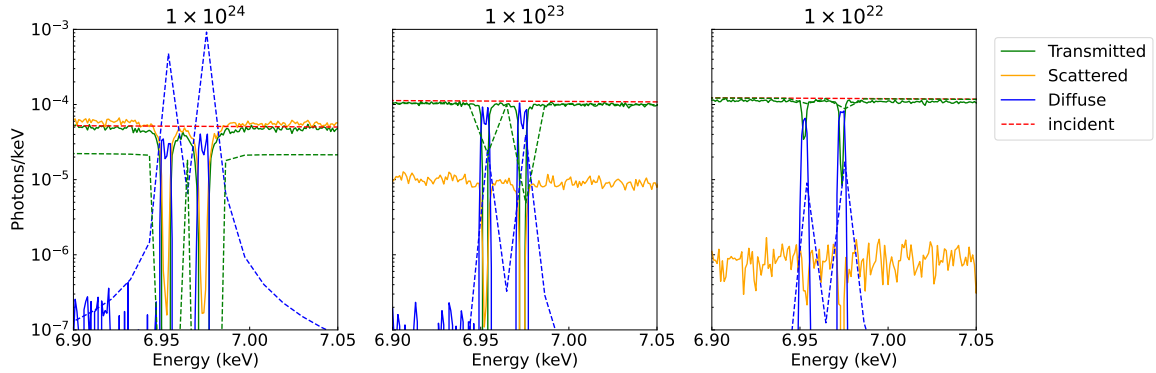

Figure 7.6: Close-up view of Figure 7.5 around the Fe XXVI Lyα.

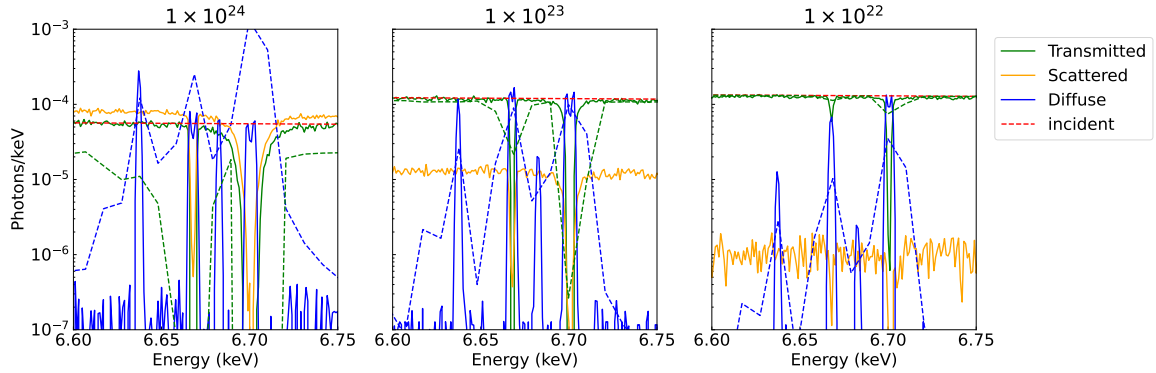

Figure 7.7: Close-up view of Figure 7.5 around the Fe XXV Heα.

Modification with α and β: We now manipulate the decomposed spectra using α and β. From their definition (Figure 7.3), α is multiplied to both diffuse and scattered emission and β to the transmitted emission. The total flux is given as

$$F_{\rm total} = \alpha(F_{\rm diffuse} + F_{\rm scatter}) + \beta F_{\rm transmitted} \tag{7.2}$$

We calculated the equivalent width of the target line and the total flux as a function of (α, β) for `MONACO` (Figure 7.8) and `XSTAR` (Figure 7.9). As the scattered component is not available in `XSTAR`, we replaced it with that of `MONACO`. Here, we calculate the equivalent width as follows. The baseline continuum level was evaluated using the continuum component,

$$F_{\rm cont} = \alpha F_{\rm scatter} + \beta F_{\rm transmitted} \tag{7.3}$$

averaged over the 6.6–6.8 keV range. The line component was assessed as a difference between the total and continuum flux as

$$F_{\rm line} = F_{\rm total} - F_{\rm cont} \tag{7.4}$$

summed over the energy bins around the line. This treatment is needed to derive absorption features having a negative equivalent width; the absorption cannot be decomposed because of its multiplicative nature, unlike other components of additive nature.

The equivalent width is evaluated as smaller in `MONACO` (Figure 7.8) and larger in `XSTAR` (Figure 7.9). The latter matches better with the observed values, so we consider based on the latter hereafter. The observed values in the dip and flaring phase of *NICER* and *Suzaku* are indicated using different symbols on the color bars in Figure 7.9.

Changes of equivalent width and flux with α and β: The equivalent width and flux changes as a function of α and β in a distinctively different manner. For example, a decrease in β yields an increase in the equivalent width and a decrease in the flux. The trend of the change is similar among different $N_{\rm H}$ setup but with different values. Using these differences, we can speculate on the main cause of how the different observed values among the three were realized.

The observed equivalent width and flux are plotted on Figure 7.9 for the three data sets. For $N_{\rm H} = 1 \times 10^{22}$ cm^{-2} (left panel), there is no (α and β) combination to explain the *NICER* dip data. The flux is large, therefore β needs to be large, but this cannot

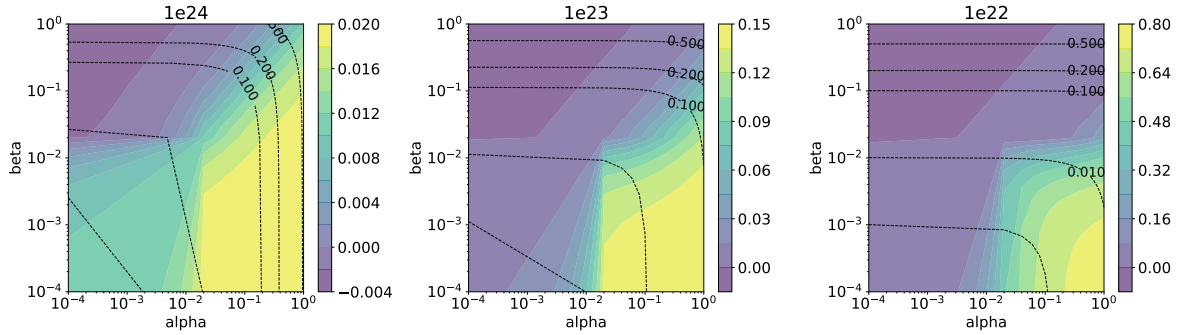

Figure 7.8: Equivalent width in eV (positive for emission, negative for absorption) of the Fe XXV Heα line obtained with `MONACO` for $\log N_{\rm H}$ (cm^{-2}) =24 (left), 23 (middle), and 22 (right). The continuum flux normalized for (α, β)=(1, 1)= 10^{38} erg s^{-1} is represented by the dotted contours.

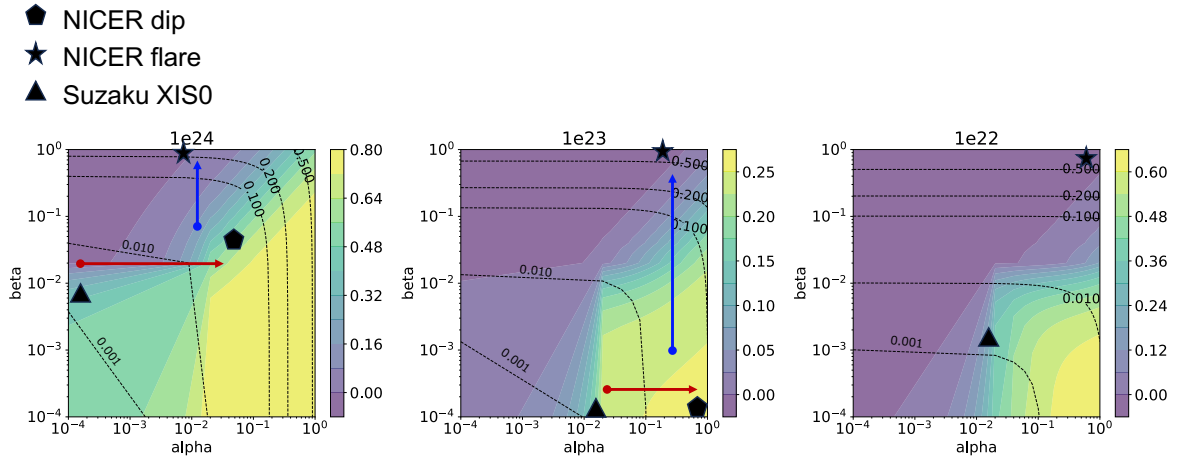

Figure 7.9: Same with Figure 7.8 but using `XSTAR`. The equivalent widths observed in *NICER* (dip phase), *NICER* (flaring phase), and *Suzaku* are indicated by different symbols on the color bars. Red and blue arrows show the major direction of the changes of (α, β) to account for the difference among the three observations.

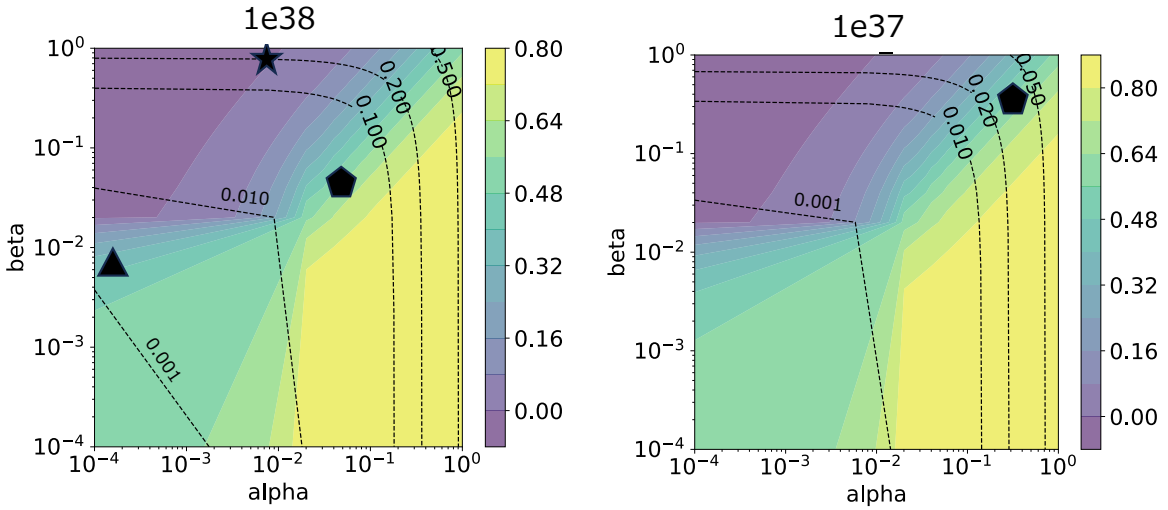

Figure 7.10: Equivalent width in eV (positive for emission, negative for absorption) of the Fe XXV Heα line obtained with `MONACO` for $L_{\rm int} = 10^{38}$ erg s^{-1} (left; the same as the left panel in Figure 7.9) and $L_{\rm int} = 10^{37}$ erg s^{-1} (right). The columns density is fixed as $\log N_{\rm H}$ (cm^{-2}) =24. The continuum flux normalized for 10^{38} erg s^{-1} is represented by the dotted contours. Other symbols follow Figure 7.9.

reproduce the equivalent width, which is also large in the case of $N_{\rm H} = 1 \times 10^{22}$ cm^{-2}. We thus ignore this lowest column density case.

***Suzaku* to *NICER* (dip): a long-term change** Both *Suzaku* and *NICER* (dip) exhibited emission lines, but with different equivalent widths and flux; both the equivalent width and the flux are larger for *NICER* (dip). Such a change can occur in the direction of increasing α as illustrated by the red arrow in the left and middle panels in Figure 7.9. This can be interpreted that α is smaller in the *Suzaku* observation and larger in the *NICER* dip observation. It is conceivable that the α value (the subtended angle by the photoionized plasma) changes over a long time scale in conjunction with the changes of the accretion states. Note that we assume that the incident flux is the same between the two observations.

***NICER* (dip phase) to *NICER* (flaring phase): a short-term change** The equivalent width changed from positive (emission) to negative (absorption) as the *NICER* observation progressed from the dip to the flaring phase over a few days. This is accompanied by an increase in flux. These can be best explained by an increase of β as indicated by the blue arrow in the left and middle panels in Figure 7.9. This can be interpreted that β is smaller in the *NICER* dip observation and larger in the *NICER* dip observation. The β value (the blocked fraction of the incident emission) can change in a short time scale within an orbit if the blocking material is provided by the matter local to the system. Indeed, based on the same concept, we will develop a model to explain rapid changes observed during the flaring phase § 7.2.3. We will argue that the change is mainly made by the change of β under the assumption that the intrinsic flux and the column density are unchanged.

Another interpretation arises if we consider the possibility that the incident flux itself changed between the two phases. This is conceivable given the variation in the mass accretion rate observed during the *NICER* dip and flaring phases (see Figure 6.7 c). For the *NICER* dip phase, we should use the simulation result with an X-ray luminosity of 1×10^{37} erg s^{-1} (Figure 7.10), which is one order smaller than the setting in Figures 7.8 and 7.9. In this case, the changes from *NICER* dip to flare requires changes of both α and β. In any case, we can attribute the changes of the observed values to these two parameters.

7.2.2 P Cygni line profile

7.2.2.1 Purpose

One of the most peculiar characteristics in the X-ray spectra of Cir X-1 is the P Cygni profiles in the highly ionized Mg, Si, S, and Fe lines in the high flux state (§ 3.4.2). This is direct evidence of the presence of the outflow motion. The highly ionized emission lines originating from the photoionized plasma have a P Cygni profile, which indicates that the photoionized plasma has an outflowing velocity. The derived velocity with *Chandra* HETGS is 1940 km s^{-1} (Schulz and Brandt, 2002), which we use in this section.

The P Cygni profile is produced in a 3D space. The incident emission suffers blue-shifted absorption, while the diffuse emission produces red-shifted emission. Due to the 3D nature, it is not possible to simulate using 1D solvers such as `XSTAR`. To begin with, `XSTAR` does not support radiative transfer through the medium that has a bulk motion. The Monte Carlo solver is particularly suited as (i) there is little additional cost to calculate in a 3D space rather than a 1D space, and (ii) the changes due to the bulk motion (i.e., large velocity gradient or Sobolev condition; § 5.2.3.2) can be naturally taken into account without any additional codes.

In the near future, we will be able to reconstruct the velocity profile of the plasma around X-ray binaries and the viewing angle by resolving line profiles using *XRISM* and interpreting them based on the 3D radiative transfer calculation. For now, we make calculations for some simple cases and compare them with the observation by *Chandra* HETGS. The cases include different viewing angles, velocity profiles, and angles subtended by the photoionized plasma.

7.2.2.2 Setup

Geometry: Figure 7.11 shows the geometry of the simulation. This is the same concept with Figure 7.3 but a velocity field is added. The axis-symmetric geometry (no dependence on the azimuthal degree ϕ) is assumed, in which the symmetric axis is perpendicular to the accretion disk. There is a dependence on the elevation angle θ: the photoionized plasma is distributed in the elevation angle $-\theta$ to θ symmetric to the disk at $\theta = 0$. The velocity profile is assumed to be uniform throughout the place in the radially outgoing direction. The elevation angle of the photoionized plasma (θ) is related to α in Figure 7.3 as $\alpha = \sin\frac{\theta}{2}$.

Three cases in Table 7.2 are simulated. The case (a) is the fiducial case, in which the velocity is 1940 km s^{-1} (Schulz and Brandt, 2002) and the plasma subtends ±30 degrees of the incident source above and below the accretion disk. The case (b) is intended

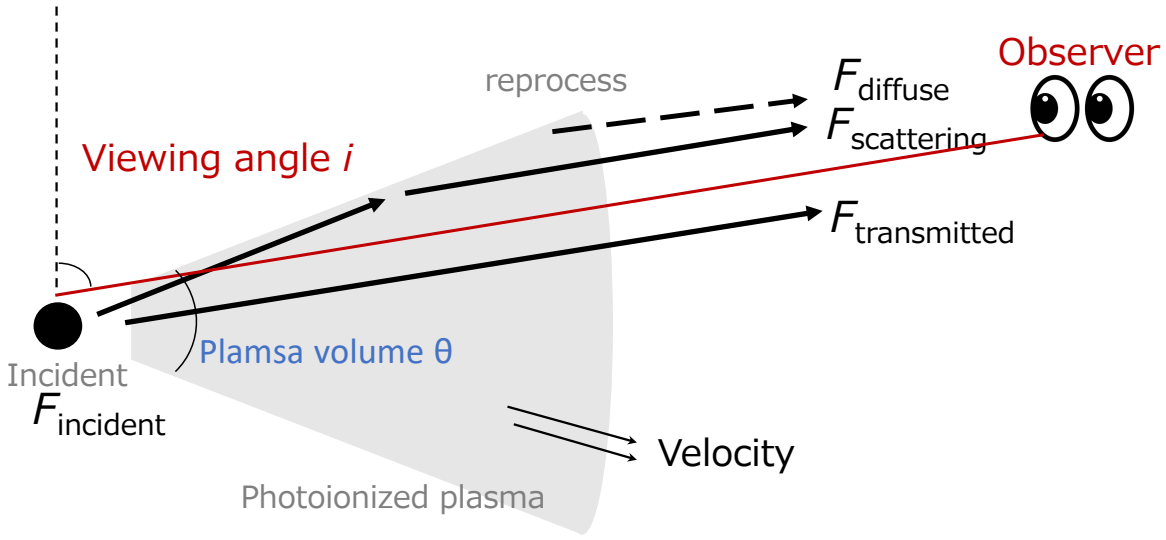

Figure 7.11: Geometry assumed in `MONACO` and `SKIRT`. We define the bulk velocity of the plasma, the range of plasma presence θ, and the inclination angle i.

to examine the difference of the velocity, and the case (c) is for the difference in the subtending angle.

TABLE 7.2: Setup for the P Cygni profile simulation.

Case	θ (deg)	v (km s^{-1})	Comparison with setup (a)
(a)	30	1940	
(b)	30	0	Different velocity.
(c)	180[a]	1940	Different angle subtended by the photoionized plasma.

[a] This corresponds to a fully subtending spherical shell.

Incident source: The incident source is the same as in the previous section (§ 7.2.1). It is a point-like source placed at the center. It has an X-ray luminosity of 1×10^{38} erg s^{-1} and the spectral energy distribution described by the disk blackbody emission of the innermost temperature of 2 keV. The ionization parameter was fixed at $\log \xi = 3.5$.

Photoionized plasma and target lines: Photoionized plasma is assumed to have a density of $n_{\text{H}} = 1 \times 10^{15}$ cm^{-3} and a column density of $N_{\text{H}} = 1 \times 10^{24}$ cm^{-2}. We target the Fe XXV line profile at 6.7 keV (§ 3.4.2). The relevant lines are summarized in Table 7.3.

Solver: We used the 3D Monte Carlo solver `MONACO` and `SKIRT` with our extension (§ 5.4.3) for this simulation. They support a radially outflowing velocity of varying elevation angles of the photoionized plasma. As all simulated photons escaping from the system have directions, the viewing angle can be selected in the post-processing. To increase efficiency, we limited the energy band of the incident source to 6.55–6.85 keV, which encompasses the Fe XXV features. We used a flat input spectrum.

TABLE 7.3: Energy levels and transitions of Fe XXV (Foster et al., 2012).

Level	Energy (keV)	Config	Term	Trans [a]	Name	Degeneracy	A coeff (s^{-1})[b]
0	0.0	1s2	$^1S_0$	(ground)	—	1	
1	6.637	1s1 2s1	$^3S_1$	M1	Heα, z[c]	3	1.93×10^{8}
3	6.665	1s1 2p1	$^3P_2$			1	
4	6.667	1s1 2p1	$^3P_2$	E1	Heα, y[c]	3	3.72×10^{13}
2	6.668	1s1 2s1	$^1S_0$			1	2.54×10^{9}
5	6.682	1s1 2p1	$^3P_2$	E1	Heα, x[c]	5	6.58×10^{9}
6	6.700	1s1 2p1	$^1P_1$	E1	Heα, w[c]	3	4.67×10^{14}

[a] Transition to the ground state. E1 for electric dipole (allowed), M1 for magnetic dipole (forbidden), E2 for electric quadruple (forbidden) transitions.
[b] Einstein A coefficient to the ground state.
[c] The w, $x+y$ and z lines are alternatively called the resonance (r), inter-combination (i), and forbidden (f) lines of the He-like line triplet.

Components: Unlike § 7.2.1, the scattered component is not taken into account for simplicity when simulated with `MONACO`. For `SKIRT`, it is included along with other components in Tabel 5.5.

7.2.2.3 Results (1) — `MONACO`

We first present the results obtained with `MONACO`.

Synthesized spectra: The output spectra are shown in Figure 7.12 (close to edge-on view; i =80–90 degrees) and Figure 7.13 (close to face-on view; i =30–40 degrees). The case (c) has a smaller statistics than the other two. The total number of input photons is similar in all three cases. In case (c), however, these photons are oriented toward a larger subtended angle in the 3D space and result in a smaller number of emergent photons at a particular viewing angle.

In all cases, two features are apparent in both the absorption and emission. From the Einstein A coefficient (Table 7.3), the stronger of the two is the Fe XXV Heα resonance line at 6.700 keV and the weaker is its inter-combination line at 6.667 keV. The line center opacity is very thick for these lines. Take the resonance line as an example. The opacity is given by

$$\tau_{\text{Fe He}\alpha,r} = \frac{1}{4\pi\epsilon_0}\frac{\pi e^2}{m_e c} gf \frac{1}{\sqrt{\pi}\Delta\nu_D} N_H A_{Fe} A_{24+} A_{1s}, \tag{7.5}$$

in which $\Delta\nu_D = \frac{E_0}{hc}\sqrt{\frac{2k_BT}{m_{Fe}}}$, E_0 is the energy of the line, gf is the weighted oscillator strength, A_{Fe} is the Fe abundance relative to hydrogen, A_{24+} is the charge fraction of Fe^{24+}, A_{1s} is the level population fraction of the ground state, m_{Fe} is the Fe atomic mass, T is the plasma temperature, and other symbols follow their conventions. For E_0 = 6.700 keV, g = 3, f = 0.72 (Foster et al., 2012), $N_H = 10^{24}$ cm^{-2} (§ 7.2.2.2), $A_{Fe} = 2.7\times10^{-5}$ (Wilms, Allen, and McCray, 2000), A_{24+} = 0.5 (Figure 5.9)A_{1s} = 1 and $T = 10^6$ K K (Figure 5.16), we obtain $\tau_{\text{Fe He}\alpha,r} \sim 4.7\times10^3$ which is ∼7000 times

larger than the opacity to the electron scattering (§ 5.1.2.3). For the absorption features, the line center opacity is large enough for the curve of growth (Figure 5.7) to be in the damping wing region, thus the absorption profile has a wide and flat bottom. For the emission features, the line center opacity is large enough to alter the profile. Indeed, the line profile has two peaks even in case (b), where there is no bulk velocity. This is what we expect as the Dijkstra profile (§ 5.2.3.2).

When these two are added, a complex line profile can be formed even with a symmetric geometry without bulk motion (Figure 7.14). This illustrates the strength of the radiative transfer modeling, in which we can interpret such an effect by decomposing the synthesized spectra into transmitted and diffuse emissions.

We compare this with the *Chandra* HETGS observation (Schulz and Brandt, 2002) for the column density of the absorption part and the equivalent width of the emission part. The former matches very well of $N_{\rm Fe} \sim 1 \times 10^{17}$ cm^{-2} both for the observation and simulation. The latter shows some discrepancy: the simulated emission equivalent width is smaller than the observation by a factor of a few. Such a deficiency of the line emission in `MONACO` simulation was also found in the previous section (§ 7.2.1). This should be further investigated in future work.

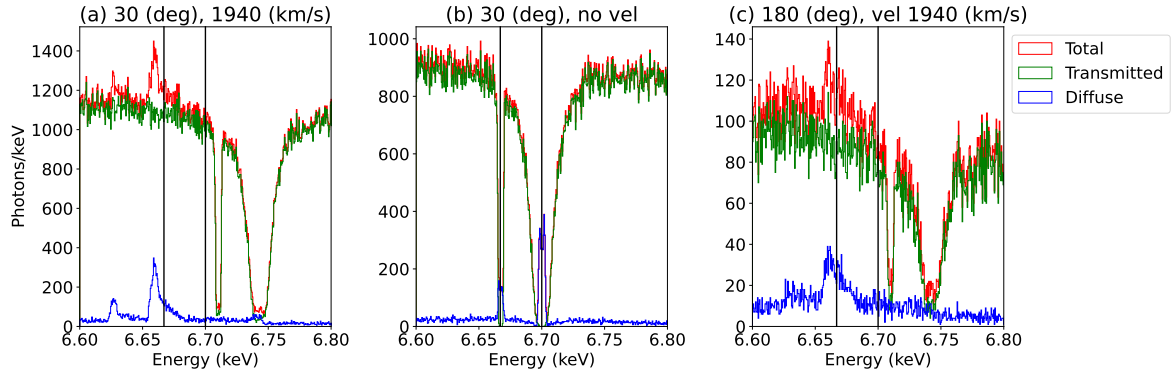

Figure 7.12: Synthesized spectra for the three cases (Table 7.2) for the viewing angle of 80–90 degree. Two vertical lines denote the rest-frame energy of the two Fe XXV lines – Heα w and y at 6.700 and 6.667 keV, respectively.

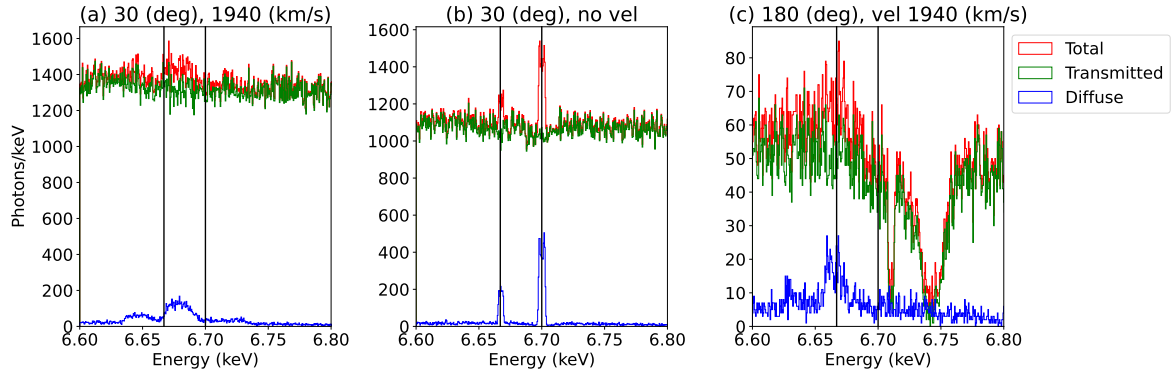

Figure 7.13: Same with Figure 7.12 but for the viewing angle of 30–40 degree.

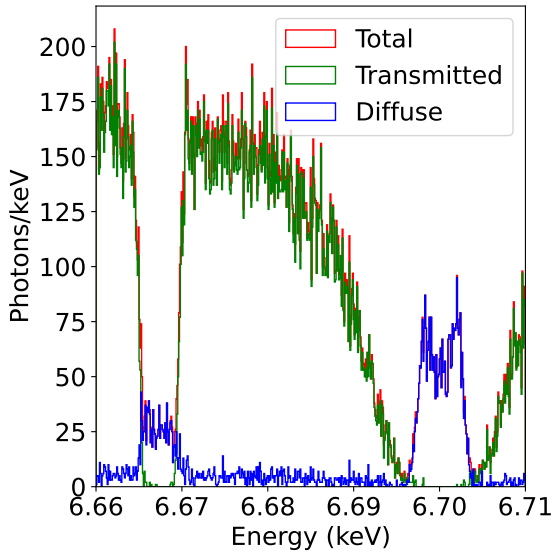

Figure 7.14: Enlarged view of panel b in Figure 7.12. Note that this complex line profile is formed even for the case with no bulk velocity. The profile was not resolved with *Chandra* HETGS with a resolution of ∼30 eV @ 6.5 keV but will be with *XRISM* with a resolution of 5 eV.

Comparison between different velocities: The effects of the difference in the bulk velocity 0 versus 1940 km s^{-1} can be studied by comparing cases (a) and (b) in Figure 7.12). For the two conspicuous transitions, the absorption is blue-shifted, while the emission is red-shifted. The velocity shift is calculated as

$$\frac{\Delta E}{E} = \frac{v}{c}, \tag{7.6}$$

resulting in v ∼2000 km s^{-1} for all features. This indicates that the velocity field is properly taken into account in the radiative transfer calculation.

The emission line profile also exhibits an asymmetry in case (a) with the bulk velocity. When projecting the radial velocity at a viewing angle of 80–90 degree, the maximum v is 1940 km s^{-1}. This is reduced by the projection effect as $\cos(90° - 80°)$ =0.9 at the minimum, which we interpret to produce a smooth profile in the blueward direction. In contrast, the absorption lines are only produced in the line of sight direction for the maximum radial velocity, which results in a symmetrical profile.

Comparison between different subtending angles: When the angle subtended by the photoionized plasma (θ) changes, the emission line profile changes. A comparison is made in Figure 7.15. This is because the velocity projected in the line of sight has a different distribution for different θ. In both cases, the largest shift in the blueward direction is at 1940 km s^{-1}. This is reduced by the cosine projection factor. For the spherical distribution ($\theta = 180$ degrees), a wider distribution is expected, resulting in a broader profile. This will be resolved soon with the use of *XRISM* and we will be able to constrain θ, thus α in § 7.2.1.

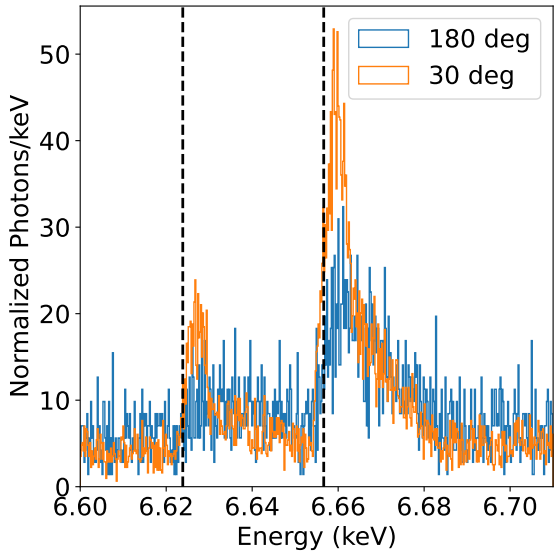

Figure 7.15: Comparison of the diffuse component in panels a and c in Figure 7.12. The spectra are normalized so that the total area is equal to 1. The two vertical lines show the energy of the two Fe XXV lines blue-shifted by 1940 km s^{-1}.

Comparison with varying viewing angle: The largest difference in the line profile is seen when we change the viewing angle i (Figures 7.12, 7.13). If the plasma is spherically symmetrically distributed (case c), the spectra do not show large variations for different viewing angles (compare panel c in Figures 7.12 and 7.13). If the plasma subtends only a part of the 4π str of the incident source, the spectra are entirely different. When seen from the viewing angle that does not go through the plasma, the spectra exhibit emission but not absorption regardless of the presence of the bulk velocity (panels a and b in Figures 7.13). When seen from the viewing angle that goes through the plasma, both the emission and the absorption contribute (panels a and b in Figures 7.13). The two are separated for the presence of the bulk velocity (panel a), forming a P Cygni profile.

7.2.2.4 Results (2) — SKIRT

We next present the results obtained with SKIRT.

Synthesized spectra: The output spectra are shown in Figure 7.16 (edge-on view; i =90 degrees) and Figure 7.17 (face-on view; i =0 degrees). SKIRT produced four lines of Heα w, x, y, and z as opposed MONACO that produced two lines of w and y. This is presumably due to a different treatment of the level population, in which MONACO assumes LTE, while SKIRT of our extension calculates NLTE (§ 5.4).

Comparison between different velocities: The effects of the bulk velocity can be studied by comparing cases (a) and (b) in Figure 7.16, in which the velocity is assumed to be 0 and 1940 km s^{-1}, respectively. For the two conspicuous transitions, the absorption is narrow and blueshifted, while the emission is broad and its peak is redshifted. The

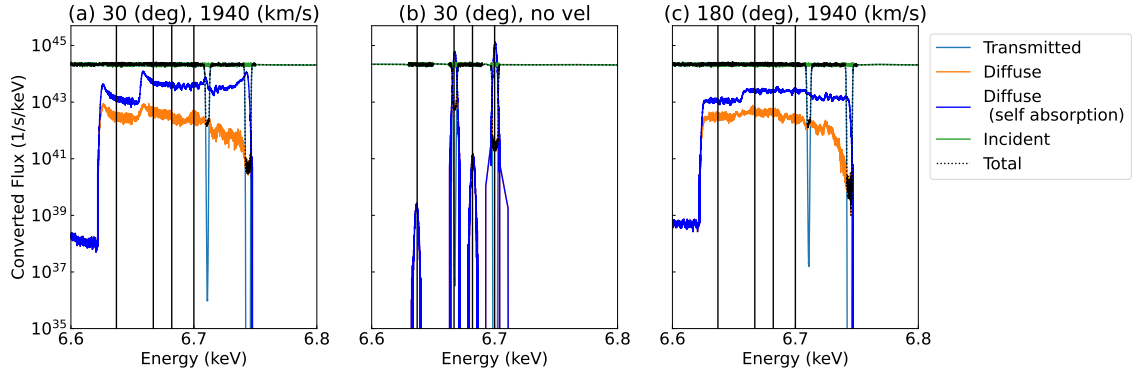

Figure 7.16: Synthesized spectra for the three cases (Table 7.2) for the viewing angle of 90 degree. Four vertical lines denote the rest-frame energy of the four Fe XXV lines – Heα w, x, y, z at 6.700, 6.637, 6.682 and 6.667 keV, respectively.

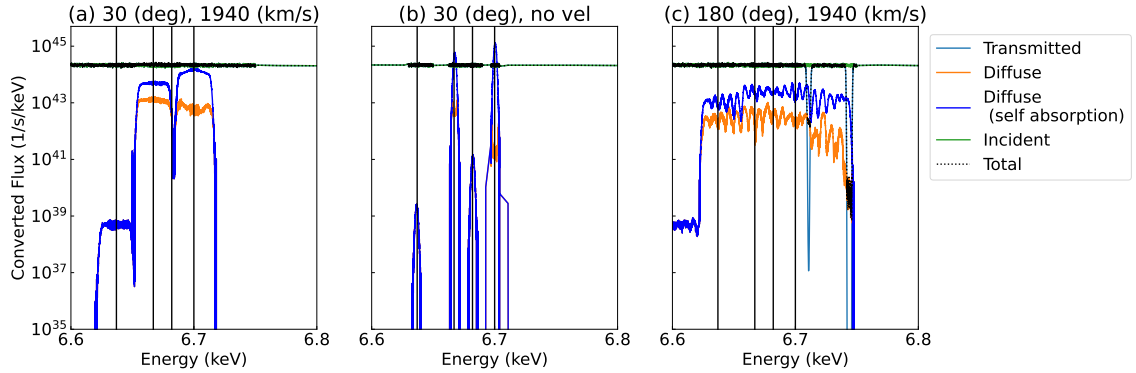

Figure 7.17: Same as Figure 7.16 but for the viewing angle of 0 degree. The jagging behavior in the diffuse components in panel c is an artifact stemming from coarse gridding in space hence Doppler velocity.

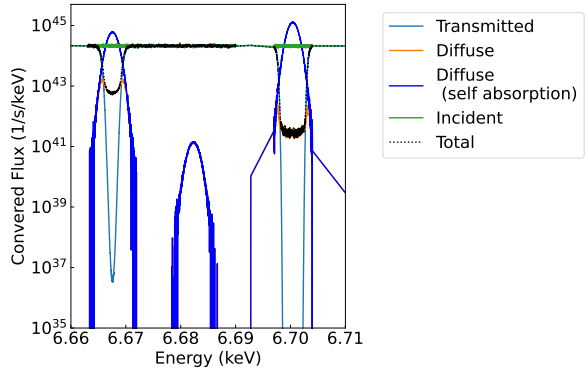

Figure 7.18: Enlarged view of panel b in Figure 7.16. Note that such line profiles can be formed even without any bulk velocity. The profile was not resolved with *Chandra* HETGS but will be with *XRISM*.

absorption lines are formed when the incident emission transmits through the plasma in the line of sight, thus they are blueshifted. The emission lines are formed from the diffuse emission, which is energy shifted according to the local velocity projected in the line of sight, thus they are broad and include blue-shifted as well as red-shifted parts. In contrast to MONACO, the emergence of blue-shifted part of the emissions is more pronounced in SKIRT. This discrepancy arises because the resultant spectra are synthesized by integrating the line-of-sight direction in MONACO(e.g., 80–90 degrees) and are also influenced by certain variations in the calculation processes between the tools.

Comparison between different subtending angles: When the angle subtended by the photoionized plasma (θ) changes, the line profiles change. When the plasma is distributed spherically (Figure 7.16 c), the profile of each emission line is flat. This implies a constant distribution of the velocity projected in the line of sight. While the plasma is segmented into multiple shells based on the XSTAR output to define the geometry, SKIRT allows for a specification of the density distribution of r^{-2} within a single shell. As the volume of each shell increases with r^2, the number of particles composing the plasma remains constant for all r. Consequently, the projected velocity distribution becomes flat. When combined with observations of sufficient spectral resolution, we can assess the velocity and density distributions with such simulations.

Comparison with varying viewing angle: The largest difference in the line profile is seen when we change the viewing angle i (Figures 7.16, 7.17). If the plasma is spherically distributed (case c), the spectra do not show large variations for different viewing angles (compare panel c in Figures 7.16 and 7.17). When seen from the viewing angle that does not go through the plasma, the spectra exhibit emission but not absorption regardless of the presence of the bulk velocity (panels a and b in Figures 7.17), which is also concluded from the MONACO results.

7.2.3 X-ray light curve changes over an orbit

7.2.3.1 Purpose

Our *NICER* AO2 observation revealed X-ray flux changes over an entire orbit (Figure 6.7). We attributed the flux changes mostly to changes in the column density of the intervening materials in the line of sight. The dip phase is caused by a thick solid material ("bulge"), while the rapid changes in the flaring phase are caused by the varying covering fraction of the fragmentary partial covering material (Figure 7.2). The observed light curve carries information about the size and filling factor of the material around the neutron star. We model and explain some of the observed features using SKIRT.

7.2.3.2 Setup

Physics: The required physics is the photoelectric absorption in the X-ray band, so we used a released version of SKIRT as implemented by Vander Meulen et al. (2023) (§ 5.4.2).

Geometry: Figure 7.19 shows the geometry of the simulation. The incident flux comes from the accretion disk surrounding the neutron star. The intervening material is placed

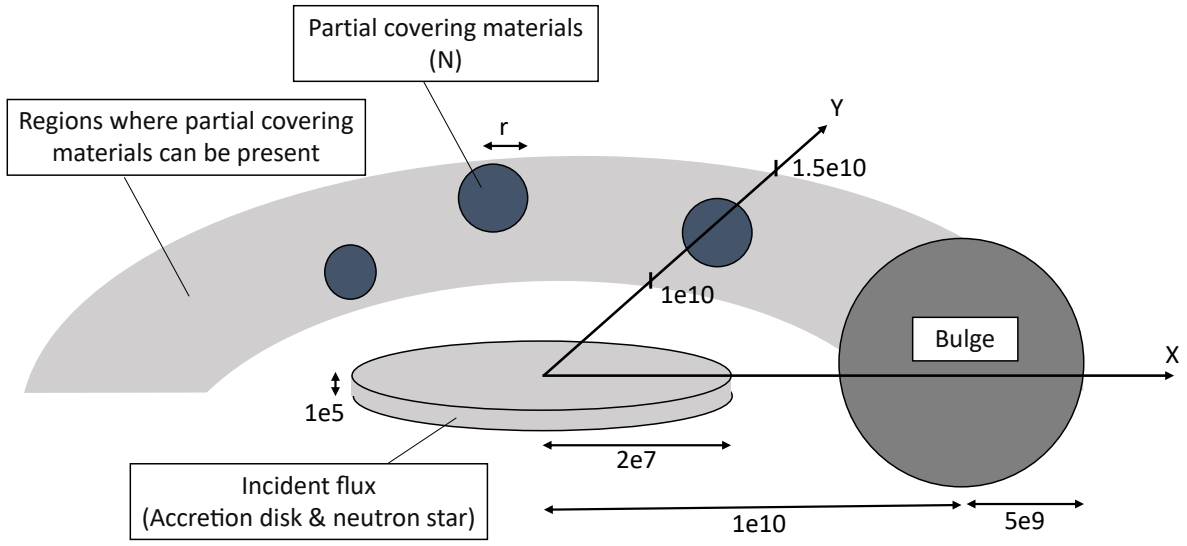

Figure 7.19: Geometry of simulation.

along the azimuth of a concentric radius fixed to the local coordinate. The observer observes the system from varying azimuthal degrees from 0 to 360 degrees in one orbit.

Incident source: First, we set up the incident source, which is the radiation from the surface of the neutron star, presumed to be at the center of the disk, as well as from the disk itself. The disk has an inner and outer radius of $R_{\rm in}$ and $R_{\rm out}$. The $R_{\rm in}$ is derived from the X-ray spectral fitting as $\sim 10^6$ cm (§ 7.1.3). For $R_{\rm out}$, we used the radius from which the disk blackbody emission contributes to the softest end of the *NICER* bandpass of 0.2 keV. The blackbody temperature is given by $T(r) = T_{\rm in}(r/R_{\rm in})^{-3/4}$ as a function of the radius for the standard disk. The emission from $R_{\rm out} \sim 2 \times 10^7$ cm contributes to the X-ray emission observed with *NICER*. For simplicity, we assume that a 2 keV blackbody radiation is uniformly emitted from both sides of the disk with an inner and outer radius of 0 and $R_{\rm out}$ and that the height of the disk H is negligible compared to $R_{\rm out}$ as $H = 1/200 R_{\rm out} = 1 \times 10^5$ cm.

Bulge: Second, we set up the bulge, which was found to be inside the photoionized plasma with the inner and outer radius of $r_{\rm in} = 1.0 \times 10^{10}$ and $r_{\rm out} = 1.5 \times 10^{10}$ cm (§ 7.1.3). The duration of the flux decrease during the dip phase (0.15 orbit) translates to the azimuthal degree occupied by the bulge and to the size of the bulge. At a distance of $r_{\rm in}$ from the disk center, the bulge radius is $\sim 0.15 \times 2\pi r_{\rm in}/2 \approx 5 \times 10^9$ cm. In `SKIRT`, we modeled the bulge with a 3D Gaussian sphere with a truncated outer radius of 5×10^9 cm and the 1σ radius of 3×10^9 cm placed at the disk plane. The total column density is 1×10^{25} cm^{-2} (§ 6.1.3).

Partial covering material: Finally, we set up the partial covering materials as follows. We used a `SKIRT` feature to model such a porous material with a number of small spherical materials of identical size (grain). It is parameterized by the total mass M, the number of grains N, the radius r of a single grain and the volume filling factor f by N grains. We distributed the grains in a cylinder with the same inner and outer radius with

the photoionized plasma and the height the same as the bulge diameter. The cylinder is limited to a phase π–2π adjacent to the bulge.

The grain parameters can be restricted from the *NICER* observations. The total mass is

$$M = Nvm_{\rm p}n_{\rm p}, \tag{7.7}$$

where $v = 4/3\pi r_{\rm grain}^3$ is the volume of a grain, $m_{\rm p} = 1.67 \times 10^{-24}$ g is the proton mass, and $n_{\rm p}$ is the proton number density.

The hydrogen equivalent column density along the line of sight is estimated as

$$N_{\rm H} \sim \sqrt[3]{f} n_{\rm p} \left(r_{\rm out} - r_{\rm in}\right) = \frac{M(r_{\rm out} - r_{\rm in})}{Nvm_{\rm p}}. \tag{7.8}$$

We substitute $N_{\rm H} = 1 \times 10^{24}$ cm^{-2} using the average values during the late dip phase.

The covering fraction during the flaring phase varies $f^{\rm (cov)}$ =0.5–1.0 (panel d in Figure 6.7). We assume that its average is equal to $\sqrt[3]{f}$. The volume filling factor is then

$$f = \frac{Nv}{0.5\pi h(r_{\rm out}^2 - r_{\rm in}^2)} = \langle f^{\rm (cov)} \rangle^3 = 0.42 \tag{7.9}$$

We thus obtain $Nv \sim 5.9 \times 10^{29}$ cm^3 and $M \sim 2 \times 10^{20}$ g. The X-ray flux increase or decrease lasts for a single *NICER* snapshot. If this is caused by a single grain, the radius of the grain is estimated as $r_{\rm grain} \sim 2\pi r_{\rm in}/100/2 \approx 1 \times 10^8$ cm.

7.2.3.3 Results

The number of grains N is the only free parameter: all the others are constrained using the aforementioned relations by observation. We ran simulations for $N \in \{20, 200, 2000\}$, which corresponds to $r_{\rm grain} \in \{1.9 \times 10^9, 8.9 \times 10^8, 4.1 \times 10^8\}$ cm. We placed the detector for the entire azimuth of 360 degrees with 1 degree apart and derived the X-ray flux observed at each detector to construct the X-ray light curve over an orbit. Note that the *NICER* AO2 observation was performed 100 times for an entire orbit, which corresponds to the average viewing angle resolution of 3.6 degrees. We also changed the viewing angles $\theta \in \{70, 75, 80, 90\}$ degree.

The result is shown in Figure 7.20, in which the normalized simulated light curves are shown in comparison to the observed light curve. First, we should clarify two major differences that should be ignored. One is that the X-ray flux has an overall trend peaking at the end of the dip phase (ϕ ~0.05) and gradually decays until the next dip. We attribute this global trend to the change in the incident source, which is not included in the simulation. The other is that the flaring phase lasts for 0.3 phases, but it was simulated to last for 0.5 phases for simplicity of modeling. Except for them, the simulation results reproduce the dip and flaring behaviors in the light curve for some viewing angles.

Dependence on N: When we change the number of grains (from left to right in the same row in Figure 7.20), the light curve changes as follows. For $N = 2000$, the changes in the light curve are rapid because many small grains contribute to the extinction of the line of sight. The detector angle resolution of 1 degree may be insufficient. For $N = 20$, the changes in the light curve are slow because a few large grains contribute to

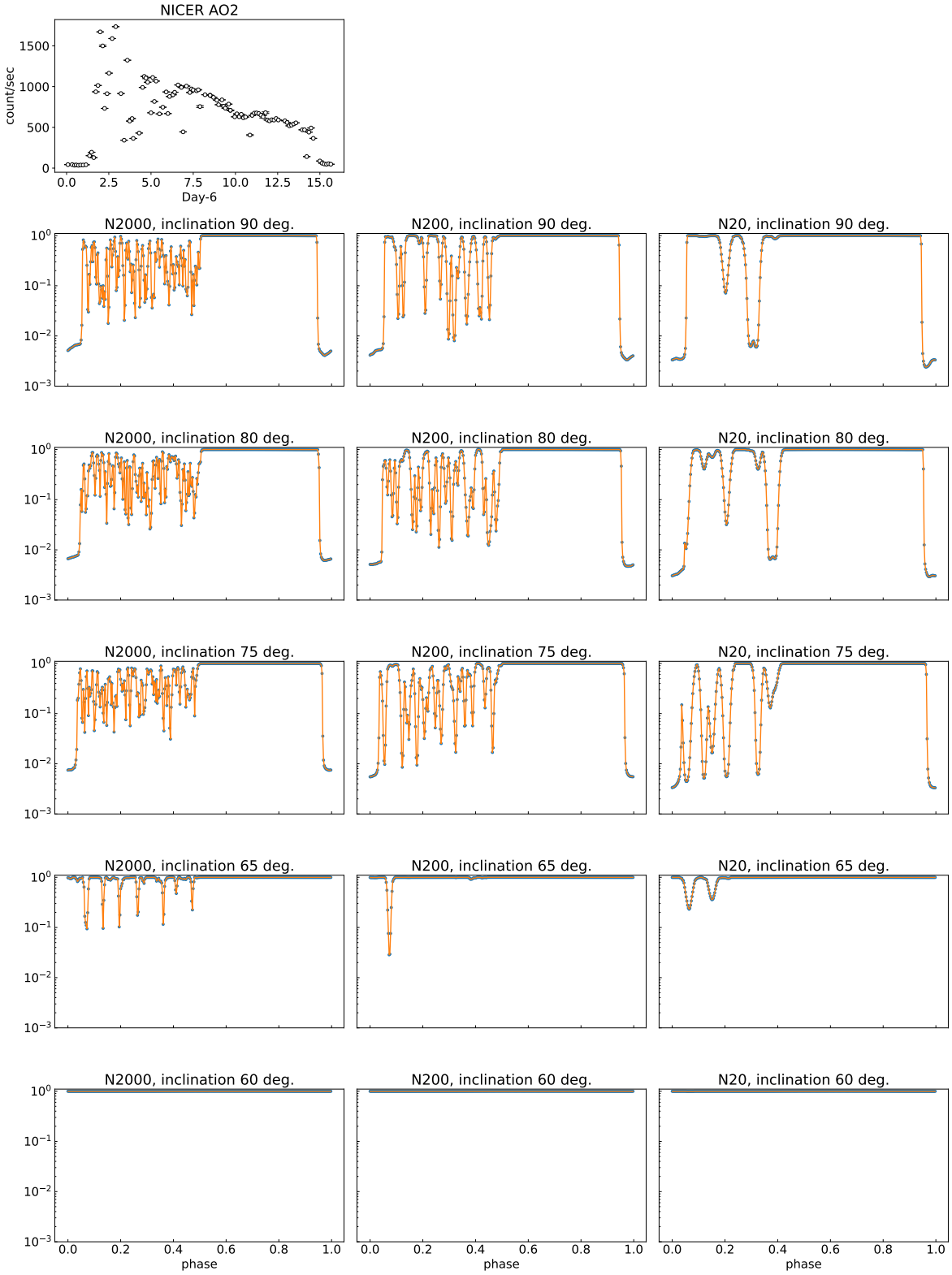

Figure 7.20: Normalized light curve calculated by `SKIRT`. Top panel shows the light curve observed by *NICER* for reference. To compare with the simulation results, the horizontal axis represents the observation date time-shifted by 6 days.

the extinction occasionally. Their size occupies an angle of a few degrees at least, and their profile is resolved with a 1-degree resolution.

Dependence on θ: When we change the viewing angle (from top to bottom in the same column in Figure 7.20), the dip and flaring behaviors disappear as they have a certain height. The bulge for the dip phase has a height that blocks the view up to the viewing angle of 65–75 degrees, while the partial covering materials for the flaring phase have a height that blocks the view larger than 60–65 degrees.

Both for the bulge and partial covering materials, the smallest inclination angle that realizes the flux decrease constrains the position of these materials. For the partial covering material, the geometry of the smallest inclination is shown in Figure 7.21. In this case, the angle θ is estimated as

$$\theta \sim \frac{\pi}{2} - \arctan \frac{1/2 \times 10^{10} + r}{1 \times 10^{10} - 2 \times 10^{7}}, \tag{7.10}$$

which ranges for ∼55–62 degree for $r = 2 \times 10^{9}$–4×10^{8} cm. The value is consistent with the simulation result (Figure 7.20), in which the extinction of the partial covering material disappears when θ increases from 60 to 65 degrees.

The same applies to the bulge as

$$\theta \sim \frac{\pi}{2} - \arctan \frac{5 \times 10^{9}}{1 \times 10^{10} - 2 \times 10^{7}}. \tag{7.11}$$

The calculated value 63 degree is almost consistent with 65 degrees. The value is consistent with the simulation result (Figure 7.20), in which the extinction by the bulge disappears when θ decreases from 75 to 65 degrees.

Constraint of viewing angle: From these results, the some major features of the X-ray light curve observed with *NICER* were qualitatively well explained. The location and size of the bulge and the partial covering materials are constrained, as well as the viewing angle. From the *NICER* AO2 observations, a relatively large inclination of $\gtrsim 75$ degrees is required, which is a new piece of evidence for the inclination angle constraint.

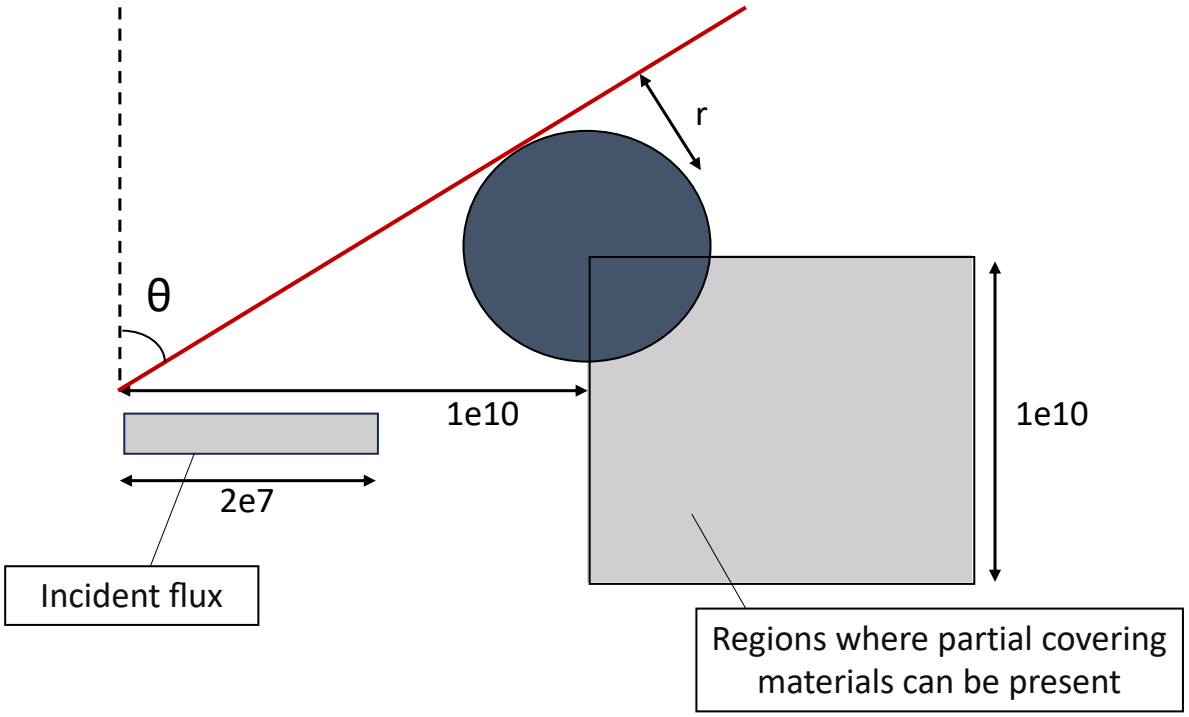

Figure 7.21: Edge-on view of the partial covering material at a minimum viewing angle that causes an extinction by the material in the line of sight. The sight line touches the innermost edge of the zone of existence of the partial covering materials.

7.3 Implications

7.3.1 Mass of the companion star

Most X-ray binaries are conclusively classified into either LMXB or HMXB, yet Cir X-1 is not. Many X-ray properties point to the LMXB nature of the source, including Type I bursts (Tennant, Fabian, and Shafer, 1986a; Tennant, Fabian, and Shafer, 1986b; Linares et al., 2010), kHz QPO (Boutloukos et al., 2006), being a Z source (Oosterbroek et al., 1995; Shirey et al., 1998; J. L. Qu, Yu, and Li, 2001), and being a dipper (e.g., Brandt et al., 1996). The only major argument so far for HMXB is the dynamical solution based on optical spectroscopy (Figure 3.4), in which the absorption features of the H Paschen series ($n \rightarrow 3$) at 8500–8800 Å were found modulated by the orbital period. By assuming that (i) the feature originates from the companion star and (ii) the inclination angle is close to face-on, a high mass solution was obtained for the companion star (Jonker, Nelemans, and Bassa, 2007). We revisit this argument.

For the interpretation that the Paschen series lines originate from the companion star, some inconsistency is found. One is the phase of the modulation. If the companion star is the origin, the maximum and minimum Doppler shifts should be observed at ϕ =0.25 and 0.75 when $\phi = 0$ is defined at the periastron. However, the measured velocity shift is maximum at $\phi = 0$ (Figure 3.1). The other is that the Paschen series lines appear in emission during the X-ray dip phase. This is not usually the case for the photospheric features of a star, unless optically-thin circumstellar structure is formed only at the phase. This is more reminiscent to the behavior of the X-ray lines originating from the photoionized plasma (§ 6.1.4), in which the change of the relative strength between the transmitted and diffuse emission makes the lines to appear either in emission or absorption, as we demonstrated in the radiative transfer calculation (§ 7.2.1). Indeed, the Paschen series lines can be easily reproduced in the radiative transfer calculation of the photoionized plasma. Figure 7.22 shows the synthesized spectra using `CLOUDY` for the low ionization degree ($\log \xi$) of –1 or –2. We used a 1D two-stream solver `CLOUDY`, which supports the optical and infrared transitions, unlike the three codes used elsewhere in this thesis. For a uniform density, this is achieved at $\mathcal{O}(100)$ times larger radius than $\log \xi = 3.5$ where the X-ray Fe lines are produced. We argue that the Paschen series lines can originate from the photoionized plasma.

Even if we accept the interpretation that the Paschen series lines originate from the companion, we will reach a LMXB solution. As we argued for the two X-ray features based on radiative transfer modeling (§ 7.2.2 and § 7.2.3), a large inclination angle is strongly favored. From the Kepler's third law,

$$\frac{M_2^3 \sin^3 \theta}{(M_1 + M_2)^2} = \frac{P}{2\pi G} K_2^3 (1 - e^2)^{3/2}, \tag{7.12}$$

in which $P = 16.68$ days is the orbital period, M_1 and M_2 is the mass of the compact object and the companion star, K_2 is the Doppler amplitude of the feature of the companion star, i is the inclination angle, and e is the eccentricity of the orbit. We substitute $K_2 = 25$ km s^{-1} and e =0.45 (Jonker, Nelemans, and Bassa, 2007) and derive the relation between M_2 and i for M_1 =1.4 and 2.2 $M_\odot$ in Figure 7.23. For a high inclination angle of > 60 degrees (§ 7.3.2), a low mass solution of $M_2 < 1 M_\odot$ is obtained.

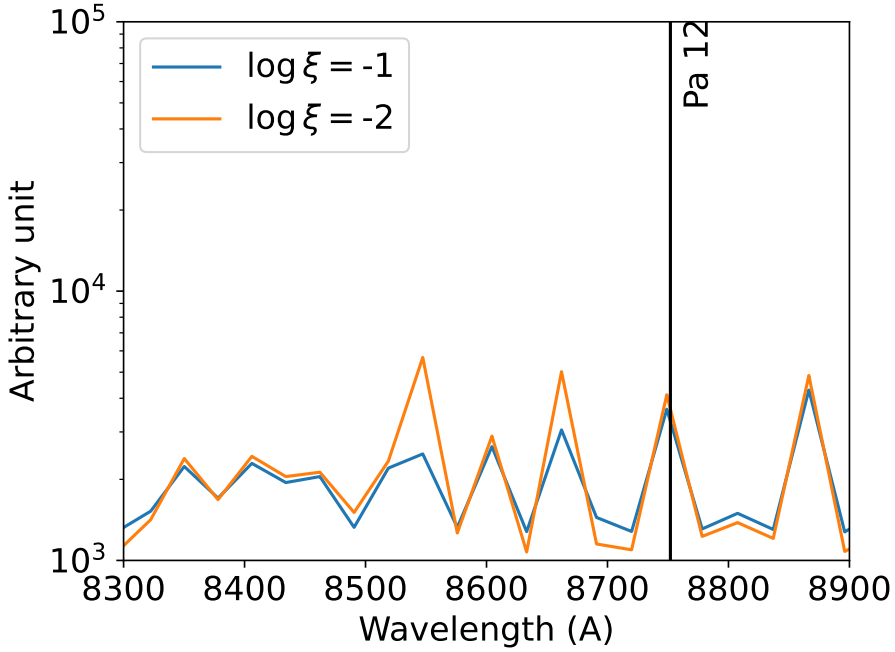

Figure 7.22: Simulated spectra of the photoionized plasma of $\log \xi$ =–1 (blue) or –2 (red) using `CLOUDY`. We assumed relatively thin plasma $N_{\rm H} = 10^{18}$ cm^{-2} and $n = 10^{10}$ cm^{-3} for demonstration purposes. Vertical lines denote the expected location of the Paschen-12 line used in Jonker, Nelemans, and Bassa (2007) for $n = 12 \rightarrow 3$.

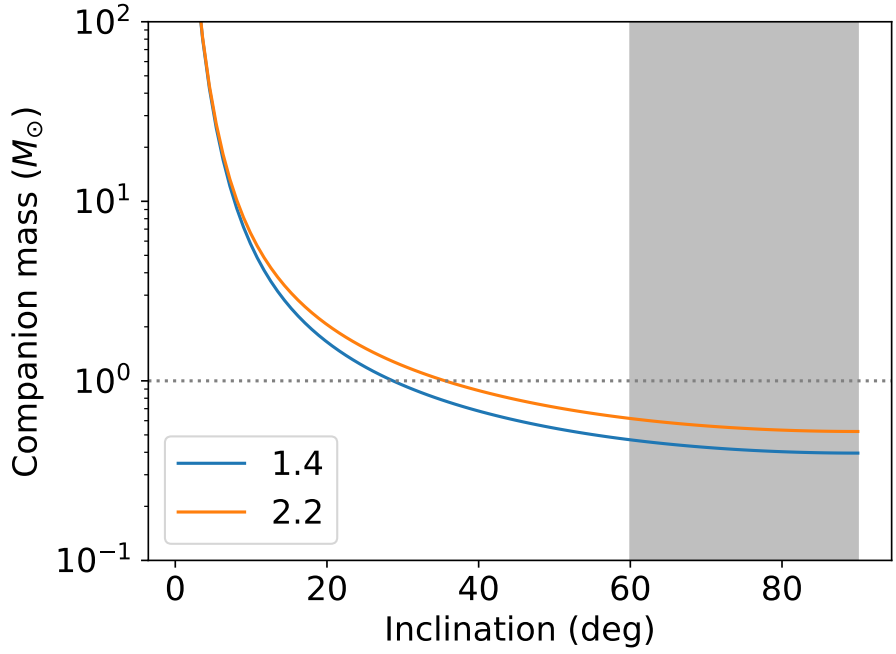

Figure 7.23: Relation between the companion mass and the inclination angle for two selected mass of the compact object.

7.3.2 Inclination angle

In LMXBs, X-ray flux changes over a binary orbit are often observed. One is the total or partial eclipse by the companion star. Others include long and short dips with a partial covering material. The presence or absence of them is related to the viewing angle (Figure 7.24). Cir X-1 exhibits long and short dips but no eclipse (Figure 6.1), which gives a stringent constraint on the inclination angle.

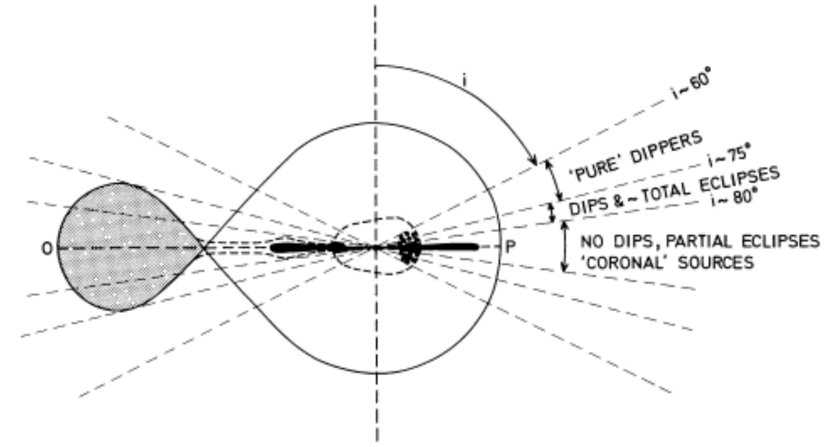

Figure 7.24: X-ray flux changes over an orbit of LMXBs (J. ; Frank, A. R. ; King, and Lasota, 1987). Different viewing angles make different modulations.

Absence of eclipse: We can constrain the upper limit of the inclination angle from the absence of eclipse. We assume a geometry in depicted in Figure 7.25 left. First, we calculated the Roche-lobe radius in the unit of the semi-major axis of the binary as

$$\frac{r_{\rm RL}}{a} = \frac{0.49q^{2/3}}{0.6q^{2/3} + \log(1+q^{1/3})}, \tag{7.13}$$

in which q is the mass ratio between the mass of the companion star and the compact object (NS). The mass ratio is derived using Figure 7.23 for each assumed inclination angle i. Under the assumption that the companion star adheres to the Roche lobe, and the NS is a point source, the inclination must be smaller than $\frac{\pi}{2} - \arctan\frac{r_{\rm RL}}{a}$. This is achieved for $i < 75$ degrees (Figure 7.25 right).

Presence of dips: These dips are considered to be caused by the accretion stream from the Lagrange point of the Roche-lobe filling companion star in a semi-detached system. Early work by Flannery and Faulkner (1975) and Lubow and Shu (1975) argued that a bulge-like structure is formed at the position where the accretion stream hits the accretion disk. The accretion stream forms a ring, which spreads inward with viscosity to eventually form an accretion disk.

J. ; Frank, A. R. ; King, and Lasota (1987) proposed a model shown in Figure 7.26, where the accretion stream hits the outer rim of the accretion disk (S_1), forming a ring. As the subsequent inflow collides with the ring at S_2, cold clouds are dispersed over the disk plane, indicated by thick dots. These cold clouds give rise to a pronounced dip in

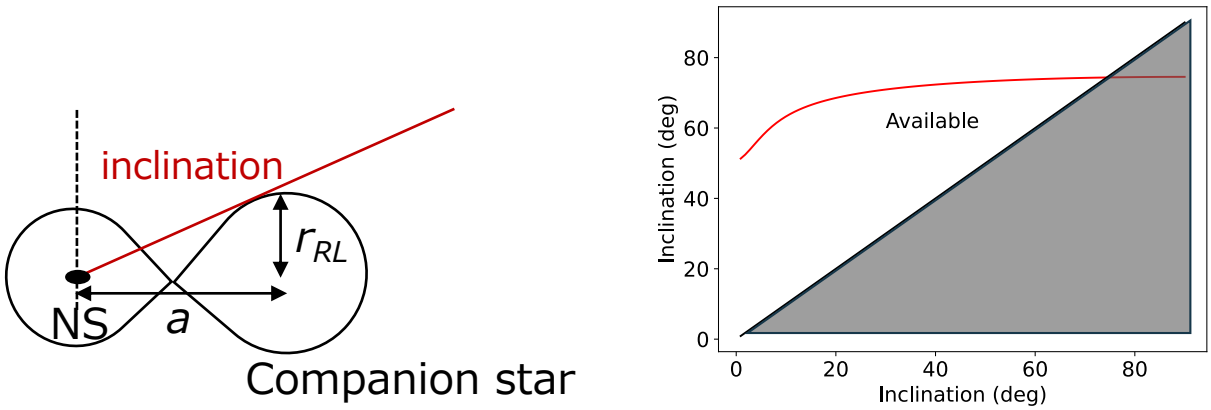

Figure 7.25: (left) Geometry used for the estimation of the inclination angle and (right) the available inclination angle.

phase ∼0.6–0.8 with an edge-on view (>60 degree), while the stream core is too thin to exhibit the dip.

This accretion stream should have a vertical structure, which implies that the hot spot has a three-dimensional structure (see Figure 2 of Lubow and Shu (1976)). Part of the accretion stream can penetrate the accretion disk and interact with the disk surface. According to this hypothesis, a dip attributed to the stream-disk interaction is anticipated at phase 0.9 in the light curve shape. A second dip is expected around phase 0.6, corresponding to the point where the residual inflow reaches the disk surface from the vertical direction (Lubow, 1989).

The idea of the accretion stream-disk interaction was further advanced by the smoothed particle hydrodynamics (SPH) simulation for representative parameters of LMXBs (binaries of a low mass star and a neutron star or a black hole) and cataclysmic variable (CVs; binaries of a low mass star and a white dwarf). Figure 7.27 shows the orbital dependency of the column density at various viewing angles for the two LMXBs (Armitage and Livio, 1996; Armitage and Livio, 1998). An increase in the column density in the phase to have the hot spot in the line of sight is apparent around phase 0.8, which is also supported by Kunze, Speith, and Hessman (2001). We consider this to be the bulge in our model (Figure 7.1) and the dependence of column density versus viewing angle is essentially the same as our result of the radiative transfer simulation (Figure 7.20).

In addition to the main dip around phase 0.8, the second dip appears at different phases depending on the simulation setup. In scenarios involving relatively small disks or when the mass transfer rate increases swiftly, some of the overflowing gas bounces after impacting the disk surface around phase 0.5. This gives rise to a second dense region on the disk surface approximately at orbital phase 0.2 (Kunze, Speith, and Hessman, 2001). In the *NICER* observation, we observed rapid flux changes in the flaring phase and several short dips in the stable phase materials (Figure 6.1), which was modeled by a number of small grains acting as a partial covering material (Figure 7.19). We constrained the volume filling factor of these grains using the X-ray light curve (Figure 7.20), which should be compared to the SPH simulations setup for Cir X-1.

In summary, the long and short dips and the flaring phase flux changes observed with *NICER* over an orbit are well explained with the accretion stream and disk interaction theories.

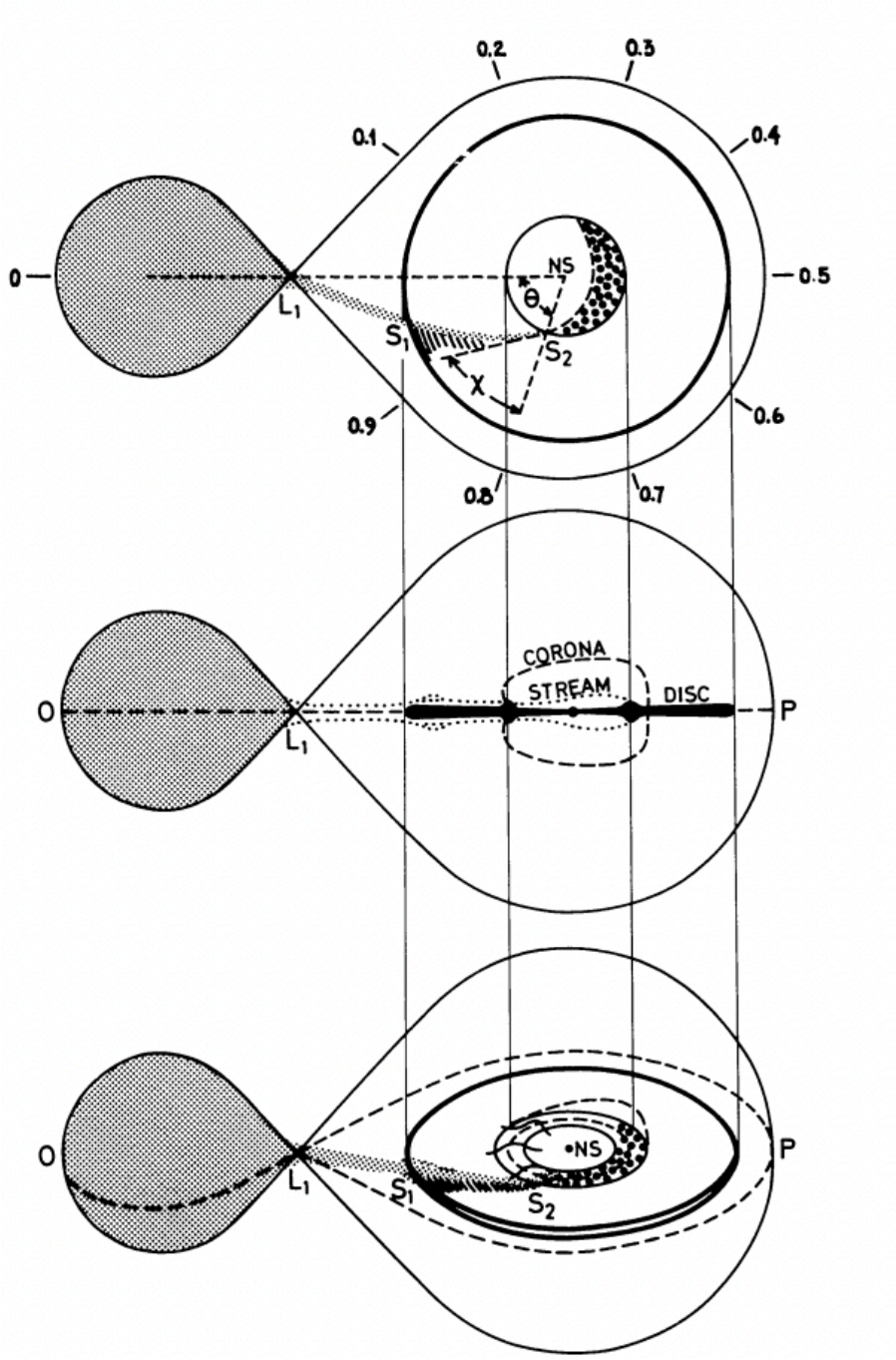

Figure 7.26: Schematic view for the dip phenomena in LMXBs (J. ; Frank, A. R. ; King, and Lasota, 1987).

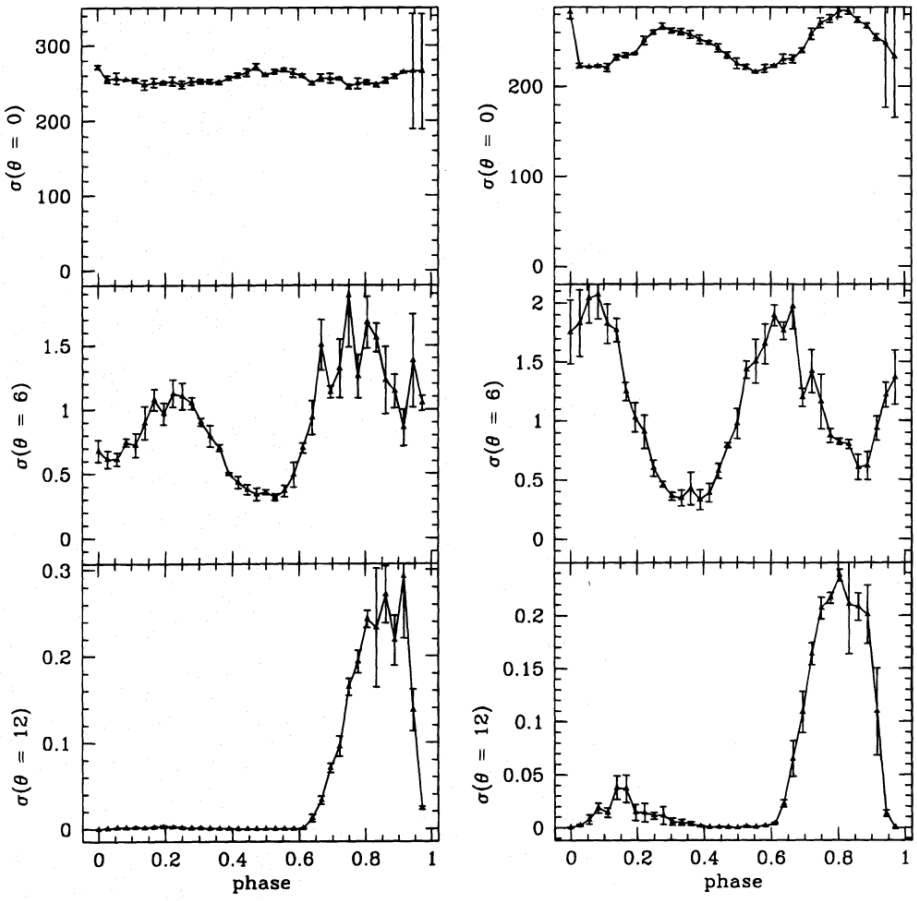

Figure 7.27: Orbital dependency of the column density σ simulated for three different viewing angles above the disk plane ($\theta = 0$) in the SPH simulation (Armitage and Livio, 1996). The simulation assumes LMXBs with a secondary of nearly zero mass ($q \sim 0$; left columns) and those satisfying the full Roche potential ($q = 0.2$; right columns).

7.3.3 Location of the photoionized plasma

In this study, we proposed a geometry, in which the photoionized plasma is located radially outward of the accretion disk (Figure 7.1). The geometry was tested by interpreting the observed Fe line absorption and emission (§ 7.2.1) and the P Cygni profile with a radial velocity of ∼2000 km s^{-1} (§ 7.2.2) based on the 3D radiative transfer. The proposed geometry is in contrast to the conventional view of the accretion disk corona (Figure 7.28), in which the photoionized plasma is located on the surface of the accretion disk.

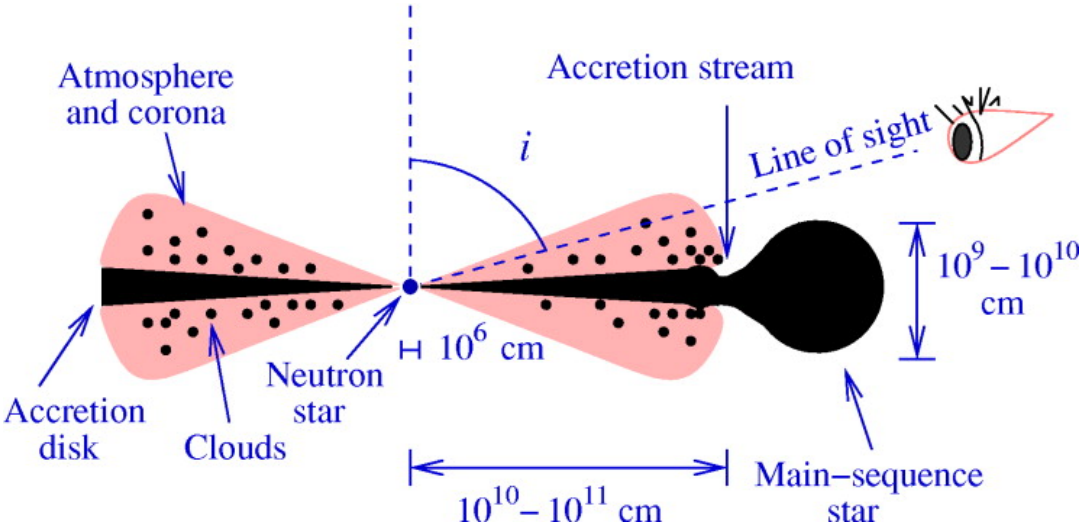

Figure 7.28: Conventional view of the location of the photoionized plasma (Jimenez-Garate, Raymond, and Liedahl, 2002).

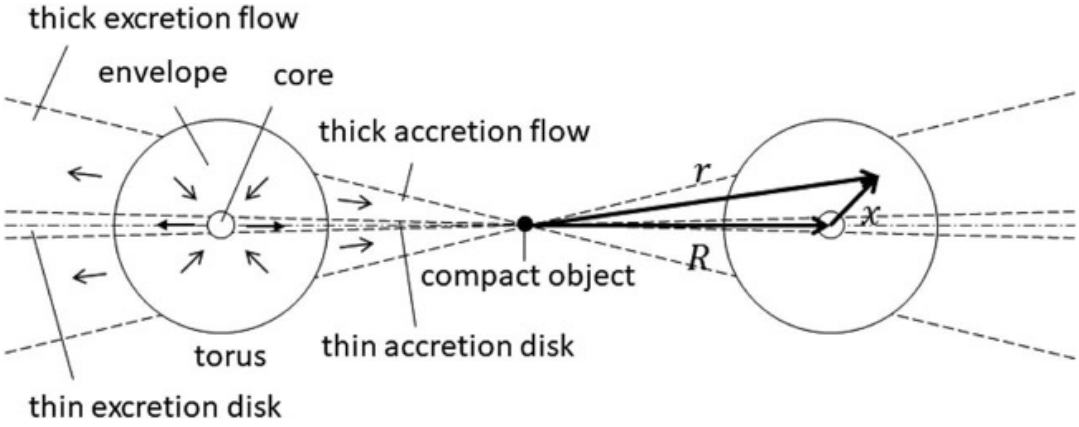

Figure 7.29: Schematic view of an accretion ring (Inoue, 2021).

In our model, the outflowing photoionized plasma is launched from the outer edge of the accretion disk. This is consistent with the "excretion" flow proposed by Inoue (2021) (see Figure 7.29). The mass transported from the companion star rotates at the circularization radius according to the constant specific angular momentum accompanying the rotational motion of the binary system, forming an accretion ring. The ring expands radially and forms a torus-like shape. Most mass moves radially inward by losing angular momentum, but some mass moves outward by gaining angular momentum

to balance the loss. The inward motion is called the accretion, while the outward motion is called the excretion. They also argued that the excretion flow can be the origin of the highly ionized Fe absorption lines. The excretion flow has a terminal velocity $v < \sqrt{2GM_1/r_c} \sim 10^3$ km s^{-1} for a compact object with a mass of $M_1 \sim 10M_\odot$. This is in the same order as the velocity observed in Cir X-1.

Chapter 8

Conclusion

Contents

8.1 Summary of Findings 176
8.2 Future Outlook 182

In § 8.1, we summarize the findings of this study in view of the five objectives outlined in § 2.1. We discuss some future prospects based on the results in § 8.2.

8.1 Summary of Findings

We listed five objectives of this study in § 2.1. For each objective, we summarize the findings achieved in this study.

Purpose 1 "To construct the coherent X-ray spectral model through the X-ray observation of Cir X-1 at the highest cadence over an entire binary orbit": In the AO2 cycle of *NICER*, we acquired the telescope time through a competitive process and conducted the observations covering an entire orbital period of Cir X-1 in August 1–16, 2020 (Figure 6.1). Due to the operational flexibility and the unprecedentedly large collecting area with moderate energy resolution, we obtained a total of 103 well-exposed spectra with the highest cadence, sufficient energy resolution, and uniform quality. Using this unique data set, we obtained the following results (§ 6.1).

1. The flux change over an orbit is repeated reproducibly by comparing to the *MAXI* light curves of preceding orbits (Figure 6.2). It is divided into three phases; dip, flaring, and stable phases (Figure 6.3).
2. We constructed spectral models for representative spectra in each phase. Despite the apparent changes, we argue that they can be described by a common spectral model with variable parameters.
3. The continuum emission is explained by a variable disk blackbody component over the entire orbit, with a minor invariable soft excess component expected from the photoionized plasma (Figure 6.7).
4. The variety of the X-ray flux changes and the continuum spectral shape is mostly attributable to rapid changes of the partial covering material in the line of sight and gradual changes of the accretion disk temperature and luminosity.
   (a) The dip phase, which occupies ∼15% of the orbit before and at the periastron, is characterized by a sudden decrease in the X-ray flux. It is attributable to a sudden increase in the absorption column of the partial covering material in the line of sight, provided that the blackbody emission from the disk changes gradually (Figure 6.5).
   (b) The following flaring phase for ∼30% of the orbit is characterized by rapid changes of the X-ray flux, which is mainly attributable to rapid changes of the covering fraction of the partially covering medium in the line of sight (Figure 6.6).
   (c) The stable phase is characterized by a gradual decrease in the X-ray flux. This is governed by the gradual change in disk blackbody emission (Figure 6.4).
5. Upon continuum emission, we found emission and absorption features of the H-like and He-like ions of Mg, Si, S, and Fe (Figure 6.8). They are presumably from the extended photo-ionized plasma. They are most evident during the dip phase, when the continuum emission of the disk blackbody is most attenuated. The Fe line feature turns from emission to absorption in the middle of the dip phase.
6. Using a pair of Lyα and Heα lines, respectively, of H-like and He-like Mg, Si, S, and Fe, we derived the change of the ionization parameter as a function of the orbital phase (Figure 6.9). The ionization parameter value remains stable,

regardless of whether the pair appears in emission or absorption, suggesting that the photoionized plasma remains almost unchanged over an orbit.

The sampling frequency of the orbital spectral variation presented in this study is much denser than in the previous Cir X-1 studies (§ 3.3–3.4). Yet, we presented a much simpler spectral model. We recognize that some spectra yielded poor fitting, but they do not alter the overall interpretation presented here.

Purpose 2 "To construct a 3D geometry of the X-ray emitting and absorbing material of the system": Based on the spectral model that accounts for most observed spectral changes over an orbit, we constructed the 3D geometry of the X-ray emitting and absorbing material (Figure 7.1). We obtained the following results (§ 7.1).

7. In the proposed geometry, a plasma photoionized by the incident X-ray emission from the accretion disk and the neutron star is located radially outside of the accretion disk, not on its surface. The disk blackbody emission is blocked in the early dip phase because of a geometrically flared medium that is present only for a small azimuth angle range of the accretion disk. The medium has some density and fragmentation structure in its tail, the variation of which generates X-ray flux and spectral changes in the late dip and flaring phases (Figure 7.2).
8. Five rationales were given for the proposed geometry based on the observations.
   (a) The consistent presence of radiation from the disk blackbody component over the entire orbital period, which changes only gradually except once during the dip phase when the normalization increases (Figure 6.7).
   (b) Large variations in continuum flux are explained by the varying column density and the covering fraction through the dip and the flaring phase (Figure 6.7).
   (c) The highly-ionized Fe lines (Fe XXV Heα and Fe XXVI Lyα) change between emission and absorption through the orbit. This requires that the relative strength of the transmitted emission through and the diffuse emission of the plasma change as a function of the orbital phase (Figure 6.8).
   (d) The intensity variation of the line emission is much smaller than the continuum emission over an orbit. This suggests that a substantial portion of the photoionized plasma is not obstructed by the blocking material, unlike incident emission from the disk and neutron star (Figure 6.8).
   (e) The degree of ionization is almost constant for each element, regardless of whether they appear in emission or absorption. This indicates that the incident emission seen by the photoionized plasma does not change through the orbit (Figure 6.9).
9. We estimated the scales of the structures. The photoionized plasma is likely to have a stratified structure of different ξ responsible for different elements. For Fe, the inner radius of the plasma is $\sim 10^{10}$ cm from the ξ value and the outer radius is 1.1-2 times that of the maximum absorbing column. The inner plasma radius is larger than the typical value of the accretion disk outer radius of LMXBs.

We came to the conclusion that the photoionized plasma is located radially outside of the accretion disk. This is in contrast to some conventional views that such a plasma

is located on the surface of the accretion disk (e.g., Jimenez-Garate, Raymond, and Liedahl, 2002).

Purpose 3 "To apply the 3D radiative transfer calculation to several selected spectral features in the observations and explore its effectiveness and limitations.": Based on the proposed geometry, we applied radiative transfer modeling to interpret three remarkable features found in the observations. In addition to the *NICER* data used for the previous two purposes, we supplemented the *Suzaku* (§ 6.2) and *Chandra* (§ 6.3) data taken in different flux states and obtained the following results (§ 7.2).

Feature 1 "Changes between line emission and absorption through an orbit" (§ 7.2.1)

10. Changes between line emission and absorption through an orbit was modeled using `XSTAR` and `MONACO`. We targeted the Fe XXV Heα lines at 6.7 keV. The lines appear as emission in the *Suzaku* data taken in the low-flux state. They appear in emission during the dip phase of the *NICER* data and absorption during the flaring phase of the *NICER* data taken in the mid flux state (Figure 7.4).
11. We performed a radiative transfer calculation and decomposed the synthesized spectra into the transmitted, scattered, and diffuse components (Figure 7.5). We added these components with weights parameterized by α and β. Here, α is the parameter that represents the angle subtended by the photoionized plasma seen from the incident source, while β is the fraction of the incident source without being blocked in the line of sight (Figure 7.3).
12. With the two parameters, we qualitatively explained the equivalent width of the line and the continuum flux in the three observations (Figure 7.9). The long-term change from the *Suzaku* to *NICER* (dip phase) is best explained by the change of α, while the short-term change from *NICER* (dip phase) to *NICER* (flaring phase) was by the change of β. The column density of the photoionized plasma cannot be smaller than 10^{22} cm^{-2} since no absorption feature is expected in any combinations of α and β.

In previous studies (Brandt et al., 1996; Schulz et al., 2008; Schulz et al., 2020), photoionized plasma was used to explain the observed X-ray emission lines. However, there were two limitations: (1) a generic (power-law) form of the incident spectrum was used to calculate the photoionized plasma, which is different from the disk blackbody emission. (2) the incident flux required to account for the derived ionization degree (ξ) was inconsistent with the continuum flux that was actually observed. We overcome and settle these limitations and inconsistencies in this work.

Feature 2 "P Cygni line profile" (§ 7.2.2)

13. The P Cygni profile observed with *Chandra* in the high flux state was simulated with `MONACO` and `SKIRT` targeting at the Fe XXV Heα line. A radial velocity was introduced, and the elevation angle subtended by the photoionized plasma was used as a model parameter. The synthesized spectra were simulated separately for the transmitted and diffuse components at different viewing angles (Figure 7.11).

14. The red-shifted emission line was reproduced in the diffuse emission, while the blue-shifted absorption line was reproduced in the transmitted emission, with a viewing angle going through the photoionized plasma. The MONACO results were compared to the observation. The emission equivalent width is smaller than the observation, presumably due to a limitation of the simulation. The absorption column matches well between the observation and the simulation (Figure 7.12).
15. The profile of the line was also simulated. With no velocity field, the absorption feature shows a flat-bottom profile in the damping wing part of the curve of growth. The emission feature shows a Dijkstra profile for an extreme resonance scattering optical depth. At a fixed radial velocity of 1940 km s^{-1}, the emission feature becomes asymmetric due to the contribution of different projected velocities in the line of sight (Figure 7.14 and 7.18).

The P Cygni profile was successfully reproduced in the 3D radiative transfer calculation when the viewing angle goes through the photoionized plasma. The line profile was also simulated in a way that the theory of radiative transfer predicts. The profile was unresolved with the X-ray grating spectra (Brandt and Schulz, 2000) with a resolution of 30 eV, but will be resolved with the X-ray microcalorimeter spectra with a resolution of 5 eV. This result (Figure 7.14) clearly demonstrates the need to interpret the data based on the 3D radiative transfer modeling.

Feature 3 "X-ray light curve changes over an orbit" (§ 7.2.3)

16. X-ray light curve changes over an orbit was modeled using SKIRT. We placed a bulge, which is very thick (10^{25} cm^{-2}) and fully covers the incident emission for ∼15% of an orbit, and partial covering material, which is moderately thick (10^{24} cm^{-2}) and partially covers the incident emission for 50% of the orbit (Figure 7.19). The partial covering material is modeled with a number of grains with fixed total mass.
17. The X-ray light curve of the dip and flaring phases was well reproduced when the viewing angle is sufficiently large. When the viewing angle is small, no variation was simulated (Figure 7.20).

A long-standing controversy about Cir X-1 is whether it is observed in the face-on or edge-on geometry. Our findings both in features 2 and 3 strongly favor the edge-on geometry (Figure 7.21).

Purpose 4 "To reveal some of the debated parameters of Cir X-1 in comparison to some theoretical studies": We compare the results obtained by the 3D radiative transfer modeling (§ 7.2) with some theoretical works, and obtained new insights into some of the debated parameters of the mysterious source Cir X-1. We argue for the LMXB nature of Cir X-1, a high inclination angle of the system, and the photoionized plasma is located outward of the accretion disk.

18. We revised the argument claiming the HMXB nature of Cir X-1 based on the Doppler shift of Paschen series lines modulated by the orbital period in the optical spectra (Jonker, Nelemans, and Bassa, 2007). We found two difficulties to consider that these features are from the companion star: Doppler shift phase and Paschen

series lines in emission. The emission can be explained by the photoionized plasma as simulated by `CLOUDY` (Figure 7.22). If this is the case, the argument for the HMXB would be negated. If, at all, we accept that the Paschen series lines originate from the companion, the measured dynamical solution leads to a low mass companion for the large inclination angle (Figure 7.23), which is strongly suggested by our simulation to explain all three features (§ 7.2). We argue for the LMXB nature of Cir X-1.

19. The absence of an eclipse and the presence of dips constrain the viewing angle. For the eclipse, we constrain the inclination to be $\lesssim$75 deg. For the dips, we constrain the inclination to be $\gtrsim$60 deg. Regarding the dips, the interaction of the accretion stream and the accretion disk in LMXBs creates a bulge-like structure at the position where the stream hits the accretion disk. Some of the accreting matter bounces away from the disk and lands at different places of the accretion disk at a smaller radius. The bulge can cause a long dip in the dip phase, and the bounced material can cause the flaring phase and short dips in the stable phase as observed with *NICER* (Figure 6.1). This is consistent with our model (Figure 7.19), with which the varying X-ray flux was explained (Figure 7.20). We argue for the high inclination angle of Cir X-1.
20. The photoionized plasma is located outside the accretion disk in our model (Figure 7.2). The P Cygni profile is found in the line emission originating from the photoionized plasma. The outflowing motion of the photoionized plasma is launched close to the outer radius of the accretion disk. This is consistent with the theory of "excretion" flow. The accretion stream forms an accretion ring at a cirularization radius. A large fraction of the mass moves radially inward by losing angular momentum (accretion flow), while some fraction moves radially outward by gaining angular momentum to offset the loss (excretion flow). The estimated velocity is $\mathcal{O}(10^3)$ km s^{-1}, which is consistent with the derived velocity in the P Cygni profile.

Purpose 5 "To compare some numerical radiative transfer codes of different solvers and implementations, to clarify their differences and limitations, and to make some further development for our purpose": We used a 1D two-stream solver code `XSTAR` and 3D Monte Carlo solver codes `MONACO` and `SKIRT`. They have different assumptions, implementations, and limitations (§ 5.4). The difference between `MONACO` and `SKIRT` was summarized in Table 5.3. Through the application of these codes to real problems, we learned the following.

21. We made a comparison between `XSTAR` and `MONACO` component by component (Table 7.1). `XSTAR` tends to overestimate line intensity, while `MONACO` tends to underestimate it in the application to feature 1 (§ 7.2.1). The scattering, which is not included in `XSTAR`, plays a non-negligible role in the continuum flux.
22. We made a comparison between `XSTAR` and `SKIRT` component by component (Table 5.5). `XSTAR` tends to overestimate line intensity, while `SKIRT` tends to underestimate it compared to the expected line strength calculated by hand (§ 5.3.3.2).
23. We made an extension to `SKIRT` so that we can calculate NLTE line intensities in the X-ray band. We showed how this can be done for all major elements of all charge states. We benchmarked the result using the Mg XII Lyα line.

As described above, all codes have advantages and disadvantages. In our study, we used them in a hybrid manner, considering their strengths and limitations, to apply them to real problems. Although we strongly urge developers to develop the code to meet data quality, no codes can be perfect. We should consider taking a hybrid approach in the future as shown in this study.

8.2 Future Outlook

We end the thesis by leaving several suggestions for future research in the field, in particular in the era of the X-ray microcalorimeter spectrometers such as *XRISM* (Tashiro, 2023), *LEM* (Khabibullin et al., 2023), and *Athena* (Pajot et al., 2018).

Orbital coverage: First is the importance of the orbital coverage of binaries. This applies not only to the X-ray binaries studied here but also to CVs and stellar binaries. A uniform data set at high cadence was the key to disentangling the X-ray emission components of Cir X-1, which had no established spectral model. The spectral model as a function of the orbital phase allows the construction of the 3D geometry model, based on which the 3D radiative transfer calculation can be performed. X-ray microcalorimeter observations may be more costly and less flexible than *NICER*, but the orbital coverage should be explored.

3D radiative transfer: We hope that we convincingly demonstrated the need for a 3D radiative transfer calculation to interpret the X-ray spectra. This will be more relevant with the X-ray microcalorimeter, which has sufficient energy resolution to resolve the line profile. Spectral features in Figures 7.14 and 7.18 will be observed in many sources. Useful information, such as the density and velocity profile around compact objects, can be obtained only with 3D radiative transfer modeling.

In this study, we did not fit the model to the data to constrain the parameters of the 3D radiative transfer model. This is mainly due to the limited quality of the spectral data. Such a fitting is technically feasible and should be done when we obtain data of improved quality.

Multi-wavelength spectroscopy: We argued that the H Paschen series lines in the optical spectra could originate from a photoionized plasma at a large radius. With high-resolution spectroscopy at multiple wavelengths, we can access photoionized plasmas of different ionization degrees at different radii. The stratified structure of the plasma, which was assumed to be uniform in this study, can be revealed in this approach.

Application to other sources: The NLTE radiative transfer is required to synthesize the simulated spectra of photoionized plasmas. X-ray binaries and active galactic nuclei (AGNs) are the two most important classes of objects of X-ray-emitting photoionized plasmas. X-ray line spectroscopy and an interpretation based on 3D radiative transfer will be a fertile field. However, note that orbital coverage cannot be made for AGNs, unlike X-ray binaries. We should always be aware that everything is not azimuthally symmetric. Even for sources for which NLTE is not required, the line opacity effects may emerge, for which 3D radiative transfer will be a viable approach. Supernova remnants and clusters of galaxies are such examples.

Development of numerical codes: Although we found the effectiveness of the radiative transfer calculation, we encountered many inconsistencies among the codes available now. For example, we found that the two-stream solver `XSTAR` tends to overestimate the line intensities, while the two Monte Carlo solvers `MONACO` and `SKIRT` tend to underestimate them. The physical origins of all major discrepancies need to be understood and

verified with observations. We also encountered limitations. `XSTAR` does not calculate the scattering for its 1D nature. The Monte Carlo solver is a prospective approach to 3D problems. What we need is a Monte Carlo code that can calculate the NLTE radiative transfer in the X-ray band with flexible 3D geometry construction capabilities and modern acceleration techniques. Neither `MONACO` nor `SKIRT` satisfy this. We made some extensions to `SKIRT` to calculate the NLTE level populations, but not the charge population, consistently with the radiation field. We strongly encourage the development of radiative transfer codes that match the quality of contemporary observations.

References

Agostinelli, S. et al. (July 2003). "Geant4—a simulation toolkit". In: *Nuclear Instruments and Methods in Physics Research Section A: Accelerators, Spectrometers, Detectors and Associated Equipment* 506.3, pp. 250–303. ISSN: 01689002. DOI: 10.1016/S0168-9002(03)01368-8. URL: https://linkinghub.elsevier.com/retrieve/pii/S0168900203013688.

Allison, J. et al. (Feb. 2006). "Geant4 developments and applications". In: *IEEE Transactions on Nuclear Science* 53.1, pp. 270–278. ISSN: 0018-9499. DOI: 10.1109/TNS.2006.869826. URL: http://ieeexplore.ieee.org/document/1610988/.

Armstrong, R. P. et al. (Aug. 2013). "A return to strong radio flaring by Circinus X-1 observed with the Karoo Array Telescope test array KAT-7". In: *Monthly Notices of the Royal Astronomical Society* 433.3, pp. 1951–1957. ISSN: 1365-2966. DOI: 10.1093/mnras/stt860. arXiv: 1305.3399. URL: http://academic.oup.com/mnras/article/433/3/1951/1218025/A-return-to-strong-radio-flaring-by-Circinus-X1.

Armitage, P. J. and M. Livio (Oct. 1996). "Accretion Disks in Interacting Binaries: Simulations of the Stream-Disk Impact". In: *The Astrophysical Journal* 470, p. 1024. ISSN: 0004-637X. DOI: 10.1086/177928. URL: http://adsabs.harvard.edu/doi/10.1086/177928.

Armitage, P. J. and M. Livio (Feb. 1998). "Hydrodynamics of the Stream-Disk Impact in Interacting Binaries". In: *The Astrophysical Journal* 493.2, pp. 898–908. ISSN: 0004-637X. DOI: 10.1086/305149. URL: https://iopscience.iop.org/article/10.1086/305149.

Arnaud, K. A. (1996). "XSPEC: The First Ten Years". In: *Astronomical Data Analysis Software and Systems V , A.S.P. Conference Series* 101, p. 17.

Arzoumanian, Z. et al. (July 2014). "The neutron star interior composition explorer (NICER): mission definition". In: ed. by T. Takahashi, J.-W. A. den Herder, and M. Bautz, p. 914420. DOI: 10.1117/12.2056811. URL: http://proceedings.spiedigitallibrary.org/proceeding.aspx?doi=10.1117/12.2056811.

Asai, K. et al. (Aug. 2014). "Sudden end of X-ray outbursts around periastron of Circinus X-1 observed with MAXI". In: *Publications of the Astronomical Society of Japan* 66.4, p. 79. ISSN: 2053051X. DOI: 10.1093/pasj/psu054. arXiv: arXiv:1405.6021v1. URL: https://academic.oup.com/pasj/article-lookup/doi/10.1093/pasj/psu054.

Baes, M. et al. (Aug. 2003). "Radiative transfer in disc galaxies – III. The observed kinematics of dusty disc galaxies". In: *Monthly Notices of the Royal Astronomical Society* 343.4, pp. 1081–1094. ISSN: 0035-8711. DOI: 10.1046/j.1365-8711.2003.06770.x. URL: https://academic.oup.com/mnras/article/343/4/1081/1063844.

Baes, M. et al. (Oct. 2011). "EFFICIENT THREE-DIMENSIONAL NLTE DUST RADIATIVE TRANSFER WITH SKIRT". In: *The Astrophysical Journal Supplement Series* 196.2, p. 22. ISSN: 0067-0049. DOI: 10.1088/0067-0049/196/2/22. URL: https://iopscience.iop.org/article/10.1088/0067-0049/196/2/22.

Baes, M. et al. (June 2016). "Composite biasing in Monte Carlo radiative transfer". In: *Astronomy & Astrophysics* 590, A55. ISSN: 0004-6361. DOI: 10.1051/0004-6361/201528063. URL: http://www.aanda.org/10.1051/0004-6361/201528063.

Baes, M., P. Camps, and K. Matsumoto (Oct. 2022). "Monte Carlo radiative transfer with explicit absorption to simulate absorption, scattering, and stimulated emission". In: *Astronomy & Astrophysics* 666, A101. ISSN: 0004-6361. DOI: 10.1051/0004-6361/202244521. URL: https://www.aanda.org/10.1051/0004-6361/202244521.

Borkowski, K. J., W. J. Lyerly, and S. P. Reynolds (Feb. 2001). "Supernova Remnants in the Sedov Expansion Phase: Thermal X-Ray Emission". In: *The Astrophysical Journal* 548.2, pp. 820–835. ISSN: 0004-637X. DOI: 10.1086/319011. URL: https://iopscience.iop.org/article/10.1086/319011.

Boutloukos, S. et al. (Dec. 2006). "Discovery of Twin kHz QPOs in the Peculiar X-Ray Binary Circinus X-1". In: *The Astrophysical Journal* 653.2, pp. 1435–1444. ISSN: 0004-637X. DOI: 10.1086/508934. URL: https://iopscience.iop.org/article/10.1086/508934.

Brandt, W. N. and N. S. Schulz (Dec. 2000). "The Discovery of Broad P Cygni X-Ray Lines from Circinus X-1 with the [ITAL]Chandra[/ITAL] High-Energy Transmission Grating Spectrometer". In: *The Astrophysical Journal* 544.2, pp. L123–L127. ISSN: 0004637X. DOI: 10.1086/317313. URL: https://iopscience.iop.org/article/10.1086/317313.

Brandt, W. N. et al. (Dec. 1996). "ASCA observations of the iron K complex of Circinus X-1 near zero phase: spectral evidence for partial covering". In: *Monthly Notices of the Royal Astronomical Society* 283.3, pp. 1071–1082. ISSN: 0035-8711. DOI: 10.1093/mnras/283.3.1071. URL: https://academic.oup.com/mnras/article-lookup/doi/10.1093/mnras/283.3.1071.

Brinkman, A. C. et al. (July 2000). "<title>Description and performance of the low-energy transmission grating spectrometer on board Chandra</title>". In: ed. by J. E. Truemper and B. Aschenbach, pp. 81–90. DOI: 10.1117/12.391599. URL: http://proceedings.spiedigitallibrary.org/proceeding.aspx?articleid=899849.

Calvelo, D. E. et al. (Jan. 2012). "Millimetre observations of a sub-arcsecond jet from Circinus X-1". In: *Monthly Notices of the Royal Astronomical Society: Letters* 419.1, pp. L54–L58. ISSN: 17453925. DOI: 10.1111/j.1745-3933.2011.01175.x. URL: https://academic.oup.com/mnrasl/article-lookup/doi/10.1111/j.1745-3933.2011.01175.x.

Camps, P. and M. Baes (Mar. 2015). "SKIRT: An advanced dust radiative transfer code with a user-friendly architecture". In: *Astronomy and Computing* 9, pp. 20–33. ISSN: 22131337. DOI: 10.1016/j.ascom.2014.10.004. URL: https://linkinghub.elsevier.com/retrieve/pii/S2213133714000511.

Camps, P. and M. Baes (Apr. 2020). "SKIRT 9: Redesigning an advanced dust radiative transfer code to allow kinematics, line transfer and polarization by aligned dust grains". In: *Astronomy and Computing* 31, p. 100381. ISSN: 22131337. DOI: 10.1016/j.ascom.2020.100381. URL: https://linkinghub.elsevier.com/retrieve/pii/S2213133720300354.

Canizares, C. R. et al. (Oct. 2005). "The Chandra High-Energy Transmission Grating: Design, Fabrication, Ground Calibration, and 5 Years in Flight". In: *Publications of the Astronomical Society of the Pacific* 117.836, pp. 1144–1171. ISSN: 0004-6280. DOI: 10.1086/432898. URL: http://iopscience.iop.org/article/10.1086/432898.

Casares, J. et al. (June 2003). "Bowen Fluorescence from the Companion Star in X1822−371". In: *The Astrophysical Journal* 590.2, pp. 1041–1048. ISSN: 0004-637X. DOI: 10.1086/375055. URL: https://iopscience.iop.org/article/10.1086/375055.

Chakraborty, P. et al. (Oct. 2020a). "Cloudy in the Microcalorimeter Era: Improved Energies for Kα Transitions". In: *Research Notes of the AAS* 4.10, p. 184. ISSN: 2515-5172. DOI: 10.3847/2515-5172/abc1dd. URL: https://iopscience.iop.org/article/10.3847/2515-5172/abc1dd.

Chakraborty, P. et al. (Sept. 2020b). "X-Ray Spectroscopy in the Microcalorimeter Era. I. Effects of Fe xxiv Resonant Auger Destruction on Fe xxv Kα Spectra". In: *The Astrophysical Journal* 901.1, p. 68. ISSN: 0004-637X. DOI: 10.3847/1538-4357/abaaab. URL: https://iopscience.iop.org/article/10.3847/1538-4357/abaaab.

Chakraborty, P. et al. (Sept. 2020c). "X-Ray Spectroscopy in the Microcalorimeter Era. II. A New Diagnostic on Column Density from the Case A to B Transition in H- and He-like Iron". In: *The Astrophysical Journal* 901.1, p. 69. ISSN: 0004-637X. DOI: 10.3847/1538-4357/abaaac. URL: https://iopscience.iop.org/article/10.3847/1538-4357/abaaac.

Chakraborty, P. et al. (May 2021). "X-Ray Spectroscopy in the Microcalorimeter Era. III. Line Formation under Case A, Case B, Case C, and Case D in H- and He-like Iron for a Photoionized Cloud". In: *The Astrophysical Journal* 912.1, p. 26. ISSN: 0004-637X. DOI: 10.3847/1538-4357/abed4a. URL: https://iopscience.iop.org/article/10.3847/1538-4357/abed4a.

Chakraborty, P. et al. (Aug. 2022). "X-Ray Spectroscopy in the Microcalorimeter Era 4: Optical Depth Effects on the Soft X-Rays Studied with Cloudy". In: *The Astrophysical Journal* 935.2, p. 70. ISSN: 0004-637X. DOI: 10.3847/1538-4357/ac7eb9. URL: https://iopscience.iop.org/article/10.3847/1538-4357/ac7eb9.

Chandra-IPI-Teams (2022). *The Chandra Proposers' Observatory Guide*. Tech. rep.

Chen, G.-X., A. K. Pradhan, and W. Eissner (Feb. 2003). "Breit Pauli R -matrix calculations for electron impact excitation of Fe XVII: a benchmark study". In: *Journal of Physics B: Atomic, Molecular and Optical Physics* 36.3, pp. 453–477. ISSN: 0953-4075. DOI: 10.1088/0953-4075/36/3/305. URL: https://iopscience.iop.org/article/10.1088/0953-4075/36/3/305.

Clark, J. S. et al. (Mar. 2003). "Near IR spectroscopy of the X-ray binary Circinus X-1". In: *Astronomy & Astrophysics* 400.2, pp. 655–658. ISSN: 0004-6361. DOI: 10.1051/0004-6361:20030017. URL: http://www.aanda.org/10.1051/0004-6361:20030017.

Clarkson, W. I., P. A. Charles, and N. Onyett (Feb. 2004). "X-ray behaviour of Circinus X-1 - I. X-ray dips as a diagnostic of periodic behaviour". In: *Monthly Notices of the Royal Astronomical Society* 348.2, pp. 458–468. ISSN: 00358711. DOI: 10.1111/j.1365-2966.2004.07293.x. URL: https://academic.oup.com/mnras/article-lookup/doi/10.1111/j.1365-2966.2004.07293.x.

Clark, D. H., J. H. Parkinson, and J. L. Caswell (Apr. 1975). "Is Cir X-1 a runaway binary?" In: *Nature* 254.5502, pp. 674–676. ISSN: 0028-0836. DOI: 10.1038/254674a0. URL: https://www.nature.com/articles/254674a0.pdf?origin=ppub%20http://www.nature.com/articles/254674a0%20https://www.nature.com/articles/254674a0.

Coriat, M. et al. (Apr. 2019). "The twisted jets of Circinus X-1". In: *Monthly Notices of the Royal Astronomical Society* 484.2, pp. 1672–1686. ISSN: 0035-8711. DOI: 10.1093/mnras/stz099. URL: https://academic.oup.com/mnras/article/484/2/1672/5287997.

D'Aì, A. et al. (July 2012). "A complete X-ray spectral coverage of the 2010 May–June outbursts of Circinus X-1". In: *Astronomy & Astrophysics* 543, A20. ISSN: 0004-6361. DOI: 10.1051/0004-6361/201118577. URL: http://www.aanda.org/10.1051/0004-6361/201118577.

Di Salvo, T. et al. (Dec. 2000). "The Discovery of a State-Dependent Hard Tail in the X-Ray Spectrum of the Luminous Z Source GX 17+2". In: *The Astrophysical Journal* 544.2, pp. L119–L122. ISSN: 0004637X. DOI: 10.1086/317309. URL: https://iopscience.iop.org/article/10.1086/317309.

Di Salvo, T. et al. (June 2001). "Detection of a Hard Tail in the X-Ray Spectrum of the Z Source GX 349+2". In: *The Astrophysical Journal* 554.1, pp. 49–55. ISSN: 0004-637X. DOI: 10.1086/321353. URL: https://iopscience.iop.org/article/10.1086/321353.

Díaz Trigo, M. et al. (Jan. 2006). "Spectral changes during dipping in low-mass X-ray binaries due to highly-ionized absorbers". In: *Astronomy & Astrophysics* 445.1, pp. 179–195. ISSN: 0004-6361. DOI: 10.1051/0004-6361:20053586. URL: http://www.aanda.org/10.1051/0004-6361:20053586.

Dijkstra, M., Z. Haiman, and M. Spaans (Sept. 2006). "Lyα Radiation from Collapsing Protogalaxies. I. Characteristics of the Emergent Spectrum". In: *The Astrophysical Journal* 649.1, pp. 14–36. ISSN: 0004-637X. DOI: 10.1086/506243. URL: https://iopscience.iop.org/article/10.1086/506243.

Ding, G. Q., J. L. Qu, and T. P. Li (Mar. 2006). "Partial Covering during Long-Term Dips in Circinus X-1". In: *The Astronomical Journal* 131.3, pp. 1693–1701. ISSN: 0004-6256. DOI: 10.1086/499921. URL: https://iopscience.iop.org/article/10.1086/499921.

Ding, G., C. Huang, and J. Qu (2012). "The Orbital Modulation for the Spectrum and Mass Accretion Rate in Circinus X-1". In: *International Journal of Astronomy and Astrophysics* 02.04, pp. 256–265. ISSN: 2161-4717. DOI: 10.4236/ijaa.2012.24033. URL: http://www.scirp.org/journal/doi.aspx?DOI=10.4236/ijaa.2012.24033.

Dumont, A.-M. et al. (Aug. 2003). "Escape probability methods versus "exact" transfer for modelling the X-ray spectrum of Active Galactic Nuclei and X-ray binaries". In: *Astronomy & Astrophysics* 407.1, pp. 13–30. ISSN: 0004-6361. DOI: 10.1051/0004-6361:20030890. URL: http://www.aanda.org/10.1051/0004-6361:20030890.

Eggleton, P. P. (May 1983). "Approximations to the radii of Roche lobes". In: *The Astrophysical Journal* 268, p. 368. ISSN: 0004-637X. DOI: 10.1086/160960. URL: http://adsabs.harvard.edu/doi/10.1086/160960.

Fender, R. et al. (Jan. 2004). "An ultra-relativistic outflow from a neutron star accreting gas from a companion". In: *Nature* 427.6971, pp. 222–224. ISSN: 0028-0836. DOI: 10.1038/nature02137. URL: https://pos.sissa.it/056/037%20http://www.nature.com/articles/nature02137.

Flannery, B. P. and J. Faulkner (Feb. 1975). "The Location of the Hot Spot in Cataclysmic Variable Stars as Determined from Particle Trajectories". In: *Monthly Notices of the Royal Astronomical Society* 170.2, pp. 325–331. ISSN: 0035-8711. DOI:

10.1093/mnras/170.2.325. URL: https://academic.oup.com/mnras/article-lookup/doi/10.1093/mnras/170.2.325.

Foster, A. R. et al. (Sept. 2012). "UPDATED ATOMIC DATA AND CALCULATIONS FOR X-RAY SPECTROSCOPY". In: *The Astrophysical Journal* 756.2, p. 128. ISSN: 0004-637X. DOI: 10.1088/0004-637X/756/2/128. URL: https://iopscience.iop.org/article/10.1088/0004-637X/756/2/128.

Foster, A. R. and K. Heuer (Aug. 2020). "PyAtomDB: Extending the AtomDB Atomic Database to Model New Plasma Processes and Uncertainties". In: *Atoms* 8.3, p. 49. ISSN: 2218-2004. DOI: 10.3390/atoms8030049. URL: https://www.mdpi.com/2218-2004/8/3/49.

Frank, J., A. King, and D. J. Raine (Jan. 2002). *Accretion Power in Astrophysics*. 2nd ed. Cambridge, UK: Cambridge University Press, pp. xi–xii. ISBN: 9780521629577. DOI: 10.1017/CBO9781139164245. URL: https://www.cambridge.org/core/product/identifier/CBO9781139164245A008/type/book%7B%5C_%7Dpart%20https://www.cambridge.org/core/product/identifier/9781139164245/type/book.

Frank, J. ; A. R. ; King, and J. .-. Lasota (1987). "The light curves of low-mass X-ray binaries." In: *Astronomy and Astrophysics* 178, pp. 137–142.

Fruscione, A. et al. (June 2006). "CIAO: Chandra's data analysis system". In: ed. by D. R. Silva and R. E. Doxsey, p. 62701V. DOI: 10.1117/12.671760. URL: http://proceedings.spiedigitallibrary.org/proceeding.aspx?doi=10.1117/12.671760.

Garmire, G. P. et al. (Mar. 2003). "Advanced CCD imaging spectrometer (ACIS) instrument on the Chandra X-ray Observatory". In: *Proceedings of SPIE*. Ed. by J. E. Truemper and H. D. Tananbaum, p. 28. DOI: 10.1117/12.461599. URL: http://proceedings.spiedigitallibrary.org/proceeding.aspx?doi=10.1117/12.461599.

Geldzahler, B. J. ; T. ; Pauls, and C. J. Salter (1980). "Continuum observations of the SNR W50 and G 74.9+1.2 at 2695 MHz." In: *Astronomy and Astrophysics* 84, pp. 237–244.

Gendreau, K. C., Z. Arzoumanian, and T. Okajima (Sept. 2012). "The Neutron star Interior Composition ExploreR (NICER): an Explorer mission of opportunity for soft x-ray timing spectroscopy". In: *Proceedings of SPIE*. Ed. by T. Takahashi, S. S. Murray, and J.-W. A. den Herder, p. 844313. DOI: 10.1117/12.926396. URL: http://proceedings.spiedigitallibrary.org/proceeding.aspx?doi=10.1117/12.926396.

Gendreau, K. C. et al. (July 2016). "The Neutron star Interior Composition Explorer (NICER): design and development". In: *Proceedings of SPIE*. Ed. by J.-W. A. den Herder, T. Takahashi, and M. Bautz, 99051H. DOI: 10.1117/12.2231304. URL: http://proceedings.spiedigitallibrary.org/proceeding.aspx?doi=10.1117/12.2231304.

Goodall, P. T., F. Alouani-Bibi, and K. M. Blundell (July 2011). "When microquasar jets and supernova collide: hydrodynamically simulating the SS 433-W 50 interaction". In: *Monthly Notices of the Royal Astronomical Society* 414.4, pp. 2838–2859. ISSN: 00358711. DOI: 10.1111/j.1365-2966.2011.18388.x. URL: https://academic.oup.com/mnras/article-lookup/doi/10.1111/j.1365-2966.2011.18388.x.

Goss, W. M. and U. Mebold (Nov. 1977). "The distance of Cir X-1". In: *Monthly Notices of the Royal Astronomical Society* 181.2, pp. 255–258. ISSN: 0035-8711. DOI: 10.

1093/mnras/181.2.255. URL: https://academic.oup.com/mnras/article-lookup/doi/10.1093/mnras/181.2.255.

Grevesse, N., A. Noels, and A. Sauval (1996). "Cosmic Abundances". In: *ASP Conference Series* 99.

Groot, P. J., R. G. M. Rutten, and J. van Paradijis (2001). "SW Sextantis in an excited, low state". In: *Astronomy and Astrophysics* 368, pp. 183–196.

Hagino, K. et al. (Oct. 2016). "A disc wind interpretation of the strong Fe Kα features in 1H 0707−495". In: *Monthly Notices of the Royal Astronomical Society* 461.4, pp. 3954–3963. ISSN: 0035-8711. DOI: 10.1093/mnras/stw1579. URL: https://academic.oup.com/mnras/article-lookup/doi/10.1093/mnras/stw1579.

Hakkila, J. et al. (Nov. 1997). "A Computerized Model of Large-Scale Visual Interstellar Extinction". In: *The Astronomical Journal* 114, p. 2043. ISSN: 00046256. DOI: 10.1086/118624. URL: http://adsabs.harvard.edu/cgi-bin/bib%7B%5C_%7Dquery?1997AJ....114.2043H.

Hamilton, A. J. S., R. A. Chevalier, and C. L. Sarazin (Jan. 1983). "X-ray line emission from supernova remnants. I - Models for adiabatic remnants". In: *The Astrophysical Journal Supplement Series* 51, p. 115. ISSN: 0067-0049. DOI: 10.1086/190841. URL: http://adsabs.harvard.edu/doi/10.1086/190841.

Harrington, J. P. (May 1973). "The Scattering of Resonance-line Radiation in the Limit of Large Optical Depth". In: *Monthly Notices of the Royal Astronomical Society* 162.1, pp. 43–52. ISSN: 0035-8711. DOI: 10.1093/mnras/162.1.43. URL: https://academic.oup.com/mnras/article-lookup/doi/10.1093/mnras/162.1.43.

Heinz, S. et al. (Dec. 2013). "THE YOUNGEST KNOWN X-RAY BINARY: CIRCINUS X-1 AND ITS NATAL SUPERNOVA REMNANT". In: *The Astrophysical Journal* 779.2, p. 171. ISSN: 0004-637X. DOI: 10.1088/0004-637X/779/2/171. arXiv: 1312.0632. URL: https://iopscience.iop.org/article/10.1088/0004-637X/779/2/171.

Heinz, S. et al. (June 2015). "LORD OF THE RINGS: A KINEMATIC DISTANCE TO CIRCINUS X-1 FROM A GIANT X-RAY LIGHT ECHO". In: *The Astrophysical Journal* 806.2, p. 265. ISSN: 1538-4357. DOI: 10.1088/0004-637X/806/2/265. URL: https://iopscience.iop.org/article/10.1088/0004-637X/806/2/265.

Hellier, C. (1996). "V1315 Aquilae and the Nature of SW Sextantis Stars". In: *Astrophysical Journal* 471, p. 949. DOI: 10.1086/178021.

Hjellming, R. M. and K. J. Johnston (June 1981). "An analysis of the proper motions of SS 433 radio jets". In: *The Astrophysical Journal* 246, p. L141. ISSN: 0004-637X. DOI: 10.1086/183571. URL: http://adsabs.harvard.edu/doi/10.1086/183571.

Hubeny, I. et al. (Oct. 2001). "Non-LTE Models and Theoretical Spectra of Accretion Disks in Active Galactic Nuclei. IV. Effects of Compton Scattering and Metal Opacities". In: *The Astrophysical Journal* 559.2, pp. 680–702. ISSN: 0004-637X. DOI: 10.1086/322344. URL: https://iopscience.iop.org/article/10.1086/322344.

Hynes, R. I. et al. (2001). "Doppler Tomography of XTE J2123-058 and Other Neutron Star LMXBs". In: *Astrotomography. Lecture Notes in Physics* 573. DOI: https://doi.org/10.1007/3-540-45339-3_26. arXiv: 0008145v1 [astro-ph].

Iaria, R. et al. (Jan. 2001a). "A Hard Tail in the X-Ray Broadband Spectrum of Circinus X-1 at the Periastron: A Peculiar Z Source". In: *The Astrophysical Journal* 547.1, pp. 412–419. ISSN: 0004-637X. DOI: 10.1086/318366. URL: https://iopscience.iop.org/article/10.1086/318366.

Iaria, R. et al. (Nov. 2001b). "Spectral Evolution of Circinus X-1 along Its Orbit". In: *The Astrophysical Journal* 561.1, pp. 321–328. ISSN: 0004-637X. DOI: 10.1086/323226. URL: https://iopscience.iop.org/article/10.1086/323226.

Iaria, R. et al. (Mar. 2002). "Study of the Circinus X-1 Broadband Spectrum at Orbital Phases Close to the Apoastron". In: *The Astrophysical Journal* 567.1, pp. 503–509. ISSN: 0004-637X. DOI: 10.1086/338507. URL: https://iopscience.iop.org/article/10.1086/338507.

Iaria, R. et al. (Jan. 2005). "On the Soft Excess in the X-Ray Spectrum of Circinus X-1: Revisitation of the Distance to Circinus X-1". In: *The Astrophysical Journal* 619.1, pp. 503–516. ISSN: 0004-637X. DOI: 10.1086/426422. URL: https://iopscience.iop.org/article/10.1086/426422.

Iaria, R. et al. (Feb. 2008). "Chandra Observation of Cir X-1 near the Periastron Passage: Evidence for an X-Ray Jet?" In: *The Astrophysical Journal* 673.2, pp. 1033–1043. ISSN: 0004-637X. DOI: 10.1086/524311. URL: https://iopscience.iop.org/article/10.1086/524311.

Inoue, H. (Aug. 2021). "Properties of the accretion ring in an X-ray binary, and accretion and excretion two-layer flows from it". In: *Publications of the Astronomical Society of Japan* 73.4, pp. 795–808. ISSN: 0004-6264. DOI: 10.1093/pasj/psab043. URL: https://academic.oup.com/pasj/article/73/4/795/6283756.

Jansen, F. et al. (Jan. 2001). "XMM-Newton observatory". In: *Astronomy & Astrophysics* 365.1, pp. L1–L6. ISSN: 0004-6361. DOI: 10.1051/0004-6361:20000036. URL: http://www.aanda.org/10.1051/0004-6361:20000036.

Jimenez-Garate, M. A., J. C. Raymond, and D. A. Liedahl (Dec. 2002). "The Structure and X-Ray Recombination Emission of a Centrally Illuminated Accretion Disk Atmosphere and Corona". In: *The Astrophysical Journal* 581.2, pp. 1297–1327. ISSN: 0004-637X. DOI: 10.1086/344364. URL: https://iopscience.iop.org/article/10.1086/344364.

Johnston, H. M. et al. (Dec. 2001). "Secular and orbital variability of Cir X-1 observed in optical spectra". In: *Monthly Notices of the Royal Astronomical Society* 328.4, pp. 1193–1199. ISSN: 00358711. DOI: 10.1046/j.1365-8711.2001.04963.x. URL: https://academic.oup.com/mnras/article-lookup/doi/10.1046/j.1365-8711.2001.04963.x.

Johnston, H. M., R. Soria, and J. Gibson (Feb. 2016). "The nature of the companion star in Circinus X-1". In: *Monthly Notices of the Royal Astronomical Society* 456.1, pp. 347–355. ISSN: 0035-8711. DOI: 10.1093/mnras/stv2669. URL: https://academic.oup.com/mnras/article-lookup/doi/10.1093/mnras/stv2669.

Johnston, H. M., R. Fender, and K. Wu (Sept. 1999). "High-resolution optical and infrared spectroscopic observations of Cir X-1". In: *Monthly Notices of the Royal Astronomical Society* 308.2, pp. 415–423. ISSN: 0035-8711. DOI: 10.1046/j.1365-8711.1999.02702.x. URL: https://academic.oup.com/mnras/article/308/2/415/1046994.

Jonker, P. G. and G. Nelemans (Oct. 2004). "The distances to Galactic low-mass X-ray binaries: consequences for black hole luminosities and kicks". In: *Monthly Notices of the Royal Astronomical Society* 354.2, pp. 355–366. ISSN: 00358711. DOI: 10.1111/j.1365-2966.2004.08193.x. URL: https://academic.oup.com/mnras/article-lookup/doi/10.1111/j.1365-2966.2004.08193.x.

Jonker, P. G., G. Nelemans, and C. G. Bassa (Jan. 2007). "Detection of the radial velocity curve of the B5-A0 supergiant companion star of Cir X-1?" In: *Monthly Notices of the Royal Astronomical Society* 374.3, pp. 999–1005. ISSN: 0035-8711. DOI: 10.1111/j.1365-2966.2006.11210.x. URL: https://academic.oup.com/mnras/article-lookup/doi/10.1111/j.1365-2966.2006.11210.x.

Kaastra, J. S., R. ; Mewe, and H. Nieuwenhuijzen (1996). "SPEX: a new code for spectral analysis of X & UV spectra." In: *11th Colloquium on UV and X-ray Spectroscopy of Astrophysical and Laboratory Plasmas*, pp. 411–414.

Kallman, T. and M. Bautista (Mar. 2001). "Photoionization and High-Density Gas". In: *The Astrophysical Journal Supplement Series* 133.1, pp. 221–253. ISSN: 0067-0049. DOI: 10.1086/319184. URL: https://iopscience.iop.org/article/10.1086/319184.

Kallman, T. R. et al. (Dec. 2004). "Photoionization Modeling and the K Lines of Iron". In: *The Astrophysical Journal Supplement Series* 155.2, pp. 675–701. ISSN: 0067-0049. DOI: 10.1086/424039. URL: https://iopscience.iop.org/article/10.1086/424039.

Kallman, T. R. and R. McCray (Dec. 1982). "X-ray nebular models". In: *The Astrophysical Journal Supplement Series* 50, p. 263. ISSN: 0067-0049. DOI: 10.1086/190828. URL: http://adsabs.harvard.edu/doi/10.1086/190828.

Kelley, R. L. et al. (Jan. 2007). "The Suzaku High Resolution X-Ray Spectrometer". In: *Publications of the Astronomical Society of Japan* 59.sp1, S77–S112. ISSN: 0004-6264. DOI: 10.1093/pasj/59.sp1.S77. URL: https://academic.oup.com/pasj/article-lookup/doi/10.1093/pasj/59.sp1.S77.

Khabibullin, I. et al. (2023). *LEM All-Sky Survey: Soft X-ray Sky at Microcalorimeter Resolution*. Tech. rep. DOI: https://doi.org/10.48550/arXiv.2310.16038. arXiv: /doi.org/10.48550/arXiv.2310.16038 [https:].

Kinkhabwala, A. et al. (Aug. 2002). "XMM-Newton Reflection Grating Spectrometer Observations of Discrete Soft X-Ray Emission Features from NGC 1068". In: *The Astrophysical Journal* 575.2, pp. 732–746. ISSN: 0004-637X. DOI: 10.1086/341482. URL: https://iopscience.iop.org/article/10.1086/341482.

Klein, O. and Y. Nishina (Nov. 1929). "Über die Streuung von Strahlung durch freie Elektronen nach der neuen relativistischen Quantendynamik von Dirac". In: *Zeitschrift für Physik* 52.11-12, pp. 853–868. ISSN: 0044-3328. DOI: 10.1007/BF01366453. URL: http://link.springer.com/10.1007/BF01366453.

Klis, M. van der (2006). "Rapid X-ray Variability". In: *Compact stellar X-ray sources. Edited by Walter Lewin & Michiel van der Klis. Cambridge Astrophysics Series, No. 39. Cambridge, UK: Cambridge University Press*, pp. 39–112. ISBN: 978-0-521-82659-4. DOI: 10.2277/0521826594.

Koyama, K. et al. (Jan. 2007). "X-Ray Imaging Spectrometer (XIS) on Board Suzaku". In: *Publications of the Astronomical Society of Japan* 59.sp1, S23–S33. ISSN: 0004-6264. DOI: 10.1093/pasj/59.sp1.S23. URL: https://academic.oup.com/pasj/article-lookup/doi/10.1093/pasj/59.sp1.S23.

Kunze, S., R. Speith, and F. V. Hessman (Apr. 2001). "Substantial stream-disc overflow found in three-dimensional SPH simulations of cataclysmic variables". In: *Monthly Notices of the Royal Astronomical Society* 322.3, pp. 499–514. ISSN: 0035-8711. DOI: 10.1046/j.1365-8711.2001.04057.x. URL: https://academic.oup.com/mnras/article/322/3/499/952521.

Kwan, J. and J. H. Krolik (Nov. 1981). "The formation of emission lines in quasars and Seyfert nuclei". In: *The Astrophysical Journal* 250, p. 478. ISSN: 0004-637X. DOI: 10.1086/159395. URL: http://adsabs.harvard.edu/doi/10.1086/159395.

Lei, Y.-J. et al. (Oct. 2007). "X-ray Spectroscopy of Dips of Cir X-1". In: *Chinese Journal of Astronomy and Astrophysics* 7.5, pp. 693–704. ISSN: 1009-9271. DOI: 10.1088/1009-9271/7/5/10. URL: https://iopscience.iop.org/article/10.1088/1009-9271/7/5/10.

Linares, M. et al. (Aug. 2010). "THE RETURN OF THE BURSTS: THERMONUCLEAR FLASHES FROM CIRCINUS X-1". In: *The Astrophysical Journal* 719.1, pp. L84–L89. ISSN: 2041-8205. DOI: 10.1088/2041-8205/719/1/L84. URL: https://iopscience.iop.org/article/10.1088/2041-8205/719/1/L84.

Liu, Q. Z., J. van Paradijs, and E. P. J. van den Heuvel (Mar. 2001). "A catalogue of low-mass X-ray binaries". In: *Astronomy & Astrophysics* 368.3, pp. 1021–1054. ISSN: 0004-6361. DOI: 10.1051/0004-6361:20010075. URL: http://www.aanda.org/10.1051/0004-6361:20010075.

Lubow, S. H. and F. H. Shu (June 1975). "Gas dynamics of semidetached binaries". In: *The Astrophysical Journal* 198, p. 383. ISSN: 0004-637X. DOI: 10.1086/153614. URL: http://adsabs.harvard.edu/doi/10.1086/153614.

Lubow, S. H. and F. H. Shu (July 1976). "Gas dynamics of semidetached binaries. II - The vertical structure of the stream". In: *The Astrophysical Journal* 207, p. L53. ISSN: 0004-637X. DOI: 10.1086/182177. URL: http://adsabs.harvard.edu/doi/10.1086/182177.

Lubow, S. H. (May 1989). "On the dynamics of mass transfer over an accretion disk". In: *The Astrophysical Journal* 340, p. 1064. ISSN: 0004-637X. DOI: 10.1086/167458. URL: http://adsabs.harvard.edu/doi/10.1086/167458.

Makishima, K. et al. (Sept. 1986). "Simultaneous X-ray and optical observations of GX 339-4 in an X-ray high state". In: *The Astrophysical Journal* 308, p. 635. ISSN: 0004-637X. DOI: 10.1086/164534. URL: http://adsabs.harvard.edu/doi/10.1086/164534%20https://ui.adsabs.harvard.edu/abs/1986ApJ...308..635M/abstract.

Margon, B. et al. (Oct. 1971). "A Pulsing X-Ray Source in Circinus". In: *The Astrophysical Journal* 169, p. L23. ISSN: 0004-637X. DOI: 10.1086/180806. URL: http://adsabs.harvard.edu/doi/10.1086/180806.

Matsuoka, M. et al. (Oct. 2009). "The MAXI Mission on the ISS: Science and Instruments for Monitoring All-Sky X-Ray Images". In: *Publications of the Astronomical Society of Japan* 61.5, pp. 999–1010. ISSN: 0004-6264. DOI: 10.1093/pasj/61.5.999. arXiv: 0906.0631. URL: https://academic.oup.com/pasj/article-abstract/61/5/999/1593752%20https://academic.oup.com/pasj/article-lookup/doi/10.1093/pasj/61.5.999.

Matsumoto, K. et al. (2023). "Self-consistent dust and non-LTE line radiative transfer with SKIRT". In: *Astronomy & Astrophysics*. DOI: https://doi.org/10.48550/arXiv.2309.02628.

Mignani, R. P. et al. (May 2002). "HST observations rule out the association between Cir X-1 and SNR G321.9-0.3". In: *Astronomy & Astrophysics* 386.2, pp. 487–491. ISSN: 0004-6361. DOI: 10.1051/0004-6361:20020224. URL: http://www.aanda.org/10.1051/0004-6361:20020224.

Mignani, R., P. A. Caraveo, and G. F. Bignami (1997). "Asymmetric Hα disk emission dominates the HST/FOS spectrum of Circinus X-1." In: *Astronomy & Astrophysics* 323, pp. 797–800.

Mihara, T. et al. (Nov. 2011). "Gas Slit Camera (GSC) onboard MAXI on ISS". In: *Publications of the Astronomical Society of Japan* 63.sp3, S623–S634. ISSN: 0004-6264. DOI: 10.1093/pasj/63.sp3.S623. arXiv: arXiv:1103.4224. URL: https://academic.oup.com/pasj/article-lookup/doi/10.1093/pasj/63.sp3.S623.

Mitsuda, K. et al. (Jan. 2007). "The X-Ray Observatory Suzaku". In: *Publications of the Astronomical Society of Japan* 59.sp1, S1–S7. ISSN: 0004-6264. DOI: 10.1093/pasj/59.sp1.S1. URL: https://academic.oup.com/pasj/article-lookup/doi/10.1093/pasj/59.sp1.S1.

Mitsuda, K. et al. (1984). "Energy spectra of low-mass binary X-ray sources observed from Tenma." In: *Publications of the Astronomical Society of Japan* 36.4, pp. 741–759. URL: https://ui.adsabs.harvard.edu/abs/1984PASJ...36..741M/abstract.

Mizumoto, M. et al. (Feb. 2019). "X-ray reverberation lags of the Fe–K line due to AGN disc winds". In: *Monthly Notices of the Royal Astronomical Society* 482.4, pp. 5316–5326. ISSN: 0035-8711. DOI: 10.1093/mnras/sty3056. URL: https://academic.oup.com/mnras/article/482/4/5316/5174972.

Murray, S. S. et al. (July 2000). "<title>In-flight performance of the Chandra high-resolution camera</title>". In: ed. by J. E. Truemper and B. Aschenbach, pp. 68–80. DOI: 10.1117/12.391591. URL: http://proceedings.spiedigitallibrary.org/proceeding.aspx?articleid=899845.

Murdin, P. et al. (1980). "Binary model of CIR X-1 ." In: *Astronomy and Astrophysics* 87, pp. 292–298.

Nakamura, F. et al. (2022). *[Fundamentals of Radiative Processes] Fukusha Sokatei no Kiso (in Japanese)*. 1st ed. NIPPON HYORON SHA CO.,LTD., p. 365. ISBN: 9784535603431.

Nasa High Energy Astrophysics Science Archive Research Center (Heasarc) (2014). *HEAsoft: Unified Release of FTOOLS and XANADU*. URL: https://ui.adsabs.harvard.edu/abs/2014ascl.soft08004N.

Neufeld, D. A. (Apr. 1991). "The escape of Lyman-alpha radiation from a multiphase interstellar medium". In: *The Astrophysical Journal* 370, p. L85. ISSN: 0004-637X. DOI: 10.1086/185983. URL: http://adsabs.harvard.edu/doi/10.1086/185983.

Nicolson, G. D. (2007). "Circinus X-1 – Return to high radio flaring state". In: *The Astronomer's Telegram*, pp. 985, 1.

Odaka, H. et al. (Oct. 2011). "X-RAY DIAGNOSTICS OF GIANT MOLECULAR CLOUDS IN THE GALACTIC CENTER REGION AND PAST ACTIVITY OF Sgr A*". In: *The Astrophysical Journal* 740.2, p. 103. ISSN: 0004-637X. DOI: 10.1088/0004-637X/740/2/103. URL: https://iopscience.iop.org/article/10.1088/0004-637X/740/2/103.

Okajima, T. et al. (July 2016). "Performance of NICER flight x-ray concentrator". In: *Proceedings of SPIE*. Ed. by J.-W. A. den Herder, T. Takahashi, and M. Bautz, p. 99054X. DOI: 10.1117/12.2234436. URL: http://proceedings.spiedigitallibrary.org/proceeding.aspx?doi=10.1117/12.2234436.

Oosterbroek, T. ; et al. (1995). "Circinus X-1 revisited: fast-timing properties in relation to spectral state." In: *Astronomy and Astrophysics* 297, pp. 141–158.

Osterbrock, D. E. and J. Michael Shull (Oct. 1989). "Astrophysics of Gaseous Nebulae and Active Galactic Nuclei". In: *Physics Today* 42.10, pp. 123–124. ISSN: 0031-9228. DOI: 10.1063/1.2811187. URL: http://physicstoday.scitation.org/doi/10.1063/1.2811187.

Paczynski, B. (Sept. 1971). "Evolutionary Processes in Close Binary Systems". In: *Annual Review of Astronomy and Astrophysics* 9.1, pp. 183–208. ISSN: 0066-4146. DOI: 10.1146/annurev.aa.09.090171.001151. URL: https://www.annualreviews.org/doi/10.1146/annurev.aa.09.090171.001151.

Pajot, F. et al. (Dec. 2018). "The Athena X-ray Integral Field Unit (X-IFU)". In: *Journal of Low Temperature Physics* 193.5-6, pp. 901–907. ISSN: 0022-2291. DOI: 10.1007/s10909-018-1904-5. URL: http://link.springer.com/10.1007/s10909-018-1904-5.

Parkinson, P. M. S. et al. (Sept. 2003). "Long-Term X-Ray Variability of Circinus X-1". In: *The Astrophysical Journal* 595.1, pp. 333–341. ISSN: 0004-637X. DOI: 10.1086/377193. URL: https://iopscience.iop.org/article/10.1086/377193.

Peraiah, A. (Nov. 2001). *An Introduction to Radiative Transfer*. Cambridge University Press, p. 492. ISBN: 9780521779890. DOI: 10.1017/CBO9781139164474. URL: https://www.cambridge.org/core/product/identifier/9781139164474/type/book.

Porquet, D. and J. Dubau (May 2000). "X-ray photoionized plasma diagnostics with helium-like ions. Application to warm absorber-emitter in active galactic nuclei". In: *Astronomy and Astrophysics Supplement Series* 143.3, pp. 495–514. ISSN: 0365-0138. DOI: 10.1051/aas:2000192. URL: http://aas.aanda.org/10.1051/aas:2000192.

Pradhan, A. K. and S. N. Nahar (Jan. 2011). *Atomic Astrophysics and Spectroscopy*. Cambridge University Press. ISBN: 9780521825368. DOI: 10.1017/CBO9780511975349. URL: https://www.cambridge.org/core/product/identifier/9780511975349/type/book.

Predehl, P. and J. H. M. M. Schmitt (1995). "X-raying the interstellar medium: ROSAT observations of dust scattering halos." In: *Astronomy and Astrophysics* 293, pp. 889–905.

Prigozhin, G. et al. (Sept. 2012). "Characterization of the silicon drift detector for NICER instrument". In: *Proceedings of SPIE*. Ed. by A. D. Holland and J. W. Beletic, p. 845318. DOI: 10.1117/12.926667. URL: http://proceedings.spiedigitallibrary.org/proceeding.aspx?doi=10.1117/12.926667.

Qu, J. L., W. Yu, and T. P. Li (July 2001). "The Cross Spectra of Circinus X-1: Evolution of Time Lags". In: *The Astrophysical Journal* 555.1, pp. 7–11. ISSN: 0004-637X. DOI: 10.1086/321460. URL: https://iopscience.iop.org/article/10.1086/321460.

Reig, P. (Mar. 2011). "Be/X-ray binaries". In: *Astrophysics and Space Science* 332.1, pp. 1–29. ISSN: 0004-640X. DOI: 10.1007/s10509-010-0575-8. URL: http://link.springer.com/10.1007/s10509-010-0575-8.

Rybicki, G. B. and A. P. Lightman (May 1985). *Radiative Processes in Astrophysics*. Wiley. ISBN: 9780471827597. DOI: 10.1002/9783527618170. URL: https://onlinelibrary.wiley.com/doi/book/10.1002/9783527618170.

Saftly, W. et al. (June 2013). "Using hierarchical octrees in Monte Carlo radiative transfer simulations". In: *Astronomy & Astrophysics* 554, A10. ISSN: 0004-6361. DOI: 10.1051/0004-6361/201220854. URL: http://www.aanda.org/10.1051/0004-6361/201220854.

Scargle, J. D. et al. (Feb. 2013). "STUDIES IN ASTRONOMICAL TIME SERIES ANALYSIS. VI. BAYESIAN BLOCK REPRESENTATIONS". In: *The Astrophysical Journal* 764.2, p. 167. ISSN: 0004-637X. DOI: 10.1088/0004-637X/764/2/167. arXiv: 1207.5578. URL: https://ui.adsabs.harvard.edu/abs/2013ApJ...764..167S/abstract%20https://iopscience.iop.org/article/10.1088/0004-637X/764/2/167.

Schulz, N. S. and W. N. Brandt (June 2002). "Variability of the X-Ray P Cygni Line Profiles from Circinus X-1 near Zero Phase". In: *The Astrophysical Journal* 572.2, pp. 971–983. ISSN: 0004-637X. DOI: 10.1086/340369. URL: https://iopscience.iop.org/article/10.1086/340369%20http://asc.harvard.edu/udocs/docs..

Schulz, N. S. et al. (Jan. 2008). "The Variable Warm Absorber in Circinus X-1". In: *The Astrophysical Journal* 672.2, pp. 1091–1102. ISSN: 0004-637X. DOI: 10.1086/523809. URL: https://iopscience.iop.org/article/10.1086/523809%20http://heasarc.gsfc.nasa.gov/docs/xanadu/xspec/index.html..

Schulz, N. S. et al. (Mar. 2020). "Origins of X-Ray Line Emissions in Circinus X-1 at Very Low X-Ray Flux". In: *The Astrophysical Journal* 891.2, p. 150. ISSN: 1538-4357. DOI: 10.3847/1538-4357/ab6dc8. arXiv: 2001.05638. URL: https://iopscience.iop.org/article/10.3847/1538-4357/ab6dc8%20http://arxiv.org/abs/2001.05638.

Serlemitsos, P. J. et al. (Jan. 2007). "The X-Ray Telescope onboard Suzaku". In: *Publications of the Astronomical Society of Japan* 59.sp1, S9–S21. ISSN: 0004-6264. DOI: 10.1093/pasj/59.sp1.S9. URL: https://academic.oup.com/pasj/article-lookup/doi/10.1093/pasj/59.sp1.S9.

Shirey, R. E. et al. (Sept. 1996). "X-Ray Timing and Spectral Evolution of Circinus X-1 versus Orbital Phase with the [ITAL]Rossi X-Ray Timing Explorer[/ITAL]". In: *The Astrophysical Journal* 469.1, pp. L21–L24. ISSN: 0004637X. DOI: 10.1086/310264. URL: https://iopscience.iop.org/article/10.1086/310264.

Shirey, R. E. et al. (Oct. 1998). "Quasi-periodic Oscillations Associated with Spectral Branches in Rossi X - Ray Timing Explorer Observations of Circinus X-1". In: *The Astrophysical Journal* 506.1, pp. 374–383. ISSN: 0004-637X. DOI: 10.1086/306247. URL: https://iopscience.iop.org/article/10.1086/306247.

Shirey, R. E., A. M. Levine, and H. V. Bradt (Oct. 1999). "Scattering and Iron Fluorescence Revealed during Absorption Dips in Circinus X-1". In: *The Astrophysical Journal* 524.2, pp. 1048–1058. ISSN: 0004-637X. DOI: 10.1086/307849. URL: https://iopscience.iop.org/article/10.1086/307849.

Steinacker, J., M. Baes, and K. D. Gordon (Aug. 2013). "Three-Dimensional Dust Radiative Transfer". In: *Annual Review of Astronomy and Astrophysics* 51.1, pp. 63–104. ISSN: 0066-4146. DOI: 10.1146/annurev-astro-082812-141042. URL: https://www.annualreviews.org/doi/10.1146/annurev-astro-082812-141042.

Stewart, R. T. et al. (Nov. 1991). *On the puzzling nature of the X-ray binary Circinus X-1*. Tech. rep. 2, pp. 212–216. DOI: 10.1093/mnras/253.2.212. URL: https://academic.oup.com/mnras/article-lookup/doi/10.1093/mnras/253.2.212.

Stewart, R. T. et al. (Apr. 1993). "Circinus X - 1: a runaway binary with curved radio jets". In: *Monthly Notices of the Royal Astronomical Society* 261.3, pp. 593–598. ISSN: 0035-8711. DOI: 10.1093/mnras/261.3.593. URL: https://academic.oup.com/mnras/article-lookup/doi/10.1093/mnras/261.3.593.

Takahashi, T. et al. (Jan. 2007). "Hard X-Ray Detector (HXD) on Board Suzaku". In: *Publications of the Astronomical Society of Japan* 59.sp1, S35–S51. ISSN: 0004-6264. DOI: 10.1093/pasj/59.sp1.S35. URL: https://academic.oup.com/pasj/article-lookup/doi/10.1093/pasj/59.sp1.S35.

Takayanagi, K. (2009). *[Atomic and Molecular Physics] Genshi Bunshi Butsurigaku (in Japanese*. 3rd ed. Asakura Publishing Co., Ltd. ISBN: 978-4-254-13681-4.

Tanimoto, A. et al. (May 2019). "XCLUMPY: X-Ray Spectral Model from Clumpy Torus and Its Application to the Circinus Galaxy". In: *The Astrophysical Journal* 877.2, p. 95. ISSN: 1538-4357. DOI: 10.3847/1538-4357/ab1b20. URL: https://iopscience.iop.org/article/10.3847/1538-4357/ab1b20.

Tarter, C. B., W. H. Tucker, and E. E. Salpeter (June 1969). "The Interaction of X-Ray Sources with Optically Thin Environments". In: *The Astrophysical Journal* 156, p. 943. ISSN: 0004-637X. DOI: 10.1086/150026. URL: http://adsabs.harvard.edu/doi/10.1086/150026.

Tashiro, M. S. (Feb. 2023). "XRISM: X-ray imaging and spectroscopy mission". In: *The Sixteenth Marcel Grossmann Meeting*. WORLD SCIENTIFIC, pp. 95–103. ISBN: 978-981-12-6976-9. DOI: 10.1142/9789811269776_0006. URL: https://www.worldscientific.com/doi/10.1142/9789811269776%7B%5C_%7D0006.

Tauris, T. M. et al. (Dec. 1999). "Circinus X-1: survivor of a highly asymmetric supernova". In: *Monthly Notices of the Royal Astronomical Society* 310.4, pp. 1165–1169. ISSN: 0035-8711. DOI: 10.1046/j.1365-8711.1999.03068.x. URL: https://academic.oup.com/mnras/article-lookup/doi/10.1046/j.1365-8711.1999.03068.x.

Tennant, A. F., A. C. Fabian, and R. A. Shafer (July 1986a). "Observation of type IX-ray bursts from Cir X-1". In: *Monthly Notices of the Royal Astronomical Society* 221.1, 27P–31P. ISSN: 0035-8711. DOI: 10.1093/mnras/221s.1.27P. URL: https://academic.oup.com/mnras/article-lookup/doi/10.1093/mnras/221.1.27P.

Tennant, A. F., A. C. Fabian, and R. A. Shafer (Apr. 1986b). "The discovery of X-ray bursts from Cir X-1". In: *Monthly Notices of the Royal Astronomical Society* 219.4, pp. 871–881. ISSN: 0035-8711. DOI: 10.1093/mnras/219.4.871. URL: https://academic.oup.com/mnras/article-lookup/doi/10.1093/mnras/219.4.871.

Tennant, A. F. (June 1987). "High-frequency oscillations from Cir X-1". In: *Monthly Notices of the Royal Astronomical Society* 226.4, pp. 971–978. ISSN: 0035-8711. DOI: 10.1093/mnras/226.4.971. URL: https://academic.oup.com/mnras/article-lookup/doi/10.1093/mnras/226.4.971.

Tomida, H. et al. (Apr. 2011). "Solid-State Slit Camera (SSC) Aboard MAXI". In: *Publications of the Astronomical Society of Japan* 63.2, pp. 397–405. ISSN: 0004-6264. DOI: 10.1093/pasj/63.2.397. URL: https://academic.oup.com/pasj/article-lookup/doi/10.1093/pasj/63.2.397.

Tomaru, R. et al. (June 2023). "A different view of wind in X-ray binaries: the accretion disc corona source 2S 0921-630". In: *Monthly Notices of the Royal Astronomical Society* 523.3, pp. 3441–3449. ISSN: 0035-8711. DOI: 10.1093/mnras/stad1637. URL: https://academic.oup.com/mnras/article/523/3/3441/7188307.

Tominaga, M. et al. (Nov. 2023). "X-Ray Spectral Variations of Circinus X-1 Observed with NICER throughout an Entire Orbital Cycle". In: *The Astrophysical Journal* 958.1, p. 52. ISSN: 0004-637X. DOI: 10.3847/1538-4357/ad0034. URL: https://iopscience.iop.org/article/10.3847/1538-4357/ad0034.

Toor, A. (July 1977). "Millisecond X-ray bursts from Circinus X-1". In: *The Astrophysical Journal* 215, p. L57. ISSN: 0004-637X. DOI: 10.1086/182477. URL: http://adsabs.harvard.edu/doi/10.1086/182477.

Tsujimoto, M. et al. (Jan. 2024). "Spectral Modeling of the Supersoft X-Ray Source CAL87 Based on Radiative Transfer Codes". In: *The Astrophysical Journal* 960.1, p. 46. ISSN: 0004-637X. DOI: 10.3847/1538-4357/ad0bfa. URL: https://iopscience.iop.org/article/10.3847/1538-4357/ad0bfa.

Tsunemi, H. ; et al. (1989). "All sky monitor on board the GINGA satellite and its performance." In: *Publications of the Astronomical Society of Japan* 41.January, pp. 391–403. URL: https://ui.adsabs.harvard.edu/abs/1989PASJ...41..391T.

Tudose, V. et al. (Oct. 2008). "A decade of radio imaging the relativistic outflow in the peculiar X-ray binary Circinus X-1". In: *Monthly Notices of the Royal Astronomical Society* 390.1, pp. 447–464. ISSN: 00358711. DOI: 10.1111/j.1365-2966.2008.13788.x. URL: https://academic.oup.com/mnras/article-lookup/doi/10.1111/j.1365-2966.2008.13788.x.

Umemura, M., J. Fukue, and H. Nomura (2016). *[Radiative Tranfer and Radiative Hydrodynamics] Fukusha Yuso to Fukusha Ryutai Rikigaku (in Japanese)*. 1st ed. NIPPON HYORON SHA CO.,LTD. ISBN: 9784535603424.

Vander Meulen, B. et al. (June 2023). "X-ray radiative transfer in full 3D with SKIRT". In: *Astronomy & Astrophysics* 674, A123. ISSN: 0004-6361. DOI: 10.1051/0004-6361/202245783. URL: https://www.aanda.org/10.1051/0004-6361/202245783.

Verner, D. A. et al. (July 1996). "Atomic Data for Astrophysics. II. New Analytic FITS for Photoionization Cross Sections of Atoms and Ions". In: *The Astrophysical Journal* 465, p. 487. ISSN: 0004-637X. DOI: 10.1086/177435. URL: http://adsabs.harvard.edu/doi/10.1086/177435.

Watanabe, S. et al. (Nov. 2003). "Detection of a Fully Resolved Compton Shoulder of the Iron K Line in the Chandra X-Ray Spectrum of GX 301-2". In: *The Astrophysical Journal* 597.1, pp. L37–L40. ISSN: 0004-637X. DOI: 10.1086/379735. URL: https://iopscience.iop.org/article/10.1086/379735.

Watanabe, S. et al. (Nov. 2006). "X-Ray Spectral Study of the Photoionized Stellar Wind in Vela X-1". In: *The Astrophysical Journal* 651.1, pp. 421–437. ISSN: 0004-637X. DOI: 10.1086/507458. URL: https://iopscience.iop.org/article/10.1086/507458.

Weisskopf, M. C. et al. (July 2000). "Chandra X-ray Observatory (CXO): overview". In: ed. by J. E. Truemper and B. Aschenbach, pp. 2–16. DOI: 10.1117/12.391545. URL: http://proceedings.spiedigitallibrary.org/proceeding.aspx?articleid=899821.

Weisskopf, M. C. et al. (Jan. 2002). "An Overview of the Performance and Scientific Results from the Chandra X-Ray Observatory". In: *Publications of the Astronomical Society of the Pacific* 114.791, pp. 1–24. ISSN: 0004-6280. DOI: 10.1086/338108. URL: http://iopscience.iop.org/article/10.1086/338108.

White, N. E., L. Stella, and A. N. Parmar (Jan. 1988). "The X-ray spectral properties of accretion discs in X-ray binaries". In: *The Astrophysical Journal* 324, p. 363. ISSN: 0004-637X. DOI: 10.1086/165901. URL: http://adsabs.harvard.edu/doi/10.1086/165901.

Wilms, J., A. Allen, and R. McCray (Oct. 2000). "On the Absorption of X-Rays in the Interstellar Medium". In: *The Astrophysical Journal* 542.2, pp. 914–924. ISSN:

0004-637X. DOI: 10.1086/317016. arXiv: 0008425 [astro-ph]. URL: https://iopscience.iop.org/article/10.1086/317016.

Yeh, J. and I. Lindau (Jan. 1985). "Atomic subshell photoionization cross sections and asymmetry parameters". In: *Atomic Data and Nuclear Data Tables* 32.1, pp. 1–155. ISSN: 0092640X. DOI: 10.1016/0092-640X(85)90016-6. URL: https://linkinghub.elsevier.com/retrieve/pii/0092640X85900166.

Yusef-Zadeh, F., M. Morris, and R. L. White (Mar. 1984). "Bipolar reflection nebulae - Monte Carlo simulations". In: *The Astrophysical Journal* 278, p. 186. ISSN: 0004-637X. DOI: 10.1086/161780. URL: http://adsabs.harvard.edu/doi/10.1086/161780.

Revisions

Table 8.1: Revisions

Date	Comments
2023/12/21	Submitted for the application of a Ph.D. degree in astronomy.
2024/02/06	Changed the style of the title page. Revised English and grammar. Revised acknowledgment and abstract. Added some results in § 7.2.1 and § 7.2.2. Revised the size of the geometry and re-simulated in § 7.2.3. Revised some summary in § 8.1.

Acknowledgements

本論文を執筆するにあたり、ご協力くださった方々に深く感謝申し上げます。

指導教官である海老沢研教授には、5年間大変お世話になりました。本研究の対象天体であるCir X-1は、修士課程1年の際、海老沢さんに「こんな変な天体があるよ」と紹介してもらったことで初めて知りました。モニタリングデータから周期的変動の特性を見出したものの、分光データが不足していたことから、*NICER*に観測提案を出してはどうか、とご助言いただきました。私にとっては初めての観測提案執筆だったため、提出期限前日は夜遅く(というか朝)まで修正を繰り返したことがとても懐かしいです。提案が承認されたのは自分の誕生日近くだったので、とても嬉しいプレゼントになりました。実際の観測結果はあまりにリッチで、一つの結果にまとめるのに結局 5 年間かかってしまいましたが、「Cir X-1のバイブル」として本博士論文が十分なものであることを願います。

宇宙科学研究所辻本匡弘准教授には、修士論文執筆の際からご指導いただきました。博士課程に進んでからは、本研究の他にも、LiteBIRD衛星における宇宙放射線の影響評価の共同研究等をさせていただきました。そこで使用したツールであるGeant4が、MONACOの中で使われているとわかった時は大変驚きました。また、ツールを使用する際にはその妥当性を物理に戻って確認するという、修士論文で徹底的に指導されたことを、本研究でも生かすことができました。来年からは民間の研究所で働きますが、この基礎を心に刻み、研究に励みます。 X線天文学は*ASTRO-H*衛星の沈黙からおよそ10年止まっていました。しかし、先日の*XRISM*衛星の打ち上げ・初期運用の成功により、再び進み始めようとしています。辻本さんはこの衛星プロジェクトに多大な貢献を果たされたと個人的には感じています。まずは、衛星試験等でお忙しい中ご指導いただいたことを改めて感謝申し上げます。私は衛星データのユーザになるだけではなく、衛星開発段階から携わりたいと思い、大学院に進学しました。その思いを汲んでいただき、衛星の地上試験に参加する機会、またプロジェクトの会議で発表する機会を多数いただきました。そこで、人類の能力を超えた装置を作るために、文字通り命を燃やす方々に出会うことができました。現実の厳しさを知るとともに、プロジェクトでものづくりをする世界に強く惹かれました。この経験は、私の進路選択に大きな影響を与えたと思います。また、困難な要求や膨大な仕事量の中でタイムマネジメントする大切さを教わりました。この5年間を通して、一番身についた力かもしれません。これからの研究者人生で共同研究をする機会があるかはわかりませんが、常に師の教えを思いだし、研究に真摯に向き合いたいと思います。ありがとうございました。

共同研究者である京都大学榎戸輝揚准教授、忠北大学早崎公威准教授には、上述した観測提案執筆の際から大変お世話になりました。中性子星をはじめとし、幅広い分野で活躍される榎戸さんと、理論家である早崎さんは、いつも違った角度からコメントをしていただきました。論文 (Tominaga et al., 2023)や観測提案の密度を格段に上げることができたと感じています。ありがとうございました。

本博士論文の柱の一つである輻射輸送シミュレーションをするにあたり、MONACOとSKIRT開発チームの皆様には大変お世話になりました。まずは、MONACOを

開発者である大阪大学小高裕和准教授に感謝申し上げます。また、使用方法についてアドバイスをいただいた海老沢研究室ポスドクの丹波翼さんに御礼申し上げます。また、シミュレーションに協力してくれた海老沢研究室新修士課程1年(現東京大学4年生)の厚地凪くんにも感謝いたします。本博士論文では当初、CLOUDYを使用することを検討しておりましたが、Vander Meulen et al. (2023)の発表のおかげで、SKIRTという素晴らしいツールを知り、活用するに至りました。著者である Ghent大学 Bert vander Muelen 氏に直接連絡を取り、大学を訪問し、使い方の修行及び研究への適用の可能性を議論させていただきました。短い時間でここまでツールに習熟できたのはBertのおかげです。ありがとうございました。宇宙研同期の松本光生くんは数年前からGhent大学に留学しており、SKIRTに対して拡張開発を施し、赤外領域でのNLTE計算を可能にしました(Matsumoto et al., 2023)。これをX線に拡張できないか、と度々議論をし、本博士論文でついに実現することができました。これは、現在、X線領域でNLTE計算を行う唯一の3D solverであると言えます。松本くんとこのような形で共同研究ができたことを心から嬉しく思います。ありがとうございました。

博士論文の方向性や議論に際し、井上一先生、Durham大学教授 Chris Done さん、東京都立大学客員研究員 Alfredo Luminariさんには多数の助言をいただきました。お礼申し上げます。

主査であるビッグバン宇宙国際研究センター茂山俊和教授、副査である国立天文台都丸隆行教授、東京大学梅田秀之准教授、外部審査員である筑波大学大須賀健教授、愛媛大学志達めぐみ講師に改めて感謝申しあげます。特に、事前説明では活発な議論をさせていただき、緊張しつつも楽しく審査を終えることができました。専門の違う5名の審査員の皆様からは、全く違う角度から質問をいただきました。その内容はそれぞれのバックグラウンドに基づく、的を射たもので、本博士論文の公聴会での発表を一層充実するものにできたと感じています。

海老沢研究室同期の大間々くん、後輩の栗原くん、望月くん、柏崎さん、森口くん、ポスドクの小川さん、金丸さん、卒業生の御堂岡さんには大変お世話になりました。楽しい大学院生活を送れたのは、皆様のおかげです。同期の八木くん、同じ居室の三浦くん、赤外グループの星くんをはじめ、6階の楽しい宇宙物理学研究系のメンバーに支えられました。

博士課程在籍期間は、修士課程の時から参加していた「きみっしょん」に加え、JAXA宇宙科学研究所の特別公開実行委員として広報活動に携わりました。さまざまな活動を一緒にさせていただいたことで、息抜きができ、楽しく研究をすることができました。特に、村上豪さん、木村駿太さん、梶谷伊織さん、榎木谷海さん、平田佳織さんとは複数の配信活動を一緒に行いました。そのご縁でお仕事を一緒にさせていただくことになったそらビ榎本麗美さんをはじめ、関係者の皆様にお礼申し上げます。趣味である三味線、尺八の師匠方には、不規則なスケジュールな中でもお稽古をつけていただき、ありがとうございました。来年からも楽器を続けていきたいと考えておりますので、引き続きご指導いただけますと幸いです。

私が天文学をやると言った時、全く異なる分野の専門家である両親は驚いたことと思います。ここまで自由に研究させてくれてありがとう。その道のプロフェッショナルである2人を尊敬します。来年からは社会人として恩返しをしていきたいと思います。

最後に、尊敬する最大の友であり、いつも支えてくれる婚約者に、心から感謝します。

ソフトウェア　本研究は、NASA/GSFC の Astrophysics Science Divisionにより提供されている High Energy Astrophysics Science Archive Research Center (HEASARC)のソフトウェア HEAsoft (Nasa High Energy Astrophysics Science Archive Research Center (Heasarc), 2014), Xspec (Arnaud, 1996), XSTAR (T. R. Kallman et al., 2004) を利用しました。また、JAXA 宇宙科学研究所の Center for Science-satellite Operation and Data Archive (C-SODA) による data obtained from Data ARchives and Transmission System (DARTS) を使用しました。理化学研究所、JAXA、*MAXI*チームによる*MAXI*データ、NICER 装置(Gendreau, Arzoumanian, and Okajima, 2012) による取得データを活用しました。

計算機資源　本研究は、宇宙航空研究開発機構スーパーコンピュータシステム『JSS3』を事業名：『科学衛星データの高次データ処理』(事業コード：DU10503) で利用しました。

研究費　本研究は、東京大学宇宙地球フロンティア国際卓越大学院プログラム、日本学術振興会科研費 21J20947、National Research Foundation of Korea (NRF) funded by the Ministry of Education (2016R1A5A1013277 and 2020R1A2C1007219)、the Research Year of Chungbuk National University in 2021 の助成を受けたものです。